Process modeling for the growth of SiC using PVT and TSSG methods

Kanaparin Ariyawong

To cite this version:

Kanaparin Ariyawong. Process modeling for the growth of SiC using PVT and TSSG methods. Materials. Université Grenoble Alpes, 2015. English. <NNT : 2015GREAI030>. <tel-01215171>

HAL Id: tel-01215171
https://tel.archives-ouvertes.fr/tel-01215171

Submitted on 13 Oct 2015

HAL is a multi-disciplinary open access archive for the deposit and dissemination of scientific research documents, whether they are published or not. The documents may come from teaching and research institutions in France or abroad, or from public or private research centers.

L'archive ouverte pluridisciplinaire **HAL**, est destinée au dépôt et à la diffusion de documents scientifiques de niveau recherche, publiés ou non, émanant des établissements d'enseignement et de recherche français ou étrangers, des laboratoires publics ou privés.

UNIVERSITÉ GRENOBLE ALPES

THÈSE

Pour obtenir le grade de

DOCTEUR DE L'UNIVERSITÉ GRENOBLE ALPES

Spécialité : **Matériaux, Mécanique, Génie civil, Electrochimie**

Arrêté ministériel : 7 août 2006

Présentée par

Kanaparin ARIYAWONG

Thèse dirigée par **Jean-Marc DEDULLE** et
codirigée par **Didier CHAUSSENDE**

préparée au sein du **Laboratoire des Matériaux et du Génie Physique**
dans **l'IMEP-2**

Modélisation des procédés de croissance de SiC en phase gazeuse (PVT) et en phase liquide (TSSG)

Thèse soutenue publiquement le **11 May 2015**,
devant le jury composé de :

Prof. Thierry DUFFAR
Professeur, U. Grenoble Alpes, Président
Prof. Gérard VIGNOLES
Professeur, U. Bordeaux 1, Rapporteur
Prof. Peter WELLMANN
Professeur, U. Erlangen-Nürnberg, Rapporteur
Dr. Alain JARDY
Directeur de recherche CNRS, U. de Lorraine, Examinateur
Dr. Gabriel FERRO
Directeur de recherche CNRS, UCB Lyon 1, Examinateur
Dr. Elisabeth BLANQUET
Directeur de recherche CNRS, U. Grenoble Alpes, Examinateur
Dr. Didier CHAUSSENDE
Directeur de recherche CNRS, U. Grenoble Alpes, Co-directeur de thèse
Prof. Jean-Marc DEDULLE
Professeur, U. Grenoble Alpes, Directeur de thèse

UNIVERSITÉ GRENOBLE ALPES

General information

This PhD thesis was conducted at the Laboratoire des Matériaux et du Génie Physique (LMGP) which is a joint research unit of CNRS and Grenoble INP. The laboratory is a research laboratory in materials science and materials for biomedical engineering and it is organized into 3 research teams: Crystal Growth (XTO), Interface between Materials and Biological Matter (IMBM), and Thin films, Nanomaterials and Nanostructures (FM2N).

The current thesis was financially supported by the European Union Seventh Framework Programme under an acronym NetFISiC (Training Network on Functional Interfaces for SiC). The main scientific of the project objective is to provide Silicon carbide material (of various polytypes) with improved and adequate functional interfaces for getting a step forward in electronic devices performance. Research efforts were dedicated to solve the problems faced by important devices like MOSFET and Schottky diodes. Besides, some fundamental research was performed both on the growth aspect and on new and innovating devices. Applications in high temperature, high power and hash environment were targeted.

The NetFISiC consortium is made of 12 European partners, including 3 companies, coming from 7 different countries. In total, 12 early stage researchers (ESR) and 4 experienced researchers (ER) were recruited and trained with the network. The consortium is divided into 3 technical work-packages:

- WP1 (Material growth and related aspects) is dedicated to the development of less mature polytypes than 4H (3C and 15R).
- WP2 (Characterization of material and functional interfaces) is in charge of studying the properties of the materials/surface and interfaces.
- WP3 (Devices and demonstrators) is in charge of the electrical testing and fabrication of the targeted devices.

This thesis was elaborated within the WP1. A close collaboration with another ESR recruited at the same laboratory and within the same work-package was made. The collaboration was focused on developing a better comprehension of the growth of SiC by PVT process using the complete experiments, characterization, and modeling approach. The topics that were tackled

are development of the process, interaction between vapor species with the crucible, foreign polytype nucleation, and nitrogen doping. The experimental results and characterization are given in Chapter 4 and 5.

Apart from the NetFISiC network, collaborations were made with Laboratoire de Science et Ingénierie des Matériaux et Procédés (SIMaP) for the thermodynamic calculations (results are given in Chapter 5) and within LMGP for the combined experiments, characterization, and numerical modeling approach for better visualization and understanding the growth of SiC by Top Seeded Solution Growth (TSSG) process (results are given in Chapter 6).

In total, eight conference proceedings including one oral presentation, and one journal paper were obtained. In addition, four journal papers are in preparations.

Acknowledgement

It is a great pleasure to acknowledge the many people for their help, support, and all kind of effort throughout the period of my PhD thesis.

First of all, I wish to express my deepest gratitude to my supervisor Prof. Jean-Marc Dedulle and my co-supervisor Dr. Didier Chaussende for giving me the opportunity to work with an interesting topic and the opportunity to collaborate with them. From the very first day until the last moment of my thesis, they gave me not only many helpful suggestions for improving my works, but they also shown me the way of becoming a real scientist. With his kindness and clear explanations, Jean-Marc really paved me the way for understanding and advancing the field of process modeling. From the many discussions we had, Didier undoubtedly helped and impressed me by his real experience and perspectives as a crystal grower. Special thanks would go to Dr. Gabriel Ferro. Through his sympathetic questions and advices, Gabriel certainly comforted me and assisted me to improve my presentation skill. I will keep all their guidance and effort as an invaluable gift they gave to me.

Second, I would like to thank Dr. Elisabeth Blanquet and Prof. Christian Chatillon for their very kind help, collaboration, and discussion throughout the work related to the thermodynamic calculations. Special thanks go to Prof. Michel Pons for his kindness and many fruitful discussions as one of the experts in the process modeling of SiC. I would really appreciate to thank to Dr. Frederic Mercier for his gentle explanations and discussions concerning the modeling of the TSSG process.

I would like also to thank to the current and former members of the Cristallogenese group, Roland Madar, Thierry Ouisse, Odette Chaix, Eirini Sarigianaidou, Pierre Bouvier, Joseph La Manna, Lucile Parent-Bert, Julien Lefebure, Sven Tengeler, Lu Shi, Martin Seisse, Le Thi Mai Hoa, Hoang-Long LE-TRAN, and Demitrios Zevgitis for their help, support, and friendships. We shared many great times both inside the laboratory and many events arranged outside. For me, they have been all like my family. Special thanks would go to my colleague Dr. Nikolaos Tsavdaris and PhD student Yun Ji Shin. Apart from the daily scientific discussions and their contributions to the many results in my thesis, they have been my good

friends. We have been through both happiness and anxiousness moments. I am honestly pleased to collaborate and be friend with them.

I would also appreciate to thank to all the members of Laboratoire des Materiaux et du Genie Physique for their kindness and hospitality. Their warm greeting created a generous working environment. Exclusively thanks would go to the former director Dr. Bernard Chenevier and the current director Dr. Franz Bruckert of the lab. The technical assistance for computing resource from Arnaud Robin is also greatly acknowledged.

I am sincerely grateful to the consortium of a European project NetFISiC (young researcher and their suporvisors) for sharing their views and experience in the field of SiC material and related techniques during the common shared training events and conferences which built me a strong scientific background in the research field. Besides, the friendships created within the network are incalculable.

I should thank to the many people writing papers as well as textbooks which I used as the references. Without them, I would not have enough information and idea to complete this thesis.

Finally, it is difficult to exaggerate my appreciation to my parents and my brother. Throughout my life, they always support me, teach me, encourage me, as well as love me.

Contents

Chapter 1 Introduction 1

Chapter 2 Silicon carbide, Growth processes and modeling 5

2.1 SiC crystal structure and polytypes 5

2.2 Basic properties and electronic applications of SiC 7

2.3 Growth processes 9

2.3.1 Growth from vapor phase 10

2.3.2 Growth from liquid phase 13

2.4 Process modeling 14

2.5 Proposes of this thesis work 17

Chapter 3 Finite Element Method (FEM) 23

3.1 Overview of the method 24

3.2 Example of heat transfer in steady state 30

3.3 A nonlinear system 36

Chapter 4 Induction heating and heat transfer 39

4.1 Physical model 39

4.1.1 Induction heating 39

4.1.2 Heat transfer 42

4.2 Boundary conditions 45

4.2.1 Electromagnetic boundary conditions 45

4.2.2 Heat transfer boundary conditions 45

4.3 Semi-transparency of SiC 47

4.4 Modeling results and validations 55

4.4.1 I-V characteristic and measurement 56

4.4.2 Geometry and temperature distribution 58

4.4.3 Effect of coil position 61

4.5 Conclusion 64

Chapter 5 Mass transport 67

5.1 Physical model 67

5.2 Boundary conditions 71

5.3 Comparative approach 76

5.3.1 Atomic fluxes balance (AFB) 76

5.3.2 Adaptable sticking coefficients 77

5.3.3 Numerical modeling 78

5.3.4 Thermodynamic calculations 82

5.3.5 Discussion 85

5.4 Effect of choice of thermodynamic databases 87

5.4.1 Equilibrium partial pressure in front of SiC-C diphasic mixture 87

5.4.2 Growth rate 88

5.4.3 Si/C ratio 90

5.4.4 Discussion 90

5.5 Coupled approach 91

5.5.1 Method and calculations 91

5.5.2 Results 95

5.5.3 Discussion 97

5.6 Interaction between vapor species and graphite crucible 100

5.6.1 Method and calculations 101

5.6.2 Results and discussion 102

5.7 General modeling results and validations 106

5.8 Conclusion 109

Chapter 6 Top Seeded Solution Growth 113

6.1 Physical model and boundary conditions for induction heating and fluid dynamics 113

6.1.1 Buoyancy convection 115

6.1.2 Forced convection 116

6.1.3 Marangoni convection 117

6.1.4 Electromagnetic convection 119

6.2 Physical model and boundary conditions for mass transfer 120
6.3 Modeling results and the effect of the process parameters 121
6.3.1 Effect of crystal rotation 126
6.3.2 Effect of frequency 130
6.4 Combined numerical and analytical modeling 134
6.5 Conclusion 142

Chapter 7 General conclusions and perspectives 145

Appendix A Physical properties 149
A.1 Electromagnetic properties 149
A.2 Properties of the gas phase 149
A.2.1 Thermal properties 149
A.2.2 Fluid flow properties 151
A.2.3 Mass transport properties 151
A.3 Properties of various materials used in the modeling 152

Appendix B List of symbols 157

Résumé 161

Chapter 1
Introduction

Silicon carbide (SiC) is a wide bandgap semiconductor material. Its properties make it adapted for electronic devices requiring high temperature, high frequency, high power, and/or hash environment operation. SiC exists in different kind of polytypes which are coming from a one-dimensional polymorphism. The difference in stacking sequences leads to different properties of each polytype, such as, bandgap, electrical breakdown voltage. This broadens the area of SiC application. The most technologically important polytypes are 3C, 4H, 6H, and 15R-SiC.

For SiC single crystal growth, the Physical Vapor Transport (PVT) process has shown its ability for the growth of high quality and large size crystals. The demonstration of 6 inch diameter SiC wafers has been achieved. "Defect-free" wafer was also claimed to be realized. However, only the 4H and 6H-SiC polytypes are commercially available. There is no 3C or 15R-SiC wafers with adequate quality for electronic devices owing to the difficulties in getting the stable growth conditions for these two polytypes. Besides, the liquid phase route, especially the Top Seeded Solution Growth (TSSG) process has brought back a huge attention concerning research and development in the past ten years. The "lower" growth temperatures used in such process and the "closer" to thermodynamic equilibrium conditions are expected to provide better control of defects generation. Though lower than PVT, the growth temperatures are still high, which makes the process very difficult to control. Due to the high temperatures (typically about 2000 °C), there is no way to measure the process parameters. The best approach to access such information is to use the modeling which serves as a tool for "process characterization". The proper model is necessary to pave the way first for a better understanding and second for a better monitoring of the growth process.

The aim of this work is to better understand the basic physical phenomena occurring in the growth reactors by making use of the numerical modeling. This present thesis will be structured as follow.

Chapter 2 is devoted to provide an overview of SiC material, its growth processes and modeling. In the first part, its crystal structure, polytypes, properties, and its applications in power electronic devices will be given. Secondly, the bulk growth processes will be described and the significant contribution of the process modeling will be discussed regarding the process development. The purposes of this thesis will then be detailed.

In Chapter 3, an introduction to the Finite Element Method (FEM) which is the basis of the numerical modeling used throughout this thesis will be given. This method is capable of solving partial differential equations (PDEs). It has been proved to be a powerful tool in the modeling of electromagnetic problems of irregular geometry. This is perfectly adapted to our case in which the induction heating of complex reactor geometry has been used. An overview of the method will be first given. Then we will provide an example of using FEM for modeling the heat transfer in steady state. Since the PDEs associated with the growth processes are generally nonlinear, an approach for solving nonlinear system will be discussed at the end of the chapter.

Chapter 4 is dedicated to the modeling of induction heating and heat transfer. This chapter is divided into four main sections. First, the physical model including induction heating and heat transfer will be given. The boundary conditions for electromagnetic and heat transfer will also be given in the second section. In the third section, we will discuss the model treating SiC as a semi-transparent media. Its spatial and temporal effect on the growth process and the limitations of such model will be also discussed. The last section focuses on the modeling results and validations. This includes the computed I-V characteristic and measurement, temperature distribution, and the effect of coil position.

In Chapter 5, the modeling of mass transport that couples the vapor species transport and the fluid flow in the PVT system will be first given. This includes again the physical model and boundary conditions. Such coupled model make used of the temperature profile computed from the induction heating and heat transfer model. Then special attention will be paid to the chemical reactions at the solid-vapor interfaces. Both ‘comparative’ and ‘coupled’ approaches will be

discussed. Those approaches are characterized by the strength of the coupling between mass transport modeling and thermodynamics. In addition to the effect of the thermodynamic databases in the full process modeling using the former approach, the capability and the extension possibility of the latter approach will be discussed. Finally, general modeling results and validations will be presented.

Chapter 6 contributes to the modeling of the TSSG process. Similar to the two former chapters, physical model and boundary conditions will be first discussed. This is followed by the study of the effects of the process parameters, namely, crystal rotation speed and operating frequency, on the growth of SiC crystals. In the last part of this chapter, a combined numerical and analytical model will be presented. This model has been developed for getting a comprehensive visualization of the interaction between the fluid flow and the step flow that will affect the surface morphology of the crystal. The validation of this model is included.

The last chapter will give the general conclusions of this thesis. Open issues and the perspective for the future work will also be discussed.

Chapter 2
Silicon Carbide
Growth processes and modeling

Silicon carbide (SiC) is a wide bandgap semiconductor material. Its potential is far beyond silicon and very highly desirable for electronic devices, especially for high power, high temperature, and high frequency applications [1]. In this chapter, SiC crystal structure and polytypes will be described followed by its basic properties and electronic applications. Then, an overview of the growth processes for producing SiC single crystals, focusing on the bulk growth technique, will be given. Finally, the importance of numerical modeling for SiC growth processes and the aims of this thesis will be discussed.

2.1 SiC crystal structure and polytypes

Silicon carbide is a solid compound consisting of 50% of carbon and 50% of silicon. Thus the stoichiometric coefficient for both silicon and carbon are unity. Concerning the structure of carbon and silicon atoms in SiC, all silicon (carbon) atoms are surrounded by four carbon (silicon) atoms forming a tetrahedron (Fig. 2.1). The nearest neighbors to any Si or C atom in the crystal are similar. The distance between same type of atom is approximately 3.08 Å [2] with small variation depending on the polytype. The bonding between Si and C atoms of SiC composes of primary covalent and partly ionic (88% covalent and 12% ionic) where the Si atoms are positively charged.

In the crystallization process, SiC establishes a special case of polymorphism called polytypism. It is the phenomenon of one-dimensional polymorphism that takes the different crystal structures with the same chemical composition. All SiC polytypes are composed of a closed-packed stacking of double layers of Si and C atoms. The stacking of double layers is easily shown in the hexagonal system with three different positions of atom pair labeled by A, B,

and C (Fig. 2.2). By creating an ordering in stacking sequences of the layers, a variety of polytypes can be constructed. Examples of different polytype stacking sequences on the (11-20) plane can be seen in Fig. 2.3. The Ramsdell notation is a common nomenclature used to described the polytypes [3]. Such notation utilizes a number and a letter in order to identify the different polytypes. The number defines the number of double layers in a unit cell, while the letter defines the symmetry of the lattice. There are three crystal symmetries in the different SiC polytypes: cubic (C), hexagonal (H), and rhombohedral (R). The three most technological important polytypes are 3C, 4H, and 6H having ABC, ABAC, and ABCACB stacking sequences, respectively. The cubic polytype is normally referred as β-SiC, whereas the hexagonal and rhombohedral ones are referred as α-SiC. More than 200 polytypes have been reported; some of them have a stacking period of several hundreds of double layer and the largest primitive unit cell of SiC contains 594 layers [4]. In addition, SiC is considered as a polar crystal. By cutting the crystal perpendicular to the c-axis, the C-Si bonds are cut and the crystal is split into two different faces, Si-face and C-face having different reactivity, i.e. different chemical and growth behavior.

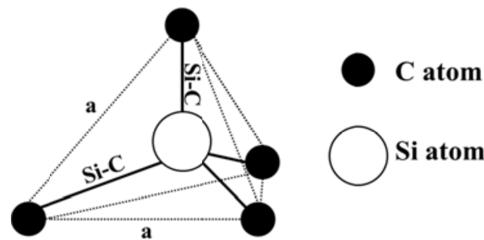

Fig. 2.1 The tetrahedral structure of Si and C atoms in SiC

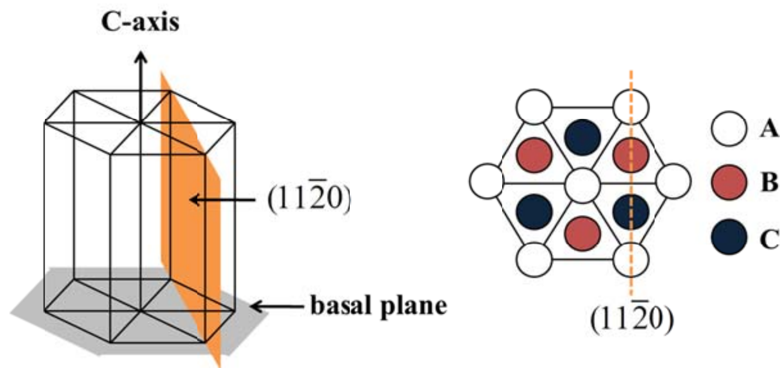

Fig. 2.2 The hexagonal system used to described the three different positions, A, B, and C of the double layer

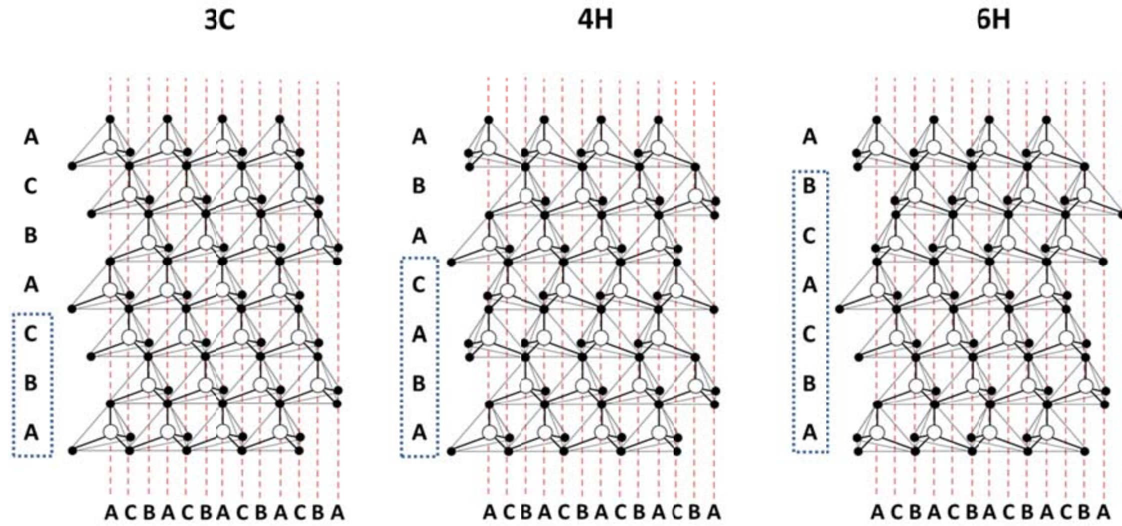

Fig. 2.3 The stacking sequences of three different polytypes: 3C, 4H, and 6H

2.2 Basic properties and electronic applications of SiC

Silicon carbide provides multiple advantages for electronic devices, especially the ones those require to operate at high power, high temperature, and high voltage. The superior properties of SiC compared to other semiconductor materials are, for example, a higher electrical breakdown field, a higher thermal conductivity, a larger saturated electron drift velocity (Table 2.1). Most of the physical properties of all SiC polytypes are identical except the large variation of electrical and optical properties. Moreover, some important electrical properties are also non-isotropic even within a given polytype. They are strongly dependent on the crystallographic direction of the current flow and the applied electric field. The wide band gap and high thermal stability make SiC based devices suitable for operating at higher temperature compared to Si based devices. Due to the high electrical breakdown field strength in SiC, the devices can be operated at high voltage with low power losses. Moreover, the heat generated from the power losses is efficiently dissipated thanks to the high thermal conductivity. The spider web diagram (Fig. 2.4) clearly shows the superior properties of 4H-SiC over Si for power electronic devices. GaN is shown to be a possible candidate for such applications but its process engineering is still far below SiC technology. Combining all these advantages of SiC, it is possible to decrease the size and increase the efficiency of the devices. An example is an announcement of the world's first all-SiC power modules consisting of SiC transistors and diodes by Mitsubishi Electric

Corporation [5]. Compared to the conventional invertor systems with IGBT power module, both size and weight of all-SiC invertor are reduced by 65% (Fig. 2.5) and the switching losses are about 55% less. These new power modules are expected to reduce power consumption as well as the size and weight of the equipment used in high power trains.

Table 2.1 Physical properties of SiC in comparison with other semiconductor materials [6]

Material	E_g (eV)	n_i (cm^{-3})	ε_r	μ_n ($cm^2/V\cdot s$)	E_c (MV/cm)	v_{sat} (10^7 cm/s)	λ (W/cm·K)	Direct/Indirect
Si	1.1	$1.5x10^{10}$	11.8	1350	0.3	1.0	1.5	I
Ge	0.66	$2.4x10^{13}$	16.0	3900	0.1	0.5	0.6	I
GaAs	1.4	$1.8x10^{6}$	12.8	8500	0.4	2.0	0.5	D
GaP	2.3	$7.7x10^{-1}$	11.1	350	1.3	1.4	0.8	I
InN	1.86	$\sim10^{3}$	9.6	3000	1.0	2.5	-	D
GaN	3.39	$1.9x10^{-10}$	9.0	900	3.3	2.5	1.3	D
3C-SiC	2.2	6.9	9.6	900	1.2	2.0	4.5	I
4H-SiC	3.26	$8.2x10^{-9}$	10	720^a 650^c	2.0	2.0	4.5	I
6H-SiC	3.0	$2.3x10^{-6}$	9.7	370^a 50^c	2.4	2.0	4.5	I
Diamond	5.45	$1.6x10^{-27}$	5.5	1900	5.6	2.7	20	I
BN	6.0	$1.5x10^{-31}$	7.1	5	10	1.0*	13	I
AlN	6.1	$\sim10^{-31}$	8.7	1100	11.7	1.8	2.5	D

Note: a - mobility along a-axis, c - mobility along c-axis, * - estimate

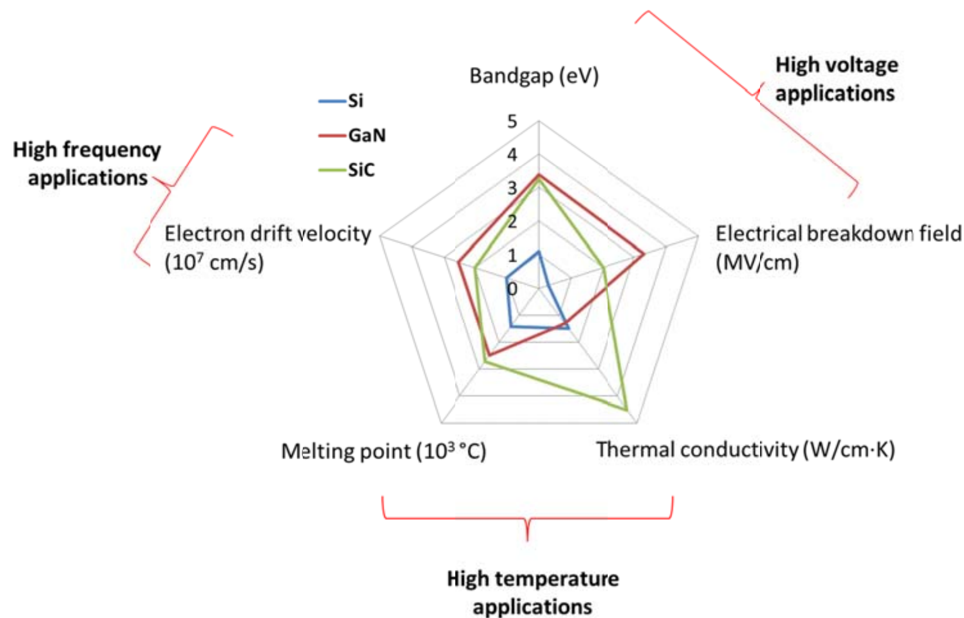

Fig. 2.4 Comparison of Si, GaN, and SiC properties for power electronic devices applications

Fig. 2.5 Size reduction of all-SiC invertor compared to conventional invertor [5]

2.3 Growth processes

Silicon carbide was discovered in 1824 by the Swedish chemist, Jons Jacob Berzelius [7], even though, its properties were not understood at that time. In 1892, E. G. Acheson invented a process to synthesize large quantities of SiC [8]. Such achievement was driven by an effort to find a material that can replace diamond for cutting and polishing applications. In the Acheson's process, a mixture of sand sawdust and coke was heated in a furnace up to 2700 °C. The product was called 'carborundum'. It exhibits a high hardness, a great refractability and infusibility. In 1905, the French chemist Henry Moissan found natural SiC in a meteorite [9]. This is the reason why mineralogists usually call natural SiC as moissanite.

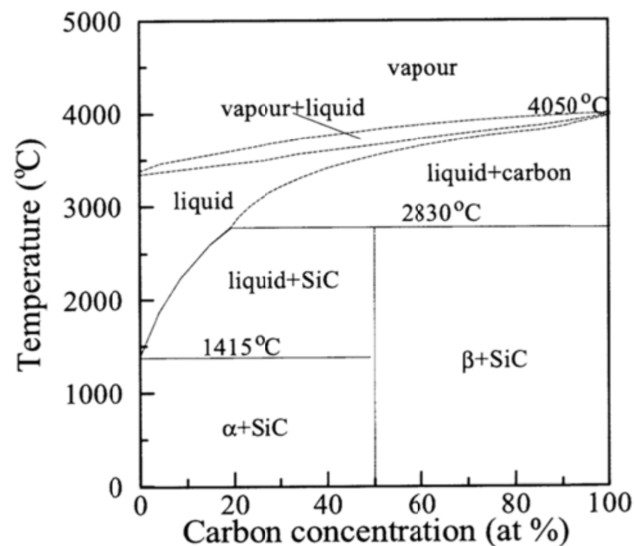

Fig. 2.6 Phase diagram of Si-C system where α and β denote solid solution of C in Si and Si in C, respectively [10]

Due to the fact that SiC does not exist in liquid phase as can be seen from the phase diagram of Si-C system (Fig. 2.6), the conventional method used to grow Si and other semiconductors based on the solidification from liquid phase cannot be applied. Alternative growth techniques are then necessary to realize the growth of SiC. Concerning the bulk growth process, a variety of growth techniques has been studied, such as, the Lely method, Modified-Lely method, High Temperature Chemical Vapor Deposition (HTCVD), Continuous Feed-PVT (CF-PVT), and Top Seeded Solution Growth (TSSG) processes. Those techniques can be grouped into two main routes: vapor phase route and liquid phase route. Overview on the growth of SiC single crystal for both routes focusing on the new emerging processes was discussed in [11].

2.3.1 Growth from vapor phase

One of the big steps in the advancement of the SiC growth process can be attributed to the invention of the Lely growth method in 1955 [12]. The schematic representation the process design and the temperature profile can be shown in Fig. 2.7a. The SiC powder source was put between the wall of graphite crucible and the porous graphite leaving the empty space at the center of the crucible. The temperature distribution is adjusted so that the center of the cylindrical growth chamber has a minimum temperature. Thus at elevated temperature, the vapor species sublimed from the source will travel toward the center. The porous graphite will then behave as a center for the nucleation. Due to the fact that the growth is performed close to the equilibrium and the growth can be assimilated to spontaneous nucleation, the growing crystals have very low defect density and are almost free of micropipe. The main drawback of this growth method is the limited and random size of the crystals.

In 1978, Tairov and Tsvetkov [13] developed the so called modified Lely growth method also known as Physical Vapor Transport (PVT) or seeded sublimation method. The concept is to sublime the SiC powder source at high temperature, the Si and C containing gas species are then transported by the physical mean (mainly diffusion) and re-crystallize at the SiC single crystal seed having a slightly lower temperature than the source. The schematic representation of this growth method is shown in Fig. 2.7b. The growth is typically carried out in a quasi-close low

porosity graphite crucible in argon ambient with low pressure and in the temperature ranges 1800-2600 °C. Compared to the Lely method, the extensive spontaneous nucleation along the inner crucible wall can be suppressed using this method. The main challenge is to control the temperature and the gas species concentration fields, which has been achieved through the support of the process modeling [14-20]. The control of the growth at the seed can then be achieved and the control of polytypes is possible to some extent [21-28]. Very recently, a complete macroscopic approach, including experiments, characterization, and modeling, to the nucleation and propagation of foreign polytype inclusions has been reported [29]. The PVT technique has attracted exceptional research efforts and is the most mature process to date. Its abilities are to produce, for example, large size boules (150 mm in diameter) with low dislocation density (EPD=2912 cm^{-2}, TSD=302 cm^{-2}, BPD=324 cm^{-2}) [30], and micropipe-free single crystalline ingots [31]. The batch nature of the process, however, results in the intrinsic limitations of the PVT process. The evolution of the geometrical parameters, namely polycrystalline powder properties and ingot dimension, contribute to the excessive changes in the growth behavior [32].

With the aims to grow high quality and high purity SiC at high growth rate, Kordina et al [33] presented the HTCVD process as an alternative method to grow SiC boules. The HTCVD geometry is considered as a vertical type growth reactor where the precursors like SiH_4 and C_3H_8 diluted in a carrier gas used as Si-source and additional C-source, respectively, are fed upward through inlets placed at the bottom of the crucible and the exhaust at the top (Fig. 2.7c). Even if the technique resembles the Chemical Vapor Deposition (CVD) technique, the growth process considerably differs from the CVD process. The chemistry of the HTCVD process requires a separated inlet for Si- and C-containing precursors and an adapted temperature distribution. The purpose is to control a 'SiC cluster cloud' formed by the homogeneous nucleation acting as a 'virtual SiC solid source' for the sublimation step [34]. The main advantages of this technique are the continuous supply of the material, the direct control of Si/C ratio, and the excellent control of purity and doping. On the other hand, there are several difficulties using HTCVD process. The surface morphology of the grown crystal is very sensitive to the growth condition, especially during the temperature ramp up. Moreover, the premature cracking of SiH_4 can lead to either parasitic depositions of Si at the cold parts of the reactor or a blocking of the inlet [33].

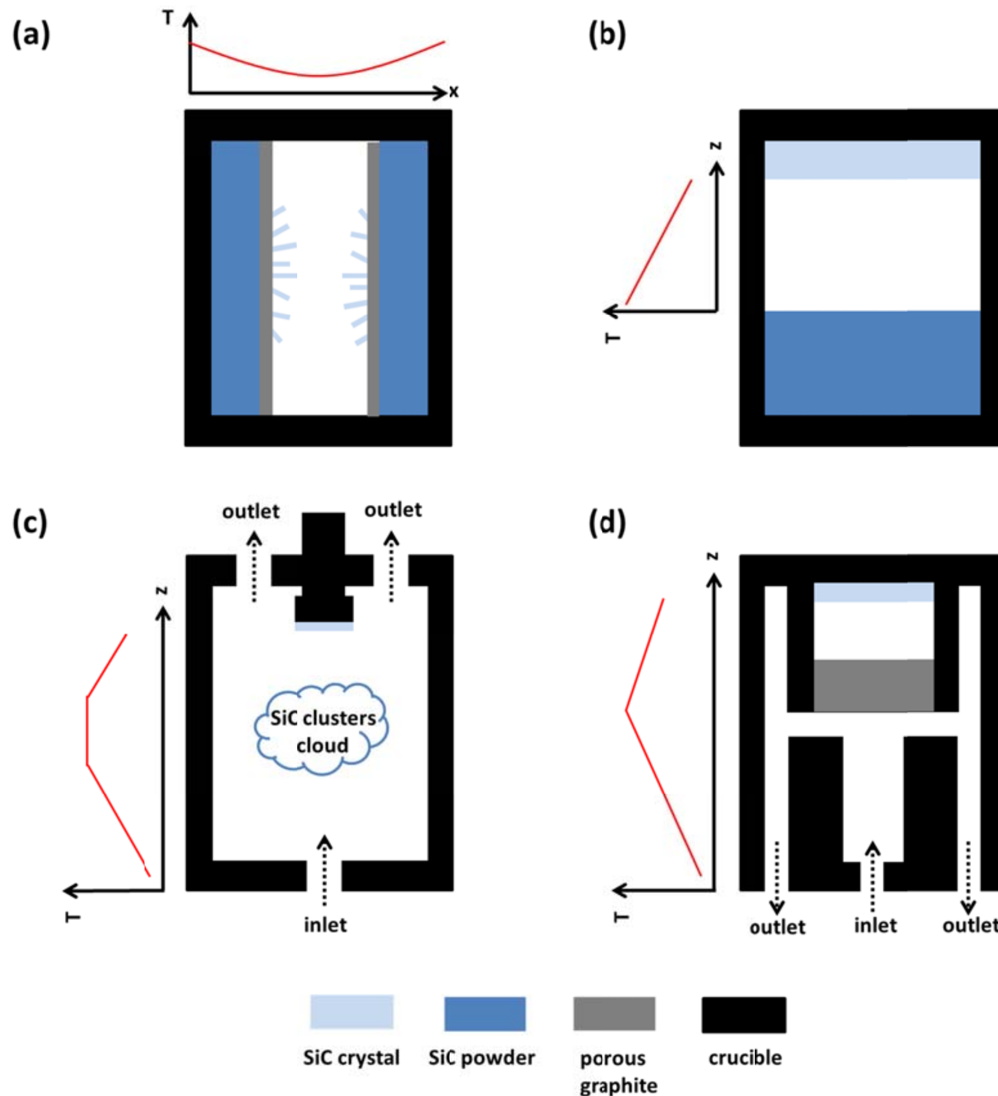

Fig. 2.7 Schematic representation of the set-up for the growth of SiC from vapor phase route: (a) Lely method, (b) Modified-Lely or PVT method, (c) HTCVD method, and (d) CF-PVT method.

A new reactor concept, continuous feed physical vapor transport (CF-PVT), was proposed by Chaussende et al [35] for the growth of SiC bulk crystal and epitaxial layers. Such process combines the advantages of the PVT process for producing single crystal and the HTCVD process for the continuous feeding of the polycrystalline SiC source. Crucible geometry was designed in such a way that both HTCVD and PVT steps are performed simultaneously (Fig. 2.7d). For the feeding step (HTCVD), tetramethylsilane (TMS) diluted in argon used as a single-precursor was injected in the inlet. The transfer zone consisting of highly porous graphite foam supports the HTCVD deposit and allows SiC to be transferred to the sublimation zone (PVT). In

fact, the strong chemical interactions related to a close space sublimation/condensation mechanism within the pores of graphite foam were shown based on the thermodynamic calculations [36] to create a link between the HTCVD and PVT steps. This means that the CF-PVT process should be considered as a whole process and not two separate zones. Controlling the feeding gas flow rate and the temperature are the main parameters of the process. They allow a precise control of the supersaturation [37] close to the seed and the control of the SiC polytypes. The main disadvantage of this technique is the less maturity of the technique itself compared to other techniques discussed above. Besides, this is the only process which has been able to demonstrate the "real bulk growth" of 3C-SiC single crystal [38].

2.3.2 Growth from liquid phase

The growth from liquid phase is the most promising route for producing the single crystal semiconductor boules. However, this was not a feasible option for SiC since SiC does not form any liquid phase in the normal engineering process conditions. The stoichiometric melt can only occur, according to the theoretical analysis [39], at the temperature and pressure exceeding 3200 °C and 10^5 bar, respectively. Moreover, the stabilization and control of the preferential polytype during the growth will be extremely difficult under such high temperature condition due to the fact that the differences in the enthalpy of formation of different polytypes are very narrow. These difficulties together with the technological breakthroughs of the vapor phase route at the end of the 20th century, as previously discussed, were the main reasons why the liquid phase route was put aside after being investigated.

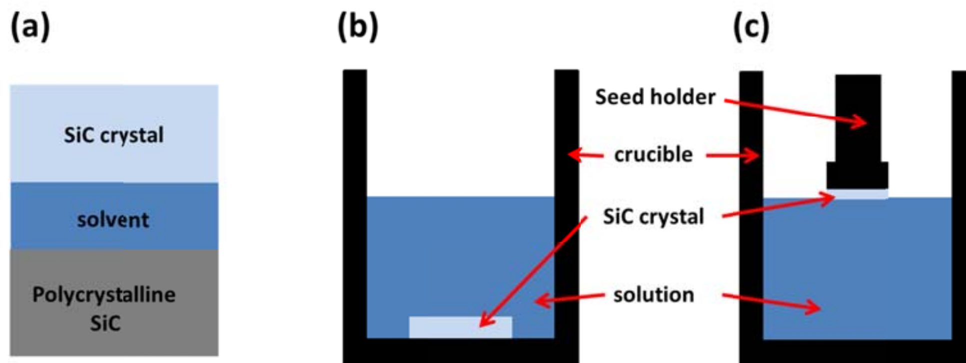

Fig. 2.8 Schematic representation of the growth set-up for SiC growth from liquid phase: (a) travelling-heater, solvent method, (b) slow cooling method, and (c) Top Seed Solution Growth (TSSG) method

Since the last ten years, the liquid phase route for the growth of SiC single crystal has attracted again attention. The potentials of using the liquid phase techniques for the growth of bulk SiC crystal were discussed [40]. In order to avoid the thermodynamic problems related to the stoichiometric melt, the use of non-stoichiometric solutions using, for instant, Si as a solvent and C as a solute has become an alternative way toward the growth of SiC from liquid phase. Examples of the liquid phase growth set-ups for SiC are shown in Fig. 2.8. On the perspectives of large diameter and reasonable boule length, the TSSG method seems to be the most feasible approach due to the intrinsic limitations of the other two methods concerning especially up-scaling [40]. In the TSSG process, the graphite crucible does not only act as a container, but also as the carbon source. The carbon dissolved from the crucible walls will be transported by both diffusion and convection to the SiC seed crystal attached to the seed holder where the temperature is relatively lower. There are some difficulties using this method. First, the manipulation of liquid silicon at high temperature is not very easy due to the high Si vapor pressure and the extreme reactivity with any container material (other than graphite and SiC). Second, several convective phenomena, such as buoyancy convection, Marangoni convection, forced convection, and electromagnetic convection, can possibly occur depending on the process conditions. Thus the control of the fluid convection in the melt is one of the main challenging issues. This will, in combination with the control of temperature profile, directly affect the growth front and its stability. In fact these problems are associated with the low C solubility in liquid Si as the latter implies using high temperature to increase the solubility limit and/or introduce some convection to enhance the mixing. An alternative approach is to use another solvent such as adding a metal to Si to increase the C solubility. However, another problem will arise concerning the purity of the crystals and especially the contamination from the solvent. Apart from such difficulties, the liquid phase route shows many excellence advantages: the elimination of harmful defect such as micropipes [41, 42], the enlargement of the crystal diameter and length [43], and the high structural quality [44].

2.4 Process modeling

In the previous section, it can be seen that many challenging topics in the growth process are related to the precise control of the physico-chemical parameters and their distribution in the growth reactor. Due to the fact that the experiments are normally carried out in a quasi-closed

graphite crucible, it is not possible to have access to such 'black box' by a simple mean without disturbing the system. This is the reason why only the experiment itself will not be able to provide a full understanding and controlling of the processes. This can be exemplified by considering Fig. 2.9. Besides the reactor geometry, the process parameters that can be controlled in general are, for example, the coil frequency, the temperature on top and bottom parts of the crucible, the growth pressure, and the seed rotation speed. Then in order to make a link between the controllable parameters and the observable parameter after the experiments, an empirical approach is normally used. Such approach, however, may not be able to provide the concrete evidence to support the results. An alternative approach is the use of numerical modeling in order to access the physico-chemical parameters and their distribution in the reactor such as, temperature, concentration, fluid velocity, and so on. This macroscopic approach creates a link between the experiment and characterization and serves as a key to open little by little the black box resulting in more and more understanding of the processes.

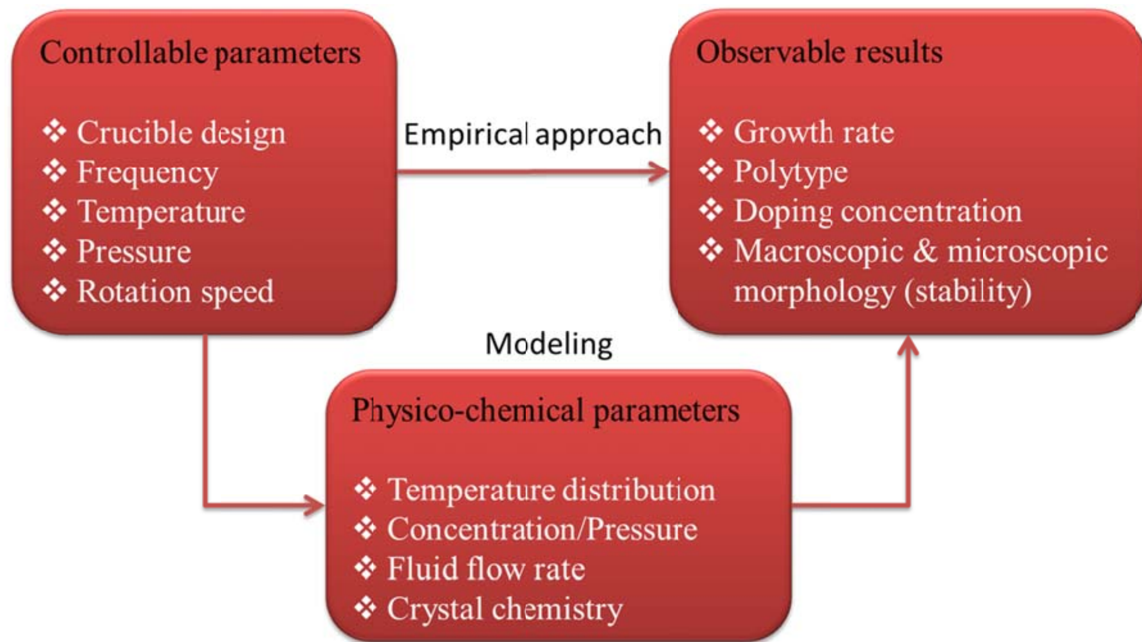

Fig. 2.9 Diagram showing that the modeling approach can be an alternative way to link between the controllable parameters and observable results

Thanks to the pioneering works on the process modeling of SiC single crystal growth of Hofmann et al [45] and Pons et al [46], many research groups started to work in parallel to develop the models and/or codes for the mass transport, chemical reactions, and mechanical stress in the crystal [21, 47-76]. Nowadays, the modeling of heat and mass transfer has reached the state of the art [77, 78]. On the other hand, different approaches and models have been proposed for the chemical reactions, especially at the solid-vapor interfaces [21, 64, 71-74]. Those models require a certain degree of connection, depending on the model, with the thermodynamics. The model for predicting the dislocation density has also been developed based on the thermal stress calculations [17] while the most recent achievement is the implementation of Alexander-Haasen (AH) model to describe the dynamics of plastic deformation in SiC where the effects of the cooling time on the final dislocation density, residual stress, and stacking faults can be studied [53].

The reliability of the modeling results can be strongly dependent on the database used in the computation. Those include, for example, the thermal conductivity, electrical conductivity, and emissivity for the solid components, and thermo-chemical data for the vapor species. Actually, this issue may become very problematic, especially for the process modeling of SiC. This is caused by the lack (or not very precise value) of the materials properties data under such high temperature normally used in the growth. As a consequence, this factor defines whether the model can be considered as to provide quantitative results or qualitative trends [11]. In addition to such issue, some other issues such as the simplification of the physical system as well as the choice of the boundary conditions can affect the modeling to some extent. These issues are caused by the fact that it is impossible to model the entire universe. We can model only the physical phenomena that we are interested in, in a defined space (and time). The other things outside will be represented by the boundary conditions of the system. Thus, it is quite important to keep in mind that the absolute or exact solutions are not very realistic and cannot be expected from the process modeling even if the quantitative results are obviously the best results we would like to know. However, providing that the databases are not "completely wrong", the numerical modeling has a strong potential to give the qualitative trend which is very useful for the development and understanding of the process. In some cases, the modeling results can even be considered on a quantitative footing.

2.5 Purposes of this thesis work

Besides many successes in applying the numerical modeling to describe the SiC growth processes, there are some strong major challenges which are not considered in a satisfactory way even in the most mature process like PVT. There are (at least) three main open questions for better understanding of the PVT process [79].

i.) How to describe correctly the heterogeneous reactions at the solid-vapor interfaces?

ii.) Is there any link between chemistry and crystal polytypes?

iii.) How the doping incorporation can be described?

Concerning the TSSG process, the control of the fluid convection and the growth front stability are the main issues toward the development of high quality SiC crystal, especially for electronic devices applications. Thus in this thesis work, we are aiming to use the numerical modeling as a tool in order to tackle those challenging fundamental and technological issues, both for the industrially used PVT process and for the emerging TSSG process. The numerical modeling results will be compared and discussed either with our experimental results if available or with the data available in the literature.

It is worth noting that in this thesis, we are not aiming to develop the code for the numerical modeling since the commercial software, such as, COMSOL multiphysics [80], CFD-ACE [81], ANSYS Fluent [82], Abaqus [83], Virtual Reactor [84], or the open source such as, OpenFOAM [85], are available. They all can treat modeling in process engineering, either specifically for the SiC growth (Virtual Reactor) or for general (coupled) physics phenomena. In this thesis, the numerical modeling was performed using COMSOL Multiphysics software. Such software package is working based on the Finite Element Analysis (FEA). Thus, an overview of the Finite Element Method (FEM) will be given in the following chapter including an example for solving the heat transfer in steady state.

References

1. Madar, R., *Materials science: Silicon carbide in contention.* Nature, 2004. **430**(7003): p. 974-975.
2. Knippenberg, W.F., *Growth phenomena in silicon carbide*. Vol. 13. 1963: Valkenburg.
3. Ramsdell, L.S., *Studies on silicon carbide.* American Mineralogist, 1947. **32**(1-2): p. 64-82.

4. Grundmann, M., *The physics of semiconductors*. 2006, Berlin: Springer.
5. http://www.mitsubishielectric.com.
6. Elasser, A. and T.P. Chow, *Silicon carbide benefits and advantages for power electronics circuits and systems.* Proceedings of the IEEE, 2002. **90**(6): p. 969-986.
7. Berzelius, J.J., *Untersuchungen über die Flussspathsäure und deren merkwürdigsten Verbindungen.* Annalen der Physik, 1824. **77**(6): p. 169-230.
8. Acheson, A., *Characterization of Electrical Properties of 4H-SiC by Imaging Techniques.* Engl. Pat, 1892. **17911**.
9. Moissan, H., CR Acad. Sci. Paris, 1904. **140**: p. 405.
10. Tairov, Y.M. and V. Tsvetkov, *Semiconductor Compounds Aiv Biv.* Handbook on Electrotechnical Materials, 1988. **3**: p. 446-471.
11. Chaussende, D., P.J. Wellmann, and M. Pons, *Status of SiC bulk growth processes.* Journal of Physics D: Applied Physics, 2007. **40**(20): p. 6150-6158.
12. Anthony, L.J., *Sublimation process for manufacturing silicon carbide crystals*. 1958, Google Patents.
13. Tairov, Y.M. and V. Tsvetkov, *Investigation of growth processes of ingots of silicon carbide single crystals.* Journal of crystal growth, 1978. **43**(2): p. 209-212.
14. Hofmann, D., et al., *Sublimation growth of silicon carbide bulk crystals: experimental and theoretical studies on defect formation and growth rate augmentation.* Journal of Crystal Growth, 1999. **198–199, Part 2**(0): p. 1005-1010.
15. Ohtani, N., et al., *Growth of large high-quality SiC single crystals.* Journal of Crystal Growth, 2002. **237–239, Part 2**(0): p. 1180-1186.
16. Augustine, G., V. Balakrishna, and C.D. Brandt, *Growth and characterization of high-purity SiC single crystals.* Journal of Crystal Growth, 2000. **211**(1–4): p. 339-342.
17. Müller, S.G., et al., *The status of SiC bulk growth from an industrial point of view.* Journal of Crystal Growth, 2000. **211**(1–4): p. 325-332.
18. Tsuge, H., et al., *Growth of Low Basal Plane Dislocation Density 4H-SiC Crystals in Controlled Temperature Distribution inside the Crucible.* Materials Science Forum, 2013. **740-742**: p. 7-10.
19. Wellmann, P., et al., *Vapor growth of SiC bulk crystals and its challenge of doping.* Surface and Coatings Technology, 2006. **201**(7): p. 4026-4031.
20. Dedulle, J.M., et al. *Free growth of 4H-SiC by sublimation method*. in *Materials Science Forum*. 2004. Trans Tech Publ.
21. Kakimoto, K., et al., *Thermodynamic analysis of SiC polytype growth by physical vapor transport method.* Journal of Crystal Growth, 2011. **324**(1): p. 78-81.
22. Tsavdaris, N., et al., *Interface Shape: A Possible Cause of Polytypes Destabilization during Seeded Sublimation Growth of 15R-SiC.* Materials Science Forum, 2014. **806**: p. 61-64.
23. Tsavdaris, N., et al., *Effect of Facet Occurrence on Polytype Destabilization during Bulk Crystal Growth of SiC by Seeded Sublimation.* Materials Science Forum, 2014. **778-780**: p. 13-16.
24. Shiramomo, T., et al., *Thermodynamical analysis of polytype stability during PVT growth of SiC using 2D nucleation theory.* Journal of Crystal Growth, 2012. **352**(1): p. 177-180.
25. Semmelroth, K., N. Schulze, and G. Pensl, *Growth of SiC polytypes by the physical vapour transport technique.* Journal of Physics: Condensed Matter, 2004. **16**(17): p. S1597-S1610.
26. Semmelroth, K., et al., *Growth of cubic SiC single crystals by the physical vapor transport technique.* Journal of Crystal Growth, 2007. **308**(2): p. 241-246.
27. Rost, H.J., et al., *Polytype stability in nitrogen-doped PVT—grown 2″—4H–SiC crystals.* Journal of Crystal Growth, 2005. **275**(1-2): p. e451-e454.
28. Schulze, N., D. Barrett, and G. Pensl, *Controlled Growth of 15R-SiC Single Crystals by the Modified Lely Method.* physica status solidi (a), 2000. **178**(2): p. 645-650.

29. Tsavdaris, N., et al., *Macroscopic Approach to the Nucleation and Propagation of Foreign Polytype Inclusions during Seeded Sublimation Growth of Silicon Carbide.* Crystal Growth & Design, 2014. **15**(1): p. 156-163.
30. Kondo, H., et al., *Development of RAF Quality 150mm 4H-SiC Wafer.* Materials Science Forum, 2014. **778-780**: p. 17-21.
31. Basceri, C., et al., *Growth of Micropipe-Free Single Crystal Silicon Carbide (SiC) Ingots Via Physical Vapor Transport (PVT).* Materials Science Forum, 2006. **527-529**: p. 39-42.
32. Moulin, C., et al., *SiC Single Crystal Growth by Sublimation: Experimental and Numerical Results.* Materials Science Forum, 2001. **353-356**: p. 7-10.
33. Kordina, O., et al., *High temperature chemical vapor deposition of SiC.* Applied Physics Letters, 1996. **69**(10): p. 1456-1458.
34. Kordina, O., et al., *Growth of SiC by "Hot-Wall" CVD and HTCVD.* physica status solidi (b), 1997. **202**(1): p. 321-334.
35. Chaussende, D., et al., *Continuous Feed Physical Vapor Transport.* Journal of The Electrochemical Society, 2003. **150**(10): p. G653.
36. Chaussende, D., et al., *Thermodynamic Aspects of the Growth of SiC Single Crystals using the CF-PVT Process.* Chemical Vapor Deposition, 2006. **12**(8-9): p. 541-548.
37. Chaussende, D., et al., *Control of the Supersaturation in the CF−PVT Process for the Growth of Silicon Carbide Crystals: Research and Applications.* Crystal Growth & Design, 2005. **5**(4): p. 1539-1544.
38. Chaussende, D., et al., *Large Area DPB Free (111) β-SiC Thick Layer Grown on (0001) α-SiC Nominal Surfaces by the CF-PVT Method.* Materials Science Forum, 2005. **483-485**: p. 225-228.
39. Tsvetkov, V., et al., *Recent progress in SiC crystal growth.* Silicon Carbide and Related Materials 1995, 1996. **142**: p. 17-22.
40. Hofmann, D.H. and M.H. Müller, *Prospects of the use of liquid phase techniques for the growth of bulk silicon carbide crystals.* Materials Science and Engineering: B, 1999. **61–62**(0): p. 29-39.
41. Yakimova, R., et al., *Micropipe Healing in Liquid Phase Epitaxial Growth of SiC.* Materials Science Forum, 2000. **338-342**: p. 237-240.
42. Filip, O., et al., *Micropipe healing in SiC wafers by liquid-phase epitaxy in Si–Ge melts.* Journal of Crystal Growth, 2004. **271**(1–2): p. 142-150.
43. Kusunoki, K., et al., *Top-Seeded Solution Growth of 3 Inch Diameter 4H-SiC Bulk Crystal Using Metal Solvents.* Materials Science Forum, 2014. **778-780**: p. 79-82.
44. Dmitriev, V. and A. Cherenkov, *Growth of SiC and SiC-AlN solid solution by container-free liquid phase epitaxy.* Journal of Crystal Growth, 1993. **128**(1–4): p. 343-348.
45. Hofmann, D., et al., *On the sublimation growth of SiC bulk crystals: development of a numerical process model.* Journal of Crystal Growth, 1995. **146**(1–4): p. 214-219.
46. Pons, M., Blanquet, E., Dedulle, J.M., Garcon, I., Madar, R., Bernard, C.,, *Thermodynamic Heat Transfer and Mass Transport Modeling of the Sublimation Growth of Silicon Carbide Crystals.* Journal of The Electrochemical Society, 1996. **143**(11): p. 3727.
47. Nishizawa, S., et al., *Numerical Simulation of Heat and Mass Transfer in SiC Sublimation Growth.* Materials Science Forum, 2002. **389-393**: p. 43-46.
48. Chen, Q., et al., *Silicon carbide crystals-Part II: Process physics and modeling.* Crystal growth technology. NY: William Andrew, 2003: p. 233-269.
49. Chen, Q.S., J.Y. Yan, and V. Prasad, *Application of flow-kinetics model to the PVT growth of SiC crystals.* Journal of Crystal Growth, 2007. **303**(1): p. 357-361.
50. Chen, X., S.-i. Nishizawa, and K. Kakimoto, *Numerical simulation of a new SiC growth system by the dual-directional sublimation method.* Journal of Crystal Growth, 2010. **312**(10): p. 1697-1702.

51. Gao, B., et al., *Analysis of SiC crystal sublimation growth by fully coupled compressible multi-phase flow simulation.* Journal of Crystal Growth, 2010. **312**(22): p. 3349-3355.
52. Gao, B. and K. Kakimoto, *Effect of the Inclusion of Transparency on the Thermal Field and Interface Shape in Long-term Sublimation Growth of SiC Crystals(<Special Issue>)Opening Up a New World of Crystal Growth on SiC).* Journal of the Japanese Association of Crystal Growth, 2013. **40**(1): p. 20-24.
53. Gao, B. and K. Kakimoto, *Dislocation-density-based modeling of the plastic behavior of 4H–SiC single crystals using the Alexander–Haasen model.* Journal of Crystal Growth, 2014. **386**: p. 215-219.
54. Gao, B. and K. Kakimoto, *Three-Dimensional Modeling of Basal Plane Dislocations in 4H-SiC Single Crystals Grown by the Physical Vapor Transport Method.* Crystal Growth & Design, 2014. **14**(3): p. 1272-1278.
55. Klein, O. and P. Philip, *Transient temperature phenomena during sublimation growth of silicon carbide single crystals.* Journal of Crystal Growth, 2003. **249**(3-4): p. 514-522.
56. Klein, O., et al., *Radiation- and convection-driven transient heat transfer during sublimation growth of silicon carbide single crystals.* Journal of Crystal Growth, 2001. **222**(4): p. 832-851.
57. Kulik, A.V., et al., *Theoretical Analysis of the Mass Transport in the Powder Charge in Long-Term Bulk SiC Growth.* Materials Science Forum, 2004. **457-460**: p. 67-70.
58. Lefebure, J., et al., *Modeling of the Growth Rate during Top Seeded Solution Growth of SiC Using Pure Silicon as a Solvent.* Crystal Growth & Design, 2011. **12**(2): p. 909-913.
59. Ma, R.-H., et al., *Integrated process modeling and experimental validation of silicon carbide sublimation growth.* Journal of crystal growth, 2003. **252**(4): p. 523-537.
60. Matukov, I.D., et al., *Modeling of facet formation in SiC bulk crystal growth.* Journal of Crystal Growth, 2004. **266**(1-3): p. 313-319.
61. Nishizawa, S., et al., *High-Quality SiC Bulk Single Crystal Growth Based on Simulation and Experiment.* Materials Science Forum, 2004. **457-460**: p. 29-34.
62. Pisch, A., et al., *Coupled Thermodynamic - Mass Transfer Modeling of the SiC Boule Growth by the PVT Method.* Materials Science Forum, 2001. **353-356**: p. 61-64.
63. Segal, A., et al., *Growth of silicon carbide by sublimation sandwich method in the atmosphere of inert gas.* Journal of crystal growth, 2000. **208**(1): p. 431-441.
64. Segal, A.S., et al., *Transport phenomena in sublimation growth of SiC bulk crystals.* Materials Science and Engineering: B, 1999. **61-62**: p. 40-43.
65. Selder, M., et al., *Global numerical simulation of heat and mass transfer for SiC bulk crystal growth by PVT.* Journal of Crystal Growth, 2000. **211**(1–4): p. 333-338.
66. Karpov, S.Y., Y.N. Makarov, and M. Ramm, *Simulation of sublimation growth of SiC single crystals.* physica status solidi (b), 1997. **202**(1): p. 201-220.
67. Bogdanov, M., et al., *Advances in modeling of wide-bandgap bulk crystal growth.* Crystal Research and Technology, 2003. **38**(3-5): p. 237-249.
68. Mercier, F., et al., *Coupled heat transfer and fluid dynamics modeling of high-temperature SiC solution growth.* Journal of Crystal Growth, 2010. **312**(2): p. 155-163.
69. Mercier, F. and S.-i. Nishizawa, *Numerical Investigation of the Growth Rate Enhancement of SiC Crystal Growth from Silicon Melts.* Japanese Journal of Applied Physics, 2011. **50**(3R): p. 035603.
70. Mercier, F. and S.-i. Nishizawa, *Comparative numerical study of the effects of rotating and traveling magnetic fields on the carbon transport in the solution growth of SiC crystals.* Journal of Crystal Growth, 2013. **362**(0): p. 99-102.
71. Chen, Q.-S., et al., *Kinetics and modeling of sublimation growth of silicon carbide bulk crystal.* Journal of crystal growth, 2001. **224**(1): p. 101-110.

72. Danielsson, Ö., U. Forsberg, and E. Janzén, *Predicted nitrogen doping concentrations in silicon carbide epitaxial layers grown by hot-wall chemical vapor deposition.* Journal of Crystal Growth, 2003. **250**(3): p. 471-478.
73. Karpov, S.Y., Y.N. Makarov, and M. Ramm, *Analytical model of silicon carbide growth under free-molecular transport conditions.* Journal of crystal growth, 1996. **169**(3): p. 491-495.
74. Nishizawa, S.-i. and M. Pons, *Growth and Doping Modeling of SiC-CVD in a Horizontal Hot-Wall Reactor.* Chemical Vapor Deposition, 2006. **12**(8-9): p. 516-522.
75. Pons, M., et al., *State of the art in the modelling of SiC sublimation growth.* Materials Science and Engineering: B, 1999. **61-62**: p. 18-28.
76. Råback, P., *Modeling of the sublimation growth of silicon carbide crystals*. 1999: Center for Scientific Computing.
77. Chen, Q., et al., *Progress in modeling of fluid flows in crystal growth processes.* Progress in Natural Science, 2008. **18**(12): p. 1465-1473.
78. Chen, X.J., et al., *Optimization of the design of a crucible for a SiC sublimation growth system using a global model.* Journal of Crystal Growth, 2008. **310**(7–9): p. 1810-1814.
79. Chaussende, D., et al., *Open Issues in SiC Bulk Growth.* Materials Science Forum, 2014. **778-780**: p. 3-8.
80. http://www.comsol.com/.
81. http://www.esi-group.com/fr/software-services/virtual-environment/cfd-multiphysics/ace-suite/cfd-ace.
82. http://www.ansys.com/fr_fr/Produits/Flagship+Technology/ANSYS+Fluent.
83. http://www.3ds.com/products-services/simulia/products/abaqus/.
84. http://www.semitech.us/products/Virtual_Reactor/.
85. http://www.openfoam.com/.

Chapter 3
Finite Element Method (FEM)

The SiC growth processes involve many physical and chemical phenomena [1]. The system of equations contains unknown multivariable functions as well as their partial derivatives; the whole process system is thus a system of partial differential equations (PDEs). In fact, PDEs are naturally governing science and engineering applications due to the complex balance equations, such as transport of mass, momentum, species, and energy. The whole class of these transport phenomena usually expressed in the integral equations over the domain results in the PDEs in the continuum approximation. Thus, the system to be solved is in reality continuous and the exact solutions can be solved mainly in the oversimplified situation. With aim to approach the true continuum solutions without oversimplification, several numerical methods of discretization have been proposed for solving such PDEs, for example, the Finite Difference Method (FDM), the Finite Volume Method (FVM), and the Finite Element Method (FEM). Even if the approaches in solving PDEs are different, these methods share important characteristics. First the continuous domain is discretized into a set of discrete subdomain called element in which their behavior is specified by the finite number of parameters. Moreover the approximated functions on each element meet the conditions of continuity between various elements of the field. Advantages and disadvantages of using these numerical methods are summarized in Table 3.1 [2]. The FDM method is relatively easy to be programmed but its ability is limited to a simple geometry and regular grid (element). The FEM is much better to treat correctly the interface problems, even if this method is less trivial for fluid dynamics than FVM. Since the crystal growth is associated mainly with the problem of boundary conditions, the FEM method is more adapted in this current PhD topic. Throughout this thesis, the FEM will be used as a tool for approximating the solutions to the boundary value problems of the PDEs system. An overview of the FEM and examples of solving heat transfer problem using this method will be presented in this chapter [3-6].

Table 3.1 Comparison of different numerical methods

Method	FDM	FVM	FEM
Principle	Taylor development	Strong form (Stokes formula)	Weak form (Galerkin method)
Geometry	simple	complex	complex
Discretization	regular grid	structured/unstructured	structured/unstructured
Programming	easy	easy for structured difficult for unstructured	difficult
Matrix	sparse	sparse	sparse
Boundary conditions	to be constructed	to be constructed	naturally constructed
Implementation	rarely implemented in commercial software	available in commercial software especially for: - Fluid mechanics - Heat transfer - Coupled multiphysics	available in commercial software especially for: - Solid mechanics - Electromagnetism - Heat transfer - Coupled multiphysics

3.1 Overview of the method

The behavior of a physical system is generally described by a system of PDEs. We are seeking for an unknown function u such that it satisfies a certain differential equation set A(u) in a domain Ω with the boundary conditions B(u) on the boundaries Γ. If the differential equations are linear we can write

$$A(u) \equiv L\,u + p = 0 \text{ in } \Omega, \text{ and} \tag{3.1}$$

$$B(u) \equiv M\,u + q = 0 \text{ on } \Gamma. \tag{3.2}$$

The unknown function u is assumed to be a function of class C_n (*n* times differentiable) in Ω for (3.1) and Γ for (3.2). L and M are differential operators of order *n*, in Ω and on Γ, respectively. A simple problem domain and boundary can be shown in Fig. 3.1. In order to find the solution, the finite element process will seek for an unknown function u in the approximation form ũ such as

$$u \approx \tilde{u} = \sum_i \phi_i u_i \,, \tag{3.3}$$

where u_i are the unknown coefficients taken by each ‘node’ i of the ‘element’ and will be determined, and ϕ_i are the basis or interpolation or shape functions.

In order to solve the system of equations using FEM, the key features is that this method states any constraint on the field variable in the “weak” form. The “strong” form of a system of constraints is actually the partial differential equations with the appropriate boundary conditions (3.1) and (3.2). It is “strong” in a sense that the field variables are required to be continuous and their partial derivatives must be also continuous up through the order of the equation. The strong form is in general difficult to solve especially for the complex domain or the interface of domains having different properties. The weak form is more permissive to the function satisfying the constraints than the strong form. For example, if *n*th-order derivative occur, only *n*-1 derivatives are need to be continuous while the discontinuous one is only needed to be integrable [4]. Thus we are considering the transformation of the strong form to the weak form.

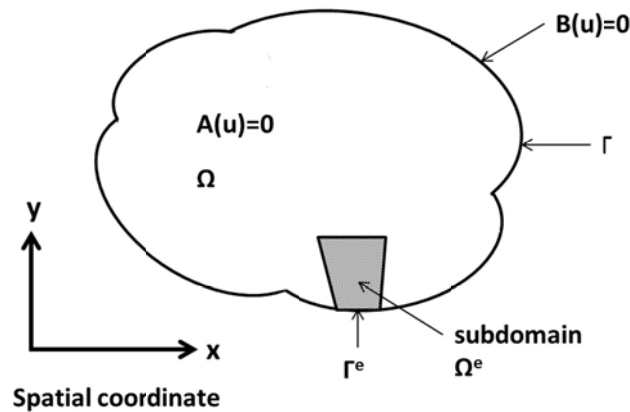

Fig. 3.1 Schematic representation of problem domain and boundary in two-dimension

The general procedure to transform the strong form to the weak form consists of four steps [4]:

1. Multiply each partial differential equation governing the system by an appropriate arbitrary function
2. Construct an integral of the inner product of the residual equation
3. Use the integration by parts (or divergence theorem, or other methods) to reduce the order of derivatives
4. Apply appropriate boundary conditions

Since the differential equations (3.1) has to be zero at each point of the domain, we can multiply (3.1) by a set of arbitrary test functions (or weight functions) w defined in the domain Ω and integrating over the domain to obtain

$$\int_{\Omega} w\,\mathrm{A}(\mathrm{u})d\Omega \equiv \int_{\Omega} w(\mathrm{Lu}+\mathrm{p})d\Omega = 0\,. \tag{3.4}$$

If (3.4) is satisfied for all w, then the differential equations (3.1) must be satisfied at all points in the domain. In fact by inserting the approximation (3.3) into (3.1), we obtain the residual or error of the differential equation. Thus Eq. (3.4) can be considered as a weighted integral of such residuals and this approximation may be called method of weighted residual. This method aims at minimizing the residual by multiplying with the test functions and integrates over the domain. If (3.4) is satisfied for any w, the residual will approach zero and the approximated solution will approach the exact solution. The accuracy of this method is dependent on the choice of the test function. One of the frequently used methods is the Galerkin method. This method assume the test functions to be similar to the shape functions such that $w_j = \phi_j$. Another example of the method to obtain the integral form is the Ritz method. In such case the problem is characterized by the energy function and the energy minimization technique is used. The integral forms obtained by two techniques are indeed equivalent. Since the energy function is not always known, the weighted residual method is more generally used.

To illustrate the transformation procedure, we may consider the system that is governed by the Poisson's equation

$$\mathrm{A}(\mathrm{u}) \equiv \mathrm{Lu}+\mathrm{p} = \nabla^2\mathrm{u} + \mathrm{p} = 0\,. \tag{3.5}$$

Equation (3.4) can be rewritten as

$$\int_{\Omega} w(\nabla^2\mathrm{u} + \mathrm{p})d\Omega = 0\,. \tag{3.6}$$

It is possible to perform integration by parts (or other methods to shift the derivatives) on Eq. (3.4). From the relation

$$\nabla \cdot (uv) = u\nabla \cdot v + v \cdot \nabla u\,, \tag{3.7}$$

we can rewrite (3.6) as

$$\int_{\Omega} \nabla \cdot (w \nabla \mathrm{u}) d\Omega - \int_{\Omega} \nabla w \cdot \nabla \mathrm{u} d\Omega + \int_{\Omega} w \mathrm{p} d\Omega = 0 . \tag{3.8}$$

Then applying the divergence theorem

$$\int_{\Omega} (\nabla \cdot v) d\Omega = \oint_{\Gamma} v \cdot n d\Gamma \tag{3.9}$$

to (3.8), we obtain

$$\int_{\Omega} \nabla w \cdot \nabla \mathrm{u} d\Omega - \oint_{\Gamma} w \nabla \mathrm{u} \cdot \mathrm{n} d\Gamma = \int_{\Omega} w \mathrm{p} d\Omega . \tag{3.10}$$

Finally, an appropriate boundary condition (3.2) can be applied in the second term of (3.10). Eq. (3.10) is called a weak form in which the order derivative is lower than those appearing in (3.5). Thus a lower order of continuity is needed for the choice of the u function as mentioned before. However, higher continuity for *w* function is required as compensation.

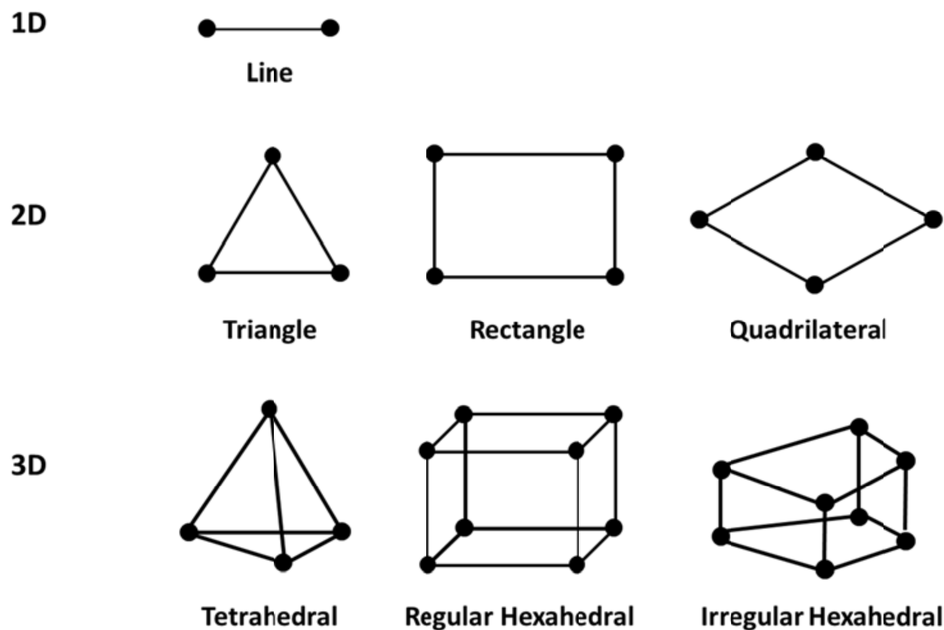

Fig. 3.2 The commonly used basic element in FEM

In order to clarify the terms 'node' and 'element', we consider the fundamental feature of FEM that is the discretization of any domain in smaller subdomains or meshes or elements of the preferred shape. The solutions to the field variable are computed at the nodes or the corners of the mesh. The variation of the field variable along the element is interpolated using the shape functions as defined by the global field variable variation (3.3). The most commonly used basic elements are shown in Fig. 3.2

It is necessary in FEM that the shape function is described to satisfy certain requirement at the node, i.e. the Lagrange basis polynomial takes the value 1 to the coordinates of node *i* and zero to coordinate of other nodes. The shape functions of the 1st order can be illustrated in Fig. 3.3. In this way any function u can be approximated to arbitrary accuracy using sufficiently small elements. The shape function can be also chosen to be higher order while the number of unknown and shape function increase with the order. The order of an element is then defined by the order of the associated shape function. Examples of triangle and tetrahedral elements with shape function up to the third order are shown in Fig. 3.4. However, the order of the shape function should not be very high in order to prevent the natural oscillations caused by the polynomial interpolation methods. Practically, the shape functions are calculated globally once and for all on the reference element while the transformation to the real element will be done by mapping operators.

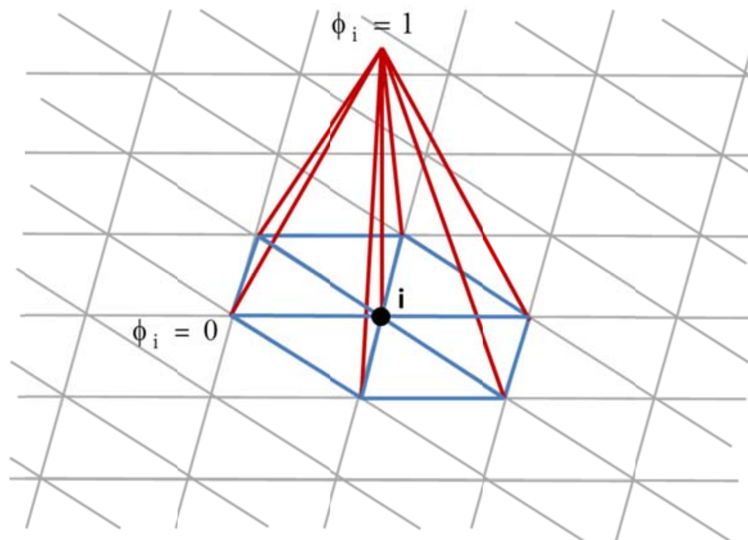

Fig. 3.3 Shape function or interpolation function of the first order

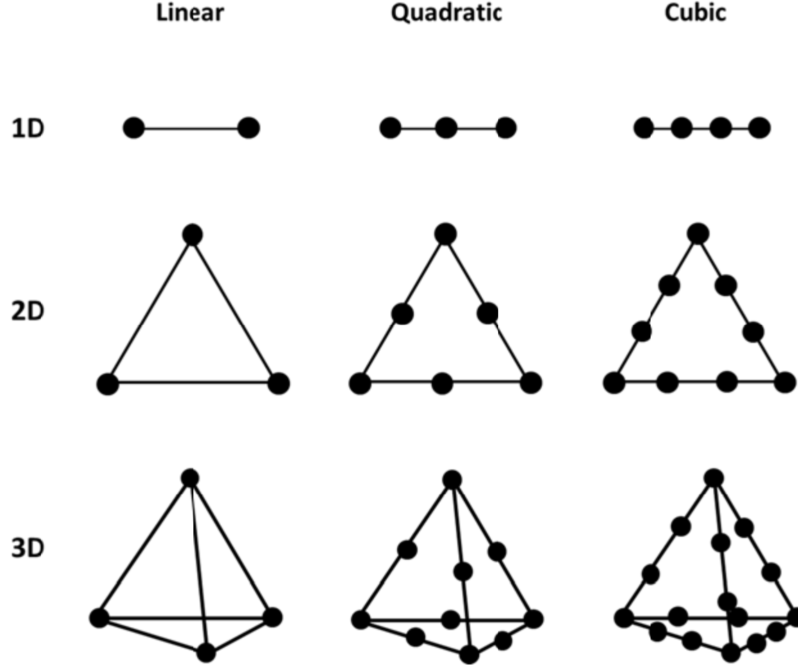

Fig. 3.4 Line, triangle, and tetrahedral elements with shape function up to third order

Using the Galerkin method where the test function and the shape function are identical, substituting (3.3) into (3.10) gives

$$\int_{\Omega} \nabla\phi_j \cdot \nabla\left(\sum_{\mathrm{i}} \phi_i \mathrm{u}_{\mathrm{i}}\right) d\Omega - \oint_{\Gamma} \phi_j \nabla\left(\sum_{\mathrm{i}} \phi_i \mathrm{u}_{\mathrm{i}}\right) \cdot \mathrm{n} d\Gamma = \int_{\Omega} \phi_j \mathrm{p} d\Omega\,, \tag{3.11}$$

which can be rearranged as

$$\left(\sum_{\mathrm{i}} \int_{\Omega} \nabla\phi_j \cdot \nabla\phi_i d\Omega - \sum_{i} \oint_{\Gamma} \phi_j \nabla\phi_i \cdot \mathrm{n} d\Gamma\right) \mathrm{u}_{\mathrm{i}} = \int_{\Omega} \phi_j \mathrm{p} d\Omega\,. \tag{3.12}$$

The above integral forms in fact allow the approximation to be obtained element by element using the procedure similar to the standard discrete system such that

$$\left[\sum_{e_v=1}^{N_{e_v}} \sum_{\mathrm{i}} \left(\int_{\Omega^e} \nabla\phi_j^e \cdot \nabla\phi_i^e d\Omega^e\right) - \sum_{e_s=1}^{N_{e_s}} \sum_{\mathrm{i}} \left(\oint_{\Gamma^e} \phi_j^e \nabla\phi_i^e \cdot \mathrm{n} d\Gamma^e\right)\right] \mathrm{u}_{\mathrm{i}} = \sum_{e_v=1}^{N_{e_v}} \int_{\Omega^e} \phi_j^e \mathrm{p} d\Omega^e\,, \tag{3.13}$$

for all $j \in [1, N_{DOF}]$. N_{e_v} and N_{e_s} are the number of volume element and surface element, respectively. The number of degrees of freedom N_{DOF} equals to the number of node (NBN) multiplied by the number of unknown per node. Equations (3.13) can be written as a set of linear equations of the form

$$\lfloor K_{ji} \rfloor [u_i] = \lfloor f_j \rfloor \tag{3.14}$$

with

$$K_{ji} = \sum_{e_v=1}^{N_{e_v}} K_{ji}^{e_v} + \sum_{e_s=1}^{N_{e_s}} K_{ji}^{e_s} \quad \text{and} \quad f_j = \sum_{e=1}^{N_{e_v}} f_j^e \,, \tag{3.15}$$

where K_{ji} is called the stiffness matrix and f_j is called the load vector. The superscript e defines the element (locally based) matrix. For the N_{DOF} degree of freedom, (3.14) is equivalent to a system of N_{DOF} equations. Such system will then be solved by appropriate numerical methods. The size of the matrix is ($N_{DOF} \times N_{DOF}$) which depends on the number and order of elements geometrically used to discretize the domain. The larger system size requires the more powerful computer for reasonable computation time.

3.2 Example of heat transfer in steady state

This example relates to the calculation of the temperature distribution in the steady state. The diffusion equation of heat can be written by the formulation representing the conservation of energy

$$\nabla \cdot (-k \nabla T) = Q \tag{3.16}$$

with the Neumann type boundary condition written by

$$-k \frac{\partial T}{\partial n} = -k \nabla T \cdot \mathbf{n} = h(T - T_{amb}), \tag{3.17}$$

where T is the temperature (field variable), k is the thermal conductivity, Q is the heat density, and h is the exchange coefficient. The weighted integral for residual of Eq. (3.13) can be written:

$$\int_{\Omega} \phi_j \left(\nabla \cdot (-k\nabla T)\right) d\Omega = \int_{\Omega} \phi_j Q d\Omega . \tag{3.18}$$

From the relation (3.7), (3.18) is simplified to

$$\int_{\Omega} k\left(\nabla \phi_j \cdot \nabla T\right) d\Omega - \int_{\Omega} \nabla \cdot \left(\phi_j k \nabla T\right) d\Omega = \int_{\Omega} \phi_j Q d\Omega . \tag{3.19}$$

Applying the divergence theorem (3.9) to (3.19), we obtain

$$\int_{\Omega} k\left(\nabla \phi_j \cdot \nabla T\right) d\Omega - \oint_{\Gamma} \phi_j k \nabla T \cdot n d\Gamma = \int_{\Omega} \phi_j Q d\Omega . \tag{3.20}$$

The boundary condition (3.17) can be directly subtract to Eq. (3.20) to achieve

$$\int_{\Omega} k\left(\nabla \phi_j \cdot \nabla T\right) d\Omega + \oint_{\Gamma} \phi_j h T d\Gamma = \int_{\Omega} \phi_j Q d\Omega + \oint_{\Gamma} \phi_j h T_{amb} d\Gamma . \tag{3.21}$$

This is a general formulation for the volume and surface integrals which can be also applied to the case where a domain is composed of materials with different physical properties (Fig. 3.5) where the continuity relations are:

$$T_1 = T_2 \text{ and} \tag{3.22}$$

$$\left(-k_1 \nabla \cdot T_1\right) \cdot n_1 + \left(-k_2 \nabla \cdot T_2\right) \cdot n_2 = 0 . \tag{3.23}$$

In this case, the integral forms (3.20) become

$$\int_{\Omega_1 \cup \Omega_2} k\left(\nabla \phi_j \cdot \nabla T\right) d\Omega - \oint_{\Gamma_1 \cap \Gamma_2} \phi_j k \nabla T \cdot n d\Gamma - \oint_{\Gamma_{1ext} \cup \Gamma_{2ext}} \phi_j k \nabla T \cdot n d\Gamma = \int_{\Omega_1 \cup \Omega_2} \phi_j Q d\Omega . \tag{3.24}$$

Due to the continuity relations at the interface (3.23), the integral of the area along the interface ($\Gamma_1 \cap \Gamma_2$) is canceled,

$$-\oint_{\Gamma_1 \cap \Gamma_2} \phi_j k \nabla T \cdot n d\Gamma = -\oint_{\Gamma_1 \cap \Gamma_2} \phi_j k \nabla T_1 \cdot n_1 d\Gamma - \oint_{\Gamma_1 \cap \Gamma_2} \phi_j k \nabla T_2 \cdot n_2 d\Gamma = 0 . \tag{3.25}$$

It can be seen that FEM is a method that meets the continuity of flow at the interfaces of the materials with different physical properties. Eq. (3.20) remains valid and the surface integral can be applied on the border of the study area ($\Gamma_{1ext} \cup \Gamma_{2ext}$) to obtain

$$\int_{\Omega_1 \cup \Omega_2} k\left(\nabla \phi_j \cdot \nabla T\right) d\Omega - \oint_{\Gamma_{1ext} \cup \Gamma_{2ext}} \phi_j k \nabla T \cdot n d\Gamma = \int_{\Omega_1 \cup \Omega_2} \phi_j Q d\Omega . \quad (3.26)$$

Next task is to discretize (mesh) the domain of study by replacing the integral over the entire volume/surface by a summation over elementary volumes/surfaces. By applying boundary condition (3.17) to (3.26), we obtain

$$\sum_{e_v} \int_{\Omega_e} k\left(\nabla \phi_j^e \cdot \nabla T\right) d\Omega_e + \sum_{e_s} \oint_{\Gamma_e} \phi_j^e h T d\Gamma_e = \sum_{e_v} \int_{\Omega_e} \phi_j^e Q d\Omega_e + \sum_{e_s} \oint_{\Gamma_e} \phi_j^e h T_{amb} d\Gamma_e . \quad (3.27)$$

Then a linear combination in the form of (3.3) is used to approximate the temperature T on the element

$$T \approx \widetilde{T} = \sum_{i=1} \phi_i T_i , \quad (3.28)$$

which results in the final weak form

$$\sum_{e_v} \sum_{i} \left(\int_{\Omega_e} k \nabla \phi_j^e \cdot \nabla \phi_i^e d\Omega_e \right) T_i^e + \sum_{e_s} \sum_{i} \left(\oint_{\Gamma_e} h \phi_j^e \phi_i^e d\Gamma_e \right) T_i^e = \sum_{e_v} \int_{\Omega_e} \phi_j^e Q d\Omega_e + \sum_{e_s} \oint_{\Gamma_e} \phi_j^e h T_{amb} d\Gamma_e$$

, (3.29)

for all $j \in [1, N_{DOF}]$.

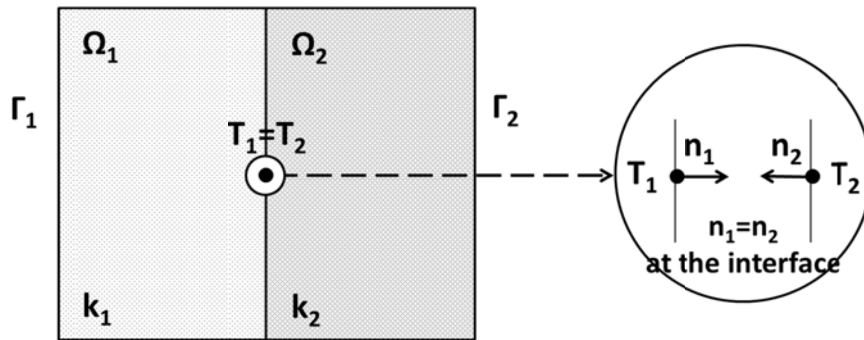

Fig. 3.5 Domains of computation with different physical properties

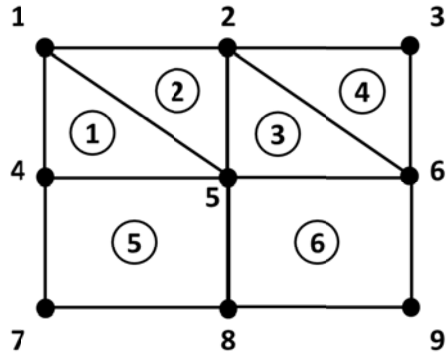

Fig. 3.6 Discretization of the computation domain

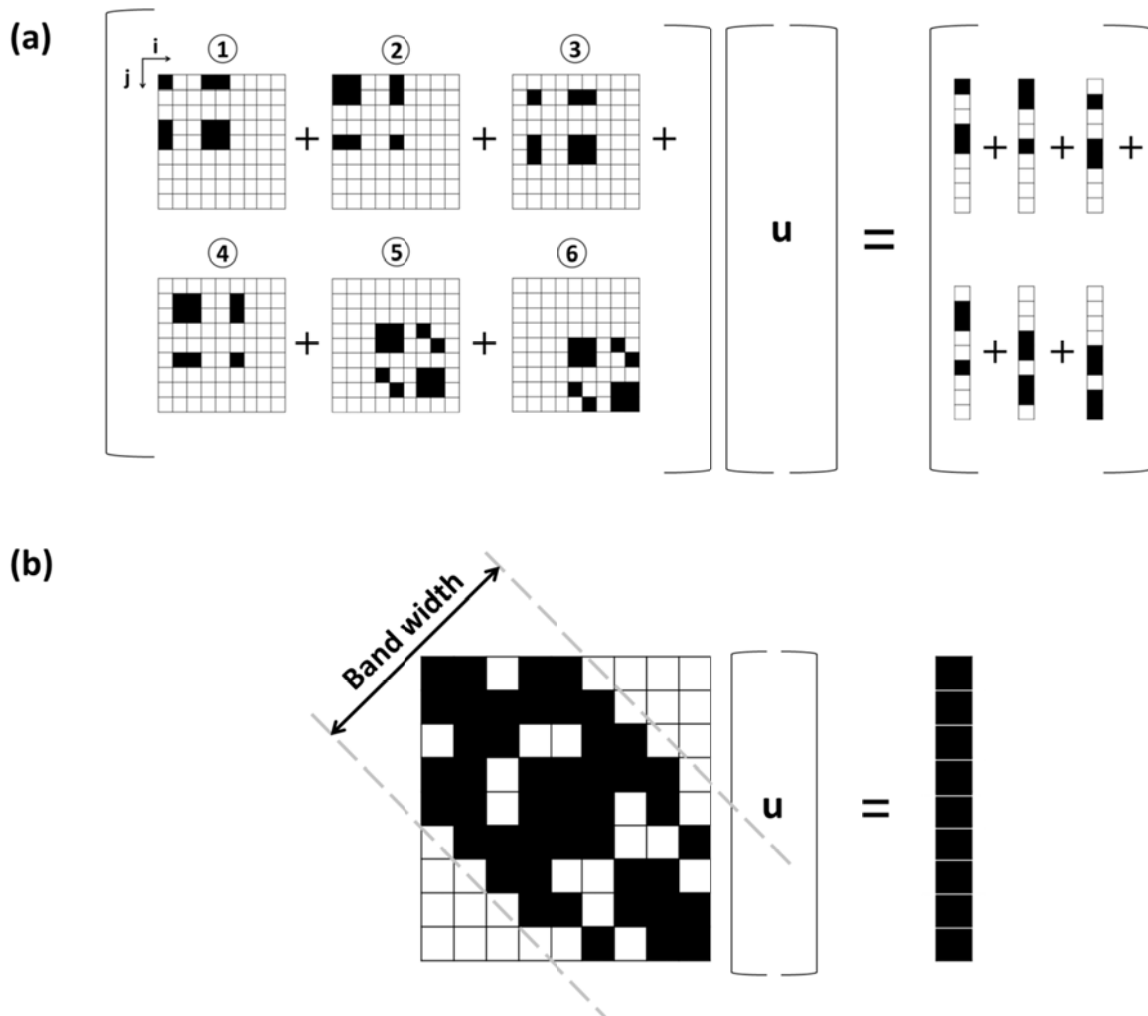

Fig. 3.7 (a) Summation of the global stiffness matrix/vector and (b) the resulting matrix/vector assembly

The next step is to define the stiffness matrix K_{ji} of the system. Considering an example of six discrete mixed type (triangle and rectangle) elements shown in Fig. 3.6, each element has its own identifying number and nodal connections corresponding to the coefficients of coupling between the nodes. Concerning the case that the properties can be found in the global coordinates, the stiffness matrix/load vector can be then written as a summation of the global matrix/vector written for each element (Fig. 3.7a). Each separated shaded area corresponds to either a single coefficient or submatrix of type K_{ji} if more than one quantity is considered at nodes. The resulting matrix/vector assembly in the global nodes numbering is shown in Fig. 3.7b with the $N_{DOF} \times N_{DOF} = 9\times9$ overall matrix dimension. This leads to a linear system with N_{DOF} unknowns (T value at the nodes) and N_{DOF} equations of the forms

$$\lfloor K_{ji} \rfloor [T_i] = \lfloor S_j \rfloor . \tag{3.30}$$

The stiffness matrix and load vector can be also called the matrix and vector integrant, respectively. These integrants are calculated numerically using the Gaussian quadrature rule which approximates the definite integral by replacing the integral of the function by a weighted sum of function values at specific points in the domain:

$$\int_{\Omega_e} f(x,y,z) d\Omega_e = \sum_k \omega_k f(\alpha_k, \beta_k, \gamma_k). \tag{3.31}$$

Weighting function (ω_k) and Gauss points (α,β,γ) are known on all types of element: 2D (triangle and quadrilateral), and 3D (tetrahedral, prism, pyramid, hexahedral).

Matrices generated by the discretization PDEs can be very large. However, most of the coefficients of this matrix are zero (see for example in Fig. 3.7b). This type of matrix is called a "sparse matrix". Methods for solving linear systems of sparse matrices are thus used to limit the number of coefficients to be stored in the memory. The matrices are then represented on the basis of knowledge of the position of the non-zero coefficients (shaded area in Fig. 3.7b). The non-zero coefficients are confined within a so-called matrix band. It can be seen that the matrix is symmetric thus only the matrix elements in the upper half of the band above the diagonal are stored in the memory. In fact, the numbering of the nodes is really important to reduce the bandwidth of the matrix therefore reducing the memory needed for the storage of coefficients.

Now a day, the industrial software functions with methods for solving systems and renumbering algorithms for optimizing the matrix bandwidth. An example of bandwidth reduction is shown in Fig. 3.8.

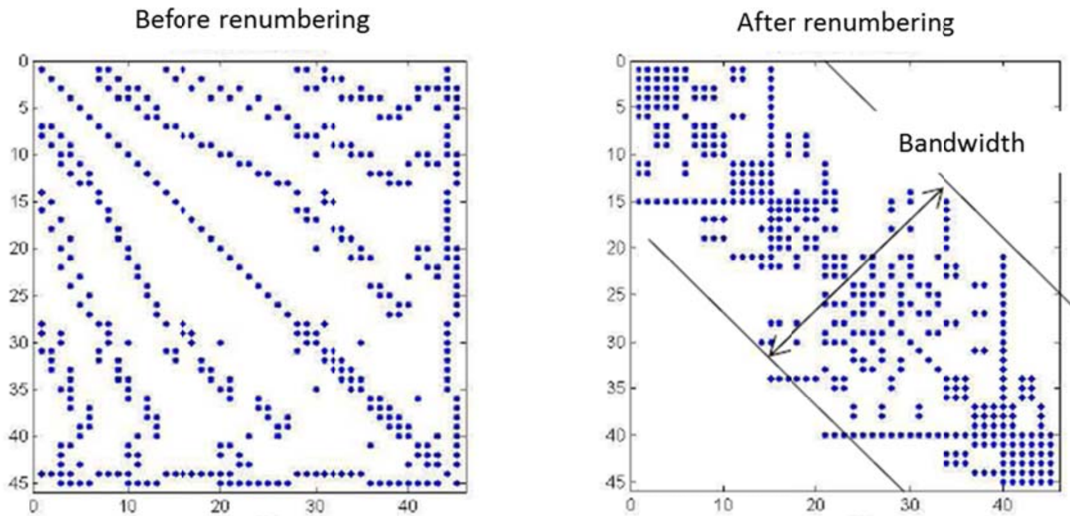

Fig. 3.8 Global matrix (45×45) before and after the renumbering process [3]

1 system of strong coupling

$$
\begin{bmatrix}
1 & 1 & 1 & 1 & & & & & \\
1 & 1 & 1 & 1 & & & & & \\
1 & 1 & 1 & 1 & & & & & \\
1 & 1 & 1 & 1 & & & & & \\
 & & & & 2 & & & & \\
 & & & & & 3 & 3 & 3 & 3 \\
 & & & & & 3 & 3 & 3 & 3 \\
 & & & & & 3 & 3 & 3 & 3 \\
 & & & & & 3 & 3 & 3 & 3
\end{bmatrix}
\begin{bmatrix} A_x \\ A_y \\ A_z \\ V \\ T \\ v_x \\ v_y \\ v_z \\ p \end{bmatrix}
$$

3 sub-systems of weak coupling

$$
\begin{bmatrix}
1 & 1 & 1 & 1 \\
1 & 1 & 1 & 1 \\
1 & 1 & 1 & 1 \\
1 & 1 & 1 & 1
\end{bmatrix}
\begin{bmatrix} A_x \\ A_y \\ A_z \\ V \end{bmatrix}
$$

Electromagnetism

$$
[2][T]
$$

Thermal

$$
\begin{bmatrix}
3 & 3 & 3 & 3 \\
3 & 3 & 3 & 3 \\
3 & 3 & 3 & 3 \\
3 & 3 & 3 & 3
\end{bmatrix}
\begin{bmatrix} v_x \\ v_y \\ v_z \\ p \end{bmatrix}
$$

Hydrodynamics

Fig. 3.9 Nodal matrix system formulation for (a) strong and (b) weak coupled techniques in solving the Magneto-thermo-hydrodynamics problems

The field of materials development and engineering processes is in reality involved in the coupled physico-chemical phenomena. Such coupled phenomena practically occur in the industrial environment, for example, electromagnetism and heat transfer in the induction heating process, and the fluid dynamics and the chemical species transport in reacting flow process. These kinds of problems are necessary to be considered in a coupled regime. The coupled phenomena are normally implemented using the two mains techniques: strong coupling and weak coupling. The former one is performed by simultaneously solve all of the coupled equations within a single resolution matrix. This method provides more accurate results with a higher cost of computational time and memory. The latter one is done by solving the equations sequentially. The overall system may be decomposed into several subsystems. This method can benefit from the computational speed using the specialized solver but with some risk concerning an instability issue. Giving the magneto-thermo-hydrodynamics problem as an example of the coupled phenomena, the number of the unknown per node is 9 (3 components of magnetic vector potential, scalar electric potential, temperature, 3 velocity components, and pressure). The matrix system at each nodal point for both strong and weak coupling techniques can be seen in Fig. 3.9. For the system of NBN nodes, the size of global matrix system calculated from the number of degrees of freedom square $(N_{DOF})^2 = (9\times\text{NBN})^2$ in the case of strong coupled is much larger than the weak coupled one $(4^2+1^2+4^2)\times\text{NBN}^2$. If the physical properties are linear, the system of (3.30) can be solved either by direct methods (MUMPS, PARDISO, SPOOLES) based on LU decomposition (LU factorization) or iterative methods (conjugated gradient, GMRES, etc.).

3.3 A nonlinear system

If the system (3.30) is nonlinear, for example the thermal conductivity is dependent on the temperature, the equation of heat transfer or operator L in (3.1) is nonlinear. This case is also a general case for fluid mechanics. In such case, the nonlinear solver based on the Newton's method is used. Thus the solution will be obtained iteratively where the initial conditions and the maximum number of iterations must be specified. The formulation representing the residual in the nonlinear system with L+1 number of iteration can be written as

$$F\left(u^{L+1}\right) = 0. \tag{3.32}$$

For the Newton-Raphson method, we can write a Taylor expansion of operator F around a solution of the previous iteration step $F(u^L)$ ignoring higher order terms as

$$F\left(u^{L+1}\right) = F\left(u^{L}\right) + \left(u^{L+1} - u^{L}\right)F'\left(u^{L}\right) = 0, \tag{3.33}$$

which can be rearranged as

$$F'\left(u^{L}\right)\left(u^{L+1} - u^{L}\right) = -F\left(u^{L}\right), \tag{3.34}$$

where $F'(u^L)$ is a Jacobian matrix of the system since it contains the first-order partial derivatives. It can be seen that now the system (3.34) is a linear equation for u^{L+1} for a given approximated solution u^L. Thus, by knowing the solution of the preceding iteration u^L, the solution of the next iteration u^{L+1} can be computed. The convergence is achieved if the relative error defined by $\frac{\left|u^{L+1} - u^{L}\right|}{\left|u^{L}\right|}$ is smaller than specified precision. A schematic representation of the Newton-Raphson method is shown in Fig. 3.10. A numerical technique generally used is to relax the sub-solution by assigning a coefficient $0 \le \alpha \le 1$ called a damping factor which is related to the increment of the solution, i.e.

$$u^{L+1} = u^{L} + \alpha \Delta u^{L+1}. \tag{3.35}$$

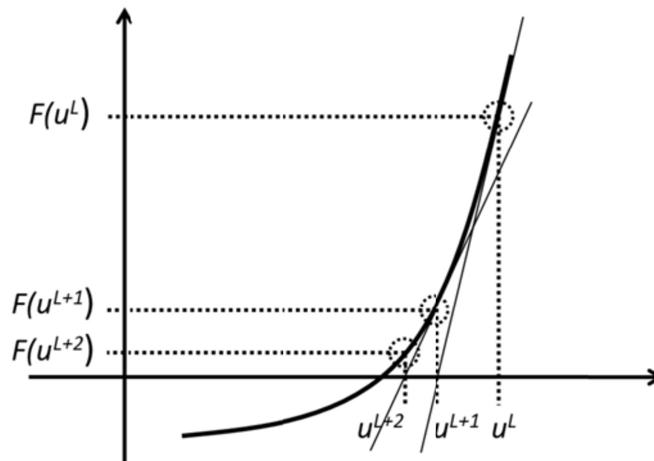

Fig. 3.10 Schematic representation of the root-finding using Newton-Raphson method

This technique is known to slow down the calculation but gives a more secure convergence. In fact, the method using the Jacobian matrix is not the only possibility but a fixed point method can be also used to directly iterate the system (3.29). However the Jacobian matrix is used to ensure the good convergence resolution method. In some industrial software, the Jacobian matrix is either symbolically or numerically assembled.

In the scope of this thesis, we limit the modeling only to steady state calculations. However, it is worth noting one of the important features of the transient FEM calculations. The term that contains a time derivative is developed either by using an implicit or explicit finite difference. The former one is better to avoid the stability problems while the latter is better in case of a large deformation. A system of the type (3.30) can be formed while the solution at the initial time and the time step has to be specified. The transient problem can be also a nonlinear problem, thus the iterations technique of the nonlinear system has to be imposed.

In summary, the FEM method has a strong capability to solve the PDEs governing the physical phenomena associated with the growth processes in a complex geometry. Such process characterization tool, however, requires proper definition of the physical systems and the boundary conditions. We will consider step by step the following systems related to the SiC growth processes. The induction heating and heat transfer system will be discussed in the next chapter. Then the system of mass transport concerning the PVT method will follow. Finally, the full TSSG process will be discussed.

References

1. Chaussende, D., P.J. Wellmann, and M. Pons, *Status of SiC bulk growth processes.* Journal of Physics D: Applied Physics, 2007. **40**(20): p. 6150-6158.
2. Dedulle, J.M., *Modélisation numérique de phénomènes physiques couplés. Aide à la compréhension et à l'optimisation dans le domaine des matériaux et procédés*, in *MEMOIRE POUR L'OBTENTION DU DIPLOME D'HDR*. 2013: Univ. Grenoble-Alpes.
3. Dedulle, J.M., *Eléments finis, Codes commerciaux*, in *Elaboration des Matériaux et Génie des Procédés (GPEIMat)* 2005, Ecole thématique Oléron, France.
4. Zienkiewicz, O.C., J. Zhu, and R.L. Taylor, *The finite element method.* Its Basis and Fundamentals. 2013, Massachusetts Butterworth-Heinemann.
5. Zimmerman, W.B., *Multiphysics Modeling With Finite Element Methods (Series On Stability, Vibration And Control Of Systems, Serie)(Series.* 2006.
6. Bathe, K.J., *Finite Element Procedures*. 2012, New Delhi: PHI Learning Private Limited.

Chapter 4
Induction heating and heat transfer

The thermal conditions in growth system were studied by means of coupled induction heating and heat transfer in the entire region of furnace. All the calculations were conducted by Finite Element Method (FEM) in a two-dimensional axisymmetric space-dimension since the growth reactor is shaped axisymmetric. In this chapter, the physical model and the boundary conditions are presented, followed by the effect of the semi-transparency of SiC. Finally, the modeling results and validations will be discussed.

4.1 Physical model

4.1.1 Induction heating

The practical method for high temperature heating of crucible is by electromagnetic induction. In this RF induction heating regime, the electromagnetic phenomenon is described by the Maxwell's equations which provide the distribution of electromagnetic field. The induced eddy currents are generated according to Lenz's law. The Ohmic resistance caused by the current dissipates energy and the crucible is consequently heated by the Joule's effect. The differential form of Maxwell equations are written by [1]

$$\nabla \times \mathbf{E} = -\frac{\partial \mathbf{B}}{\partial t}, \tag{4.1}$$

$$\nabla \times \mathbf{H} = \mathbf{J}_f + \frac{\partial \mathbf{D}}{\partial t}, \tag{4.2}$$

$$\nabla \cdot \mathbf{D} = \rho_f, \tag{4.3}$$

$$\nabla \cdot \mathbf{B} = 0. \tag{4.4}$$

If low frequency (f < 1 MHz) is used in the experiments [2], the currents and the electromagnetic field vary slowly and the dimension of the growth reactor is small compared to the wavelength. In this case, the Maxwell's equations for quasi-static approximation under the assumption that $\partial \mathbf{D}/\partial t = 0$ is valid. The elimination of the displacement current density term reduces the computational cost. Under the assumption that the magnetic field is time-harmonic with an angular frequency ω, there is however no computational cost for including the displacement current in Ampere's law. Thus the Maxwell-Ampere's law (4.2) can effectively be used [3].

From (4.4), the magnetic field **B** can be formulated by the magnetic vector potential **A** such that

$$\mathbf{B} = \nabla \times \mathbf{A}\,, \tag{4.5}$$

From Eq. (4.1), the relation becomes

$$\nabla \times \left(\mathbf{E} + \frac{\partial \mathbf{A}}{\partial t} \right) = 0. \tag{4.6}$$

The expression for electric field can be written in terms of a vector potential and scalar potential in such a way that it provides a zero curl, thus

$$\mathbf{E} = -\nabla V - \frac{\partial \mathbf{A}}{\partial t}. \tag{4.7}$$

The current density is proportional to the force per unit charge **f** and the electrical conductivity. In the system heated by induction, the force that drives the charge to produce current is a current caused by electromagnetic force and the externally generated current density $\mathbf{J}_e$. Thus the free current density can be written

$$\mathbf{J}_f = \sigma \mathbf{f} + \mathbf{J}_e = \sigma(\mathbf{E} + \mathbf{v} \times \mathbf{B}) + \mathbf{J}_e. \tag{4.8}$$

The total current density **J** can thus be written as

$$\mathbf{J} = \mathbf{J}_f + \mathbf{J}_d = \sigma(\mathbf{E} + \mathbf{v} \times \mathbf{B}) + \frac{\partial \mathbf{D}}{\partial t} + \mathbf{J}_e\,. \tag{4.9}$$

From (4.5), (4.7), and (4.8), the Maxwell-Ampere's law (4.2) for linear materials can be written

$$\frac{1}{\mu_0\mu_r}\nabla\times\nabla\times\mathbf{A} = \sigma\left(-\nabla V - \frac{\partial \mathbf{A}}{\partial t}\right) + \varepsilon_0\varepsilon_r \frac{\partial}{\partial t}\left(-\nabla V - \frac{\partial \mathbf{A}}{\partial t}\right) + \sigma\mathbf{v}\times\left(\nabla\times\mathbf{A}\right) + \mathbf{J}_e . \tag{4.10}$$

This forms an equation of two potentials: scalar potential V and vector potential $\mathbf{A}$. In fact, these two potential are not uniquely defined from the electric (4.7) and magnetic (4.5) fields since it is possible to impose extra conditions on V and $\mathbf{A}$ providing that $\mathbf{E}$ and $\mathbf{B}$ are not affected. For example, substituting a set of potentials

$$\widetilde{V} = V - \frac{\partial \Psi}{\partial t} \text{ and} \tag{4.11}$$

$$\widetilde{\mathbf{A}} = \mathbf{A} + \nabla\Psi . \tag{4.12}$$

will give the same electric and magnetic field

$$\mathbf{E} = -\nabla\left(\widetilde{V} + \frac{\partial \Psi}{\partial t}\right) - \frac{\partial}{\partial t}\left(\widetilde{\mathbf{A}} - \nabla\Psi\right) = -\nabla\widetilde{V} - \frac{\partial \widetilde{\mathbf{A}}}{\partial t}. \tag{4.13}$$

$$\mathbf{B} = \nabla\times\left(\widetilde{\mathbf{A}} - \nabla\Psi\right) = \nabla\times\widetilde{\mathbf{A}} \tag{4.14}$$

Thus, it is necessary to add the constraint (gauge transformation) to ensure the unique solution. For a particular gauge transformation of the form $\Psi = -iV/\omega$, providing that

$$\widetilde{\mathbf{A}} = \mathbf{A} - \frac{i}{\omega}\nabla V \text{ and} \tag{4.15}$$

$$\widetilde{V} = 0 , \tag{4.16}$$

equation (4.10) can be reduced to the magnetodynamic equation for the vector potential:

$$\frac{1}{\mu_0\mu_r}\nabla\times\nabla\times\mathbf{A} + \left(i\omega\sigma - \omega^2\varepsilon_0\varepsilon_r\right)\mathbf{A} - \sigma\mathbf{v}\times\left(\nabla\times\mathbf{A}\right) = \mathbf{J}_e \ , \tag{4.17}$$

The work done per unit time per unit volume can be expressed as

$$-\mathbf{E}\cdot\mathbf{J} = \sigma\frac{\partial \mathbf{A}}{\partial t}\cdot\frac{\partial \mathbf{A}}{\partial t}. \tag{4.18}$$

By assuming the relaxation time for heat dissipation is much shorter than the time scale for heat conduction, the volume density of the generated heat power can be computed from the mean value of (4.18). Thus, power delivered per unit volume can be formulated by

$$Q = \sigma\langle -\mathbf{E}\cdot\mathbf{J}\rangle = \frac{1}{2}\sigma\omega^2\left(\mathbf{A}\cdot\mathbf{A}^*\right). \tag{4.19}$$

4.1.2 Heat transfer

Heat transfer in the reactor is defined by the movement of energy according to the temperature difference. Three mechanisms are considered in the studied systems: conduction, convection, and radiation. The energy equation used to describe the temperature distribution in the growth reactor is of the form

$$C_p\frac{\partial}{\partial t}(\rho T) + C_p\nabla\cdot(\rho\mathbf{v}T) - \nabla\cdot(k\nabla T) = Q_{th}\ . \tag{4.20}$$

The local heat generation in unit volume Q_{th} is obtained from the electromagnetic induction heating calculated by Eq. (4.19). Eq. (4.20) is written based on the major assumption that the heat production and consumption (exothermic and endothermic) according to chemical reactions in the gas mixture does not contribute much to the heat transfer for the sublimation process studied in this thesis. Moreover, the quasi-steady state is assumed during crystal growth process. Therefore, the governing stationary state equation for thermal energy simplifies to

$$C_p\nabla\cdot(\rho\mathbf{v}T) - \nabla\cdot(k\nabla T) = Q_{th}\ . \tag{4.21}$$

The temperature distribution profile in the system can be solved from Eq. (4.21). The first term on the left hand side is related to the translational heat transfer. Normally the solid parts in the growth system do not move so this term becomes zero. In the gas phase especially in the growth chamber, the term for heat transfer by convection does not vanish. The computation of the convective heat flux requires the knowledge of the mean velocity of the vapor species, which can be obtained only from the modeling of fluid dynamics and mass transport. Thus, the iteration steps are needed for the computation. The basic iteration procedure is associated with the following steps:

1. Guessing the initial value of the fluid velocity (typically we impose the case of no convective heat transfer so the fluid velocity is zero), the temperature distribution can be solved using the induction heating and heat transfer modules

2. Using the temperature profile computed from the 1st step, the fluid velocity can now be solved using the reacting flow module

3. Performing the calculation as done in the 1st step of the procedure using the updated fluid velocity computed from the 2nd step

The iteration process will be done until the convergence of the calculations is obtained; usually after several iteration steps. However if the heat transfer by radiation is taken into accounted, it becomes the dominant contribution at the solid-vapor interface. The similar conclusion was reported from the estimation of the heat transfer quantities [4]. The temperature distribution in the growth chamber without and with convective heat transfer is shown in Fig. 4.1a and Fig. 4.1b, respectively. The convective heat transfer modifies slightly the temperature distribution in the gas phase. The upward convection flow pushes the isotherms toward the seed crystal. The changes in the isothermal shape when taking convective heat transfer into account is in agreement with [5] resulting in the steeper axial temperature gradient toward the seed crystal. The temperature at the solid-vapor interfaces are very slightly modified as can be seen for example for the radial temperature profile along the SiC seed crystal (Fig. 4.2) and overall temperature gradient is not affected by the gas convection in this work. This is in contrast to [5] due to the fact that the gas velocity was amplified in order to numerically demonstrate the effect of the convective heat transfer in such work. In the scope of this thesis, only the heterogeneous reactions at the solid-vapor interface are considered while the chemical reactions are neglected in the gas mixture. Since the exclusion of convective heat transfer does not affect critically the computational accuracy, the convective heat transfer can be neglected in order to reduce the computational cost. It is worth noting that neglecting the convective heat transfer is one of the major assumptions in many numerical simulation works [2, 4, 6, 7].

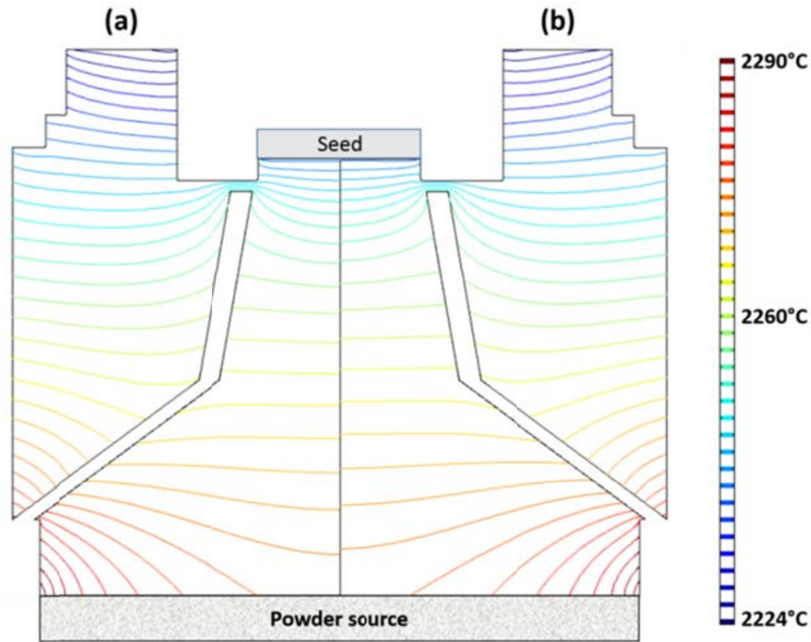

Fig. 4.1 Distribution of isothermal lines in the growth chamber calculated (a) without convective heat transfer and (b) with convective heat transfer. The temperature difference between adjacent isothermal lines is 2 K.

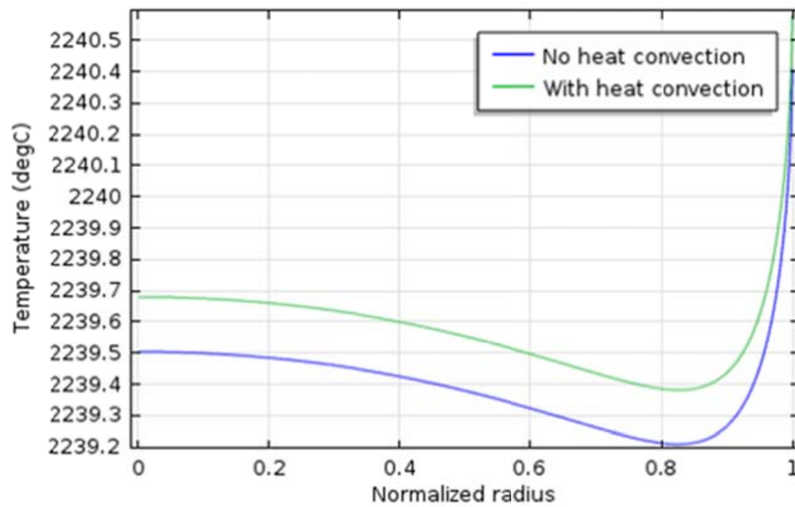

Fig. 4.2 Temperature profile along the seed radius

4.2 Boundary conditions

4.2.1 Electromagnetic boundary conditions

In the simulation of open boundary problem, some mathematical transformation is needed. A set of boundary conditions must be imposed for the magnetic model. The zero vector potential is applied on the limiting box corresponding to infinity distance from the coil. Moreover, due to the axisymmetric design of the reactor, a zero normal induction field is defined at the symmetry axis.

4.2.2 Heat transfer boundary conditions

A set of boundary conditions are formulated for the heat transfer problem. First, the zero-temperature gradients is imposed at the symmetry axis. Second, the thermal flux boundary conditions related to the radiation are fixed at boundaries of the cavities. The net inward flux is calculated from the difference between the irradiation and the radiosity written as

$$-\mathbf{n}\cdot\left(-k\nabla T\right)=G-J\,, \tag{4.22}$$

where G is the total arriving flux or the irradiation. The generalized equation for the irradiative flux including the mutual irradiation G_m coming from other surfaces and the ambient irradiation G_{amb} can be written as

$$G=G_m+G_{amb}=G_m+F_{amb}\sigma T_{amb}^4\,. \tag{4.23}$$

By considering a geometry shown in Fig. 4.3Fig. 4.**3**, a point x is able to see both the other points on the surface Γ' and the surrounding ambient Γ_{amb}. If the points on the other surfaces have a local radiosity *J'*, the mutual irradiation at point x can be determined from the integral

$$G_m=\int_{\Gamma'}\frac{(-\mathbf{n}'\cdot\mathbf{r})(\mathbf{n}\cdot\mathbf{r})}{\pi|\mathbf{r}|^4}J'd\Gamma\,, \tag{4.24}$$

where the local radiosity is projected onto point x when computing the heat flux arrived from x'. The second term represent the ambient irradiation where F_{amb} is the ambient view factor. This function describes the proportion of view from each point covered by ambient conditions. Its value can vary from zero to unity at all point depending on the geometry. Thus the ambient view

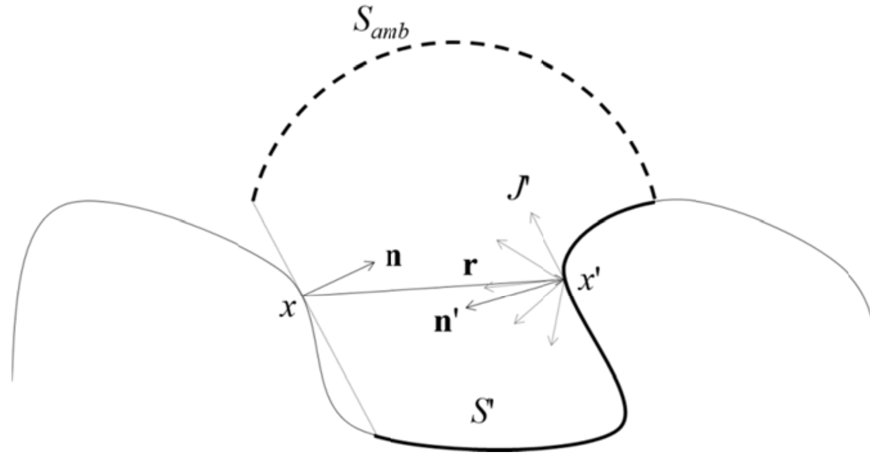

Fig. 4.3 Computation of mutual irradiation and ambient view factor

factor can be written in terms of the integral of the surrounding surfaces Γ' (having a view factor of *F'*):

$$F_{amb} = 1 - F' = 1 - \int_{\Gamma'} \frac{(-\mathbf{n}' \cdot \mathbf{r})(\mathbf{n} \cdot \mathbf{r})}{\pi |\mathbf{r}|^4} d\Gamma . \tag{4.25}$$

The radiosity J is determined by the summation of the reflected radiation and the emitted radiation, thus

$$J = rG + \varepsilon_e \sigma T^4 , \tag{4.26}$$

where r here denotes the reflectivity. Since most opaque bodies exhibit ideal gray bodies' behavior, the absorptivity α equals to emissivity ε_e and the relation with reflectivity can be expressed:

$$\alpha = \varepsilon_e = 1 - r . \tag{4.27}$$

Consequently, the expression for surface-to-surface radiation assuming ideal gray bodies becomes

$$-\mathbf{n} \cdot (-k \nabla T) = \varepsilon_e (G - \sigma T^4). \tag{4.28}$$

The thermal flux boundary conditions associated with the radiative phenomenon of the reactor outer wall are implemented by assuming that the surrounded ambients behave like a blackbody where its emissivity and reflectivity equal to unity and zero, respectively. Moreover, the mutual irradiation equals to zero and the ambient view factor equals to unity. Therefore, the boundary condition for the surface-to-ambient radiation becomes

$$-\mathbf{n}\cdot\left(-k\nabla T\right)=\varepsilon_e\sigma\left(T_{amb}^4-T^4\right). \tag{4.29}$$

4.3 Semi-transparency of SiC

In general an opaque body was assumed for all materials used in the growth system within a fixed range of wavelength $\Lambda\in\{\lambda_1,\lambda_2\}$. This means that the radiative heat transfer was taken into account only at the solid-vapor boundaries where the non-reflected waves are completely absorbed and emitted. However, some materials exhibit a semi-transparency behavior. In such case the absorption process does not take place only at the solid-vapor interface but parts of the energy were also absorbed and transmitted in the material medium itself. This phenomenon has been shown to have a strong influence in the crystal growth process [8]. Concerning the process modeling for the growth of SiC, the effects of semi-transparency were reported [5, 9, 10]. The overall temperature field is slightly affected by the semi-transparency while the local effect on the crystal and its vicinity is significant. First, the influence on the temperature distribution in the crystal may affects directly the thermal stress and hence the dislocation density. Moreover the temperature distribution close to the crystal-vapor interface affects the shape of the growing crystal [10]. In this section, we are considering the method to treat SiC as a semi-transparency material and then we will discuss the effects on the growth process and the validation of this model.

In order to compute the heat exchange in the semi-transparent medium, the band-energy method is used [8]. The schematic representation of the band-energy method is shown in Fig. 4.4. The system domain containing the semi-transparent medium can be decomposed into two enclosures. The first enclosure corresponds to the range of wavelength Λ_1 where SiC is opaque so the heat fluxes emitted from surface (1) interact with the surface (2). The second enclosure corresponds to the wave in a range Λ_2 where the SiC is transparent so the heat fluxes emitted

from (1) directly interact with (3). In each enclosure, the boundary conditions for heat transfer by radiation are governed by (4.28). Thus the total radiative heat fluxes associated with each surface can be written:

$$Q_r = -\mathbf{n} \cdot (-k\nabla T) = q_{\Lambda_1} + q_{\Lambda_2} \qquad \text{on (1)} \tag{4.30}$$

$$Q_r = -\mathbf{n} \cdot (-k\nabla T) = q_{\Lambda_1} \qquad \text{on (2)} \tag{4.31}$$

$$Q_r = -\mathbf{n} \cdot (-k\nabla T) = q_{\Lambda_2} \qquad \text{on (3),} \tag{4.32}$$

where $q_{\Lambda 1}$ and q_{Λ_2} are the radiative heat fluxes of wavelength Λ_1 and Λ_2, respectively. The general expression shown in relation (4.30) was obtained from the superposition of the contributions of each enclosure. Differently speaking, this semi-transparency model superposes the opaque and the transparent bodies.

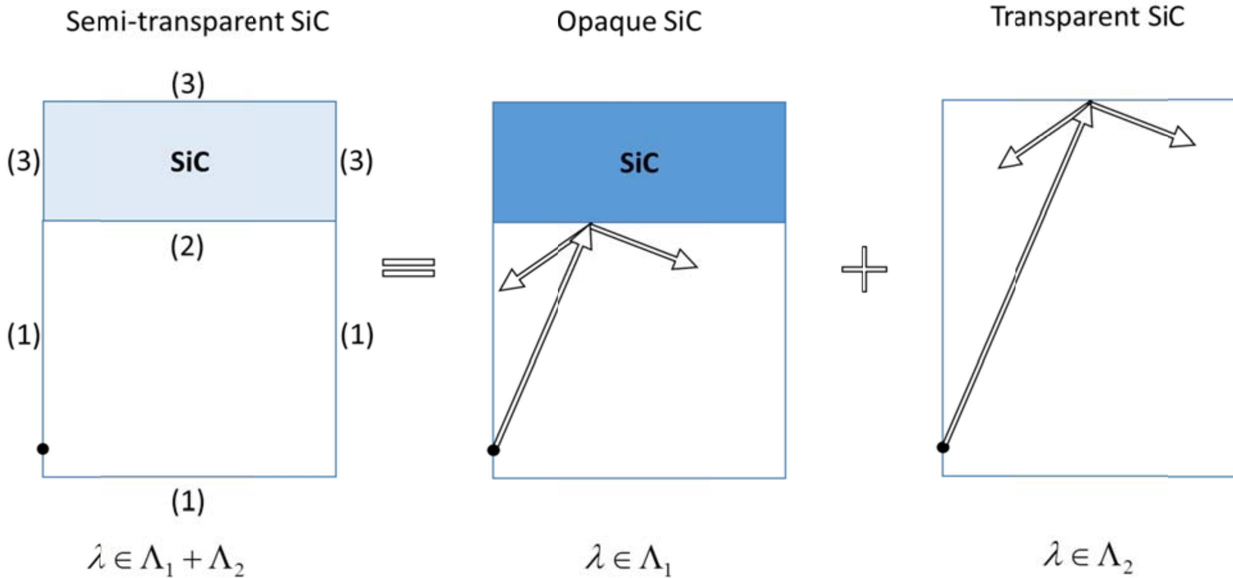

Fig. 4.4 Schematic representation of the band-energy method

Concerning the effects of the semi-transparency of SiC, the temporal variation of the temperature profiles during the growth process is studied using the quasi-steady approach. This is a reasonable approach considering that the SiC growth is a slow and long term process. As a

geometric simplification, the crystal shape is taken as rectangular. Thus the temporal variation of the growth stage is characterized by the increase in the thickness of the crystal: 0.05 cm, 1cm, and 2cm. The results from the semi-transparency model are also compared with the opaque and transparent models. Fig. 4.5a shows the comparison of the temperature profile in the growth chamber computed from different model at the initial stage of the growth. The global shapes of the isothermal lines are not strongly affected by the choice of the model. However the temperature distribution in the vicinity of the SiC crystal is substantially affected (Fig. 4.5b). The effect on the SiC crystal itself is still not clear at this stage due to the small size of the crystal.

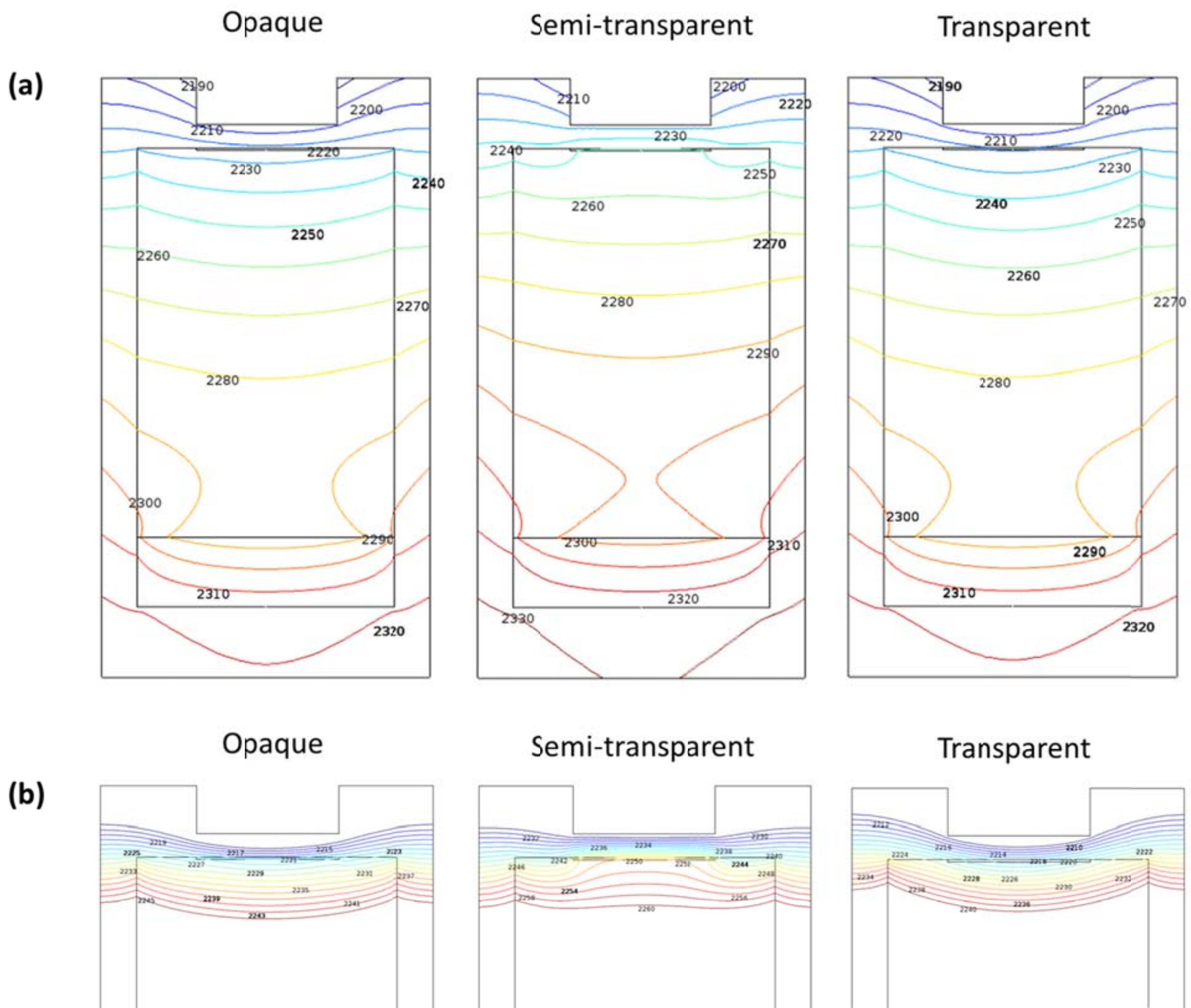

Fig. 4.5 Temperature profile (a) in the growth chamber and (b) in the vicinity of the SiC crystal at the initial stage of the growth

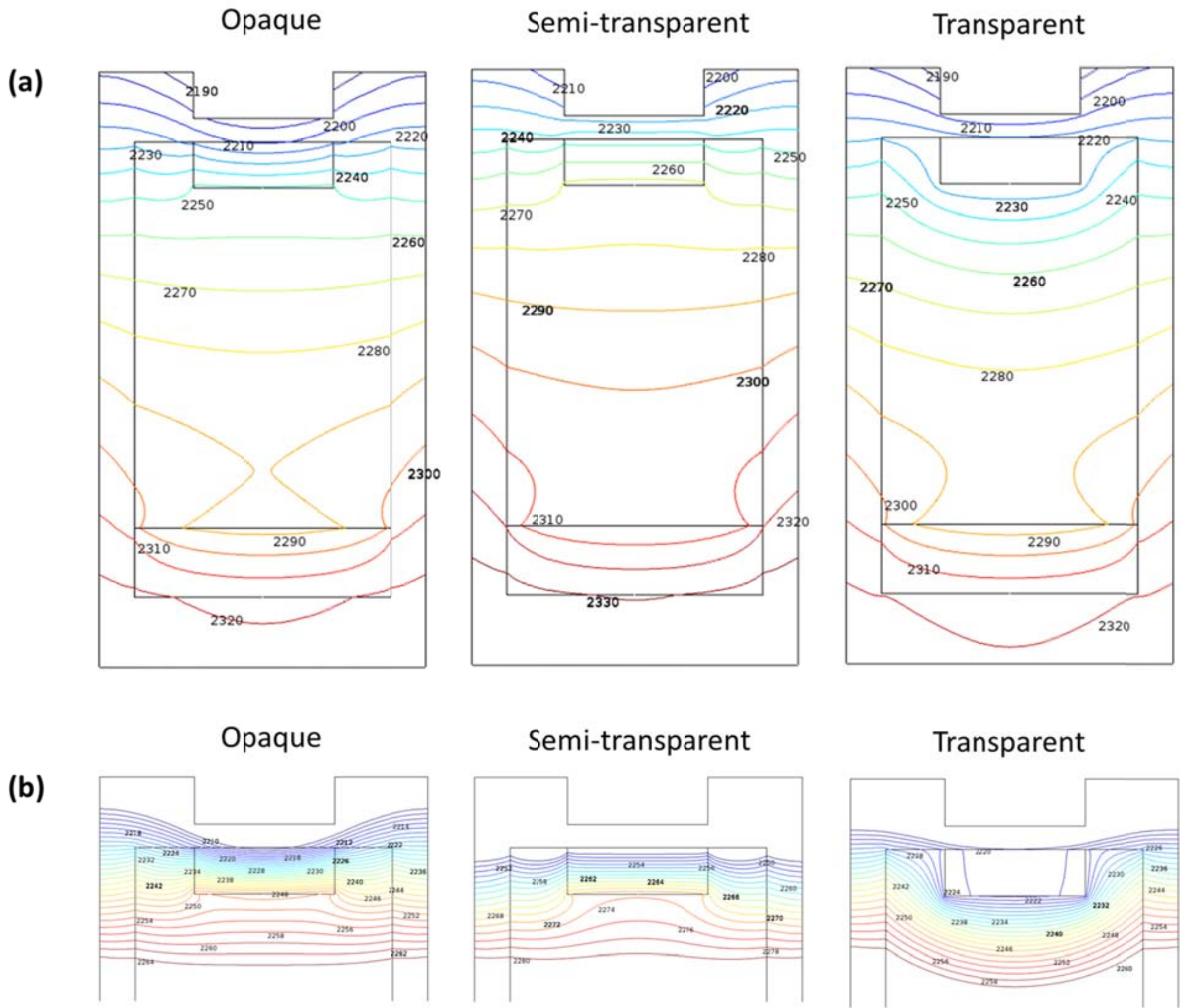

Fig. 4.6 Temperature profile (a) in the growth chamber and (b) in the vicinity of the SiC crystal after 1 cm of SiC growth

At the second time step or after 1cm of the crystal growth, we can observe clearly the effect on the temperature distribution inside the crystal in Fig. 4.6a with the close-ups images in Fig. 4.6b. The opaque body prohibits the transmission of the wave. The radiative heat transfer takes place only at the crystal-vapor interface. Thus the heat will be transfer from this interface toward the backside of the crystal only by the conduction. In addition to conductive heat transfer in the crystal, the backside of the crystal is also irradiated in the case of semi-transparent body. Since the radiative heat transfer is very efficient and dominates at high temperature, this causes the higher temperature at the crystal-graphite interface, and the reduction of axial temperature

gradient inside the crystal and the growth cavity. The temperature profile along symmetry axis from the source powder to the backside of the crystal at the symmetry is plotted in Fig. 4.7 for better visualization. For the transparent body, the crystal is almost isothermal where the axial temperature difference inside the crystal is less than 10 K. However, the axial temperature gradient in front of the crystal increases. In this case, the radiation takes place only at the crystal-graphite interface. Thus, the heat transfer at the crystal vapor interface is governed only by the conduction. Concerning the conservation of energy at the boundary of two materials, the continuity relation can be obtained and rearranged as

$$\frac{\nabla T_1 \cdot \mathbf{n}}{\nabla T_2 \cdot \mathbf{n}} = \frac{k_2}{k_1}. \tag{4.33}$$

The ratio of the temperature gradient normal to the interface of difference materials (axial temperature gradient in this case) is inversely proportional to the ratio of their thermal conductivities. As a result, the temperature gradient in the vapor is higher than the crystal due to the smaller thermal conductivity. The axial temperature profiles are modified mainly in the vicinity of the growing crystal while similar profile is predicted far from it. The overall increase in the temperature in the growth chamber treating the SiC as a semi-transparent body compared to the opaque and the transparent cases (Fig. 4.7) is attributed to the increase in the surface area exposed normal to the radiative heat flux.

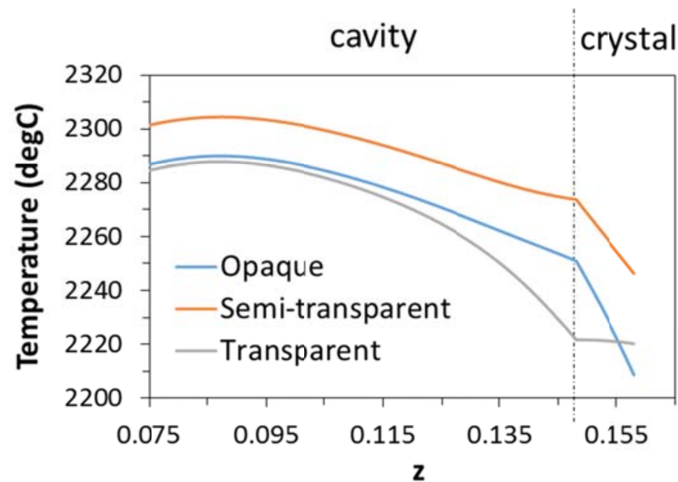

Fig. 4.7 Temperature profile along the symmetry axis from source powder toward crystal-graphite interface

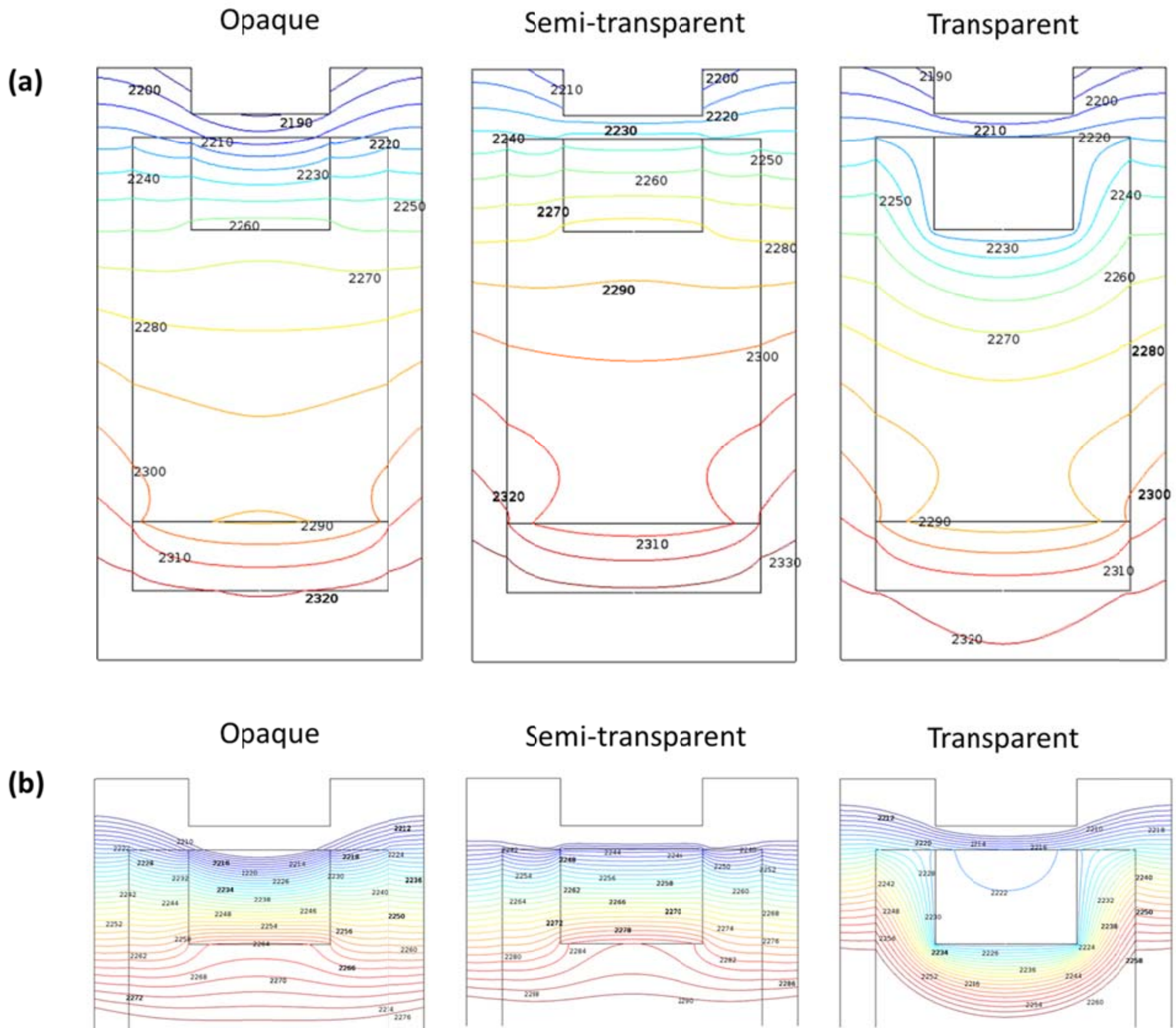

Fig. 4.8 Temperature profile (a) in the growth chamber and (b) in the vicinity of the SiC crystal after 2 cm of SiC growth

At the last time step of the growth studied in this section (2 cm crystal), the shapes of the temperature profile in the growth cavity are almost similar comparing opaque and semi-transparent (Fig. 4.8a). Moreover, the temperature distributions inside the crystal show the same tendency as in the previous stage discussed above (Fig. 4.8b). The temporal effects of the optical properties of SiC on the temperature profile on the crystal growth front are shown in Fig. 4.9. For the opaque body, the temperature along the crystal radius changes from convex (toward the growth direction) to concave shapes (Fig. 4.9a) when the crystal grows thicker. The semi-transparent body preserves the concave temperature profile for all of the time steps (Fig. 4.9b). In

these two cases, the temperature increases when the crystal thickness increases. On the other hand, the temperature at the growth front is almost constant in the case of transparent body (Fig. 4.9c) due to the weak conductive heat transfer in the vapor.

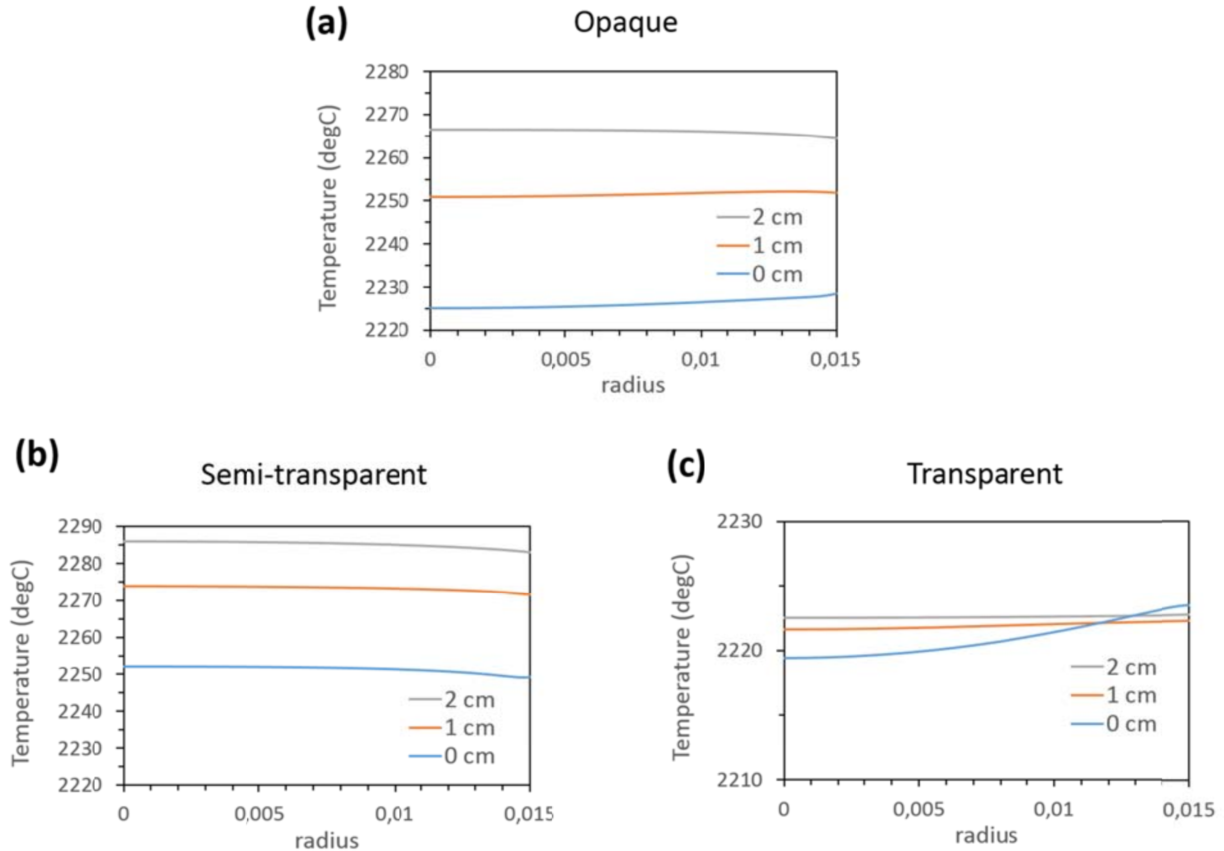

Fig. 4.9 Temperature profile on the crystal growth front along the crystal radius for (a) opaque, (b) semi-transparent, and (c) transparent cases.

We have shown that, if the SiC acts as a semi-transparent body, its effects should not be neglected for the two main reasons. First, the variation of the temperature profile at the growth front and its surrounding surfaces has a strong impact on the global mass transport. As a consequent, the growth rate or the interface shape of the growing crystal will unavoidably be affected. Moreover, the computation of thermo-elastic stress and dislocation density have to be reconsidered due to the drastic changes in the axial and radial temperature gradient in the SiC crystal. However, the experimental results concerning the interface shapes of the growing crystal

are better described by the model with opaque SiC. Thus, it is very important to discuss about the validity and limitations of the semi-transparent model. First of all, we are considering the monochromatic plane wave of wavelength λ having an initial intensity I^0 and propagating through the material of thickness *h*. In the simplest case where the reflection and dispersion are neglected, the wave transmitted through the material will be attenuated due to the absorption. The relation between the initial intensity and the outgoing intensity can be written [8]

$$I_\lambda^h = I_\lambda^0 \exp(-\alpha_\lambda z), \tag{4.34}$$

where the absorption coefficient α_λ can be correlated to the skin depth (the distance that it take to reduce the amplitude by factor of 1/*e*) by

$$\delta_\lambda = \frac{1}{\alpha_\lambda}. \tag{4.35}$$

We may define the spectral optical thickness for which its magnitude is dimensionless such as

$$\tau_\lambda = \frac{\delta_\lambda}{h} = \frac{1}{\alpha_\lambda h}. \tag{4.36}$$

The material is opaque if $\tau_\lambda << 1$ whereas it becomes transparent if $\tau_\lambda >> 1$ for the wavelength λ. Regarding the band-energy method for treating SiC as a semi-transparent body, we considered that SiC is opaque for some range of wavelengths (such as Λ_1) but transparent for others (such as Λ_2). Moreover, the transmitted wave is assumed to travel through to crystal without interaction with the crystal itself. Such assumption is accurate only if the ranges of wavelength in which τ_λ is of the same order as unity is negligible. This is the first limitation of the model. The second consideration is the dependency of the absorption coefficient of SiC on the temperature, polytype, wavelength, and the doping level [11-15]. There are some discrepancies in those experimental observations so it is not very easy to draw any strong conclusion here. For the optical band, the absorption coefficient having very low values was mostly observed in a relatively pure crystal (low doping concentration) while increasing when the charge carrier concentration increases [12]. Most of the non-zero value of α_λ varies from few cm^{-1} to several thousand cm^{-1}. So let's consider here the two extreme cases, $\alpha_\lambda = 1$ cm^{-1} (lower limit) and

$\alpha_\lambda = 1000$ cm^{-1} (upper limit). The SiC crystal will become transparent if $\tau_\lambda >> 1$ meaning that the crystal thickness should be at least one order of magnitude lower than δ_λ, i.e., thinner than 0.1 cm and 0.0001 cm for the lower and upper limits, respectively. If the SiC crystal used as a seed is a bit less than 0.1 cm (as used in a standard growth process), the upper limit predicts that SiC is always opaque. On the other hand, the lower limit predicts that the transparency should affect only the initial stage of the growth (few hundred microns) while the crystal becomes opaque after. This requires also that the seed and the newly grown layer must be relatively pure. Otherwise SiC crystal is always opaque.

The more simplified consideration can be analogous to the poor conductor ($\sigma << \omega\varepsilon$). In such case, the skin depth is independent of the frequency and can be calculated from [1]

$$\delta = \frac{2}{\sigma}\sqrt{\frac{\varepsilon}{\mu}}. \tag{4.37}$$

It is found that the skin depth is very low in SiC (few tens of microns). Moreover this relation shows that the skin depth is reduced if the electrical conductivity increases. Since the electrical conductivity can be increased by increasing the doping concentration, the crystal can become opaque in a highly doped condition. This is the case in our PVT growth system since the (nitrogen) doping level reaches high 10^{18} to low 10^{19} cm^{-3} even in an unintentional doping experiment. Another argument for the invalidity of the semi-transparent model in our PVT process can possibly relate to the temperature dependence of the energy bandgap in semiconductors. In most of the semiconductor materials, the bandgap decreases as the temperature increases. The use of very high temperature during the PVT growth process can drastically reduce the bandgap in SiC crystal. As a consequence, SiC crystal becomes an opaque body with respect to the radiative heat fluxes at the growth temperature. For these reasons, we will assume that the SiC is an opaque body in this thesis.

4.4 Modeling results and validations

In order to validate the model, the modeling results have to be compared with the experimental results. Since the computation is mainly performed for the steady state of the growth, then the best case should be the comparison between the modeling results and the experimental

observation during the growth experiment. However, this is not always very easy due to the limitation in the real time measurement especially for the validation of the induction heating and heat transfer discussed in this chapter. The creation of an open space for measurement or an introduction of the external probe would substantially disturb the system. Thus in this section we are aiming to verify the modeling with the real time measurements if they are possible otherwise the after growth observations will be used to compared. The modeling results include the I-V characteristic of the induction coil and the effect of coil position. A list of physical properties of materials used in the simulations can be found in *appendix A*.

4.4.1 I-V characteristic and measurement

In the set-up for SiC crystal growth, the control of power supply and geometry of the reactor is very crucial, for example, for the optimization of the power consumption and controlling the thermal gradient in the growth chamber where the mass transport takes place. The topological connection of the power generator, capacitors, and the reactor is shown in Fig. 4.10a. The equivalent RLC parallel circuit with resistance in series with inductor is drawn in Fig. 4.10b. In such RLC circuit, there are two types of power losses: active losses due to the resistive components in the system and the reactive losses due to the inductance. The apparent power S (VA) defined as a measure of alternating current power is the vector summation of active P (Watts) and reactive Q (VAR) powers, and it is a product of root-mean-square of circuit voltage and current written by

$$S = V_{rms} I_{rms} = \sqrt{P^2 + Q^2} \, . \tag{4.38}$$

Since the growth of bulk SiC needs rather high temperature of around 1700-2300 °C, the power generator must be able to provide enough active power to heat the crucible up to the such temperature. Moreover, the capacitance is necessary to be integrated in order to generate enough reactive power consumed by the inductor. By mean of an adaptation of the impedance, the optimum design of the coil can be obtained when the impedance of the equivalent R-L-C circuit is near the impedance of the power generator so that the system functions as close as possible to the resonance condition. This optimal design can be obtained by modifying the geometric parameters of the coil such as, the number of turns, the diameter and the height, and the capacitors (frequency). Since the circuit topology of our reactor is a parallel circuit, the parallel

resonance is considered for optimal design. The advantage of the parallel resonance is for example, the current is magnified through the work coil thus the power generator only need to carry part of the load current that actually does the real work. In the experiment, the current through the work coil was measured through the strength of the magnetic field around it using the clamp-on ammeter. The I-V curve was plotted in Fig. 4.11 and compared with the results computed by the numerical modeling. It can be seen that the total RMS current can reach few hundred ampere while the current carried by the generator is normally much lower (up to tenfold). Similar I-V tendency between the numerical results and the measurements is obtained. Further investigations of the effects of the process parameters will be discussed both in the next sections and in the next chapter where the mass transport calculations are discussed.

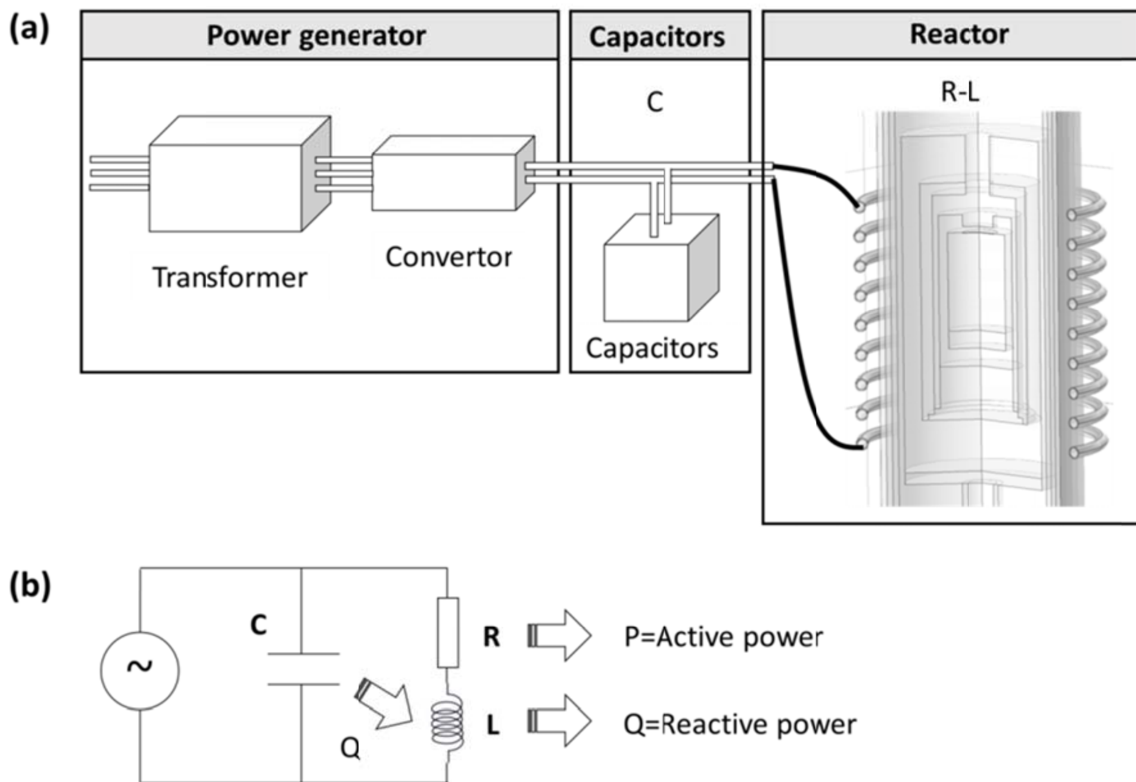

Fig. 4.10 (a) Schematic representation of topological connection of power generator, capacitors, and reactor, and (b) the equivalent RLC parallel circuit

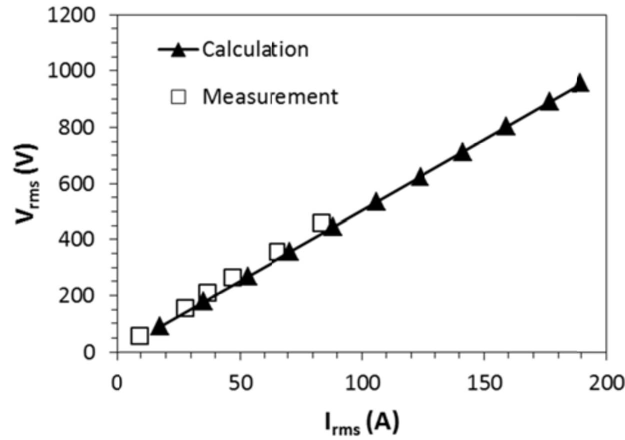

Fig. 4.11 Characteristic curve of current through the work coil and the voltage drop

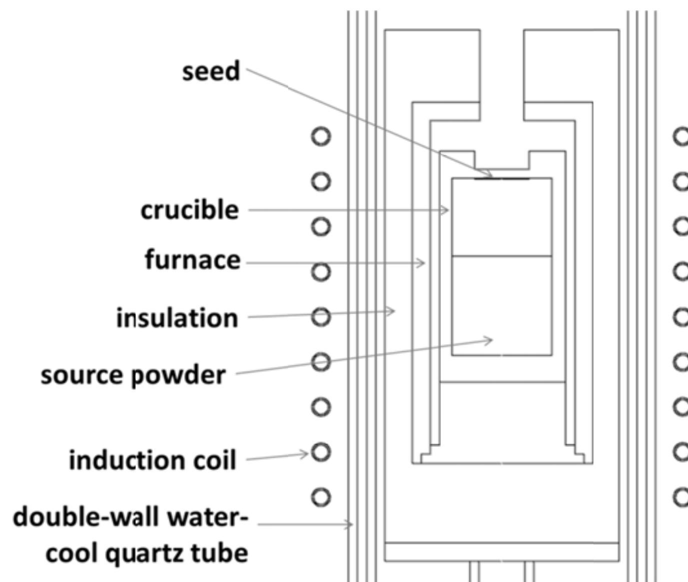

Fig. 4.12 Schematic drawing of inductively heated PVT growth reactor for SiC

4.4.2 Geometry and temperature distribution

A typical geometry used in the experiment is shown in Fig. 4.12. It consists of the induction coil, doubled-wall water-cool quartz tube, insulation, the external graphite crucible (called furnace), and the inner graphite crucible (called crucible). The SiC powder source was filled at the bottom part while SiC single crystal seed was attached to the top part of the crucible. The furnace acts as a susceptor which is directly heated by induction while the inner crucible is mainly heated by the radiation from the furnace. The proportion of the heat due to the inductive losses and the

radiation is dependent on the geometry and the electromagnetic skin depth. In case of good conductor materials ($\sigma >> \omega\varepsilon$), the skin depth can be calculated from an expression

$$\delta = \sqrt{\frac{2}{\sigma\mu\omega}} . \tag{4.39}$$

It can be seen that the skin depth is inversely proportional to the operating frequency. In this PVT reactor, the generator is operating at 100 kHz so the penetration depth is around 5 mm. This value is smaller than the thickness of the furnace (10 mm). The typical magnetic vector potential distribution at the growth temperature is shown in Fig. 4.13a. The joule losses are deduced from this distribution. Thus the heating power is focused mainly on the outer surface of the furnace as shown in Fig. 4.13b due to the skin effect. Then the heat transfer in the reactor from the calculated joule losses distribution is calculated. The temperature distribution profile of the reactor is obtained and shown in Fig. 4.14. The coil position is adjusted in order to create the hot point in the powder source and cold point at the seed. Thus, this temperature gradient creates the driving force for the sublimation of the powder source and the condensation at the seed.

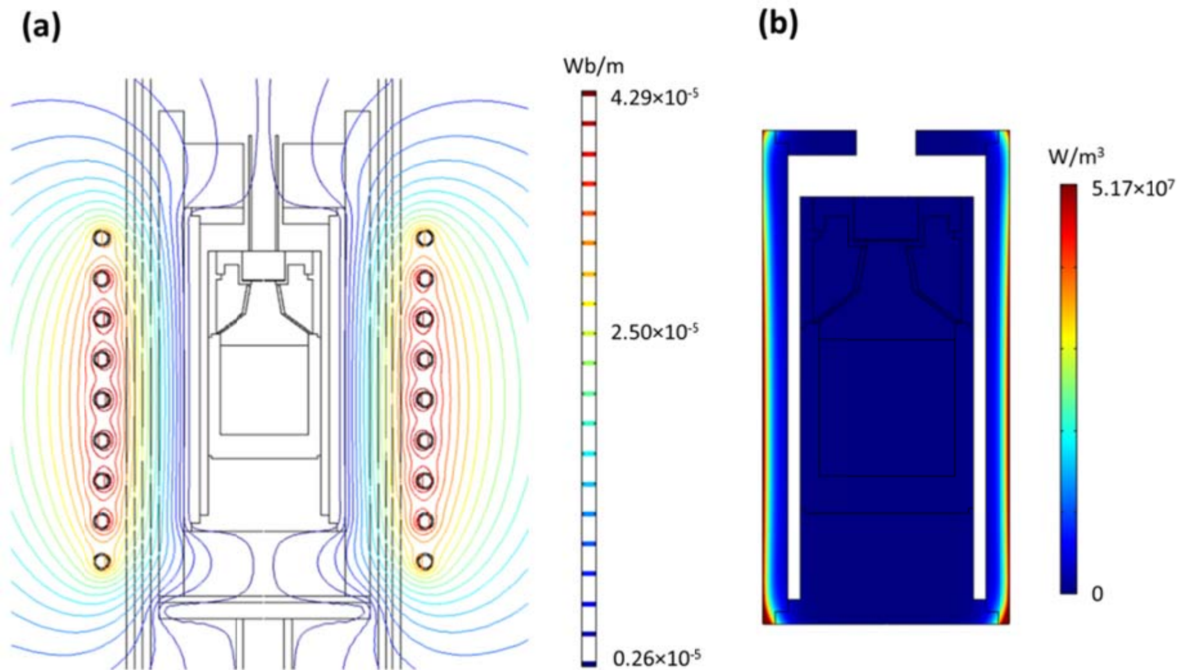

Fig. 4.13 (a) Magnetic vector potential contour in the reactor and (b) the resistive power losses dissipated in the furnace and crucible

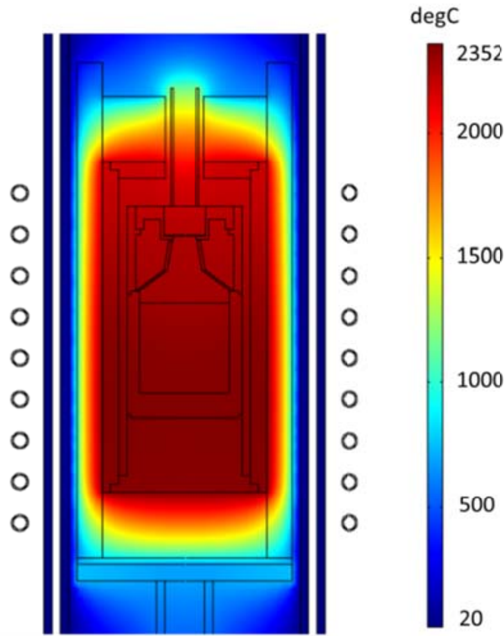

Fig. 4.14 Temperature distribution in the PVT growth reactor

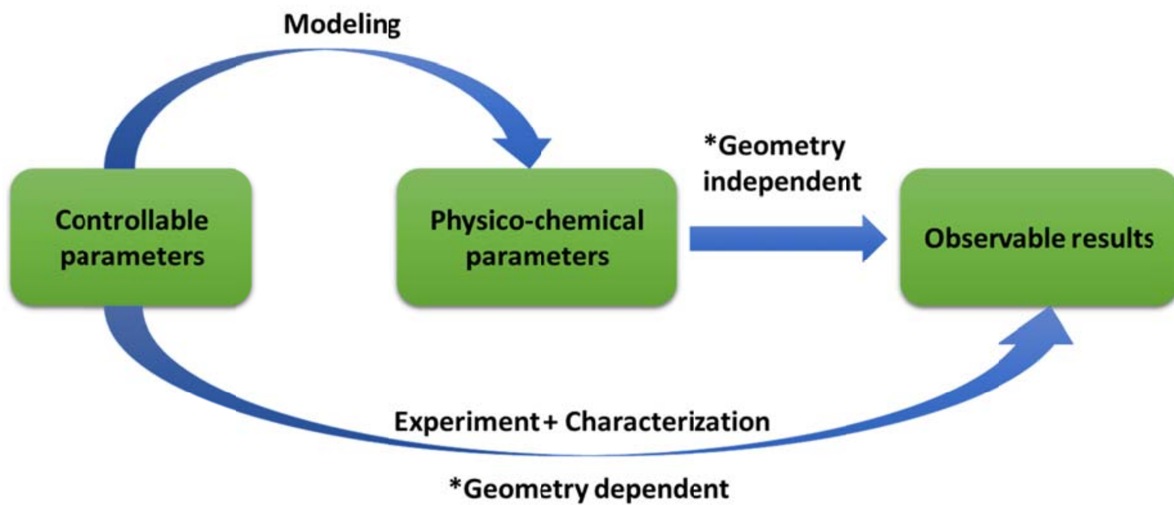

Fig. 4.15 Capability of numerical modeling in solving the “reactor dependent” problem

In general, the geometrical design of the crucible strongly influences the growth process [16, 17]. By comparing, for example, the simple geometry defined in section 4.3 and more complex geometry shown in this section (Fig. 4.14), the temperature distribution in the growth chamber are different. This will further affect the distribution of other physico-chemical

parameters. Their values and distributions are dependent on the geometry. In fact, this is one of the reasons why the crystals growers face the problem called "reactor dependency". With the same set of input or controlled parameters, the observed results may be differing to one another due to the effect of reactor design. This will lead to the discrepancies concerning the interpretation of the experimental results as well as the conclusions. On the contrary, the numerical modeling of the growth process grants us the possibility to enter the physico-chemical parameters (Fig. 4.15). Then those parameters can be compared directly with the observations, making used of analytical or theoretical approaches. Such comparisons are geometry independent, thus the problem of reactor dependent can be minimized. This point clearly shows the potential of the numerical modeling in the growth processes.

4.4.3 Effect of coil position

The adjustment of the coil position is one of the simplest ways to control the temperature gradient inside the growth chamber. This is much easier than dealing with the crucible geometry. In order to study the effect of the coil position on the temperature distribution, three coil positions are simulated and compared. The reference coil position is chosen to be similar to the geometry shown in Fig. 4.14. The others are shifted up either by 1 or 2 cm. In all cases, the temperature on top of the crucible is fixed at 2200 °C. The isothermal lines and the temperature gradient streamlines are shown in Fig. 4.16. For the reference coil position, the hot point locates at the bottom corner of the crucible containing SiC powder source (Fig. 4.16a). The temperature gradient streamlines direct upward from the hot point to the cold point (top parts of the crucible). The curvatures (or shapes) of these streamlines follow the distribution of the isothermal contours. In the growth cavity the average temperature gradient computed by the temperature difference between top part of the source (T_{source}) and the seed crystal (T_{seed}) at the symmetry axis is almost 9 K/cm. If the coil position is shifted upward by Δz, the hot point shifts upward by almost double the distance of Δz. The temperature distribution and the temperature gradient streamlines are modified mainly in the powder source. First, the temperature gradient streamlines direct both upward and downward directions in the powder source (Fig. 4.16b-c). Moreover, T_{source} decreases faster than T_{seed} (Fig. 4.16d), thus the average temperature gradient decreases from almost 9 to 6.5 and 4.5 K/cm by shifting up the coil position by 1 and 2 cm, respectively.

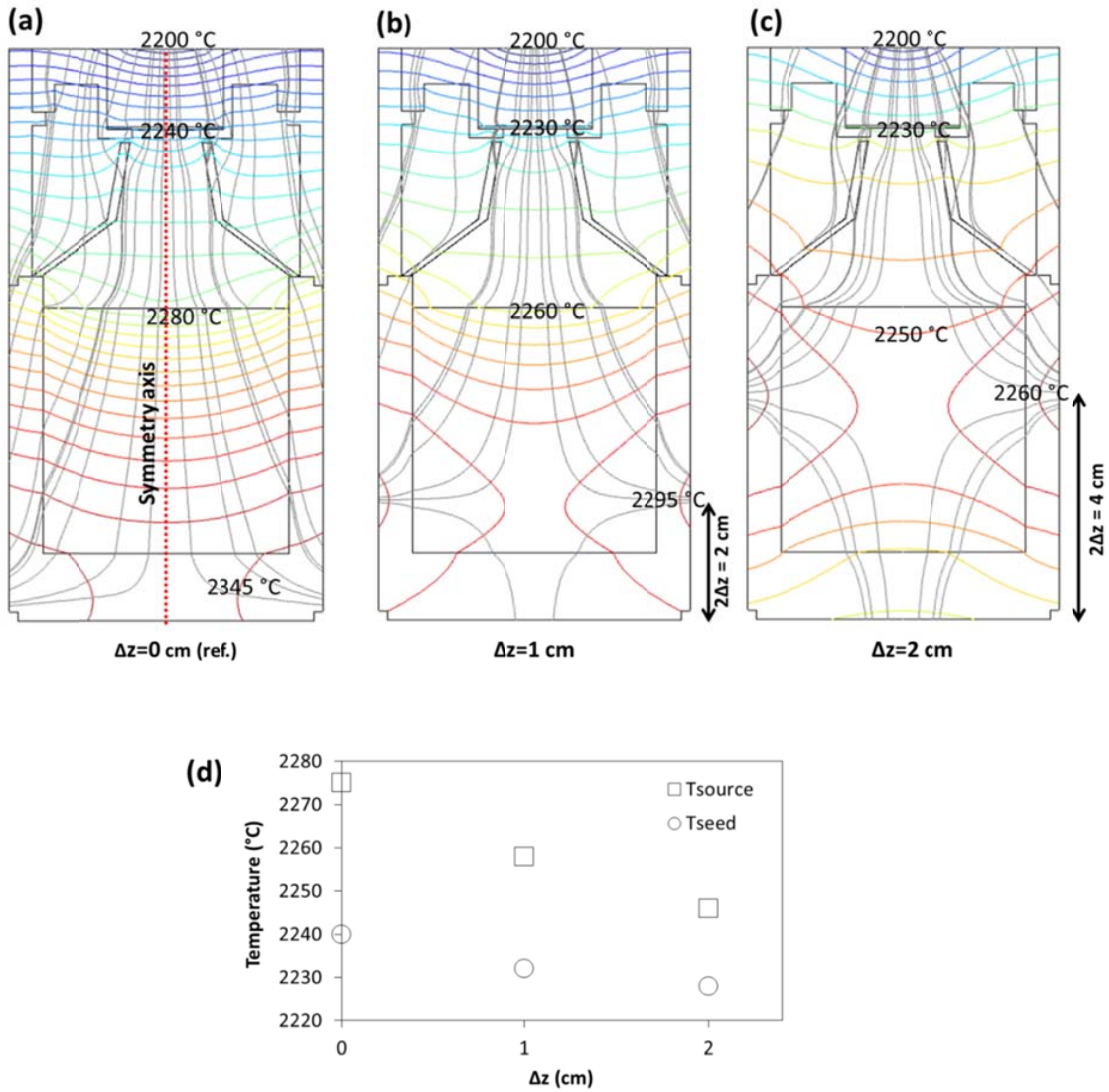

Fig. 4.16 Isothermal contour (color lines) and temperature gradient streamlines (gray lines) in the crucible for (a) reference coil position z=0, (b) z=1 cm, and (c) z=2 cm with (d) T_{source} and T_{seed} plotted as a function of the position of the coil

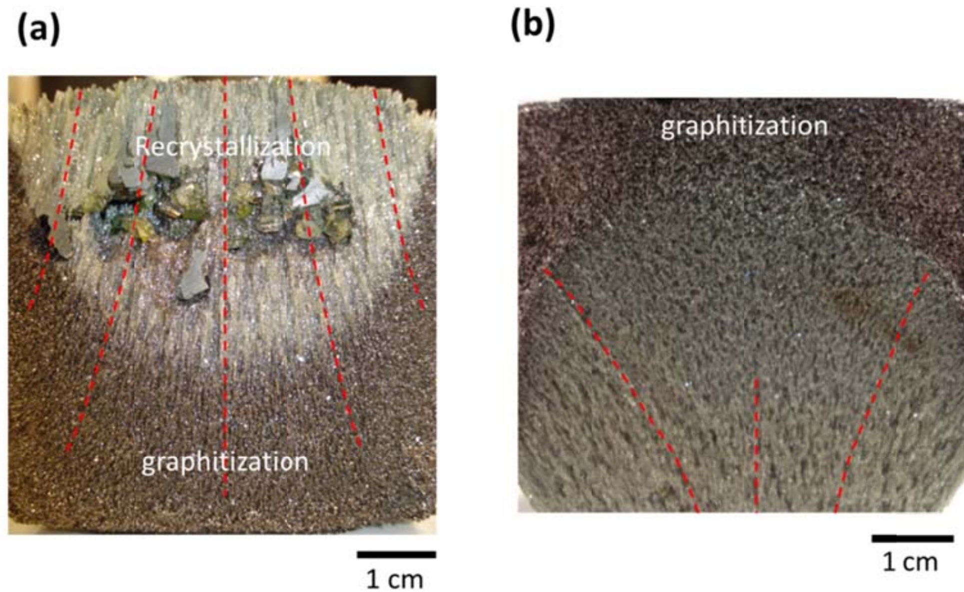

Fig. 4.17 Powder skeleton after the experiments using (a) reference and (b) +2 cm coil positions

Even if the present model considers only the sublimation from the top part of the powder and that the species diffusion is mainly governed by the mass diffusion, the temperature gradient streamlines might be used as preliminary modeling results to predict the diffusion path of SiC species in the source powder. This kind of transport leads to a needle-like structure as observed in the powder “skeleton” after growth [18, 19] and also observed systematically in our experiments shown in Fig. 4.17. The hot points seen from the red zone of Fig. 4.16 are the regions where the powder sources are strongly graphitized. The displacement of the hot point and change of the diffusion path structure due to the change of the coil position computed from the numerical modeling are in good agreement with the experimental observations. Once the species sublime, part of them will diffuse through the porous powder to top part of the powder and transport to the seed (and other relatively cold points). The bottom part of the powder will be sublimed faster than the other parts due to the higher temperature and finally becomes graphitized due to the non-congruent nature in sublimation of SiC. The top part of the powder does not become graphitized but recrystallized due to three possible mechanisms. First, the sublimation rate at the top part of the powder is slower than the bottom part resulting from the inhomogeneous temperature distribution inside the source material. Second, the vapor species coming from the hot point at the lower position diffuse and pass through this top part where they

can partly recrystallize. According to the thermodynamic mechanism [20], the combination of these two mechanisms contributed to the recrystallization phenomena on the top part of the source. The last possible mechanism could be the back flow of the SiC vapor species caused by the re-sublimation of the seed. This will be discussed in details in the next chapter. As a consequence, the strongly graphitized area is expected to be located at the bottom of the crucible for the standard coil position. When the coil position is shifted up by 2 cm, the strongly graphitized area locates close to the powder-vapor interface. In this case, part of the sublimed species will diffuse through the porous powder to top part of the powder and transport to the seed (and other relatively cold points) while another part will diffuse down to the bottom of the crucible due to the temperature gradient. Since the sublimation rate is high on the top part of the powder and there is no supplied SiC vapor from the bottom part, the powder becomes graphitized in this area. This can limit the growth of SiC due to two possible effects. First, the growth rate will be decreased due to the reduction of the temperature gradient. Furthermore, the efficiency of the growth concerning the powder consumption may be decreased since some amount of the powder (downward diffusion) does not contribute to the crystal growth. This effect of increasing the coil position is confirmed by the experiments where the growth rate decreases by more than a factor of three, i .e. from around 200 μm/h to 60 μm/h. The theoretical analysis of the mass transport in the powder charge was proposed based on the Darcy's law where the evolution of the powder concerning the porosity and graphitization degree in a long-term growth of bulk SiC crystal can be predicted [21, 22].

4.5 Conclusion

The coupled induction heating and heat transfer were implemented in the growth furnace. Their physics represented by the electromagnetic equations, heat transfer equations, and momentum and continuity equations were numerically solved with the defined boundary conditions. The heat transfer by conduction was shown to be negligible and SiC crystal was treat as an opaque body. This coupled model provides the temperature distribution in the reactor which is necessary for the mass transport modeling. Two types of modeling results and validations were shown. First, similar I-V tendency between numerical and measurements was obtained. Second, a direct comparison of the diffusion path of SiC species in the source powder and the temperature gradient streamlines was made regarding the effect of the coil position.

Good agreements were obtained. The numerical modeling was also shown to be able to assist the crystal grower to get access to the physico-chemical parameters and minimize the reactor dependent issue.

References

1. Griffiths, D.J. and R. College, *Introduction to electrodynamics*. Vol. 3. 1999: Prentice hall Upper Saddle River, NJ.
2. Pons, M., Blanquet, E., Dedulle, J.M., Garcon, I., Madar, R., Bernard, C.,, *Thermodynamic Heat Transfer and Mass Transport Modeling of the Sublimation Growth of Silicon Carbide Crystals.* Journal of The Electrochemical Society, 1996. **143**(11): p. 3727.
3. *COMSOL Multiphysics Reference Manual*. 2013.
4. Chen, Q., et al., *Silicon carbide crystals-Part II: Process physics and modeling.* Crystal growth technology. NY: William Andrew, 2003: p. 233-269.
5. Klein, O., et al., *Radiation- and convection-driven transient heat transfer during sublimation growth of silicon carbide single crystals.* Journal of Crystal Growth, 2001. **222**(4): p. 832-851.
6. Chen, X., S.-i. Nishizawa, and K. Kakimoto, *Numerical simulation of a new SiC growth system by the dual-directional sublimation method.* Journal of Crystal Growth, 2010. **312**(10): p. 1697-1702.
7. Gao, B., et al., *Analysis of SiC crystal sublimation growth by fully coupled compressible multi-phase flow simulation.* Journal of Crystal Growth, 2010. **312**(22): p. 3349-3355.
8. Dupret, F., et al., *Global modelling of heat transfer in crystal growth furnaces.* International Journal of Heat and Mass Transfer, 1990. **33**(9): p. 1849-1871.
9. Böttcher, K. and D. Schulz, *Crystal Interface Shape Simulation during SiC Sublimation Growth.* Materials Science Forum, 2003. **433-436**: p. 111-114.
10. Gao, B. and K. Kakimoto, *Effect of the Inclusion of Transparency on the Thermal Field and Interface Shape in Long-term Sublimation Growth of SiC Crystals(<Special Issue>)Opening Up a New World of Crystal Growth on SiC).* Journal of the Japanese Association of Crystal Growth, 2013. **40**(1): p. 20-24.
11. Wellmann, P.J., et al., *Optical quantitative determination of doping levels and their distribution in SiC.* Materials Science and Engineering: B, 2002. **91–92**(0): p. 75-78.
12. Weingärtner, R., et al., *Determination of charge carrier concentration in n- and p-doped SiC based on optical absorption measurements.* Applied Physics Letters, 2002. **80**(1): p. 70.
13. Patrick, L. and W. Choyke, *Optical Absorption in n-Type Cubic SiC.* Physical Review, 1969. **186**(3): p. 775-777.
14. Groth, R. and E. Kauer, *Absorption freier Ladungsträger in α-SiC-Kristallen.* physica status solidi (b), 1961. **1**(5): p. 445-450.
15. Dubrovskii, G.B., A.A. Lepneva, and E.I. Radovanova, *Optical absorption associated with superlattice in silicon carbide crystals.* physica status solidi (b), 1973. **57**(1): p. 423-431.
16. Pons, M., et al., *State of the art in the modelling of SiC sublimation growth.* Materials Science and Engineering: B, 1999. **61-62**: p. 18-28.
17. Ramm, M.S., et al., *Optimization of sublimation growth of SiC bulk crystals using modeling.* Materials Science and Engineering: B, 1999. **61-62**: p. 107-112.

18. Liu, X., et al., *The behavior of powder sublimation in the long-term PVT growth of SiC crystals.* Journal of Crystal Growth, 2010. **312**(9): p. 1486-1490.
19. Wellmann, P.J., et al., *In situ visualization and analysis of silicon carbide physical vapor transport growth using digital X-ray imaging.* Journal of Crystal Growth, 2000. **216**(1-4): p. 263-272.
20. Fujimoto, T., et al., *A Thermodynamic Mechanism for PVT Growth Phenomena of SiC Single Crystals.* ECS Journal of Solid State Science and Technology, 2013. **2**(8): p. N3018-N3021.
21. Kulik, A.V., et al., *Theoretical Analysis of the Mass Transport in the Powder Charge in Long-Term Bulk SiC Growth.* Materials Science Forum, 2004. **457-460**: p. 67-70.
22. Wang, X., D. Cai, and H. Zhang, *Increase of SiC sublimation growth rate by optimizing of powder packaging.* Journal of Crystal Growth, 2007. **305**(1): p. 122-132.

Chapter 5
Mass transport

The mass transport of the vapor species in the gas mixture is coupled between the species transport and the fluid flow making use of the temperature profile computed from the induction heating and heat transfer as describe in the previous chapter. In this chapter, the physical model is presented followed by the boundary conditions concerning both comparative and coupled approaches. The effect of the choice of thermodynamic databases using the former approach will be discussed. Then the chemical model concerning the interaction between vapor species and graphite crucible will be given. Finally the general modeling results and validations will be presented.

5.1 Physical model

In order to model the fluid flow, it is necessary to justify whether the flow regime can be described by the standard continuum approach or the statistical mechanics. Concerning the dimensionless analysis, the Knudsen number is normally used to characterize the flow regime and is defined by

$$Kn = \frac{\lambda}{L_C}, \tag{5.1}$$

where is λ the molecular mean free path and L_C is the characteristic length of the fluid flow. The flow behavior is classified by four different flow regimes [1]:

1. Continuum flow ($Kn < 0.01$)
2. Slip flow ($0.01 > Kn > 0.1$)
3. Transition flow ($0.1 > Kn > 10$)
4. Free molecular flow ($Kn > 10$).

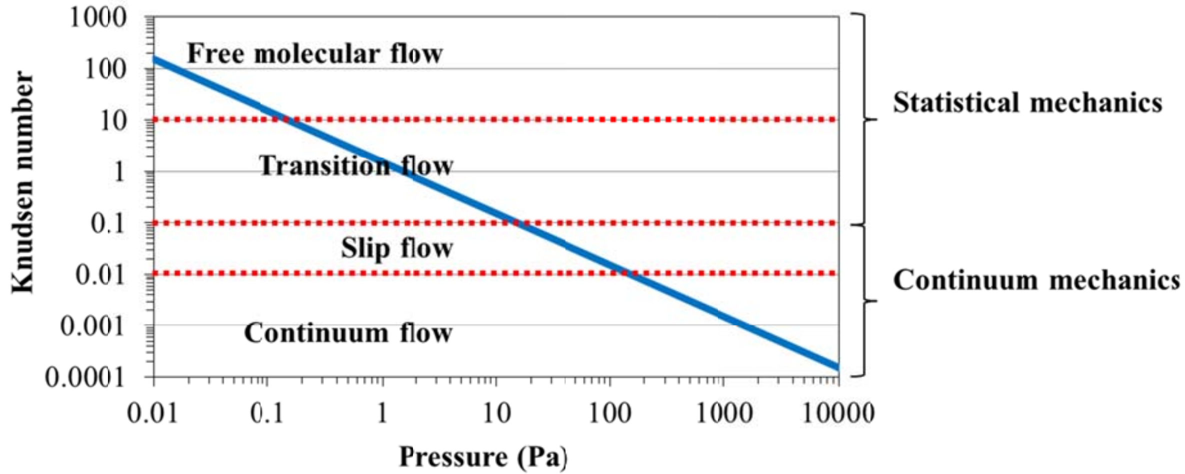

Fig. 5.1 Knudsen number of the vapor phase in the sublimation growth of SiC as a function of the growth pressure for the fixed temperature at 2500 K. The characteristic length is assumed to be the distance between source and seed (4 cm). The average value of the Lennard-Jones parameter of the vapor species is used for the diameter of the vapor molecules.

In the first case, the mean free path of molecule is negligible compared to the characteristic length of the flow thus the fluid can be considered as a continuum medium. As the Knudsen number increases a little, the no-slip boundary conditions (zero fluid velocity at the wall) does not hold valid. The Knudsen layer of thickness about one mean free path exists at the fluid-solid interfaces resulting in a finite value of the fluid at the wall (slip velocity). With further increase of the Knudsen number (transition flow), the mean free path is comparable to the characteristic length where the continuum approximation is no longer valid. The flow behavior has to be described by statistical mechanics. If the Knudsen number is very large, the collision between fluid molecules becomes negligible compared to the interaction with the wall. The statistical mechanics without collision can be used to treat such free molecular flow regime. In case of an ideal gas, the Knudsen number can be reformulated as

$$Kn = \frac{k_B T}{\sqrt{2} d^2 P L_C}, \tag{5.2}$$

where k_B is the Boltzmann constant, d is the particle shell diameter, and P is the total pressure. In the growth of SiC from the vapor phase, an example of the Knudsen number plotted as a function of the growth pressure is shown in Fig. 5.1. It is clear that the continuum approximation is

applicable for the modeling of the fluid flow in the growth of SiC using PVT method where the growth pressure is typically higher than 100 Pa (1 mbar). Thus the governing equations describing fluid dynamics in the physical vapor transport process are the Navier-Stokes equations. The general form of the equation for the fluid motion, the momentum equation is expressed as

$$\rho \frac{\partial \mathbf{v}}{\partial t} + \rho(\mathbf{v} \cdot \nabla)\mathbf{v} = \nabla \cdot \left(-p\mathbf{I} + \overline{\boldsymbol{\tau}}\right) + \mathbf{F}, \tag{5.3}$$

where $\mathbf{F}$ is the volume force and $\overline{\boldsymbol{\tau}}$ is the viscous stress tensor written by

$$\overline{\boldsymbol{\tau}} = \mu\left(\nabla\mathbf{v} + (\nabla\mathbf{v})^T\right) - \frac{2}{3}\mu(\nabla \cdot \mathbf{v})\mathbf{I}. \tag{5.4}$$

In order to take into account the conservation of mass, the mass continuity equation is included:

$$\frac{\partial \rho}{\partial t} + \nabla \cdot (\rho\mathbf{v}) = 0. \tag{5.5}$$

Moreover, the conservation for the ith species in a gas mixture is given by the species balance equation:

$$\frac{\partial \rho\omega_i}{\partial t} + \nabla \cdot \mathbf{j}_i + \rho(\mathbf{v} \cdot \nabla)\omega_i = R_i. \tag{5.6}$$

Here, R_i denotes the reaction rate of the ith species. The total diffusive mass flux $\mathbf{j}_i$ is composed of two terms. The first term $\mathbf{j}_i^F$ is the flux due to a gradient of concentration described by Fick's law. The second term, the thermodiffusion flux $\mathbf{j}_i^T$ is the flux due to the temperature gradient described by the Soret's effect. Thus the total diffusive flux becomes

$$\mathbf{j}_i = \mathbf{j}_i^F + \mathbf{j}_i^T. \tag{5.7}$$

Concerning the interaction of species in the multicomponent diffusion, the governing equations for the flow behavior are better described by the Maxwell-Stefan equations written as

$$\mathbf{j}_i = -\rho\omega_i \sum_{j=1}^{N} \widetilde{D}_{ij} \mathbf{d}_j - \frac{D_i^T}{T} \nabla T \ , \tag{5.8}$$

where $\widetilde{D}_{ik}$ is the multicomponent diffusion coefficient which can be computed using the binary diffusion coefficient by the matrix transformation written as follows:

$$\frac{x_i x_j}{D_{ij}} = -\omega_i \omega_j \frac{\sum_{k \neq i} (adjB_i)_{kj}}{\sum_{k \neq i} \widetilde{D}_{ik} (adjB_i)_{kj}} \tag{5.9}$$

where $(adjB_i)_{kj} = \widetilde{D}_{jk} - \widetilde{D}_{ik}$ and $i \neq k$. The term $(adjB_i)_{kj}$ represents the kj^{th} component of the adjoint of matrix B_i. The diffusional driving force d_j is defined by

$$\mathbf{d}_j = \nabla x_j + \frac{1}{P}(x_j - \omega_j)\nabla P - \rho\omega_j \mathbf{g}_j + \omega_j \sum_{l=1}^{Q} \rho\omega_l \mathbf{g}_l \ , \tag{5.10}$$

where $\mathbf{g}_j$ denotes the external force acting on species j. The coefficient D_i^T refers to the thermal diffusion coefficient. In this thesis, we use the Maxwell-Stefan model as the governing equations for the flow behavior since it is more comprehensive than the Fick diffusion model. The former takes into account the interaction between the gas species while the latter one does only for the interaction between gas species and the bulk material (solvent). In fact, Fick's model is the limit case of the Maxwell-Stefan model when the gas mixture is highly diluted. In the standard PVT set up, the crucible is not completely closed. First, graphite itself is not a tight material because of its porosity. Second, the joint between different graphite parts are possible leak that allows exchanges between the inner part of the crucible and the reactor's chamber. This argument is verified since the growth rate is a function of the ambient pressure. Moreover by introducing the nitrogen gas flow outside the growth cavity one can obtain even heavily nitrogen doped SiC crystal. Thus we assume that the internal pressure (inside the growth cavity) equals to the external pressure P in (5.10) due to the exchange of the gas. Thus the total pressure of the gas mixture in the growth cavity is constant. Moreover, there is no external force acting on the vapor species. The diffusional driving force (5.10) is now only a function of mole fraction gradient ∇x_j

. If the thermal diffusion coefficient is very low, the Soret's effect can be also neglected. This is the case for the growth of SiC by sublimation method. We now rewrite the mass flux (5.8) as

$$\mathbf{j}_i = -\rho\omega_i \sum_{j=1}^{N} \widetilde{D}_{ij} \nabla x_j \,. \tag{5.11}$$

It is more convenient to consider the molar flux instead of the mass flux. By using the relation

$$\omega_i = \frac{x_i M_i}{M}, \tag{5.12}$$

where M is the mean molar mass defined by

$$M = \sum_{i=1}^{N} x_i M_i \,, \tag{5.13}$$

the diffusive molar flux can be written

$$\frac{\mathbf{j}_i}{M_i} = -\frac{\rho x_i}{M} \sum_{j=1}^{N} \widetilde{D}_{ij} \nabla x_j \,. \tag{5.14}$$

5.2 Boundary conditions

The molar flux at the reacting boundaries $\mathbf{N_i}$ is described by the summation of two contributions:

$$\mathbf{N_i} = \frac{\mathbf{j_i}}{M_i} + \frac{\rho x_i}{M} \mathbf{v} \,. \tag{5.15}$$

The first term is the diffusive molar flux defined in (5.14). The second term is the convective molar flux. At the solid-vapor interface, the large volume change caused by the sublimation or condensation reactions at the interfaces produces the advective flow or Stefan's flow velocity:

$$\mathbf{v} = -\left(\frac{RT}{PM} \sum_{i=1}^{N-1} M_i N_i \right) \mathbf{n} \,, \tag{5.16}$$

where M is the mean molar mass. Here, the summation includes only the reactive species since the inert gas does not participate in the heterogeneous reactions. It can be seen from both (5.15)

and (5.16) that there is a coupling between the fluid flow and the mass transfer since the velocity of the fluid at the reacting boundary has to be computed from the net species fluxes. At the non-reacting boundaries, such as at the graphite walls where the deposition does not occur, all the velocity components are set to zero. It is worth noting that the contribution of the buoyancy force in the fluid dynamics of the vapor phase is much smaller than the effect of Stefan flow in the PVT process under the practical growth conditions. This follows the fact that such growth process is typically carried out in low pressure. The buoyancy force is then very small. The macroscopic flow of the reactive vapor species owing to the sublimation/condensation processes determines the flow pattern since the velocity magnitude in the growth cell taking into account the Stefan flow (10^{-3} m/s) can be three order of magnitude higher than the velocity field caused by purely buoyancy flow (10^{-6} m/s) [2]. Thus by taking the Stefan flow into account, the buoyancy force can be neglected.

We assume that there is no homogeneous vapor phase reaction. Only the heterogeneous reactions at the solid-vapor interface are considered. The boundary molar flux was formulated by the Hertz-Knudsen model

$$N_i = N_i^{ads} - N_i^{des} = \left(\gamma_i P_i - \alpha_i P_i^*\right)\sqrt{\frac{1}{2\pi M_i RT}}\,, \tag{5.17}$$

where N_i is the net molar flux of the ith vapor species participating in the heterogeneous reactions, P_i is the partial pressure, P_i* is the equilibrium partial pressure, M_i is the molar mass, R is the gas constant, T is the temperature, γ_i and α_i are the sticking and evaporation coefficients, respectively. The transport of atom or molecule from the vapor phase to the solid phase is associated with several processes, including, the adsorption, diffusion, desorption, and incorporation [3]. Here, the sticking coefficient refers to the probability that an atom in the gas phase adsorbs, diffuses, and finally incorporates to the bulk solid by attachment to the kink site at a step edge. The reverse process is assumed for the definition of the evaporation coefficient where the atom finally desorbs from the surface. The schematic representation of the Hertz-Knudsen model is shown in Fig. 5.2. A thin Knudsen layer exists between the solid SiC crystal and the vapor as mentioned in [4] where its thickness is approximately one of the mean free path of the molecules [5]. Within such layer, two different molecular streams of adsorbed (N_i^{ads}) and

desorbed (N_i^{des}) fluxes interact with the each other which in turn alters the distributions of both streams. As a result, the distribution of vapor molecules associated with the adsorbed fluxes is not similar to the bulk vapor. Due to the complexity of the altered distribution function, the Knudsen layer is commonly neglected. Such assumption is reasonable in the case of low Knudsen number [6]. This is the case for the growth of SiC using PVT method with the growth pressure typically above 100 Pa (Fig. 5.1). Thus, the adsorbed molecules are assumed to possess the bulk vapor distribution up to the solid wall. Since both adsorption and desorption mechanisms take place at the same time, then the net species molar flux N_i is the difference between the adsorbed and desorbed fluxes. The adsorbed flux is a function of the partial pressure of the vapor species while the desorbed flux is a function of the equilibrium partial pressure.

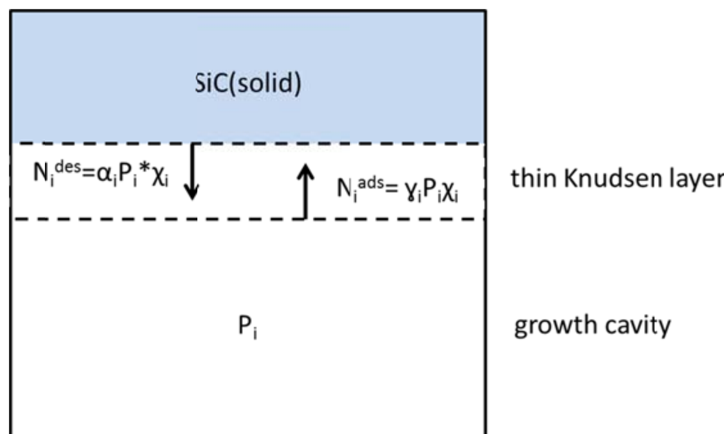

Fig. 5.2 Schematic representation of Hertz-Knudsen model for surface reaction kinetics with a thin Knudsen layer between the solid SiC surface and vapor

The evaporation coefficients correlate the free vaporization to the equilibrium vaporization flow. In general [7-12], the sticking coefficient is assumed to be equal to the evaporation coefficient even if this statement seems to be valid only under equilibrium conditions [13]. In fact, this assumption requires also that the individual vapor-surface interactions (adsorption, diffusion, and incorporation) are reciprocal so they must be indistinguishable under a time reversal [14]. Due to the lack of experimental data on the sticking coefficient, we will also assume that $\alpha_i = \gamma_i$. By substituting the Hertz-Knudsen formulation

(5.17) to (5.15), the surface normal component of the molar fluxes are used as the boundary conditions for the condensation/sublimation in the forms of

$$N_i = \gamma_i \left(P_i - P_i^*\right)\chi_i = \left(-\frac{Px_i}{RT}\sum_{j=1}^{N}\widetilde{D}_{ij}\nabla x_j + \frac{Px_i}{RT}\mathbf{v}\right)\cdot \mathbf{n}\,, \tag{5.18}$$

where **n** is the normal vector to the surface, and

$$\chi_i = \sqrt{\frac{1}{2\pi M_i RT}}\,. \tag{5.19}$$

The condensation/sublimation rate is proportional to the difference between the actual partial pressure and the equilibrium partial pressure. If the species partial pressure is higher than its equilibrium pressure at the temperature of the crystal surface, the vapor state is supersaturated and the net molar flux becomes positive (growth). On the opposite, the vapor is in the undersaturated state if the species partial pressure is lower than its equilibrium pressure, and the flux becomes negative (sublimation). Eq. (5.18) can also be reformulated in terms of the unknown variable for solving the species transport problem (mole fraction) using the relation $x_i = P_i/P$:

$$N_i = \gamma_i \left(x_i P - P_i^*\right)\chi_i = \left(-\frac{Px_i}{RT}\sum_{j=1}^{N}\widetilde{D}_{ij}\nabla x_j + \frac{Px_i}{RT}\mathbf{v}\right)\cdot \mathbf{n}\,. \tag{5.20}$$

The sublimation growth of SiC is usually carried out in a reduced pressure of a neutral gas (Ar) in a semi-closed graphite crucible. In such growth environment, the SiC source powder decomposes into a Si-rich gas phase, graphite, and the remaining SiC. Due to this non-congruent nature in sublimation of SiC, the three-phase heterogeneous equilibrium “SiC-C-vapor” can be assumed at the source-vapor interface. The equilibrium partial pressure of the vapor species can be determined uniquely as a function of temperature. The three main Si-C vapor species are Si, Si_2C, and SiC_2 [15-17] as identified and quantified by high temperature mass spectrometry using Knudsen effusion cell. With such a Si-rich gas phase, the crystallization process leads to

stoichiometric SiC crystals. It is worth nothing that SiC can accept a slight deviation from stoichiometry, mainly in terms of C deficiency [18], but this deviation from stoichiometry is rather small and will not be considered.

From the process modeling point of view, the implementation of the stoichiometry condition is not unique as different approaches can be found. Gao et al. [9] do not consider any stoichiometry constraint at growth interface. In the case of the close space sublimation method [19], the stoichiometric sublimation of the source is imposed. Furthermore, as the sublimation rate and the condensation (growth) rate are assumed to be identical, meaning that no accumulation of either Si or C is allowed, the condensation is thus stoichiometric. By using the two-phase heterogeneous equilibrium "SiC-vapor" [20] for the silicon carbide surface, there exists one thermodynamic degree of freedom, thus the vapor phase composition cannot be determined uniquely. The equation of stoichiometric incorporation was then suggested to close the set of equations. However, the forced convection induced by the boundary Stefan flow and the multicomponent diffusion effects were neglected in this model by assuming a dilute system in which the concentration of carrier gas prevails over the reactive species. The modification of this model to include these two effects was presented [4]. In such case, however, they consider one-dimensional mass transport for the axial mass fluxes while the radial ones are determined from the concrete model of mass exchange between the growth chamber and the external environment. Ma et al. [10] assumed that reactive vapor species in the growth chamber mix at perfect stoichiometric condition and the growth rate can be determined from the one-dimensional mass transport-kinetics.

In the PVT growth of SiC, the mole fraction of silicon is higher than the one of carbon in the vapor phase. The Si/C ratio close to the crystal surface should be larger than unity for a wide range of growth temperatures. From (5.18), assuming that the sticking coefficient of all species is unity, one would expect a higher global silicon flux than the carbon flux, resulting in a silicon excess in the condensed phase, i.e. in the crystal. By introducing the evaporation coefficients extracted from high temperature mass spectrometry studies [16, 21] in the modeling of SiC bulk growth [22], the total pressure of the reactive vapor species over solid SiC were found to decrease. In fact, the imbalanced silicon and carbon fluxes at the growing crystal should still be occurring because the stoichiometric condition was not imposed. It is very important to take into

account the stoichiometric incorporation for the process modeling of SiC single crystal growth in order to realize the actual growth mechanism and understand the process. Two main approaches used to tackle such problem will be presented and discussed: the comparative approach and the coupled approach.

5.3 Comparative approach

In this approach, we will consider the growth cavity as a whole system consisting of vapor phase (Si, Si_2C, SiC_2, Ar) and the condensed phase including SiC due to the presence of SiC seed and SiC powder source, and C due to the presence of graphite crucible and the graphitized powder source. This allows us to prior assume the three-phase heterogeneous equilibrium “SiC-C-vapor”. The temperature dependent vapor phase composition is obtained from [23]. The evaporation coefficients extracted from high temperature mass spectrometry during the sublimation of “SiC-C” diphasic mixture [16, 21] shall be used at all the solid-vapor interfaces. We will present the three models to take into account the stoichiometric incorporation of Si and C atoms into SiC crystal grown from PVT method. These models are built based on the two methods: the atomic fluxes balance, and the adaptable sticking coefficient(s). The terms comparative approach means that both numerical and thermodynamic modeling are performed and compared. The appropriate boundary conditions for stoichiometric condition are discussed in terms of both kinetics and thermodynamic mechanisms.

5.3.1 Atomic fluxes balance (AFB)

To strain the stoichiometric incorporation of Si and C atoms at the crystal-vapor interface, one possibility is to balance the atomic silicon and carbon fluxes:

$$F_{Si} = N_{Si} + 2 \times N_{Si_2C} + N_{SiC_2} = F_C = N_{Si_2C} + 2 \times N_{SiC_2} . \tag{5.21}$$

This condition can be formulated by using the weak constraint. With this method, an extra unknown called the Lagrange multiplier has been added to the system of unknowns to ensure the constraint residual equation. From equation (5.21), the weak constraint residual equation is of the forms:

$$\phi = F_{Si} - F_C = N_{Si} + N_{Si_2C} - N_{SiC_2} = 0 . \tag{5.22}$$

5.3.2 Adaptable sticking coefficients

We are developing the second method by considering the decomposition of the molar flux at the boundary. From Eq. (5.21), the atomic fluxes balancing equation can be rewritten:

$$F_{Si} = \gamma_{Si}\Phi_{Si} + 2\times\gamma_{Si_2C}\Phi_{Si_2C} + \gamma_{SiC_2}\Phi_{SiC_2} = F_C = \gamma_{Si_2C}\Phi_{Si_2C} + 2\times\gamma_{SiC_2}\Phi_{SiC_2}\text{, where} \tag{5.23}$$

$$\Phi_i = \left(x_i P - P_i^*\right)\chi_i\,. \tag{5.24}$$

The first assumption for this method is that the sticking coefficient represents the maximum kinetically limited deposition rate. We propose here two models to take the stoichiometry problem into account. The first method is to modify the sticking coefficient of Si, and Si_2C species but keeping the one of SiC_2 unchanged. From now on we will call this model "Mod2". This model is based on the consideration that the species flux providing more C than Si atoms should be kept at its highest deposition rate. In other words, SiC_2 is considered as a rate determining species. Thus γ_{SiC2} is the unmodified value. Then, Si and Si_2C species fluxes which provide mainly Si should be reduced to match the carbon flux. This can be done by modifying their sticking coefficients to have the lower values, meaning that these two species deposit into the growing crystal at the rate lower than their maximum kinetically limited rate in order to obey the stoichiometry condition. Rearrangement of equation (5.23) using the modified sticking coefficients γ_{Si}^* and $\gamma_{Si_2C}^*$ gives

$$\gamma_{Si}^* = \frac{\gamma_{SiC_2}\Phi_{SiC_2}}{\Phi_{Si} + \frac{\gamma_{Si_2C}^*}{\gamma_{Si}^*}\Phi_{SiC_2}}\,. \tag{5.25}$$

From Eq. (5.25), one unknown modified sticking coefficient is remained undefined. In order to close the equation system, another assumption is necessary. Here we assume that the ratio of the initial experimentally observed values and the modified ones are equal:

$$\frac{\gamma_{Si_2C}^*}{\gamma_{Si}^*} = \frac{\gamma_{Si_2C}}{\gamma_{Si}}\,. \tag{5.26}$$

The modified sticking coefficient of Si species can be determined from (5.25) and the one of Si_2C from (5.26). These modified sticking coefficients are dependent on boundary molar fluxes of the reactive species.

The second model is to modify the sticking coefficient of Si species but keep the other two constant. We will call this model “Mod1”. The assumption for this method is to keep the carbon supply species at their maximum kinetically limited rates. In this case, assumption (5.26) is not necessary and the modified sticking coefficient of Si species is expressed by

$$\gamma_{Si}^{*} = \frac{\gamma_{SiC_2}\Phi_{SiC_2} - \gamma_{Si_2C}\Phi_{Si_2C}}{\Phi_{Si}}. \qquad (5.27)$$

5.3.3 Numerical modeling

The growth system is similar to the one shown in Fig. 4.12. The temperature distribution in the growth chamber was calculated as described in the previous chapter. The temperature on the symmetry axis is 2300 °C at the seed and 2340 °C at the source. The vapor species sublimed from the hot source powder will become supersaturated and deposit on the colder seed side. When computing the mass transport, all methods discussed in the previous section provide stoichiometric incorporation of Si and C atoms into SiC crystal. Without the stoichiometry condition, the Si/C ratio of the solid would be around 2.15 which is much larger than the limit of experimental values [18]. Thus the stoichiometry condition must be taken into account. The distributions of the species mole fraction along the symmetry axis close to the seed are plotted in Fig. 5.3. The overall species distribution looks very similar for the model without the stoichiometry condition (no constraint) and the one with the atomic fluxes balance. However, in the region very close to the seed surface, there are the distortions of the mole fraction curve when using atomic fluxes balance. The mole fraction gradients of Si rich species (Si, Si_2C) decrease while the one of the C rich species (SiC_2) increases. At the seed surface, the mole fractions of all reactive species are unchanged compared to the case without the stoichiometry condition. Thus from (5.20), only the diffusive fluxes are adjusted in order to respect the stoichiometric constraint but not the convective ones and the Stefan’s velocity remains unaffected.

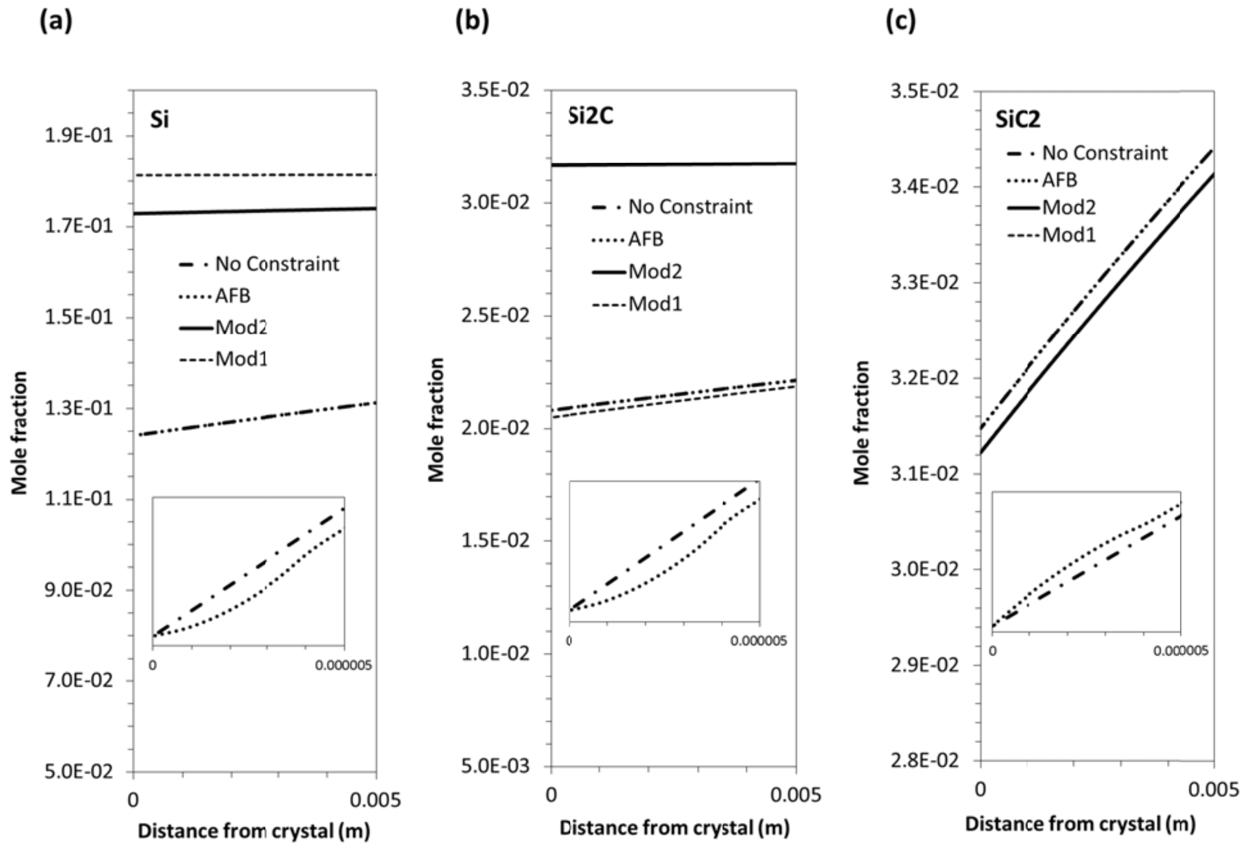

Fig. 5.3 Distribution of mole fraction of the reactive species: (a) Si, (b) Si_2C, and (c) SiC_2, along the symmetry axis. Inset shows the magnification of mole fraction very close to the seed-vapor interface where 0 represents the surface of the crystal

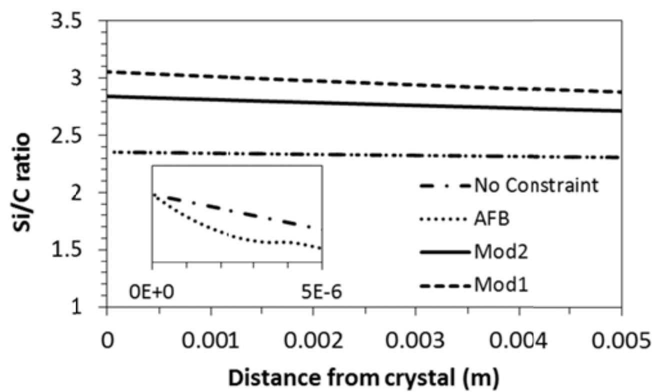

Fig. 5.4 Calculated Si/C ratio along the symmetry axis with (inset) the magnified view in the area close to the seed-vapor interface

With the adaptable sticking coefficients method including Mod2 and Mod1 models, both mole fraction and mole fraction gradient distributions are differing from the initial system without constraint. With Mod2, the mole fraction gradients of Si and Si_2C decrease, while the one of SiC_2 is almost constant. With Mod1, the mole fraction gradient of Si decreases while the ones of Si_2C and SiC_2 are almost constant. Since the modification of sticking coefficient means the modification of the net flux (5.20), both diffusive and convective fluxes are adjusted to obey the stoichiometric requirement.

The summation of the species mole fraction must be unity. Thus small deviations of the SiC_2 mole fraction in Mod2 and the deviations of Si_2C and SiC_2 in Mod1 from the initial system without constraint are observed (Fig. 5.3) even if their sticking coefficients are kept unchanged in the method considered. The Si/C ratio distribution along the symmetry axis is plotted in Fig. 5.4. The distributions of Si/C ratio look very similar when using the atomic fluxes balance compared to the system without constraint. However, their gradients change in the area very close to the seed surface as a result of the changes of mole fraction gradient of the vapor species as shown in Fig. 5.3. With the adaptable sticking coefficients method, the vapor phase becomes richer in Si, not only along the symmetry axis but also everywhere in the growth cavity because less Si flux contributes to the condensed phase.

The radial distribution of the total species molar fluxes obtained from all models are plotted in Fig. 5.5. If we assume a simple heterogeneous reaction of the forms

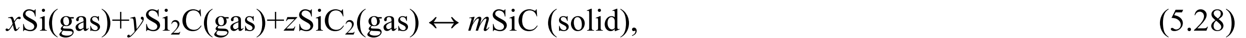

$$x\mathrm{Si(gas)}+y\mathrm{Si_2C(gas)}+z\mathrm{SiC_2(gas)} \leftrightarrow m\mathrm{SiC\ (solid)}, \qquad (5.28)$$

where x, y, z, and m are the stoichiometric coefficients at the crystal-vapor interface, the stoichiometric coefficients can be estimated from Fig. 5.5. For the formation of 1 mole of SiC, we define x/m, y/m, and z/m as the partial contribution to the crystal growth from Si, Si_2C, and SiC_2 species, respectively. The species contribution (molar flux) and partial contribution at the symmetry axis are shown in Fig. 5.6a and Fig. 5.6b, recpectively. The partial contribution is plotted with aim to compare better the contribution of various species regardless of the growth rate. Those diagrams clearly show that there is a large excess of Si contribution to the growth of SiC crystal if the stoichiometry condition is not implemented. The species contribution that leads to the formation of the stoichiometric SiC in such case is enclosed in the dashed rectangle.

Compared to the model without any constraint, the atomic fluxes balance leads to the increase of the growth rate. In contrast, the growth rate decreases when Mod2 and Mod1 are used. When considering the stoichiometric growth of SiC, SiC_2 appears to be the main contribution to the growth regardless of the choice of the model. The contribution of Si is higher than Si_2C when using the atomic fluxes balance and Mod2 models. On the other hand, Si_2C contributes more or less in a similar amount than Si when using Mod1.

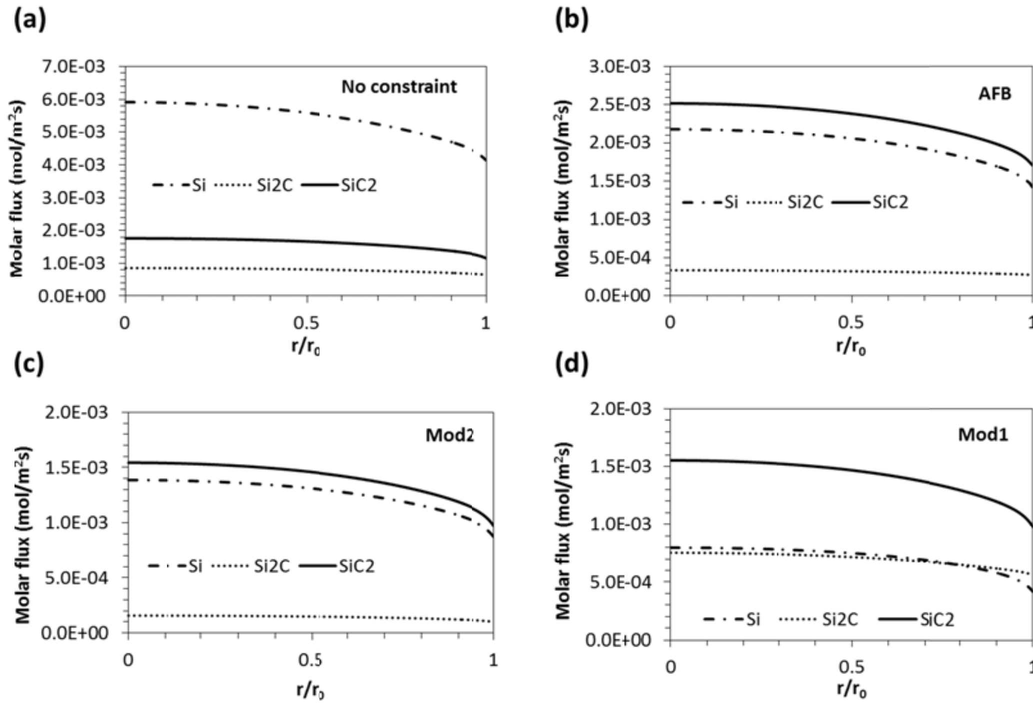

Fig. 5.5 The total molar fluxes plotted along the seed radius (a) without any consideration of SiC stoichiometry, and using (b) weak constraint formulation, (c) Mod2, and (d) Mod1

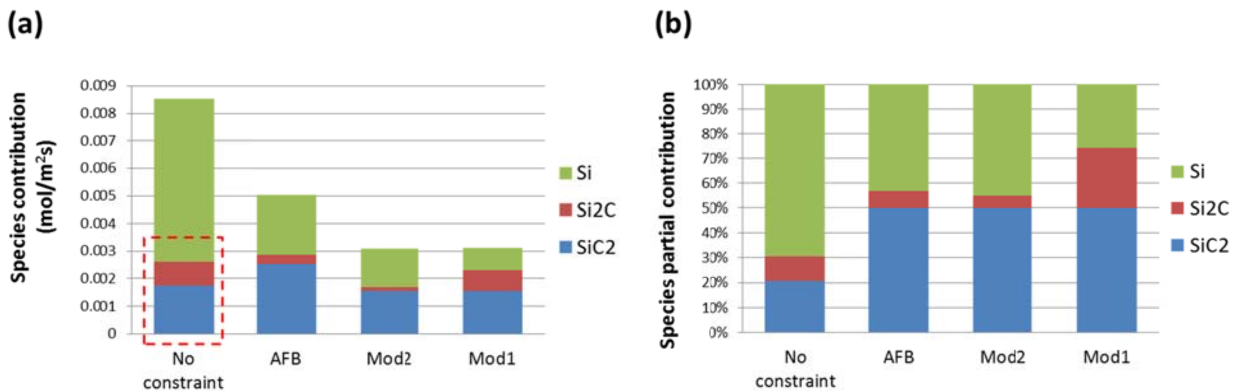

Fig. 5.6 (a) Species contribution and (b) species partial contribution at the symmetry axis

According to (5.20), the modified sticking coefficient is dependent on the species fluxes. Thus it is not a constant value but slightly varying along the seed radius. By subtracting these radial dependent sticking coefficients back into the Hertz-Knudsen formula and re-calculate the mass transport modeling, similar results of stoichiometric SiC growth are obtained. When using the atomic fluxes balance, the apparent sticking coefficient can be computed by assuming that the change in the adsorbed flux is caused by the change in the sticking coefficient:

$$\tilde{\gamma}_i = \gamma_i \frac{N_i^{AFB}}{N_\mathbf{i}}, \tag{5.29}$$

where N_i^{AFB} is the total molar flux of the ith species when using the atomic fluxes balance and N_i is the one without the stoichiometry condition. This is done only to allow us to compare the results obtained from this method to another method. The subtraction of the apparent sticking coefficients back into the Hertz-Knudsen formula does not bring the same results as in the case of modified sticking coefficient and the stoichiometry cannot be obtained. The sticking coefficients and the apparent sticking coefficients are shown in Table 5.1. By using the atomic fluxes balance, the apparent sticking coefficients of Si and Si_2C decrease by around 60%, while the one of SiC_2 increases around 40%. With Mod2, the ones of Si and Si_2C decrease by almost 97%. When using Mod1, only the sticking coefficient of Si decreases by almost 99%.

Tabel 5.1 Sticking coefficient

Species	Sticking coefficient			
	No constraint	AFB	Mod2	Mod1
Si	0.0400	0.0147	0.0013	0.0005
Si2C	0.0300	0.0119	0.0010	0.0300
SiC2	0.0700	0.1002	0.0700	0.0700

5.3.4 Thermodynamic calculations

According to the previous section, the adaptable sticking coefficients method requires the assumption to fix one (Mod2), or two (Mod1) sticking coefficient(s) of the vapor species and each method considers the importance of each species in different ways. Thus, in order to

investigate the importance of the reactive species, the thermodynamic calculations are carried out. The schematic representation of the calculations is shown in Fig. 5.7 and the calculations procedure in a fixed volume is as followed. First, at the source powder with temperature T_1, the SiC source with equal amount of Si and C (1 mole each) decomposes into Si-C vapor in equilibrium with SiC and graphite. The equilibrium amount of the ith vapor species is $n_{i,1}$. Second, a set of $n_{i,1}$ used as an initial amount of vapor species is equilibrated at temperature T_2 which is lower than T_1 by forcing the system not to form the solid SiC. A new set of the equilibrium amount of the ith vapor species is obtained $n_{i,2}$. Third, again a set of $n_{i,1}$ is used as an initial amount but now the system is allowed to form solid SiC at temperature T_2. The amount of vapor species in this case is now $n_{i,3}$ in equilibrium with solid SiC (and other condensed phases if they are stable). Contribution of the ith species to the formation of solid SiC could be calculated from the change in the amount of vapor from when we do not allow the solid phase to when we allow solid phase to be formed. We will define this quantity as the species contribution:

$$\tau_i = n_{i,2} - n_{i,3}\,. \tag{5.30}$$

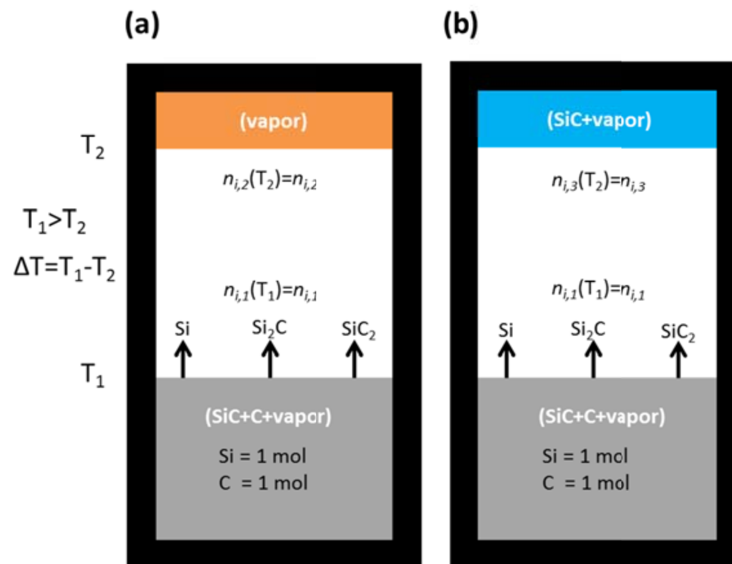

Fig. 5.7 Schematic representation of the thermodynamic calculations. The three phase equilibrium (SiC-C-gas) at temperature T1 is assumed at the source side. At the seed side having temperature T2 (T2<T1), (a) no any condensed phase is not allow to form, while (b) the condensed phase such as SiC is allowed to form.

Similar approach was done in [24] as a simple approximation to investigate how the gas phase composition changes when the species are transported from the gas phase down to the substrate. Two sets of equilibrium thermodynamics calculations were performed. For the first set of calculations, the temperature difference between seed and source are kept constant at 50˚C but varying T_1 and T_2. For the second set, the effect of temperature difference is studied by varying T_1 but T_2 is kept constant.

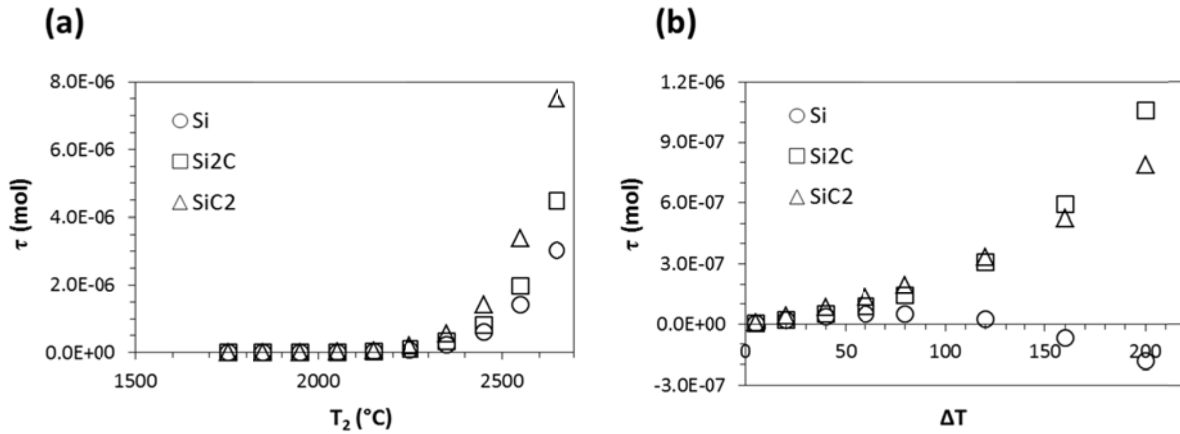

Fig. 5.8 Species contribution for the formation of solid SiC with varying conditions: (a) ΔT is fixed at 50 °C and (b) T_2 is fixed at 2200 at °C.

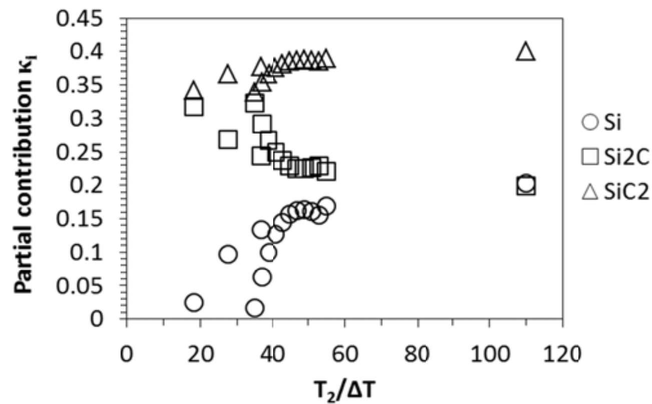

Fig. 5.9 Species partial contribution as a function of $T_2/\Delta T$

The species contribution τ_i of the three dominant vapor species is shown in Fig 5.8. For the fixed ΔT, the SiC_2 species contributes most in the SiC growth followed by Si_2C, and Si respectively (Fig. 5.8a). The contribution of all vapor species increase while increasing the

growth temperature. In this case, it does not matter if T_2 or T_1 is used to plot since ΔT is constant. When T_2 is fixed at 2200 °C, the order of each species contributions is similar to the first case at low ΔT (Fig. 5.8b). However, at high ΔT in which τ_{Si2C} is larger than τ_{SiC2}, τ_{Si} becomes negative meaning that the Si vapor is produced from SiC instead of consuming. Further increase of ΔT, i.e. for ΔT=300 °C, leads to the formation of Si in the liquid phase. However, such extreme conditions where the net Si flux leads to the emission of Si vapor species or the precipitation of extra condense phase are out of the scope of this work and will not be considered in this model. By considering the heterogeneous reaction (5.30), the species partial contributions $\kappa_i = \tau_i / \left(\tau_{Si2C} + 2\tau_{SiC2}\right)$ are plotted in Fig. 5.9 as a function of seed temperature divided by temperature difference ($T_2/\Delta T$). At high $T_2/\Delta T$ ratio, the species partial contribution of Si and Si_2C are quite similar. As $T_2/\Delta T$ decreases, the partial contribution of Si and SiC_2 decreases while the one of Si_2C increases. The partial contribution of Si_2C is approaching SiC_2 and the one of Si is approaching zero. The general trend is that the partial contribution of SiC_2 is always much larger than Si at this temperature range.

5.3.5 Discussion

The atomic fluxes balance method improves the initial system's boundary conditions. This method does not change the Stefan flow, but adapts the diffusive flux just near the seed to obtain stoichiometry. In contrast, both mole fraction and mole fraction gradient are affected when using the adaptable sticking coefficients method. Thus, the question arises for which method corresponds more to the physics of the crystal growth?

The chemical description of the non-congruent condensation from a complex vapor phase is still an open issue. The recent paper from Fujimoto et al. [25] is an interesting approach as it allows a comprehensive understanding of vapor phase composition variations in P-T-x phase diagram. It was pointed out that, the SiC source powder thermally decomposes into Si-C vapor with a composition of v_1 and solid carbon. As the temperature is lower at the seed side, vapor v_1 solidifies to form SiC single crystal and the vapor phase composition becomes v_2 which is richer in Si compared to v_1. From Fig. 5.6, both methods show that the Si/C ratio is higher on the seed side than the source side. Thus both methods seem to be acceptable regarding the analysis of phase diagram discussed in such report.

According to the definition of the Stefan flow, an additional or removal of species should influence the mean flow of the fluid next to the interface. With the stoichiometry conditions, the net total fluxes at the boundary are changed. As a consequence, the Stefan velocity and the convective fluxes are affected. The method of adaptable sticking coefficients is in agreement with this argument but not the atomic fluxes balance one. In the latter case, only the diffusive fluxes are affected but not the convective fluxes. Further argument concerning the weakness of such method can be discussed as followed. We assumed that the sticking coefficient is identical to the evaporation coefficient obtained from the high temperature mass spectrometer studies of the SiC sublimation process. In such process, the SiC powder would soon become SiC-C diphasic mixture. Thus the obtained evaporation coefficients are associated with the sublimation from SiC-C but not from pure SiC. It was shown that the evaporation coefficients decrease due to the increase in the carbon content at the SiC powder grains [21]. As a result, a set of sticking coefficients from our assumption may not be appropriated even for the initial system without constraint. The adaptable sticking coefficient method allows us to take into account the stoichiometry condition with is not included from the evaporation coefficient taken from the evaporation of SiC-C diphasic mixture itself. Thus, the adaptable sticking coefficients method appears to be a better description concerning the kinetics mechanism of the crystal growth than the atomic fluxes balance method.

The analysis of thermodynamic calculation results aims at answering to the question: which of Mod2 or Mod1 models is more appropriated? By comparing between the species partial contributions obtained from the global modeling in Fig. 5.6 and the species partial contribution in Fig. 5.9, the species partial contribution obtained from Mod1 are quite similar to the results obtained from the thermodynamic calculations at high $T_2/\Delta T$. When decreasing $T_2/\Delta T$, the numerical results start to deviate from the thermodynamics results. However, only Mod1 can preserve the general trend where the partial contribution of SiC_2 is much larger than Si. Thus, Mod1 gives the best agreement with the thermodynamic calculations for all the growth conditions. We may note that, by changing the growth conditions (T_1 and ΔT) using Mod1 for the numerical modeling, the partial contributions of Si and SiC_2 can be decreased, while the one of Si_2C can be increased following the tendency shown in Fig. 5.9.

In this section, it is worth noting also that the similar thermodynamic database [23] was used in both numerical modeling and thermodynamic calculations to ensure the compatibility when comparing those two sets of results. The new question arises concerning the effect of the choice of the thermodynamic database on the full process modeling. This will be discussed in the following section.

5.4 Effect of choice of thermodynamic databases

While developing a numerical model for the global process simulation, a careful analysis and choice of the databases is crucial. To date different thermodynamic databases are available for describing the vapor phase in equilibrium in the Si-C chemical system. They are differing by the methods used for their measurements. The first attempt for the gaseous phase study of the Si-C system was done by Drowart et al. [15] using mass spectrometry. The composition of the gas phase and enthalpies of formation for the main species were determined. Some other works related to the determination of equilibrium partial pressure of vapor species in Si-C system were proposed. Thermodynamic analysis of equilibrium processes in the gas phase during silicon carbide sublimation done by Lilov [26] has shown that the composition and the stoichiometry of the gas phase were strongly dependent on temperature. High-temperature mass spectrometry with a multiple Knudsen-cell furnace was used in [16, 17]. The enthalpies of the formation for Si, Si_2, Si_3, Si_2C, and SiC_2 molecules were determined. The SGPS database for Si-C system was compiled by SGTE group [27] using data from [28]. This database can be found in commercial software, such as FactSage [29]. Another database origin is the JANAF table [23]. The aim of this section is to assess the different thermodynamic databases available and compare them regarding the global modeling of SiC growth by PVT. The calculated results namely, growth rates and Si/C ratios in front of the seed crystal are compared and discussed.

5.4.1 Equilibrium partial pressure in front of SiC-C diphasic mixture

The temperature dependent equilibrium partial pressure of the three main vapor species in Si-C system according to JANAF, Lilov, Rocabois et al., and SGPS databases is plotted in Fig. 5.10. For JANAF and Rocabois databases, similar behavior of species partial pressure is observed in 2000-2700 K temperature range. Si partial pressure is the highest followed by SiC_2 and Si_2C, respectively. Si_2C is always higher than SiC_2 in the SGPS database while Si is still the

dominant one. For the thermodynamic analysis done by Lilov, Si is the dominant specie at low temperature whereas SiC_2 dominates at high temperature. Since the sublimation and condensation rates are a function of species equilibrium partial pressure based on the Hertz-Knudsen model, the differences in the temperature dependent equilibrium partial pressure of the species discussed here should result in different sublimation and condensation rates and also different Si/C ratios in the gas phase.

5.4.2 Growth rate

The growth rate, calculated at the center of the seed, versus inverse of growth temperature is plotted in Fig. 5.11a. A linear dependence is observed and all databases show similar tendencies. The growth rate increases by increasing the temperature and all the values are located within the same order of magnitude for a given growth temperature. From this result, there is no significant discrepancy when comparing different databases. However, by plotting directly the growth rate as a function of temperature (Fig. 5.11b) at more detailed linear scale, slight differences can be observed. The higher the temperature is, the larger the differences in the absolute values. The growth rate can be differed by up to a factor of two at 2300 °C.

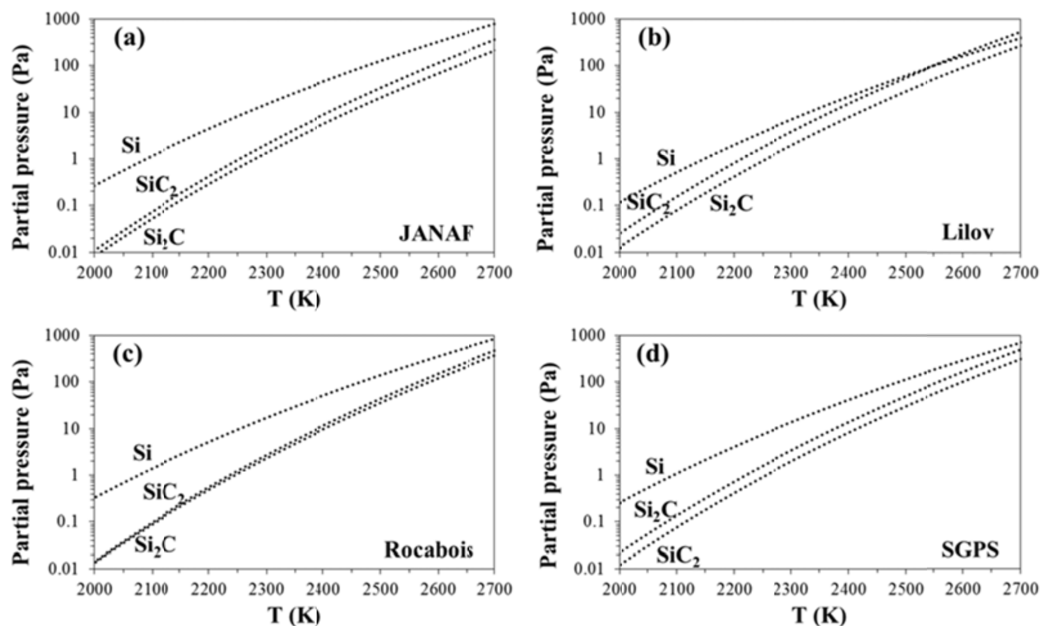

Fig. 5.10 Equilibrium partial pressure of the three main vapor species (Si, Si2C, SiC2) in the Si-C system as a function of temperature, calculated from (a) JANAF, (b) Lilov, (c) Rocabois, and (d) SGPS databases.

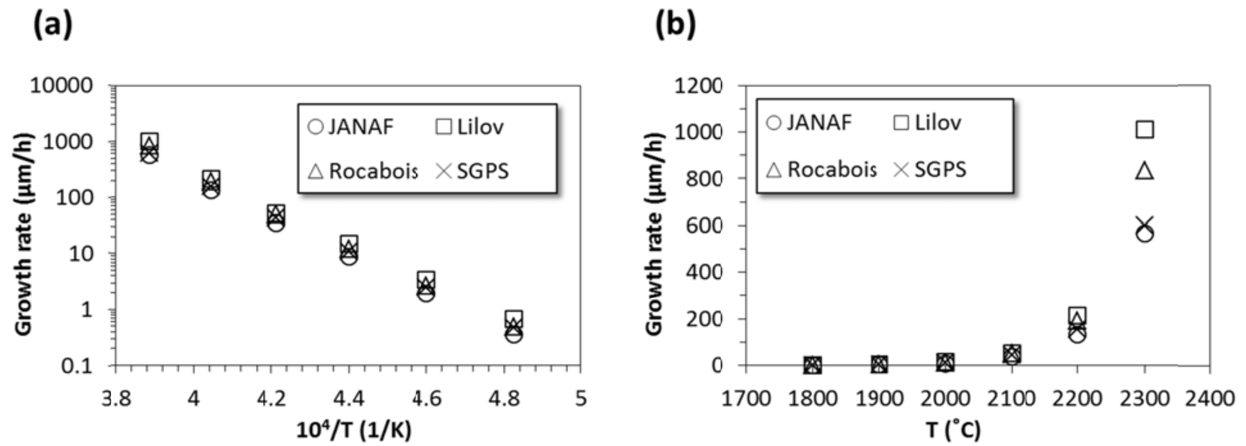

Fig. 5.11 (a) Growth rate calculated at the center of the seed in a log scale as a function of inverse growth temperature and (b) growth rate versus growth temperature in a linear scale

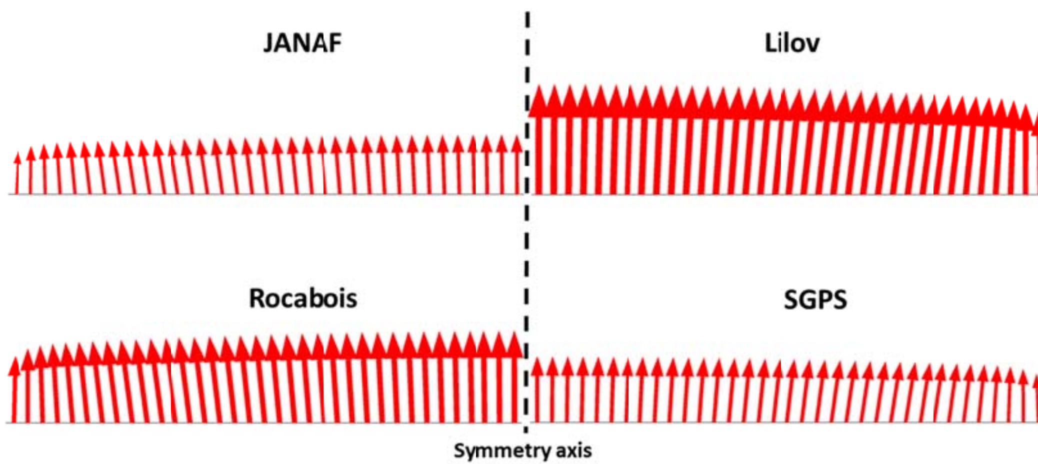

Fig. 5.12 Growth rate profile calculated from the carbon flux on the seed surface when using different thermodynamic databases. Calculations were made for the growth temperature of 2300 °C in 12 mbar argon ambient.

Example of results from process simulation is shown in Fig. 5.12. The growth rate can be calculated by the total flux normal to the seed surface of either carbon or silicon since the conditions for stoichiometric growth of SiC are applied (Mod1). The carbon flux at the seed surface is drawn in the axisymmetric configuration. Qualitatively, the carbon flux profiles give similar shape of the crystal front (slightly convex).

5.4.3 Si/C ratio

Si/C in the gas phase just in front of the crystal surface is plotted in Fig. 5.13a. The Si/C ratio decreases when the temperature increases (Fig. 5.13b). At any temperature, the Lilov database gives a much lower Si/C ratio. In all cases the Si/C ratio is higher than 1. Again with all databases, similar tendencies are obtained for both the Si/C ratio distribution along the seed diameter and for the temperature dependence of the Si/C ratio. However there exists a discrepancy when comparing the absolute values. This discrepancy expands as the temperature decreases. A factor of three for such discrepancy is observed at 1800 °C.

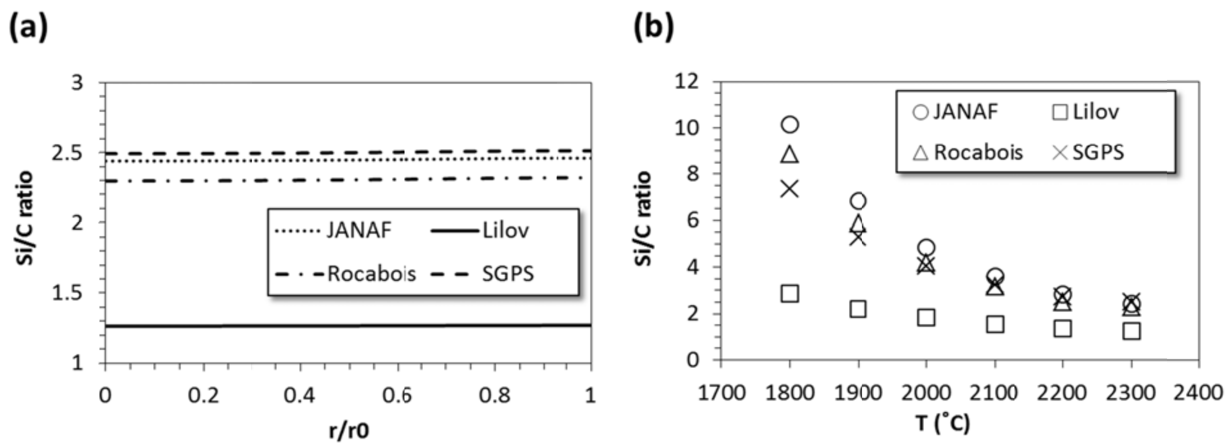

Fig. 5.13 (a) Si/C ratio in the gas phase plotted along the seed radius grown at 2300 °C in 12 mbar argon ambient and (b) Si/C ratio in front the a crystal at the symmetry axis plotted as a function of growth temperature

5.4.4 Discussion

From each of these examples, the results calculated from different databases show the same trend and the same order of magnitude. Thus choice of database would not be a problem when performing the numerical simulation for the process development. However, when further refinement of the model is required, for example, if one wants to tackle the problem of 2D nucleation [30, 31] and the studies of nitrogen incorporation, even slight discrepancy could become crucial. The change in thermodynamics database is expected to affect the contribution of each vapor species to the formation of SiC crystal. As a consequence, the model implementing the stoichiometric incorporation used in the numerical modeling has to be verified again with the thermodynamic calculations. This kind of issue is practically very inconvenient for further

development of the model. Our prior assumption that the three-phase heterogeneous equilibrium "SiC-C-vapor" exists entirely in the growth chamber reduces the thermodynamic degree of freedom of the heterogeneous process. This prevents the variation of the state variable at the growth interface. Thus the kinetics parameters, such as the sticking coefficients, have to be modified in order to realize the stoichiometric growth of SiC as we have done so far. In fact, the problem of sticking coefficient still remains as an open issue. They are very complex and should include energetic and kinetic terms, i. e., temperature, velocity, surface roughness [6, 32, 33]. The experimental values will be necessary to improve the accuracy of the model. However, an alternative approach to avoid dealing with the evaporation and sticking coefficient as well as cross-checking the thermodynamic databases will be presented in the following section.

5.5 Coupled approach

Apart from the problem of boundary conditions for considering the stoichiometry of SiC in the growth process modeling, there are also other strong issues which are not considered in a satisfactory way. This is the case for instance for the thermochemistry of the Si-C system and its coupling to mass transfer. Recently, it has been reconsidered and a better understanding of the solid-vapor interface chemistry was reported [25, 34]. But two essential questions are still open: i) how to treat the thermochemistry of the solid SiC crystal? ii) How the latter could be coupled to the numerical modeling of the process? In this section, we present a method to take into account the stoichiometric incorporation of vapor species. More importantly, the proposed method gives an assessment to the chemistry of solid SiC crystal, i.e. the activities of both Si and C atoms in the crystal during the PVT growth process. This approach employs the fully coupling between numerical modeling and the thermodynamic calculations.

5.5.1 Method and calculations

In contrast to the comparative method, this coupled method does not prior assume the three-phase heterogeneous equilibrium (SiC-C-vapor with variance = 0). Thus at the crystal-vapor interface, the equilibrium partial pressure cannot be computed directly from the temperature of the solid phase (SiC-gas with variance = 1). The extra thermodynamic degree of freedom is compensated by the condition for SiC stoichiometry via the consideration of SiC solid solution (s, s). By treating SiC as a solid solution, following the work done in [34] the Si and C

components can be considered in the non-stoichiometric Si_xC_y compound according to the equilibrium

$$Si_xC_y = x\mathrm{Si}\ (\text{in } SiC_{(s,\ s)}) + y\mathrm{C}\ (\text{in } SiC_{(s,\ s)}). \tag{5.31}$$

Since the SiC crystal is nearly stoichiometric [18], *x* and *y* are close to unity and the equilibrium constant for reaction (5.31) is written by

$$K_p^1(T) = \frac{a_{Si} \cdot a_C}{a_{SiC}}. \tag{5.32}$$

This equilibrium constant is calculated from the standard free enthalpies obtained from the JANAF thermochemical database [23] by the following expression

$$\Delta_r G°(T) = -RT \ln K_p(T) \tag{5.33}$$

The activity of the pure components equal to unity by the definition of the standard state considering that there is only small deviation from the stoichiometric composition. The equilibrium state in SiC with excess C (SiC-C) gives a_C=1 with the minimum value of a_{Si} while a_{Si}=1 with minimum value of a_C for SiC with excess Si. In the non-stoichiometry domain of SiC compound (just before the precipitation of either C or Si at the surface), the Si and C activities vary between SiC-C and SiC-Si phase limits at a given temperature. The formation of the three main vapor species can be attributed to the following reactions:

$$\mathrm{Si}\ (\text{in } SiC_{(s,\ s)}) = \mathrm{Si(g)}, \tag{5.34}$$

$$2\mathrm{Si}\ (\text{in } SiC_{(s,\ s)}) + \mathrm{C}\ (\text{in } SiC_{(s,\ s)}) = Si_2C\mathrm{(g)}, \tag{5.35}$$

$$\mathrm{Si}\ (\text{in } SiC_{(s,\ s)}) + 2\mathrm{C}\ (\text{in } SiC_{(s,\ s)}) = SiC_2\mathrm{(g)}. \tag{5.36}$$

The corresponding equilibrium constant for reactions (5.34)-(5.36) are respectively

$$K_p^2(T) = \frac{P_{Si}^*}{a_{Si}}, \tag{5.37}$$

$$K_p^3(T) = \frac{P_{Si_2C}^*}{a_{Si}^2 a_C}, \tag{5.38}$$

$$K_p^4(T) = \frac{P^*_{SiC_2}}{a_{Si} a_C^2}\ . \tag{5.39}$$

Since the standard state defines a_{SiC}=1, a_C can be written in terms of a_{Si} (5.32) and the equilibrium partial pressure of each vapor species is a function of a_{Si} and its equilibrium constant (temperature dependent).

In order to couple the thermodynamic mechanisms with the mass transport modeling we consider separately the chemistry of the solid phases at the source and seed surfaces. On the source surface, the SiC compound sublimes non-congruently and probably the source will be soon a mixture of SiC-C. Thus a_C=1 and the equilibrium partial pressure of the vapor species is depending only on the temperature. On the seed surface, the incident mass fluxes sublimed from the source are transported by diffusion and convection to the seed surface. A partial condensation due to the lower temperature occurs and this condensation naturally produces a SiC-Si system due to the large excess incident Si flux. Then the condensed system sublimes more Si than C which means that the excess Si can be re-sublimed toward the source. The growing crystal remains closely stoichiometric and the amount of back flow or the re-sublimation fluxes depend on both the temperature of the seed and the incident fluxes. Thus in a steady-state regime for the growth at the surface of SiC seed, a mass balance equation (5.21) expressing the stoichiometric condition for the incorporation of Si and C atoms is imposed. From (5.17), the SiC stoichiometry condition (5.21) becomes

$$\gamma_{Si} P_{Si} \chi_{Si} + \gamma_{Si_2C} P_{Si_2C} \chi_{Si_2C} - \gamma_{SiC_2} P_{SiC_2} \chi_{SiC_2} = \alpha_{Si} P^*_{Si} \chi_{Si} + \alpha_{Si_2C} P^*_{Si_2C} \chi_{Si_2C} - \alpha_{SiC_2} P^*_{SiC_2} \chi_{SiC_2}\ . \tag{5.40}$$

In this model, we assume that the condensation coefficients of all vapor species are γ_{SiC} representing the mean condensation mechanism. The same assumption is applied for the evaporation coefficients so the mean evaporation coefficient is α_{SiC}. Using the assumption that $\alpha_{SiC} = \gamma_{SiC}$, the solution of (5.40) is independent of the condensation and evaporation coefficients. Thus from the relations (5.32), and (5.37)-(5.39), Eq. (5.40) is rewritten

$$K_2 \chi_{Si} a_{Si} + K_1 K_3 \chi_{Si_2C} a_{Si} - K_1^2 K_4 \chi_{SiC_2} \frac{1}{a_{Si}} = A\ , \tag{5.41}$$

where the differences in Si and C fluxes condensing on the seed surface is denoted by

$$A = P_{Si}\chi_{Si} + P_{Si_2C}\chi_{Si_2C} - P_{SiC_2}\chi_{SiC_2}\,. \tag{5.42}$$

Eq. (5.41) can be rearranged in forms of the quadratic equation:

$$\left(K_2\chi_{Si} + K_1K_3\chi_{Si_2C}\right)\cdot a_{Si}^2 - Aa_{Si} - K_1^2K_4\chi_{SiC_2} = 0\,. \tag{5.43}$$

The analytic solutions of Eq. (5.43) are

$$a_{Si} = \frac{A \pm \sqrt{A^2 + 4\cdot\left(K_2\chi_{Si} + K_1K_3\chi_{Si_2C}\right)\cdot\left(K_1^2K_4\chi_{SiC_2}\right)}}{2\cdot\left(K_2\chi_{Si} + K_1K_3\chi_{Si_2C}\right)}\,. \tag{5.44}$$

Since all parameters are real and the discriminant $A^2 + 4\cdot\left(K_2\chi_{Si} + K_1K_3\chi_{Si_2C}\right)\cdot\left(K_1^2K_4\chi_{SiC_2}\right)$ is always positive, the two roots are real and unequal. It can be further proved that one root is positive and another one is negative. The negative value of activity has no physical meaning. Thus there exists only one positive value of Si activity that verifies the steady-state of growth. The corresponding C activity can be computed using Eq. (5.32). One may note that by adding the Si_2 and/or Si_3 species in the vapor phase, the quadratic equation (5.43) becomes either cubic or quartic equations which should still be possible to solve analytically or numerically. However, these additional species should not affect the calculated Si activity since the vapor pressure of Si is around two orders of magnitude higher than Si_2 and Si_3 even in the extreme case at SiC-Si phase limit [34]. Thus in general growth conditions, the error from excluding these two species should results in less than 1% error of the calculated activity.

Recall the Hertz-Knudsen formulation for the condensation-sublimation at the seed surface (5.20), we know from (5.37)-(5.39), (5.42) and (5.44) that the equilibrium partial pressure is a function of the partial pressure of all vapor species. Thus Eq. (5.20) may be written as

$$\gamma_i\left(x_iP - f(x_1,x_2,x_3)\right)\chi_i = \left(-\frac{Px_i}{RT}\sum_{j=1}^{N}\widetilde{D}_{ij}\nabla x_j - \frac{x_i}{M}\left(\sum_{i=1}^{N-1}M_i\gamma_i\left(x_iP - f(x_1,x_2,x_3)\right)\chi_i\mathbf{n}\right)\right)\cdot\mathbf{n}\,. \tag{5.45}$$

As we can see from Eq. (5.45), there are 3 unknowns (x_1, x_2, x_3) and three equations are available for i=1, 2, and 3. Thus a close set of equations is formed for the mass transfer boundary conditions at the seed-vapor interface.

5.5.2 Results

The geometry used in this study and the temperature profile is shown in Fig. 5.14a. The distributions of activity Si and C atoms along the seed radius are shown in Fig. 5.14b. These radial variations are caused by the radial temperature gradient and the different incident fluxes along the seed crystal. Under the specific growth conditions, the activity of Si atom is larger than the one of C at the center of the seed but smaller at the seed periphery. The opposite situation can be obtained by changing the growth conditions, such as the crucible geometry. This shows the possibility to control the chemistry of the growing crystal precisely along the crystal radius.

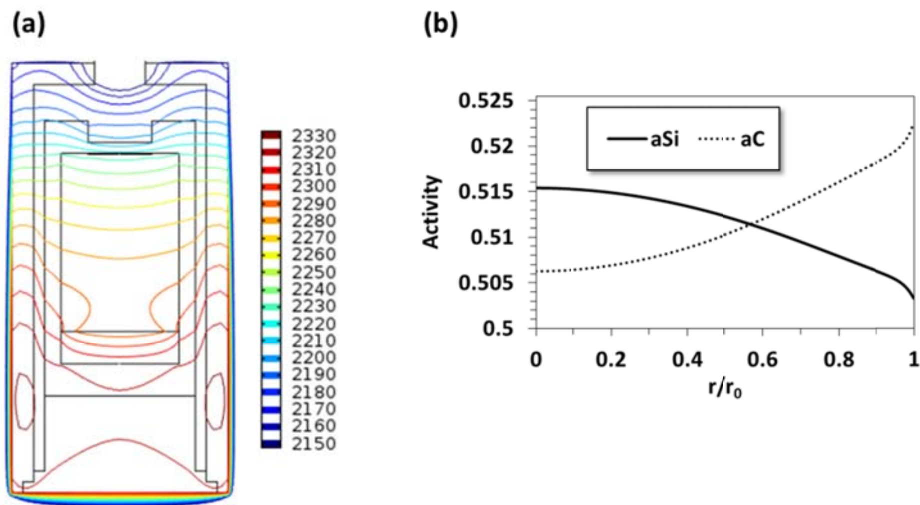

Fig. 5.14 (a) Geometry and temperature distribution and (b) activities of Si and C atoms radially distributed along the seed surface from center (r=0) toward the periphery ($r=r_0$) for given growth conditions: P = 5 mbar and ΔT=59 °C

In this section we will focus on the variation of activities of the C and Si components with respect to the process parameters. At constant seed temperature, the effect of pressure and temperature difference ($\Delta T=T_{source}-T_{seed}$) between source and seed on the activities of Si and C in solid SiC is shown and compared to the limit of Si and C activities at the SiC-Si and SiC-C phase boundaries (Fig. 5.15). The activities and ΔT shown in such figure are taken at the symmetry axis. The temperature differences ΔT are obtained by adjusting the coil position. At low ΔT, the

activities of both Si and C atoms are close to the SiC-C phase boundary while progressively changing toward SiC-Si phase boundary upon increasing ΔT. If ΔT is too large either by increasing the source temperature or decreasing the seed temperature, the seed will not be able to produce enough Si back flow and at that time the condensation will produce a SiC-Si mixture. This can be seen by extrapolate the curves in Fig. 5.15. Similarly if ΔT is negative meaning a reversed temperature gradient, the seed composition should be a SiC-C mixture from the extrapolation. This is the case when the seed sublimes instead of grows and will soon become graphitized due to the non-congruent sublimation.

From SiC-C toward SiC-Si phase boundaries, the activities changing rates are enhanced by decreasing the total pressure. This behavior is attributed to the interactions between the reactive vapor species and the argon gas. Since the argon gas does not incorporate in the SiC compound, there is a strong back diffusion flow of this gas from the seed toward the source which retards the sublimation and deposition rates. Decreasing the argon pressure enhances the sublimation rate and the excess of Si in the vapor composition. Then more Si back flow is expected. As a result, the activities of Si and C are shifted toward the SiC-Si phase limit.

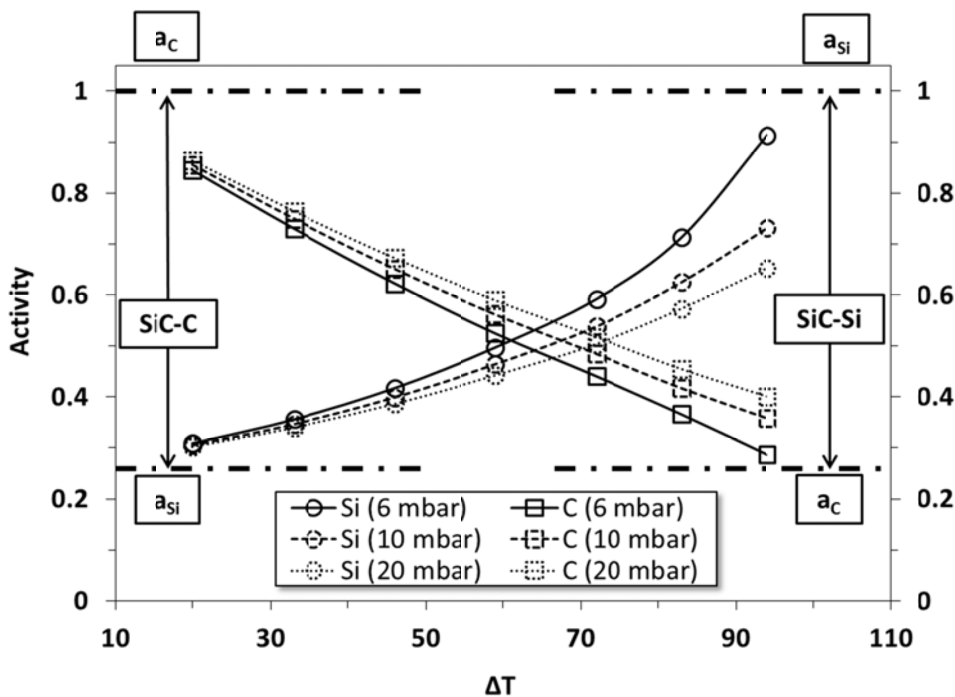

Fig. 5.15 Activities of Si and C in solid SiC crystal with varying seed-source temperature difference and the effect of the pressure. The seed temperature is fixed at 2225 °C (±2 °C). The dashed-dotted lines show the limit of the activities at the SiC-Si and SiC-C phase boundaries

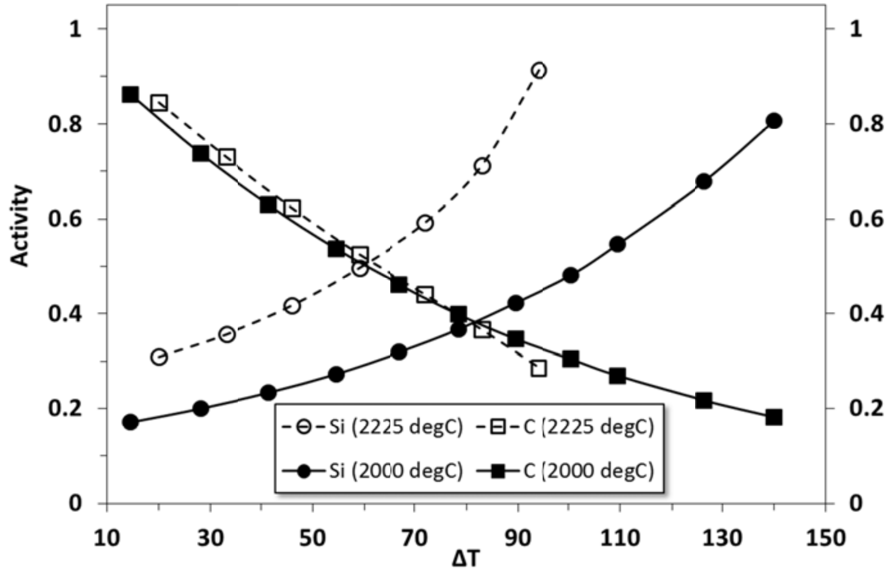

Fig. 5.16 The behavior of activities of Si and C atoms in SiC crystal as a function of ΔT at different seed temperature but similar growth pressure of 6 mbar

The behavior of the Si and C activities in SiC solid solution as a function of ΔT when decreasing the seed temperature is plotted in Fig. 5.16. The results are compared with the previous case. It can be seen that the window for the growth of pure phase SiC when using low seed temperature is broader, such as larger ΔT can be used. Moreover, the crossing between the two activities shifts to the higher ΔT. This can be explained by the reduction of the *A* parameter shown in (5.42). The difference in Si and C fluxes condensed on the crystal surface is smaller at lower growth temperature keeping ΔT constant. Thus the system requires larger ΔT in order to move from C-rich to Si-rich SiC crystal.

5.5.3 Discussion

In case of an ideal solution, the activity is proportional to the mole fraction according to the Raoult's law. This may not be the case for SiC since the non-stoichiometry domain is not described. However, we would estimate the tendency of the condensed phase composition to be similar to the tendency of the activities of the solid components. This means that at the seed surface during the growth, C atoms is dominant if the system is closer to SiC-C phase limit while it is the Si ones in the conditions closer to SiC-Si phase limit. Since the solid phase remains pure SiC without any extra phase inclusion within the two phase limits, the dominant atoms when the system is close to each phase limit could be correlated to the formation of the non-stoichiometric

point defects, such as, C interstitials in the C-rich crystal, and C lattice vacancies, Si antisites, and Si interstitial in the Si-rich crystal assuming that the Si lattice sites are saturated. A theoretical analysis of the formation of non-stoichiometric point defects in SiC single crystal was proposed for the growth under equilibrium condition [35]. The results showed that the concentration of different type of both Schottky and Frenkel defects are dependent on the partial pressure of silicon vapor. It may be possible to apply the results from our process modeling concerning the equilibrium partial pressure of Si to such analysis in order to study the behavior of the defects under the real growth conditions.

The capability of this model in predicting the state (Si- or C-rich) of the growing crystal should be able to correlate to the occurrence of cubic or hexagonal polytype with the growth conditions. A quantitative LEED study suggested that a cubic stacking sequence is induced by the surface reconstruction with the excess Si [36]. This was found only when the surface of 4H-SiC (0001) is Si enriched during the annealing process. It is still unclear if this mechanism is applicable for the growth process where much higher temperature is used. Normally at such high temperature, the 3C polytype is thermally instable and transform to the hexagonal polytype due the solid state transformation caused by the imperfections of the crystal [37]. Birnie et al. [18] found the predominant 3C-SiC grains when equilibrate the 3C-SiC grains in Si-rich environment while 6H-SiC grains are predominant in the C-rich environment. The interesting point is that such experiments were done at very high temperature (2400 °C). This might suggest that the mechanism proposed by [36] overcomes the solid state transformation. The growth of cubic SiC prefers the low growth temperature typically below 2000 °C to prevent the polytype transformation. Using such low temperature, growth of 3C-SiC on 3C-SiC can be stabilized using the separated Si container [38]. This extra Si source increases the Si partial pressure by 25-30%. Keeping low temperature at the seed, very large ΔT (500 °C) and very low pressure (10^{-3}-10^{-4} mbar) were used in [39] and the 3C-SiC can be grown on both 6H(0001) and 3C(100) substrates. All the experimental results discussed here suggest that the cubic polytype of SiC is preferable for the growth under Si rich condition. Thus, we may propose a guideline for the stabilization of SiC polytype according the chemistry at the growing surface predicted from our model. First, the growth environment providing the crystal chemistry closer to the SiC-Si phase limit, i.e. high ΔT and/or low pressure, should result in higher probability for the nucleation of cubic polytype. The crystal imperfections such as stress and defects should be also minimized in

order to avoid the polytypic transformation. Moreover, the growth under low ΔT and/or high pressure bringing the crystal chemistry closer to SiC-C phase limit should be preferable for stabilizing the hexagonal polytype.

Another model was proposed for the transformation of SiC polytypes during the growth of an epitaxial layer [40]. Such model was suggested based on the time variation of the concentration of carbon vacancies N_V^C in a transition layer. Averaged data concerning the concentration of N_V^C [41] reveals that N_V^C in the 4H, 15R, 6H, and 3C-SiC are 7.3×10^{20}, 15.1×10^{20}, 16.3×10^{20}, and 33.6×10^{20} cm^{-3}, respectively. The introduction of carbon vacancies due to an excess of Si results in the compression of the crystal lattice. Thus a cubic structure of the growing layer is more favorable than the hexagonal structure in term of energy. If the C deficiency is dominant in the crystal, our model predicts the carbon vacancies to be maximized in the growth condition close to SiC-Si phase limit. Such growth condition should be favorable for the formation of cubic polytype as discussed earlier. Thus our model is in very good agreement with the vacancy model of the heteropolytype epitaxy of SiC [42]. The extra information accessible by our model is the variation of the activities with the growth conditions. This may serve as a basis to control the amount of N_V^C to stabilize the preferential SiC polytype in the growth experiment.

To fabricate n- and p-type SiC epilayer, nitrogen and aluminum are generally used as a dopant, respectively. The spectroscopic evidences from Choyke [43] and Davis et al. [44] shown that the nitrogen atom occupies the C site in SiC crystal while the aluminum atom substitute the Si site [45]. Larkin et al. [46] proposed that the Si/C ratio in the CVD growth reactor strongly affect the doping incorporation for epilayer grown on 6H-SiC Si-face. Nitrogen and carbon compete for the C sites while aluminum and Si compete for the Si sites of the growing SiC epilayer. This is the well-known 'site-competition' model. Even though, it is still not clear why this model is failed to describe the behavior on the C-face. The incorporation mechanism of nitrogen, aluminum, and boron was also proposed by Kimoto et al. [45]. Such mechanism involves the structure of the growing surface under Si- or C-rich condition. The surface coverage is differed depending on whether it is Si- or C-face. The C coverage increases with increasing C/Si ratio on Si face thus preventing the incorporation of N atoms. On the other hand, the surface

on C-face is believed to be terminated with C atoms independent on the C/Si ratio in the range of 1-2. Thus the site-competition model does not effectively work for the growth on C-face. Concerning the CVD process, the amount and ratio of injected precursor gas are controllable. However this is not the case for PVT since the compositions are always enriched with Si by considering only the vapor phase itself. Indeed the surface chemistry of the growing crystal was completely unknown. Thus in order to quantify the doping incorporation, the information predicted from our model could be correlated with the surface coverage. For example, the growth conditions bringing the surface chemistry far from SiC-C phase boundary should multiply the competitiveness of the nitrogen providing higher nitrogen incorporation rate. Nevertheless, this requires the extension of the model to include N into the system.

Three examples concerning the point defects formation, occurrence of cubic or hexagonal polytype, and the quantitative doping incorporation showed the capability of the newly proposed modeling approach. The knowledge of the chemistry of the growing SiC crystal provides one step further for understanding and developing the growth process. Moreover, it is possible to extend the proposed coupled approach to consider the interaction between the vapor species and the graphite container.

5.6 Interaction between vapor species and graphite crucible

In seeded sublimation growth process (PVT) of SiC single crystals, graphite container is generally used. Despite the small number of gaseous species commonly considered (Si, Si_2C, SiC_2), the heterogeneous reactions between vapors and solids are very complex. The shape of the crystal growth front does not only depend on the isothermal shape but also on the global mass transport and chemical reactions considering for example, the heterogeneous adsorption/desorption processes and the interaction with the graphite crucible or tantalum crucible [47]. To optimize the growth process for obtaining high quality crystal, the shape of the growing crystal becomes an important issue. For example, the changes in the curvature of the crystal shape can induce polytype destabilization [48].

Several reports mentioned the important role of the graphite crucible as a carbon provider for the crystal growth [2, 49-52]. The strongest supporting report for this issue was the work done by Herro et al. [49]. With the starting amount of 88% of ^{13}C in the source powder, the

crystal consisted of only 40% of ^{13}C after growth. Numerical modeling results concerning the interaction between the vapor species and the graphite wall were presented [2]. However, no detail of the calculation was given. In this section, we are considering the chemical reactions of the vapor species with the graphite wall. We will focus on the effects of additional mass transport to the growing crystal and the resulting crystal growth front shape.

5.6.1 Method and calculations

In the previous section, we consider the equilibrium condition between the solid solution of SiC and the vapor phase for the growing SiC crystal. In this case we may apply the same procedure but replace SiC solid solution crystal by C solid representing the graphite wall. Concerning the etching process, elementary processes should include the element of the material to etch. In this study we assume that the excess Si vapor does not incorporate into the graphite wall but interact with it and produce SiC_2 species. This is supported by the fact that what is experimentally observed on most of the crucible walls is graphite corrosion and not SiC deposition. Thus a heterogeneous (C-vapor) reaction occurring at the graphite wall is assumed to be

$$Si(g) + 2C(s) = SiC_2(g), \tag{5.46}$$

with the corresponding equilibrium constant

$$K_p^5(T) = \frac{P_{SiC_2}^*}{P_{Si}^* a_C^2}. \tag{5.47}$$

In this case the standard state defines a_C=1, the equilibrium partial pressure of SiC_2 vapor species in front of the graphite surface can be written as a function of the equilibrium partial pressure of Si and its equilibrium constant. In order to close a set of equations, a mass balance equation for stoichiometric SiC (5.21) will be replaced by another mass balance equation considering that the silicon atoms will not be incorporated into the graphite wall

$$F_{Si} = N_{Si} + N_{SiC_2} = 0. \tag{5.48}$$

Substituting (5.17) to the above equation to obtain

$$\gamma_{Si}P_{Si}\chi_{Si} + \gamma_{SiC_2}P_{SiC_2}\chi_{SiC_2} = \alpha_{Si}P^*_{Si}\chi_{Si} + \alpha_{SiC_2}P^*_{SiC_2}\chi_{SiC_2}. \tag{5.49}$$

Again, we assume that the evaporation and sticking coefficients of the vapor species are represented by the mean value at the wall of graphite crucible α_C and γ_C that also follows the relation $\alpha_C = \gamma_C$. Thus, from the equilibrium constant relations (5.47), Eq. (5.49) is rewritten

$$\chi_{Si}P^*_{Si} + K_5\chi_{SiC_2}P^*_{Si} = P_{Si}\chi_{Si} + P_{SiC_2}\chi_{SiC_2}, \tag{5.50}$$

The equilibrium partial pressure of Si can be obtained:

$$P^*_{Si} = \frac{P_{Si}\chi_{Si} + P_{SiC_2}\chi_{SiC_2}}{\chi_{Si} + K_5\chi_{SiC_2}}. \tag{5.51}$$

Since the equilibrium partial pressure of SiC_2 species can be computed from the equilibrium partial pressure of Si, these equilibrium partial pressures can be subtracted back into the boundary condition at the graphite wall which is in fact similar to (5.20). Then a closed set of equations as shown in (5.45) can be formulated at the C-vapor interface. The important point to consider in this case is the mean sticking coefficient γ_C at the graphite surface. We should now define this value as an etching coefficient. Even if the solution of (5.51) is independent on the etching coefficient, the value of this coefficient will determine the reactivity of the graphite container with the vapor species. The crucible with good quality should be inert to the reactive gases and the etching coefficient becomes zero. In this section, we consider a small deviation from the perfect inert graphite wall. Thus we set a very low value (γ_C=0.0005) of the etching coefficient in order to investigate the effect of the etching of the crucible in the process modeling.

5.6.2 Results and discussion

The schematic representation of the growth chamber used in the experiment and modeling is shown in Fig. 5.17a. The two main graphite parts consist of, the graphite guide (part A), and the seed holder (part B). For the modeling without graphite etching, only the deposition of polycrystalline SiC is allowed on the graphite walls. On the other hand, when using the model integrated with the graphite etching, both the deposition of polycrystalline and the consumption

of graphite container due to etching are allowed. The inward fluxes of Si and SiC_2 species and the etching rate are plotted along the vertical coordinate (Fig. 5.17b). The inward flux of Si species and the outward flux of SiC_2 species increase toward the seed surface. The strong etching rate is found close to the seed crystal.

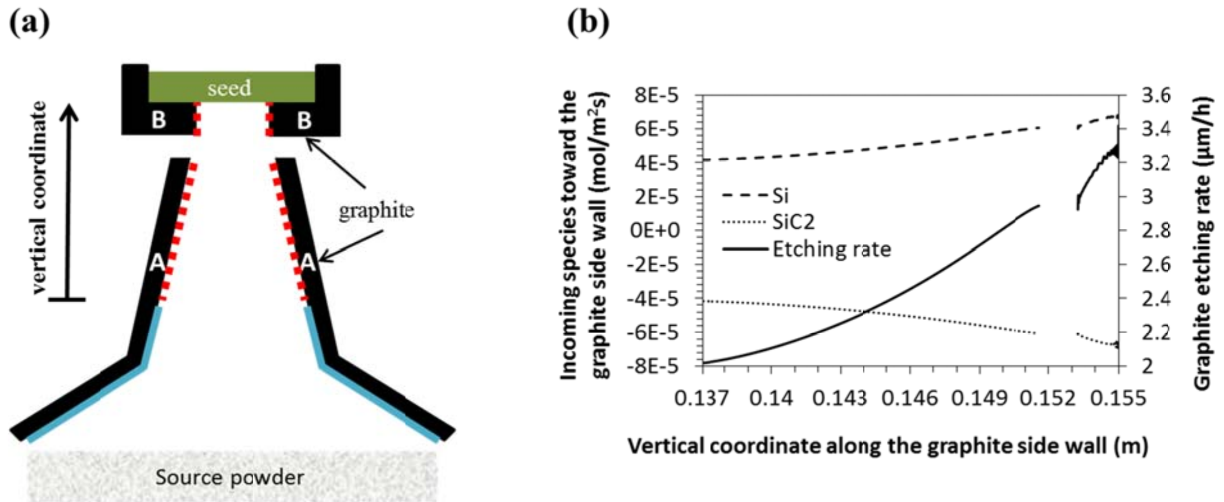

Fig. 5.17 Schematic representation of the graphite parts in the growth chamber. Dotted lines show the area where the graphite etching takes place in both graphite part A and B. Solid lines show the area where the growth of SiC polycrystalline takes place. (b) Incoming fluxes toward the graphite side wall and the corresponding etching rate.

The crystal growth rates are shown in Fig. 5.18 for both models: with and without graphite etching. At the initial stage of growth (Fig. 5.18a), the crystal shape is predicted to be convex without the graphite etching. On the other hand, with the graphite etching model, the growth rate becomes higher all along the seed radius. The additional fluxes are delivered from the graphite wall to the growing crystal mainly at the crystal periphery. This is clearly seen from the difference in the growth rate (ΔRg) compared between the two models. Thus the crystal shape becomes slightly concave with the graphite etching model. As the growth proceeds and the growing crystal becomes bigger, i.e., for the crystal of 1 mm in thickness, the growth rates become higher at the crystal center but lower at the edge for both models (Fig. 5.18b). This is mainly caused by the decreasing of the additional mass flux produced from graphite part B when the growing crystal covers half of its area. However, this does not mean that the additional flux produced from part A has no effect since the initially concave shape crystal cannot be obtained

without the etching form this part. As a result, the crystal front becomes convex at certain time interval after the initial stage and keeps its shape until the final stage of growth.

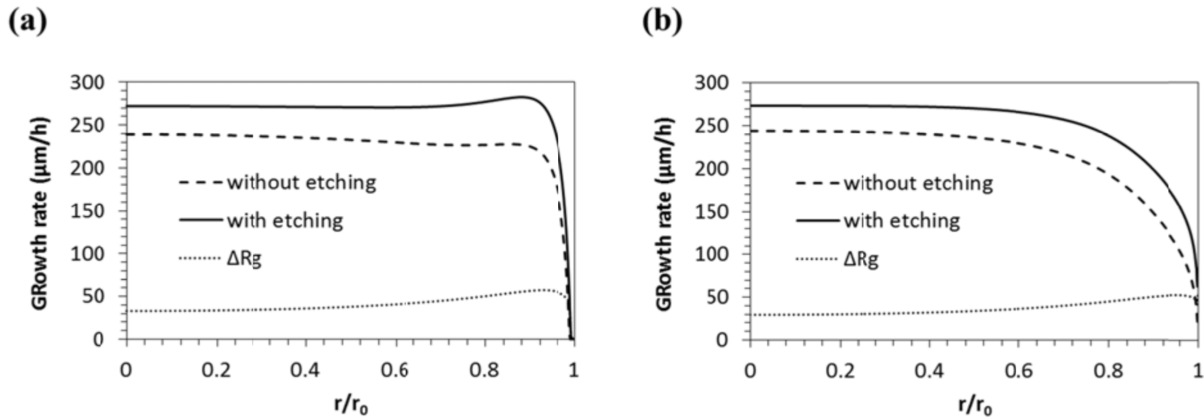

Fig. 5.18 Growth rate of SiC single crystal as a function of normalized radial distance from the center of the crystal (a) at the initial stage of growth and (b) after 1 mm of crystal thickness.

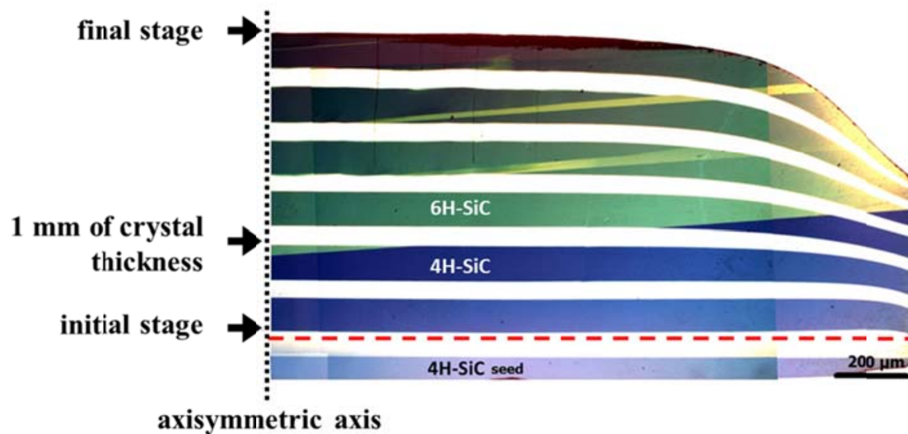

Fig. 5.19 Crystal cross section image shows the crystal evolution during the growth of SiC single crystal by PVT method. For better visualization of the crystal shape evolution, periodic nitrogen marking has been implemented. The dashed line serves as a guide for comparison. The initial crystal shape is slightly concave while it becomes convex after 1 mm of crystal thickness.

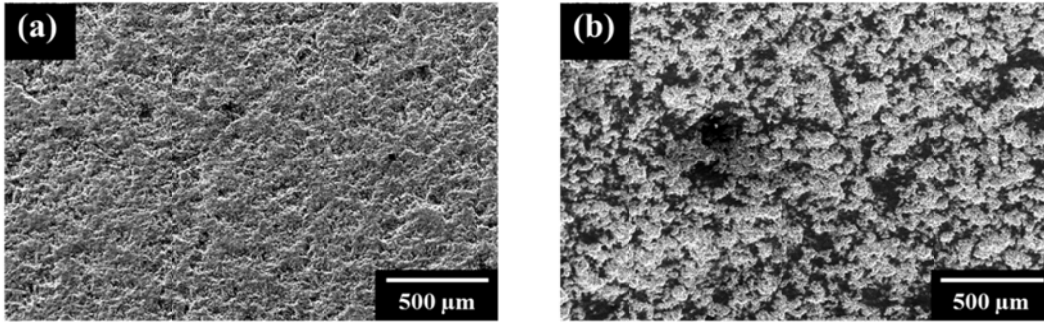

Fig. 5.20 SEM images of graphite material used in the experiment (a) before the growth and (b) after the growth of 20 hours.

The simulation results were compared with the experimental ones. Observing only the final global shape of the crystal is usually not enough and may lead to the wrong conclusion. That is why we have periodically marked the interface with nitrogen injection during the growth run, which ensures a perfect tracking of the crystal shape evolution (Fig. 5.19). At the initial stage, the growth front exhibits a slightly concave shape. After a certain time interval, the crystal front changes to slightly convex shape. The graphite etching model is then fit better to the experimental result. As a direct evidence of gas phase interaction with graphite, Fig. 5.20 shows two SEM images of the graphite wall surface, before and after 20 hours of SiC growth. The surface morphology of the graphite part drastically changes during the growth, with an apparent increase of surface roughness and porosity.

We also tried to investigate the effect of the graphitization degree of the graphite container on the SiC growth process as first pointed out in reference [52]. Usually the graphitization degree of the crucible increases due to the heat treatment at high temperature. The authors demonstrated that increasing the graphitization degree retards the reaction with the Si species and thus retards the growth of crystal. With the same idea, we used two different graphite parts (graphite guide): the standard graphite as received from the supplier and the same graphite part but annealed at 2300 °C for 8 hours. Two growth experiments were performed using these two parts. However, we obtained the same results from these two experiments in contrast to the work done in [52]. Even if the graphite parts were annealed at high temperature in our case, no difference in the diffraction peaks of the heat treated and non-treated graphite parts was observed from XRD measurement. Thus, the crystallinity does not change, neither in the bulk material nor

in the area close to the surface. The latter case was confirmed using grazing incidence X-ray diffraction. SEM observations were conducted in order to investigate the surface effect of the heat treatment. However, we could not observe any remarkable difference in surface morphology of the graphite parts in both heat treated and non-heat treated ones. We can thus conclude that all the evolutions observed in our case are only coming from the interaction between the graphite wall surfaces and the gaseous species and not from the evolution of the graphite itself upon annealing. Our graphite is perfectly stable with time upon heat treatment at high temperature.

5.7 General modeling results and validations

The typical temperature distribution in the growth chamber and the fluid velocity are shown in Fig. 5.21. The highest temperature at the bottom corner of the growth chamber brings about the highest sublimation rate and large Stefan flow in front of such area. The main part of the fluid velocity is directed from the source to the seed. Part of the fluid goes toward the bottom part of the graphite guide due to the Stefan flow caused by the formation of the polycrystal. The distribution of partial pressure of all the vapor species are shown in Fig. 5.22. The accumulation of the SiC species has a highest value close to the powder source. Thus the diffusive flux of SiC species is directed from the source to the seed. On the other hand, the partial pressure of argon gas shows the reverse accumulation behavior. The diffusive flux of argon is directed from the seed to the source which opposes its convective flux. This is corresponding to the boundary condition of the total zero deposited argon flux at all boundaries. The argon gas following the convective flow of the sublimed species will accumulate in front of the seed. Thus the concentration of argon in front of the seed is higher than the powder and a reversed concentration gradient is created. The highest sublimation rate is located at the lateral part and the lowest is located at the center. The back flows of the Si-rich species are also observed at the center of the source powder. This may result in the recrystallization in the powder source at its central part which may block the path ways of the sublimated species in the bulk powder below the surface. The high sublimation rate in the lateral part of the powder can lead to the fast graphitization rate since the sublimation of SiC is non-congruent.

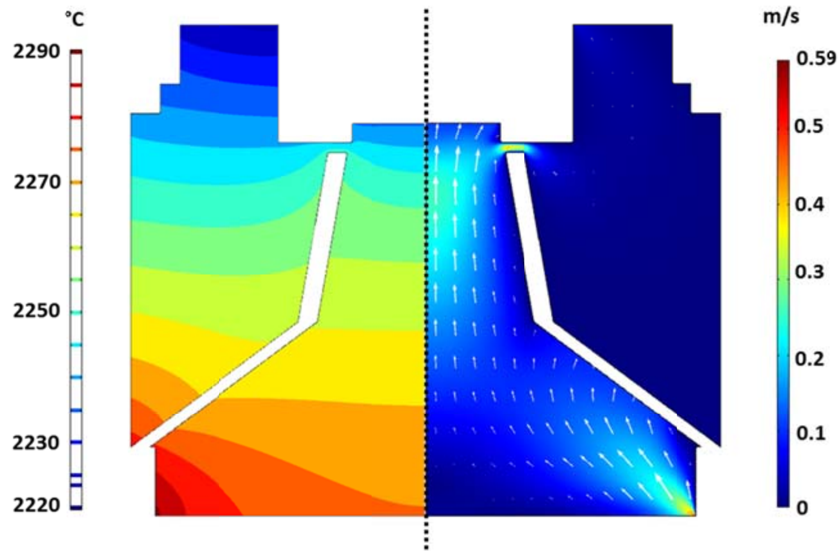

Fig. 5.21 (left) Temperature distribution and (right) velocity distribution

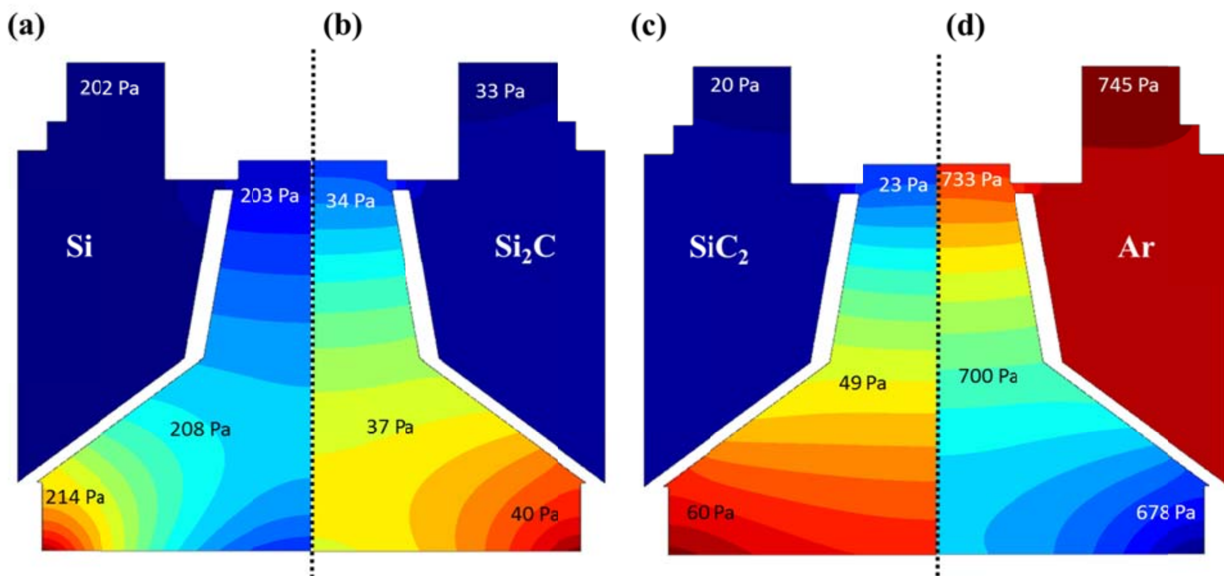

Fig. 5.22 Distribution of species partial pressure in the growth chamber: (a) Si, (b) Si_2C, (c) SiC_2, and (d) Ar

The distribution of supersaturation computed from the difference between the pressure of the limiting species (carbon) and its equilibrium partial pressure (SiC-gas) in the growth cavity is shown in Fig. 5.23a. The area where the growth of SiC takes place is characterized by the positive supersaturation. Apart from the seed area, the deposition at the bottom part of the

graphite guide is predicted. This unwanted deposition limits the growth of SiC concerning the consumption of the powder source. The deposition on the periphery of the graphite seed holder was also predicted from the model. The extra chamber created by the modification of this seed holder aims to generate another heat sink in the growth chamber. This extra heat sink having a lower temperature compared to the graphite part close to the seed helps to prevent the growth of SiC polycrystal near the SiC single crystal [53]. There is nether the deposition on the seed holder closed to the seed, nor on top part of the graphite guide. Other parts of graphite crucible surrounding the growth chamber were also free from the deposition of SiC polycrystal. These results are in good agreement with the experimental observations (Fig. 5.23b-c).

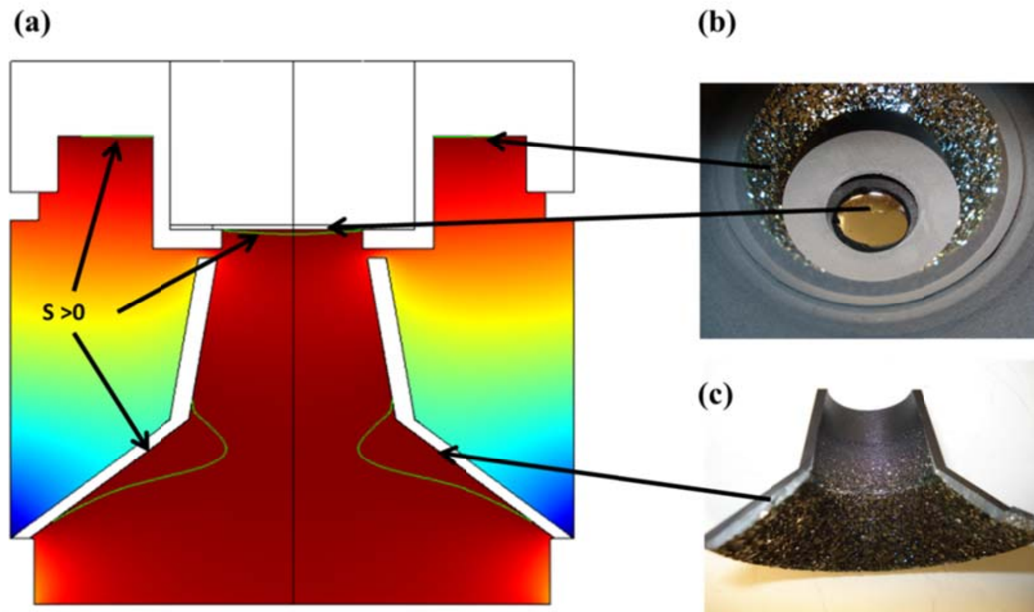

Fig. 5.23 (a) Distribution of supersaturation (S) in the growth chamber and the experimental observations (b) at the seed holder, and (c) at the graphite guide

The typical pressure dependent growth rate is shown in Fig. 5.24a. The growth rates calculated from the modeling are in good agreement with the experiments. The growth rate decreases with increasing the total pressure. As mentioned earlier, the total species flux consists of the two main components: diffusive and convective fluxes. The total growth rate can be also decomposed into both contributions which are illustrated in Fig. 5.24b. The contribution from the diffusion is always higher than the one from the convection. At high growth pressure, the total growth rate is almost similar to the growth rate computed only from the diffusion. As the

pressure decreases, the contribution from the convective becomes stronger. The shape of the growing crystal at different pressure is shown on Fig. 5.25. As the pressure increases, the crystal shape tends to be more flat. The control of the interface shape of the crystal and its evolution during the growth has been shown to be one of the important key issues for the occurrence of foreign polytype inclusions [31, 54].

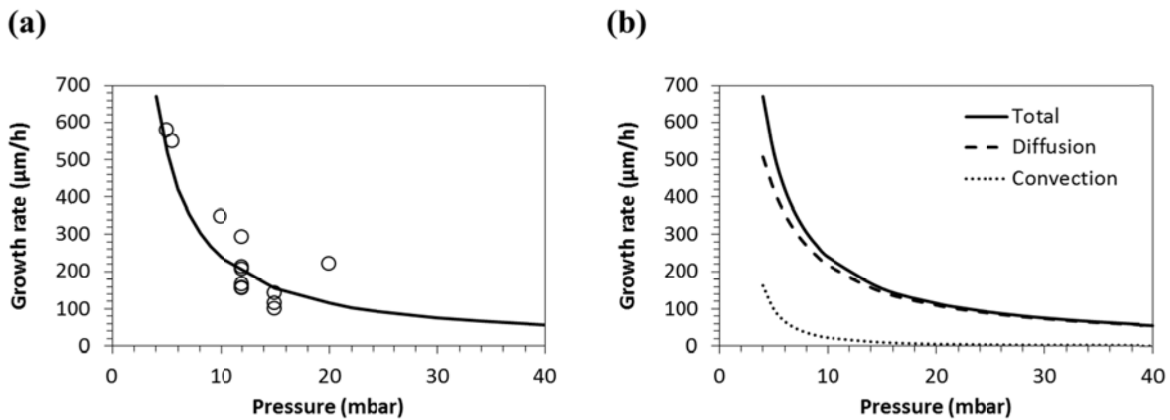

Fig. 5.24 (a) Growth rate as a function of the growth pressure compared with the experimental results and (b) contributions of diffusion and convection in the growth rate

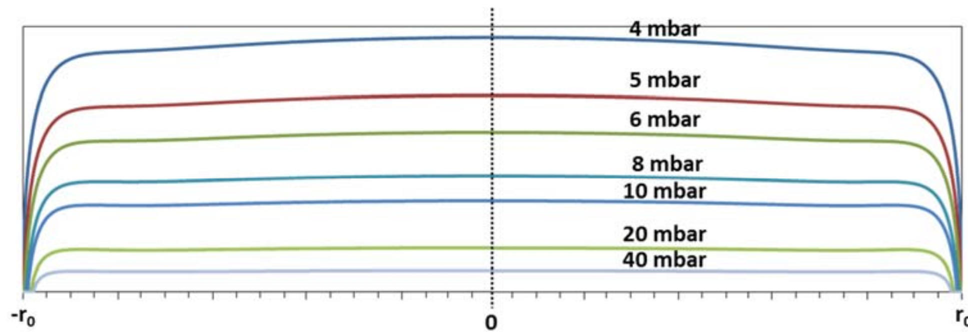

Fig. 5.25 Crystal shape for difference of growth pressures

5.8 Conclusion

The physical model and boundary conditions concerning the transport of vapor species coupled with the fluid flow have been described where special attention has been paid to the chemical reactions at the solid-vapor interfaces. The crystallization process of sublimation growth SiC leads to stoichiometric SiC even if the sublimation process is non-congruent. In the modeling of sublimation growth, the implementation of Hertz-Knudsen model at the crystal-

vapor interface results in the non-stoichiometric growth. The stoichiometric incorporation of the vapor species has been taken into account by both comparative and coupled approaches. The comparative approach requires a prior assumption that the three phase heterogeneous equilibrium exists entirely in the growth chamber. Such approach has to deal with the kinetic parameters (the sticking coefficients) since the thermodynamic degree of freedom is reduced. On the other hand, the coupled approach, treating SiC as a solid solution, requires a strong coupling with thermodynamics of the crystal growth. This model has been shown to be more comprehensive for the growth process for two main reasons. First good agreement between modeling and experiments were achieved concerning the growth/etching areas, growth rate, and interface shape of the crystal. Second, it really opens the way to have an access to the chemistry of SiC crystal. The physico-chemical parameters of the solid phase, activities of Si and C in the SiC compound, can be linked to controllable parameters: temperature and pressure. Further correlations with the observable parameters such as, point defects density, stable polytypes, and doping concentration are possible. However, this requires an extension of the model.

References

1. Pitakarnnop, J., *Rarefied gas flow in pressure and vacuum measurements.* ACTA IMEKO, 2014. **3**(2): p. 60-63.
2. Ramm, M.S., et al., *Optimization of sublimation growth of SiC bulk crystals using modeling.* Materials Science and Engineering: B, 1999. **61-62**: p. 107-112.
3. Burton, W.-K., N. Cabrera, and F. Frank, *The growth of crystals and the equilibrium structure of their surfaces.* Philosophical Transactions of the Royal Society of London. Series A, Mathematical and Physical Sciences, 1951: p. 299-358.
4. Segal, A.S., et al., *Transport phenomena in sublimation growth of SiC bulk crystals.* Materials Science and Engineering: B, 1999. **61-62**: p. 40-43.
5. Cercignani, C., *Rarefied gas dynamics: from basic concepts to actual calculations*. Vol. 21. 2000: Cambridge University Press.
6. Bond, M. and H. Struchtrup, *Mean evaporation and condensation coefficients based on energy dependent condensation probability.* Physical Review E, 2004. **70**(6).
7. Barrett, J. and C. Clement, *Kinetic evaporation and condensation rates and their coefficients.* Journal of colloid and interface science, 1992. **150**(2): p. 352-364.
8. Bogdanov, M.V., et al., *Advances in modeling of wide-bandgap bulk crystal growth.* Crystal Research and Technology, 2003. **38**(3-5): p. 237-249.
9. Gao, B., et al., *Analysis of SiC crystal sublimation growth by fully coupled compressible multi-phase flow simulation.* Journal of Crystal Growth, 2010. **312**(22): p. 3349-3355.
10. Ma, R.-H., et al., *Integrated process modeling and experimental validation of silicon carbide sublimation growth.* Journal of crystal growth, 2003. **252**(4): p. 523-537.
11. Pound, G.M., *Selected Values of Evaporation and Condensation Coefficients for Simple Substances.* Journal of Physical and Chemical Reference Data, 1972. **1**(1): p. 135-146.

12. Råback, P., et al., *A practical model for estimating the growth rate in sublimation growth of SiC.* Materials Science and Engineering: B, 1999. **61–62**(0): p. 89-92.
13. Rahimi, P. and C.A. Ward, *Kinetics of evaporation: statistical rate theory approach.* Int. J. of Thermodynamics, 2005. **8**(1): p. 1.
14. Kolasinski, K.K., *Surface science: foundations of catalysis and nanoscience*. 2012: John Wiley & Sons.
15. Drowart, J., G. De Maria, and M.G. Inghram, *Thermodynamic Study of SiC Utilizing a Mass Spectrometer.* The Journal of Chemical Physics, 1958. **29**(5): p. 1015-1021.
16. Rocabois, P., C. Chatillon, and C. Bernard, *Thermodynamics of the Si-C system I. Mass spectrometry studies of the condensed phases at high temperature.* High Temperatures. High Pressures, 1995. **27**(1): p. 3-23.
17. Rocabois, P., et al., *Thermodynamics of the Si-C system II. Mass spectrometric determination of the enthalpies of formation of molecules in the gaseous phase.* High Temperatures. High Pressures, 1995. **27**(1): p. 25-39.
18. Birnie III, D.P. and W.D. Kingery, *The limit of non-stoichiometry in silicon carbide.* Journal of materials science, 1990. **25**(6): p. 2827-2834.
19. Karpov, S.Y., Y.N. Makarov, and M. Ramm, *Analytical model of silicon carbide growth under free-molecular transport conditions.* Journal of crystal growth, 1996. **169**(3): p. 491-495.
20. Segal, A., et al., *Growth of silicon carbide by sublimation sandwich method in the atmosphere of inert gas.* Journal of crystal growth, 2000. **208**(1): p. 431-441.
21. Pisch, A., et al., *Evaporation Behavior of SiC Powder for Single Crystal Growth-An Experimental Study on Thermodynamics and Kinetics.* Materials Science Forum, 2000. **338-342**: p. 91-94.
22. Pisch, A., et al., *Coupled Thermodynamic - Mass Transfer Modeling of the SiC Boule Growth by the PVT Method.* Materials Science Forum, 2001. **353-356**: p. 61-64.
23. Chase, M.W., *NIST-JANAF thermochemical tables*. 1998.
24. Forsberg, U., et al., *Nitrogen doping of epitaxial silicon carbide.* Journal of Crystal Growth, 2002. **236**(1-3): p. 101-112.
25. Fujimoto, T., et al., *A Thermodynamic Mechanism for PVT Growth Phenomena of SiC Single Crystals.* ECS Journal of Solid State Science and Technology, 2013. **2**(8): p. N3018-N3021.
26. Lilov, S., *Study of the equilibrium processes in the gas phase during silicon carbide sublimation.* Materials Science and Engineering: B, 1993. **21**(1): p. 65-69.
27. *SGTE, S. G. T. E. 38402 Saint Martin d'Heres, France*
28. Lacaze, J. and B. Sundman, *An assessment of the Fe-C-Si system.* Metallurgical Transactions A, 1991. **22**(10): p. 2211-2223.
29. *Information on* http://www.factsage.com
30. Shiramomo, T., et al., *Thermodynamical analysis of polytype stability during PVT growth of SiC using 2D nucleation theory.* Journal of Crystal Growth, 2012. **352**(1): p. 177-180.
31. Kakimoto, K., et al., *Thermodynamic analysis of SiC polytype growth by physical vapor transport method.* Journal of Crystal Growth, 2011. **324**(1): p. 78-81.
32. Caputa, J.P. and H. Struchtrup, *Interface model for non-equilibrium evaporation.* Physica A: Statistical Mechanics and its Applications, 2011. **390**(1): p. 31-42.
33. Tsuruta, T., *A microscopic formulation of condensation coefficient and interface transport phenomena.* Energy, 2005. **30**(6): p. 795-805.
34. Honstein, G., C. Chatillon, and F. Baillet, *Thermodynamic approach to the vaporization and growth phenomena of SiC ceramics. I. SiC and SiC–SiO< sub> 2</sub> mixtures under neutral conditions.* Journal of the European Ceramic Society, 2012. **32**(5): p. 1117-1135.
35. Garshin, A.P., E.N. Mokhov, and V.E. Shvaiko-Shvaikovskii, *A Theoretical Analysis of the Formation of Nonstoichiometric Point Defects in SiC Single Crystals Grown under Equilibrium*

Conditions at Different Partial Pressures of Silicon Vapor. Refractories and Industrial Ceramics, 2003. **44**(4): p. 199-204.
36. Starke, U., et al., *Stacking Transformation from Hexagonal to Cubic SiC Induced by Surface Reconstruction: A Seed for Heterostructure Growth.* Physical Review Letters, 1999. **82**(10): p. 2107-2110.
37. Dompoint, D., et al., *Kinetics of the 3C-6H polytypic transition in 3C-SiC single crystals: A diffuse X-ray scattering study.* Journal of Applied Physics, 2011. **110**(5): p. 053508.
38. Semmelroth, K., et al., *Growth of cubic SiC single crystals by the physical vapor transport technique.* Journal of Crystal Growth, 2007. **308**(2): p. 241-246.
39. Furukawa, K., et al., *Bulk Growth of Single-Crystal Cubic Silicon Carbide by Vacuum Sublimation Method.* Japanese Journal of Applied Physics, 1993. **32**(Part 2, No. 5A): p. L645-L647.
40. Lebedev, A.A. and S.Y. Davydov, *A vacancy model of the heteropolytype epitaxy of SiC.* Semiconductors, 2005. **39**(3): p. 277-280.
41. Lebedev, A.A., *Influence of native defects on polytypism in SiC.* Semiconductors, 1999. **33**(7): p. 707-709.
42. Lauga, E. and T.M. Squires, *Brownian motion near a partial-slip boundary: A local probe of the no-slip condition.* Physics of Fluids, 2005. **17**(10): p. 103102.
43. Freer, R., ed. *The Physics and Chemistry of carbides, Nitrides and Borides. Volume 185*. Applied Sciences. Vol. 185. 1990, DTIC Document.
44. Davis, S.G., D.F. Anthrop, and A.W. Searcy, *Vapor Pressure of Silicon and the Dissociation Pressure of Silicon Carbide.* The Journal of Chemical Physics, 1961. **34**(2): p. 659.
45. Kimoto, T., A. Itoh, and H. Matsunami, *Incorporation mechanism of N, Al, and B impurities in chemical vapor deposition of SiC.* Applied Physics Letters, 1995. **67**(16): p. 2385.
46. Larkin, D.J., et al., *Site-competition epitaxy for superior silicon carbide electronics.* Applied Physics Letters, 1994. **65**(13): p. 1659-1661.
47. Karpov, S.Y., et al., *Analysis of sublimation growth of bulk SiC crystals in tantalum container.* Journal of Crystal Growth, 2000. **211**(1–4): p. 347-351.
48. Tsavdaris, N., et al., *Interface Shape: A Possible Cause of Polytypes Destabilization during Seeded Sublimation Growth of 15R-SiC.* Materials Science Forum, 2014. **806**: p. 61-64.
49. Herro, Z.G., et al., *Investigation of mass transport during PVT growth of SiC by 13C labeling of source material.* Journal of Crystal Growth, 2003. **258**(3-4): p. 261-267.
50. Liu, J., et al., *Effects of Source Materials and Container on Growth Process of SiC Crystal.* Crystal Growth & Design, 2006. **6**(9): p. 2166-2168.
51. Selder, M., et al., *Global numerical simulation of heat and mass transfer for SiC bulk crystal growth by PVT.* Journal of Crystal Growth, 2000. **211**(1–4): p. 333-338.
52. Liu, J., et al., *Effects of graphitization degree of crucible on SiC single crystal growth process.* Diamond and related materials, 2006. **15**(1): p. 117-120.
53. Pons, M., et al., *State of the art in the modelling of SiC sublimation growth.* Materials Science and Engineering: B, 1999. **61-62**: p. 18-28.
54. Tsavdaris, N., et al., *Effect of Facet Occurrence on Polytype Destabilization during Bulk Crystal Growth of SiC by Seeded Sublimation.* Materials Science Forum, 2014. **778-780**: p. 13-16.

Chapter 6
Top Seeded Solution Growth

So far, we have been focused on the process modeling of SiC growth from the vapor phase. In this chapter, growth from liquid phase will be considered as we will discuss the modeling of the Top Seeded Solution Growth (TSSG) process. Physical model and boundary conditions will be discussed first. Then the modeling results concerning the effects of the process parameters including crystal rotation speed and operating frequency will be given. Finally, we will present the combined numerical and analytical modeling to describe the interaction between fluid flow and the step flow at the growth front and its validation.

6.1 Physical model and boundary conditions for induction heating and fluid dynamics

The typical configuration of the TSSG reactor is shown in Fig. 6.1. Pure liquid silicon used as a solvent is placed in the high density graphite crucible. Similar to the PVT process described in the 4th chapter, the induction heating is employed as a method to heat the graphite crucible. Almost all the sets of equation and the numerical procedure are the same. However, there are two main differences in the TSSG model. First, we assume the incompressible flow of fluid in order to save the computational cost. The fluid density is now constant so the continuity equation (5.5) becomes

$$\rho \nabla \cdot \mathbf{v} = 0 . \qquad (6.1)$$

The divergence of the fluid velocity vanishes, so the momentum conservation equation (5.3) for the steady state calculation becomes

$$\rho(\mathbf{v} \cdot \nabla)\mathbf{v} = \nabla \cdot \left(-p\mathbf{I} + \bar{\tau}\right) + \mathbf{F} = \nabla \cdot \left(-p\mathbf{I} + \mu\left(\nabla \mathbf{v} + (\nabla \mathbf{v})^T\right)\right) + \mathbf{F} . \qquad (6.2)$$

Second, the induction heating and the fluid dynamics are coupled in this model. The fluid flows computed from the Navier-Stokes equation (6.2) will be coupled with the governing stationary

state equation for thermal energy (4.21) in the convective heat transfer term. The coupled heat transfer and fluid dynamics modeling of high-temperature SiC growth from solution was presented [1] with aim to study different convective flows. In fact, understanding the carbon transport from the source, i.e. the graphite crucible to the crystal is a key issue for the further development of a bulk SiC solution growth process. It will become more and more critical as we will address the growth of large size, high quality crystal at high temperature. Practically, carbon distribution and transport in liquid will directly affect:

i.) The control of nucleation and growth front stability
ii.) The prevention of parasitic deposition
iii.) The prevention of dendritic growth after nucleation
iv.) The increase of the growth rate.

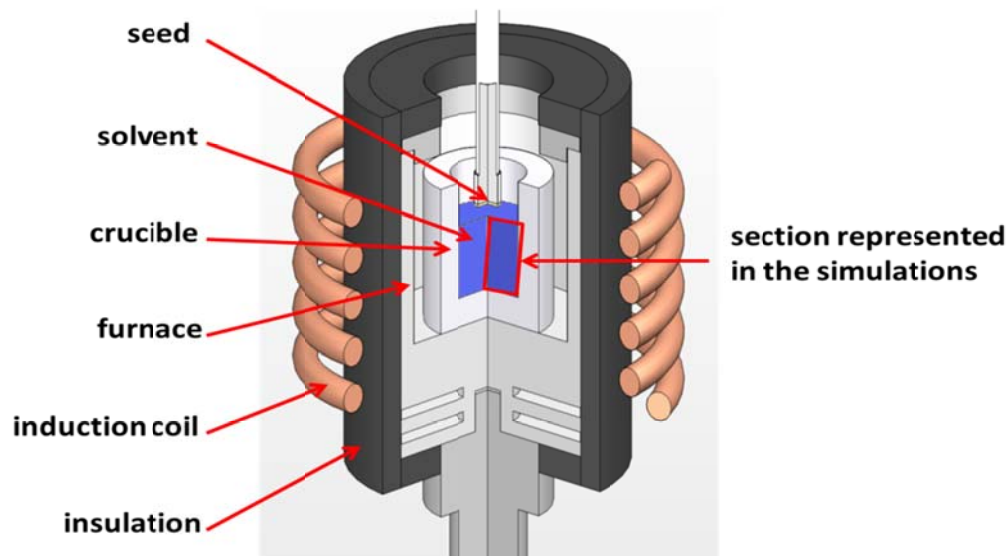

Fig. 6.1 Schematic representation of the TSSG setup. The red parallelepiped is the liquid cross section for the representation of the modeling results shown later in this chapter

The accelerated crucible rotation technique (ACRT) has been proposed to solve such problems (i-iii) by enhancing the solute transport, which gives rise to a better homogeneity [2]. Moreover, ACRT has already proven its ability to increase the growth rate during SiC solution growth but its role is not trivial [3]. Actually, the fluid flow pattern is far from being controlled. In case of

pure silicon, the carbon solubility is always very small below 2000°C [4]. Thus the solutal contributions to the convection can be neglected and the convective flow pattern is governed by "only" four main contributions (Fig. 6.2): the buoyancy convection, the forced convection, the Marangoni convection, the electromagnetic convection [1].

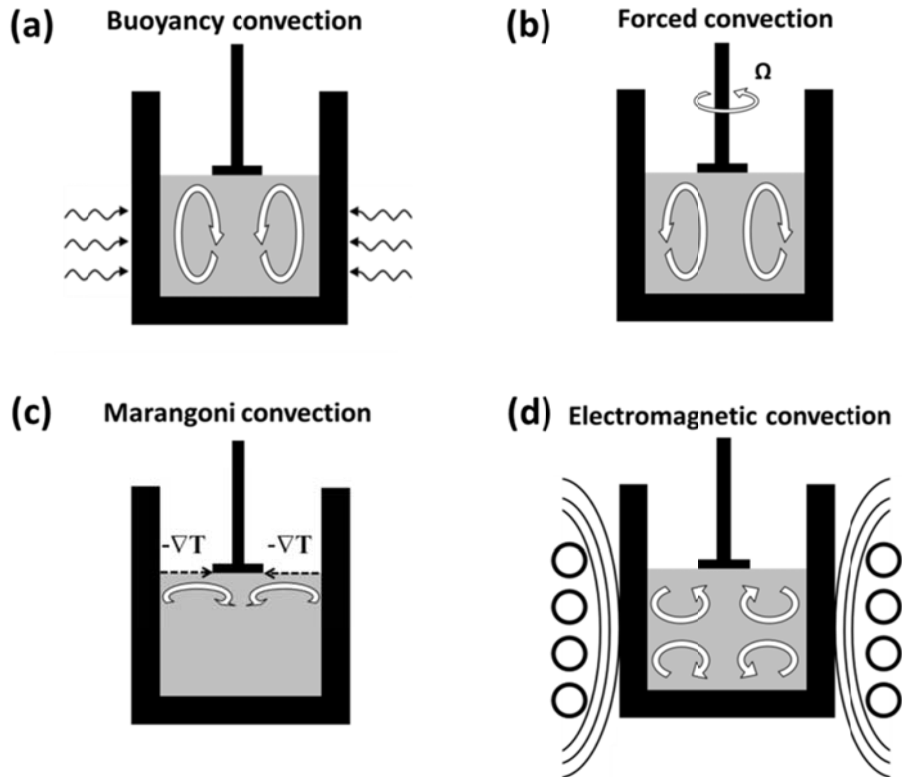

Fig. 6.2 The four main contributions governing the convective flow pattern: (a) buoyancy convection, (b) Forced convection, (c) Marangoni convection, and (d) electromagnetic convection

6.1.1 Buoyancy convection

The presence of temperature gradient in liquid leads to the density variation which is the cause of the buoyancy convection. Thus the Boussinesq approximation has to be used to take into account the buoyancy flow when using the incompressible flow model. Such approximation states that the density differences are adequately small except in the terms that multiply by the acceleration due to gravity. Accordingly, the density is a constant value in all the equations

solved in the model except for the buoyancy term in the momentum equation: the volume force term **F** in (6.2). The volume force concerning the buoyancy force can be written

$$\mathbf{F} = \mathbf{F}_{\text{buo}} = \Delta\rho\mathbf{g} = -\beta\rho_0(T - T_0)\mathbf{g}\,. \tag{6.3}$$

The Boussinesq approximation is accurate when $\beta(T - T_0) << 1$. This is the case for the TSSG process for the growth of SiC. If the crucible is heated from the side wall, the fluid will flow up along the side wall and the convection pattern caused by the buoyancy force will be similar to Fig. 6.2a. On the other hand, the fluid will flow up at the center of liquid if the crucible is heated from the bottom and the flow directions will be reversed compared to Fig. 6.2a. The intensity of the buoyancy convection can be estimated from one of the dimensionless numbers, the Rayleigh number computed from the product of the Grashof number and the Prandtl number. The Grashof number is the ratio of the buoyancy to the viscous forces:

$$Gr = \frac{g\beta\Delta TL^3}{\nu^2} = \frac{g\beta\rho^2\Delta TL^3}{\mu^2}\,. \tag{6.4}$$

The Prandtl number is the ratio of momentum diffusivity to the thermal diffusivity defined as

$$\mathrm{Pr} = \frac{\nu}{\kappa} = \frac{C_p\mu}{k}\,. \tag{6.5}$$

Thus, the Rayleigh number can be written

$$Ra = Gr \cdot \mathrm{Pr} = \frac{g\beta\Delta TL^3}{\nu\kappa} = \frac{g\beta\rho^2\Delta TL^3 C_p}{\mu k}\,. \tag{6.6}$$

Two critical values (Ra_{c1}, Ra_{c2}) of the Rayleigh number can be used to characterize the stability of the flow. The transition from no flow to steady flow occurs at Ra_{c1}=1708 [5]. The transition from steady flow to the unsteady and time-dependent flow occur at Ra_{c2}=40000 [6]. From (6.6), it can be seen that the buoyancy convection can be controlled by the liquid height and the axial temperature gradient.

6.1.2 Forced convection

The rotation of either seed or crucible directly induces the fluid movement in the azimuthal direction. The force convection caused by the crystal rotation is implemented via the boundary condition for the azimuthal fluid velocity at the seed-liquid interface:

$$v_\phi = \Omega_{seed} r . \quad (6.7)$$

The steady state liquid motion in a rotating liquid is two-dimensional with respect to the coordinate axis rotating with liquid [7]. The appearance of such two-dimensional flow to an observer staying in a stationary frame with respect to the rotating fluid is a set of spiral streamlines rising or falling with a common axis of a symmetry axis of the rotation. In a two-dimensional axisymmetric configuration used in the simulations, the flow in the azimuthal direction (out-of-plane) is uncoupled with the radial and axial directions (in-plane) so such spiral movement cannot be observed. However, the flow in the rz-plane induced by the azimuthal flow is still correctly described. To exemplify, the crystal acts as a centrifugal fan drawing in the fluid axially, transmit angular momentum to it in the boundary layer and then expelling it tangentially [8]. Such mechanism causes the flow pattern shown in Fig. 6.2b where the back flow is caused by the presence of the crucible wall. In this case, the Reynolds number defined as a ratio of inertial force to viscous,

$$\mathrm{Re} = \frac{v_{stir} L}{\nu}, \quad (6.8)$$

can be used to describe the stability of the flow. For a flow in a pipe of diameter d, the laminar flow occurs when $\mathrm{Re}_d < 2000$ while the turbulent flow occurs when $\mathrm{Re}_d > 4000$ [9]. In between those two critical values, a transition flow where both laminar and turbulent flows are possible depending on other factors such as the smoothness of the flow. The forced convection can be controlled by adjusting the rotation speed and the radius of the seed (or crucible).

6.1.3 Marangoni convection

The Marangoni convection appears when the surface tension of the interface, in this case the liquid-gas interface, is dependent on the temperature such as

$$\gamma(T) = \gamma_0 + \chi(T - T_0). \quad (6.9)$$

where χ is the Marangoni coefficient describing temperature derivative of the surface tension. The governing equation describing the Marangoni effect at the interface is written by

$$\mathbf{n}\cdot\bar{\tau}\cdot\mathbf{s}=\frac{\partial\gamma}{\partial s}=\chi\frac{\partial T}{\partial s}, \tag{6.10}$$

where $\mathbf{s}$ is the tangential vector along the interface. Such equation specifies that the shear stress on the surface is proportional to the temperature gradient on such surface. The shear force in the plane tangential to the interface can be written as

$$\mathbf{n}\cdot\bar{\tau}\cdot\mathbf{s}=\begin{bmatrix}1 & 0\end{bmatrix}\begin{bmatrix} 2\mu\dfrac{\partial \mathrm{v}_n}{\partial s} & \mu\left(\dfrac{\partial \mathrm{v}_n}{\partial s}+\dfrac{\partial \mathrm{v}_s}{\partial n}\right)\\ \mu\left(\dfrac{\partial \mathrm{v}_n}{\partial s}+\dfrac{\partial \mathrm{v}_s}{\partial n}\right) & 2\mu\dfrac{\partial \mathrm{v}_s}{\partial n}\end{bmatrix}\begin{bmatrix}0\\1\end{bmatrix}=\mu\left(\frac{\partial \mathrm{v}_n}{\partial s}+\frac{\partial \mathrm{v}_s}{\partial n}\right). \tag{6.11}$$

If the free surface does not deform, $\mathrm{v}_n=0$. From (6.10) and (6.11), we obtain the relation

$$\chi\frac{\partial T}{\partial s}=\mu\frac{\partial \mathrm{v}_s}{\partial \mathrm{n}}. \tag{6.12}$$

We are taking into account the Marangoni force via a set of boundary conditions expressing the balancing of the temperature gradient on the surface with the shear stress (6.12). Such boundary condition is implemented by a weak form finite element formulation. The weak contribution

$$\int_\Gamma \phi\chi\left(\frac{\partial T}{\partial s}\right)d\Gamma-\int_\Gamma \phi\mu\left(\frac{\partial \mathrm{v}_s}{\partial n}\right)d\Gamma=0 \tag{6.13}$$

replaces the condition on the tangential component of fluid velocity from the Slip boundary condition where ϕ is the test function for the tangential component of fluid velocity at the surface. On the liquid surface, if the temperature is higher at the crucible-liquid interface compared to the area near the seed crystal, the Marangoni force will cause the movement of fluid from the crucible wall toward the seed. The Marangoni convection for such case is shown in Fig. 6.2c. In order to determine the intensity of the flow affected by the Marangoni force, the Reynolds-Marangoni number can be used:

$$\mathrm{Re}_M=\frac{-\chi\Delta TL}{\rho\nu^2}. \tag{6.14}$$

This is in relation with the Reynolds number [10] such that

$$\mathrm{Re} = 1.2\,\mathrm{Re}_M^{2/3}. \tag{6.15}$$

The Marangoni convection is quite difficult to control. Even though, a special type of crucible configuration was implemented in the numerical modeling study with aim to minimize such effect on the SiC crystal growth [1].

6.1.4 Electromagnetic convection

Electromagnetic stirring is normally the side effect of the heating used in experiments. The movement of charges in the magnetic field induces the Lorentz force. This is the case for our growth system in which the magnetic field and the current flow in liquid are presented due to the induction heating. In such case, the volume force computed from the time-averaged Lorentz force can be written

$$\mathbf{F}_{EM} = \frac{1}{2} real\left(\mathbf{J} \times \mathbf{B}^*\right). \tag{6.16}$$

It is possible to estimate the effect of electromagnetic force on the fluid velocity [11] from the screen parameter

$$R_w = \mu_0 2\pi f \sigma_{liquid} L^2, \tag{6.17}$$

and the Alfven velocity,

$$U_A = B_{\max}\left(\mu_0 \rho\right)^{-1/2}. \tag{6.18}$$

The average velocity in bulk liquid can be computed from

$$U = 0.6 U_A R_w^{-1/4}. \tag{6.19}$$

In general, electromagnetic force density is highest at the area close to the crucible wall due to the skin effect. Thus, the fluid velocity should be much higher near the crucible wall. An example of the fluid convection caused by the electromagnetic force is shown in Fig. 6.2d. The electromagnetic convection is in many cases undesirable since it is difficult to control.

6.2 Physical model and boundary conditions for mass transfer

In contrast to the PVT modeling, the electromagnetic computation is coupled with the fluid dynamics. Indeed the electromagnetic, heat transfer, and fluid dynamics are coupled in the TSSG model while the modeling of mass transfer will be computed using the results from such coupled calculations. This is possible since both solutal Marangoni and solutal buoyancy convection can be neglected in this study as mentioned in 6.1. Moreover, the transport of diluted species is considered in this model. The governing equation describing the carbon transport is the steady state convection-diffusion equation written by

$$-D\nabla^2 C + \mathbf{u}\cdot\nabla C = 0\,. \tag{6.20}$$

In the growth of SiC using the TSSG process, the crucible is not only a container but also the carbon source, meaning thus that the crucible-liquid interface does not only induce mechanical stirring but is also the place of a complex reaction/dissolution of solute. The equilibrium concentration of carbon is imposed on both crucible-liquid and crystal-liquid interfaces

$$C_{eq} = \frac{\rho_{Si}}{M_{Si}}\frac{x_{Ceq}}{1-x_{Ceq}}\,, \tag{6.21}$$

where x_{Ceq} is the mole fraction of carbon. Similar to the PVT process, the dissolution and crystallization areas can be evidenced by the supersatuation defined from the deviation of the concentration from equilibrium

$$S = C - C_{eq}\,. \tag{6.22}$$

The crystallization takes place when $S > 0$, while the dissolution takes place when $S < 0$. The incorporation of solute in the solid crystal should depend also on the interface velocity. However, if the supersaturation is very small and the growth rate is low, it is reasonable to assume a thermodynamic quasi-equilibrium at the solid-liquid interface. The growth rate can be computed form the diffusive flux of carbon atom normal to the seed surface:

$$R_g = \frac{M_{SiC}}{\rho_{SiC}}\left(-D\nabla C\cdot\mathbf{n}\right). \tag{6.23}$$

The growth rates evaluated using this method has shown a pretty good agreement with the experiments [12].

6.3 Modeling results and the effect of process parameters

Concerning the modeling of induction heating in the TSSG process, distributions of both in-phase and out-of-phase magnetic fluxes (vector potentials multiply by radius) in Wb are shown in Fig. 6.3. The maximum Joule losses density is located close to the top part of the furnace. This is corresponding to location of the highest out-of-phase magnetic flux caused by the induced current. The out-of-phase magnetic fluxes in liquid dissipate mainly close to the liquid-crucible interface. These contribute to the Lorentz force which is one of the four main contributions to the convection pattern in liquid. As mentioned in 6.1, the control of fluid flow and carbon transport in liquid will directly affect the stability of the growth. In this section, the numerical modeling will be used as a tool to monitor such fluid flow and mass transport behaviors with respect to the variation of the process parameters. Simulation using a specific set of growth conditions in a fixed geometry will be used as a reference to compare with the results obtained when varying the growth parameters. These reference conditions include:

1. no crystal rotation
2. 14 kHz coil frequency
3. 1700 °C growth temperature at the seed

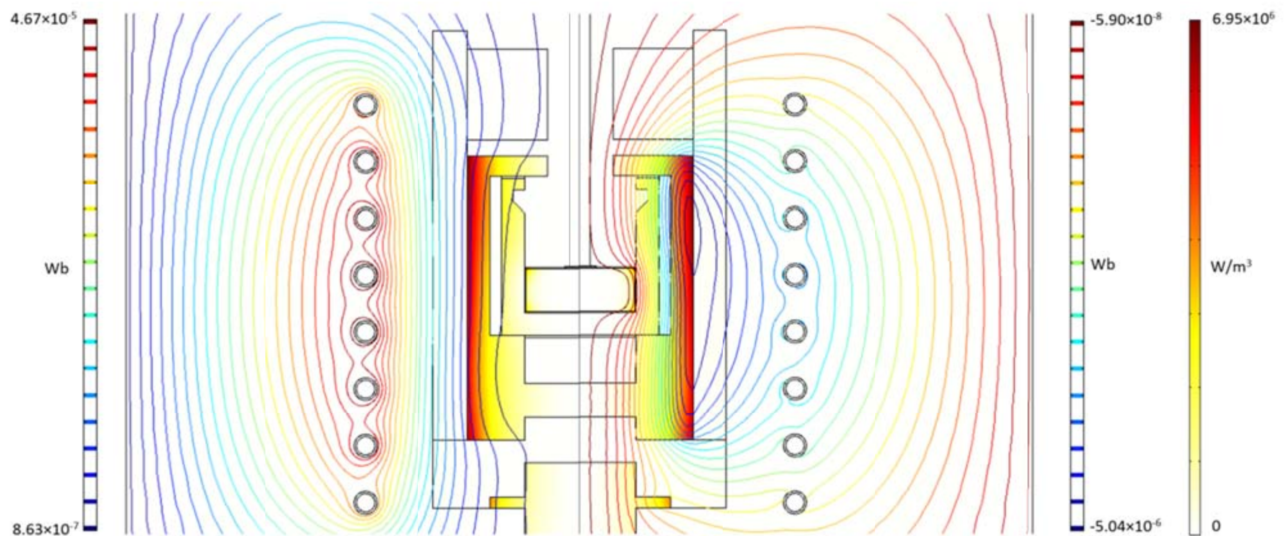

Fig. 6.3 Schematic representation of (left) in-phase and (right) out-of-phase magnetic flux contours with the Joule losses density shown in the continuous color scale

The typical accessible parameters in liquid using the numerical modeling with such reference growth conditions are shown in Fig. 6.4. Temperature distribution in liquid shows the location of the hot point at the bottom corner of the crucible while the cold point locates at the crystal (Fig. 6.4a). The axial temperature difference is around 4˚C corresponding to an axial temperature gradient of 2˚C/cm. The combined convective flows result in the complex flow pattern (Fig. 6.4b). The direct flow from the bottom of the crucible toward the seed along the symmetry axis and the highly turbulence flow near the crucible wall are observed. The distribution of carbon concentration is directly associated with the convection pattern. High carbon concentration is observed close to the symmetry axis (Fig. 6.4c). The supersaturation in liquid silicon is shown in Fig. 6.4d. Carbon dissolve from the graphite crucible in the undersaturated area ($S<0$), transport by diffusion and convection, and crystalize in the supersaturated area ($S>0$), i.e. at the seed.

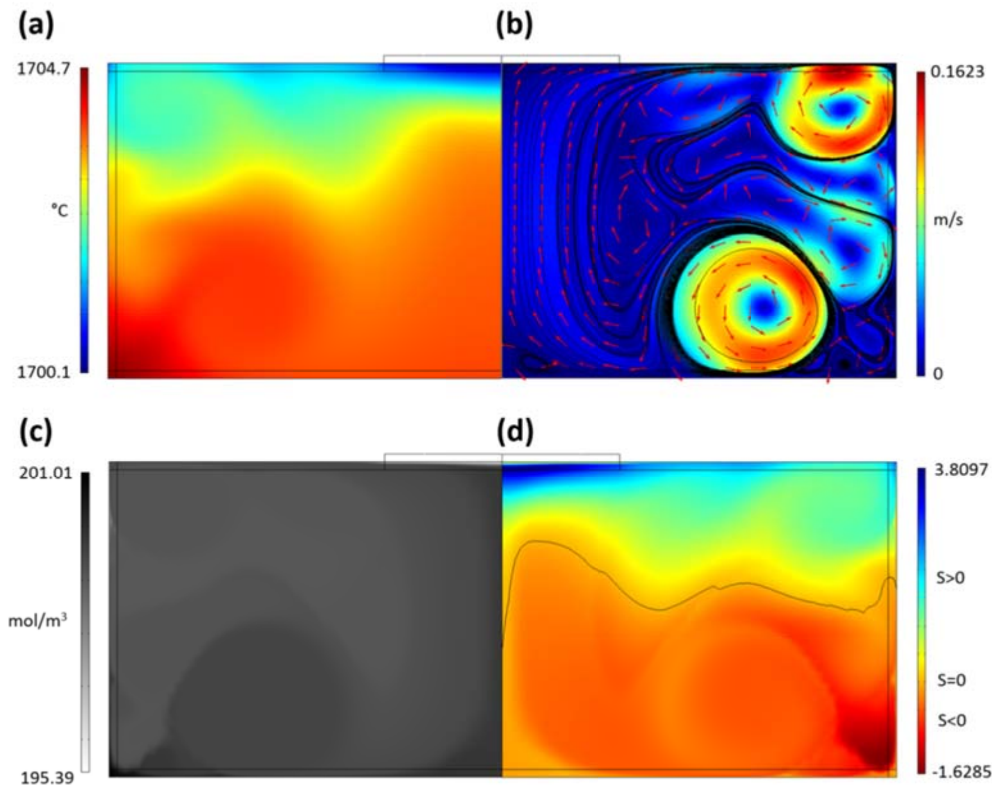

Fig. 6.4 Simulation results for (a) temperature, (b) fluid velocity, (c) carbon concentration, and (d) supersaturation in liquid. In (b), red arrows indicate the normalized fluid velocity vectors and the black solid lines represent the velocity streamlines. The black line (S=0) in (d) is drawn to separate the supersaturated and undersaturated areas

The fluid flow pattern was shown to be very complex (Fig. 6.4b), thus it is interesting to investigate the origin of such pattern. In order to do this, two approaches will be discussed. For the first approach, an analysis of dimensionless number is performed. The calculation results are shown in Table 6.1. The calculated Rayleigh number indicates that the axial temperature gradient results in a steady flow. This suggests also that the effect of the buoyancy flow in our system is quite small and should not be a cause of such turbulence. The Reynolds number computed from the Reynolds-Marangoni number suggests that the flow is only at the lower limit of the transition flow. The Marangoni effect should be dominant at the liquid surface but the flow along the liquid surface does not even follow the Marangoni convection. The Reynolds number computed from the average velocity and Alfven velocity predicts the stronger transition flow. Due to the fact that such computation is making use of the average velocity in the bulk liquid and the effect of electromagnetic force decreases with the distance from the wall, the fluid velocity above such average value can be expected near the wall. As a consequent, the turbulent flow caused by the electromagnetic convection should appear locally close to the side wall [1].

Table 6.1 Dimensionless number analysis

Dimensionless number	Symbol	Value
Grashof	Gr	$4.46e^{-5}$
Prandtl	Pr	$1.47e^{-2}$
Rayleight	Ra	$6.58e^{3}$
Reynolds (computed from 20 rpm crystal rotation)	Re	$2.00e^{3}$
Reynolds (computed from Reynolds-Marangoni number)	Re	$2.22e^{3}$
Reynolds (computed from Alfven velocity)	Re	$2.28e^{3}$

The second approach is done using the numerical modeling itself. As suggested by the dimensionless analysis, the electromagnetic convection seems to be the main contribution to the resulting flow pattern. Thus, we are performing the two separated studies: the flow pattern caused by the combination of buoyancy and Marangoni convection and the flow pattern caused by the EM convection. The calculated temperature profiles and the flow patterns are shown in Fig. 6.5. With the combined buoyancy and Marangoni convections, the upstream flow along the crucible wall and downstream flow along the symmetry axis are predicted with a small vortex of

the flow on top of liquid next to the side wall (Fig. 6.5a). This is in agreement with Fig. 6.2a-b since the crucible is mainly heat from the side wall and the hottest point on the liquid surface does not locate exactly at the side wall. In case of purely electromagnetic force, a strong turbulent with many vortexes is observed close to the side wall, while the upward flow is observed at the symmetry axis (Fig. 6.5b). Such observed flow pattern is very similar the pattern occurring when all of the contributions are taken into account. Thus, the electromagnetic convection is the main contribution for our growth process which is in agreement with the dimensionless analysis discussed earlier. Another important feature worth noticing is the fact that the temperature profiles clearly follow the convection pattern. This suggests that the heat transfer by momentum is more efficient than the diffusion. In order to confirm this, we can compute the Peclet number representing the ratio of the rate of convection to the rate of diffusion

$$Pe = \mathrm{Re} \cdot \mathrm{Pr} = \frac{\rho \mathrm{v} \mathrm{L} C_p}{k}. \tag{6.24}$$

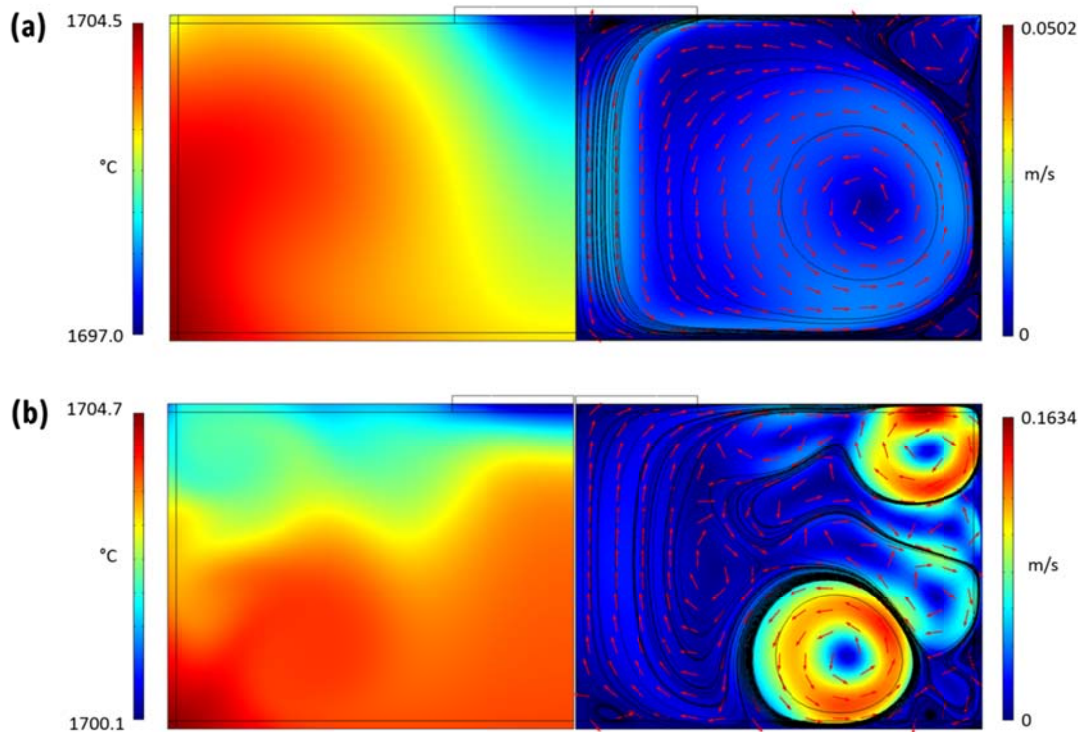

Fig. 6.5 (left-hand side) Temperature and (right-hand side) velocity profiles when taking into account (a) a combination of buoyancy and Marangoni convections and (b) only an electromagnetic convection

Using the average velocity of liquid (v=0.04 m/s), we obtain *Pe* = 36 meaning that the heat transfer by convection (momentum) dominates the heat transfer process in liquid (*Pe* >> 1). In Fig. 6.5, the fluid velocity is higher in the presence of the Lorentz force. The electromagnetic convection increases the heat transfer rate and decreases the temperature gradient in liquid. As a result, the temperature at the seed is lower than the case of the combined buoyancy and Marangoni convection, while the temperature at the hot point (the bottom corner of the crucible) is almost constant.

For further investigation, distribution of Lorentz force density in liquid Si is shown in Fig. 6.6. The force is concentrated near to the crucible wall due to the skin effect. The maximum value of the Lorentz force is located on top of liquid. This corresponds to the maximum out-of-phase magnetic flux located at the furnace above the liquid surface (Fig. 6.3). Close to the crucible wall, the Lorentz force acting on the upper part of liquid pushes down while the one acting at the bottom part pushes up the liquid. Such concentrated and non-uniform distribution of Lorentz force density should be responsible for the strong turbulence near the crucible wall. It is important to note also that both buoyancy and Marangoni convections computed without the EM force is over estimated. In fact, their intensities should become smaller when the electromagnetic force is taken into account since the temperature gradient is smaller (Fig. 6.5) due to the heat mixing.

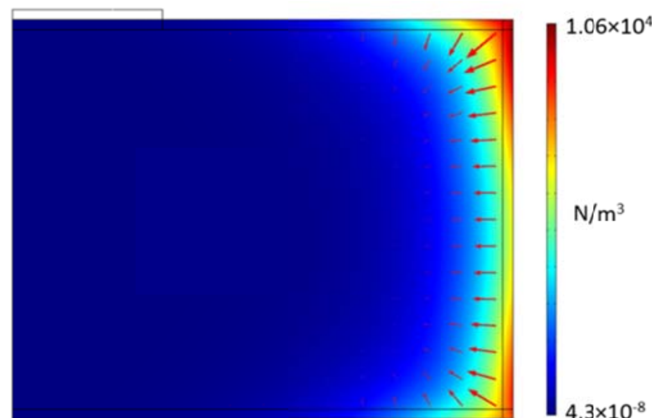

Fig. 6.6 Distribution of Lorentz force density in liquid

6.3.1 Effect of crystal rotation

First of all, the effect of only forced convection caused by the seed rotation is studied. As shown in Fig. 6.7, the fluid velocity increases when increasing rpm. The convection pattern is similar to 6.2b for small rotation speed (20 - 40 rpm). In such cases, a large vortex of fluid flow where the flow is upward at the symmetry axis and downward at the side wall is observed. This is comparable to the case when the Taylor-Proudman cell boundary expands to the fill the crucible, thus the stagnation surface preventing the complete bulk liquid mixing vanishes [7]. However at high rotation speed (100 - 200 rpm), an open stagnant surface occurs close to the symmetry axis. In such cases, the Reynolds numbers are 10000 and 20000, respectively. Those are far exceeding the critical value for the turbulent flow. Possibly the seed rotation itself can induce the turbulent flow in liquid if the rpm is too high.

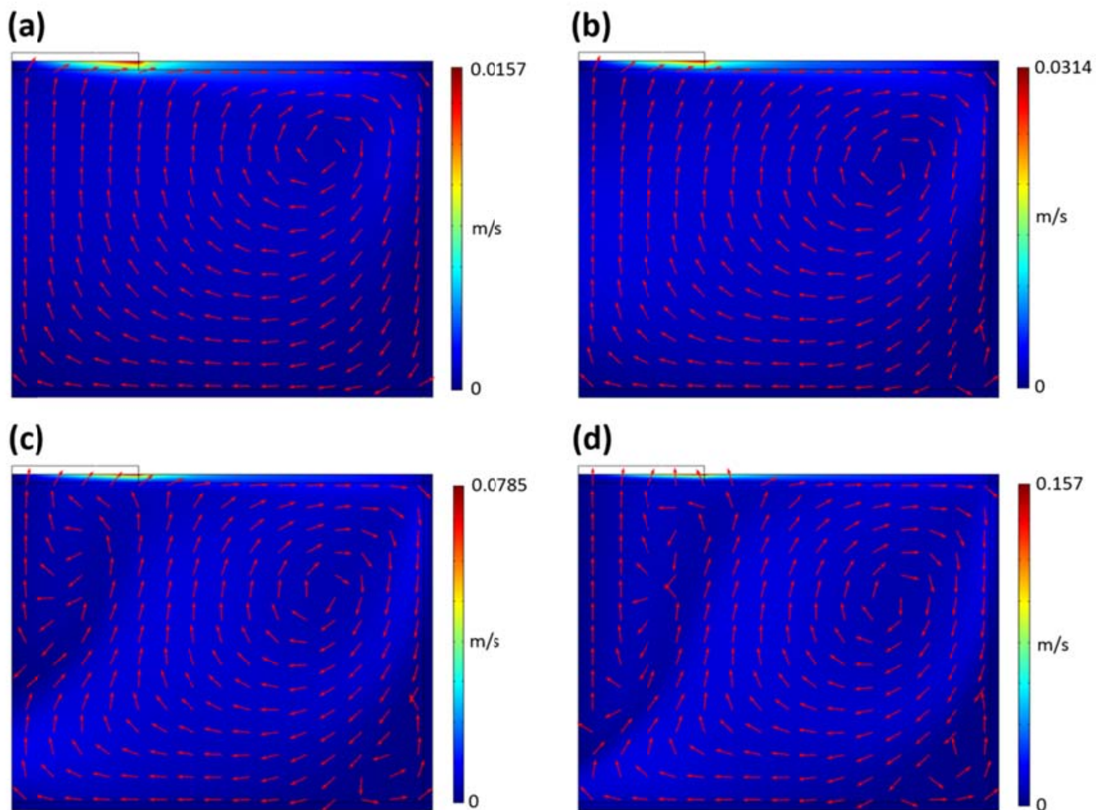

Fig. 6.7 Velocity field in liquid when taking into account only forced convection caused by crystal rotation at (a) 20 rpm, (b) 40 rpm, (c) 100 rpm, and (d) 200 rpm

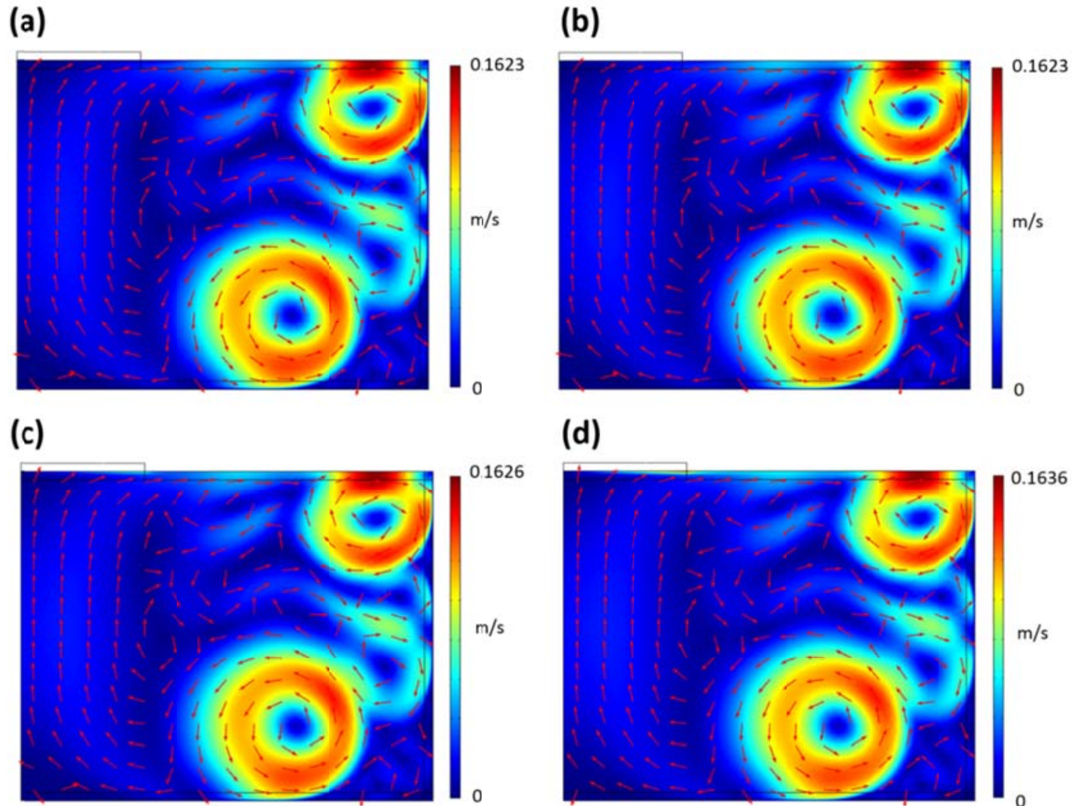

Fig. 6.8 Velocity field in liquid when taking into account all the contributions presented liquid in the case of seed rotation at (a) 20 rpm, (b) 40 rpm, (c) 100 rpm, and (d) 200 rpm

By taking into account other contributions presented in liquid, the strong turbulence is observed. The effects of the crystal rotation even at high rotation speed in the flow pattern near the side wall are suppressed (Fig. 6.8). However, the magnitude of fluid velocity just below the seed increases if rpm increases. All components of fluid velocity in front of the seed crystal (0.1mm below the seed) increase with the rotation speed (Fig. 6.9). The azimuthal component of fluid velocity v_ϕ very close to the crystal follows relation (6.7). At high rpm, v_ϕ is the main contribution to the velocity magnitude close to the rotating crystal, while it is v_r at low rpm. The axial component v_z is one of the key parameters governing the mass transport in the axial direction. The increase in the axial component of the fluid velocity when increasing the rotation speed will enhance the transport rate of carbon in liquid toward the crystal surface, thus the growth rate is expected to increase.

The distributions of carbon concentration along the symmetry axis are plotted in Fig. 6.10. The full scale plot shows similar distribution of carbon concentration profiles in liquid for

different rpm (Fig. 6.10a). The negative and positive concentration gradients normal to the crystal and the crucible surfaces indicate the growth and dissolution, respectively. Close to the seed surface, the concentration gradient increases as the rpm increases (Fig. 6.10b). Thus the growth rate should be increasing following such trend. In fact, the axial concentration gradient varies along the seed. The growth rates plotted along the seed radius using various rpm are shown in Fig. 6.11a. The growth rates at the center of the seed plotted as a function of rpm is compared with the experimental results using the same growth conditions (Fig. 6.11b). Good agreement between experiments and calculations can be obtained below 200 rpm. At 200 rpm, the calculation of growth rate deviates from the experimental value. This may be caused by the fact that the flow at such high rpm is actually in the turbulent regime since the Reynolds number (20000) is far exceeding the critical value (4000) for the transition from the transition flow to the turbulent flow. Thus, the behavior of the flow should be treated by transient model and/or the three-dimensional model for better accuracy.

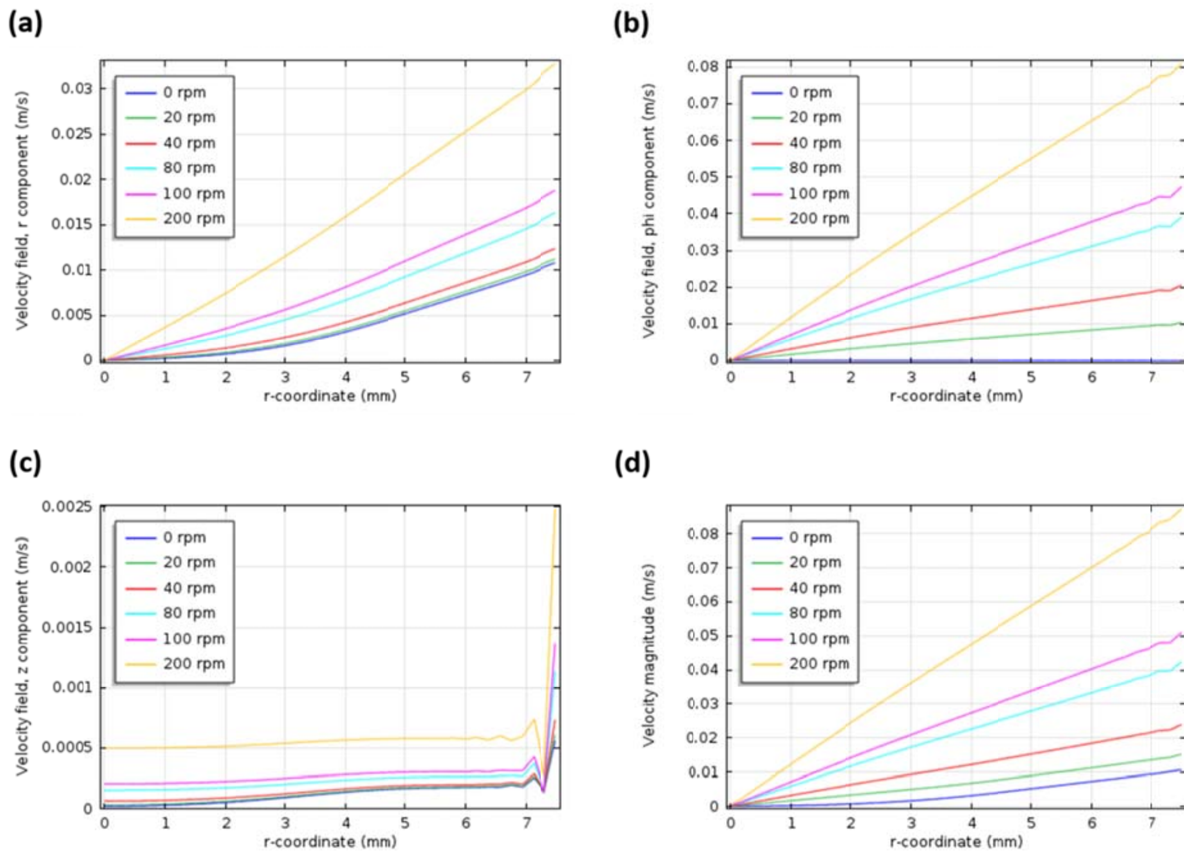

Fig. 6.9 Distribution of (a) radial, (b) azimuthal, (c) axial components, and (d) magnitude of velocity field in liquid at 0.1 mm below the seed along the seed radius

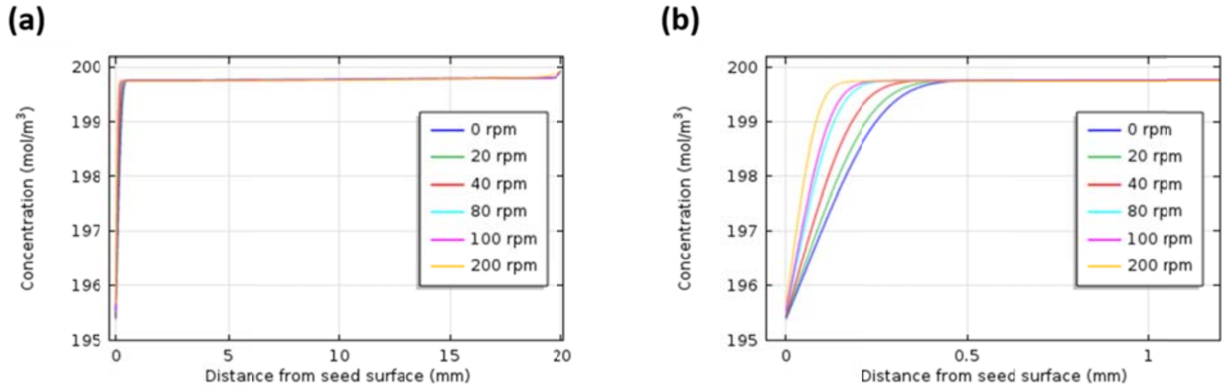

Fig. 6.10 Carbon concentration profile along the symmetry axis (a) from the seed to the crucible surface and (b) in the area close to the seed for different rotation speeds

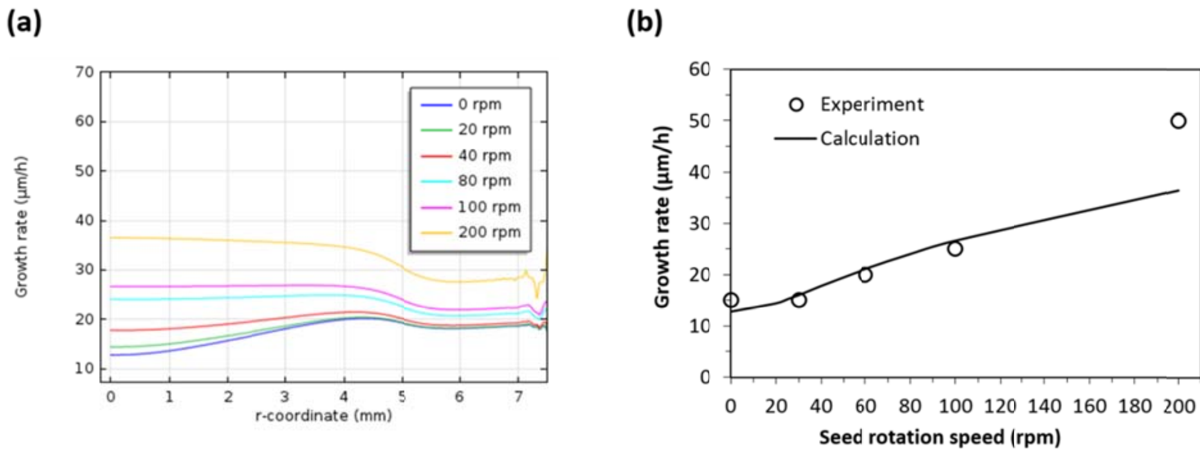

Fig. 6.11 (a) Growth rate profile along the seed radius for various rotation speed and (b) growth rates at the seed center plotted as a function of the rotation speed compared with the experimental results

For further understanding of the results concerning the growth rate computation, Eq. (6.23) can be analyzed. Such equation contains the diffusive flux which is a gradient of the concentration as a function of space near the crystal-liquid interface. We may rewrite the diffusive flux normal to the seed surface as

$$-D\nabla C \cdot \mathbf{n} = D\frac{\Delta C}{\Delta z}. \tag{6.25}$$

Concerning the boundary layer model assuming that the momentum boundary layer is much thicker than the solute boundary layer, the growth rate can be determined purely from the diffusion in the solute boundary layer. Thus (6.25) can be rewritten

$$-D\nabla C\cdot\mathbf{n}=\frac{D}{\delta_D}\left(C-C_{eq}\right). \tag{6.26}$$

This equation specifies that the growth rate is proportional to the supersaturation and inversely proportional to the diffusion boundary layer thickness (δ_D). The distribution of carbon concentration in front of the seed (Fig. 6.10b) shows that the supersaturations are almost constant for all the rotation speed. On the other hand, the solute boundary layer thickness decreases when increasing the rotation speed. This is also the case for the area close to the seed periphery. Thus, in these systems, the growth rate was enhanced by the reduction of the boundary layer thickness due to the seed rotation. Note that this model does not consider the interface attachment kinetics which allows the concentration at the interface to be higher than the equilibrium value [13].

6.3.2 Effect of frequency

The use of an external magnetic field has been recently proposed and theoretically investigated [14-16]. In [15], the authors separated both heating and electromagnetic mixing by computing respectively a resistive heating to control the temperature distribution and an AC field generated by an induction coil, the latter affects only the fluid velocity. With a specific design of the growth configuration [15], i. e., the combination of using one-turn coil placed above liquid surface and the low frequency (typically 50 Hz) was found to be more effective for carbon transport enhancement. This theoretical case is very promising but its technical implementation is not industrially straight forward. Thus, in this section, we are considering a technically relevant single coil system where the electromagnetic field is used for both heating and mixing. We will mainly focus on the effect of coil frequency on the fluid flow and mass transport. The crystal temperature was kept constant at 1700˚C. The coil currents were adjusted to get the suited temperature when varying the frequency from 5 to 100 kHz. The distribution of Lorentz force density in liquid for different coil frequency is shown in Fig. 6.12. The Lorentz force is concentrated only at side wall of the container for 100 kHz while it extends to the inner part of liquid when the frequency decreases. For further analysis, the maximum value of the Lorentz force density in liquid and the Reynolds number computed from the average velocity and Alfven velocity are plotted as a function of the coil frequency in Fig. 6.13a and Fig. 6.13b, respectively. The maximum Lorentz force density and the Reynolds number increase as the frequency decrease.

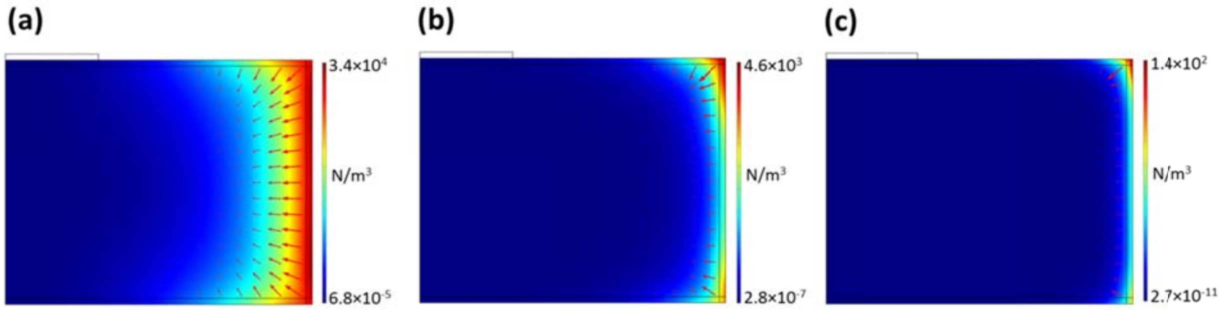

Fig. 6.12 Distribution of Lorentz force density in liquid for different coil frequency: (a) 5 kHz, (b) 25 kHz, and (c) 100 kHz

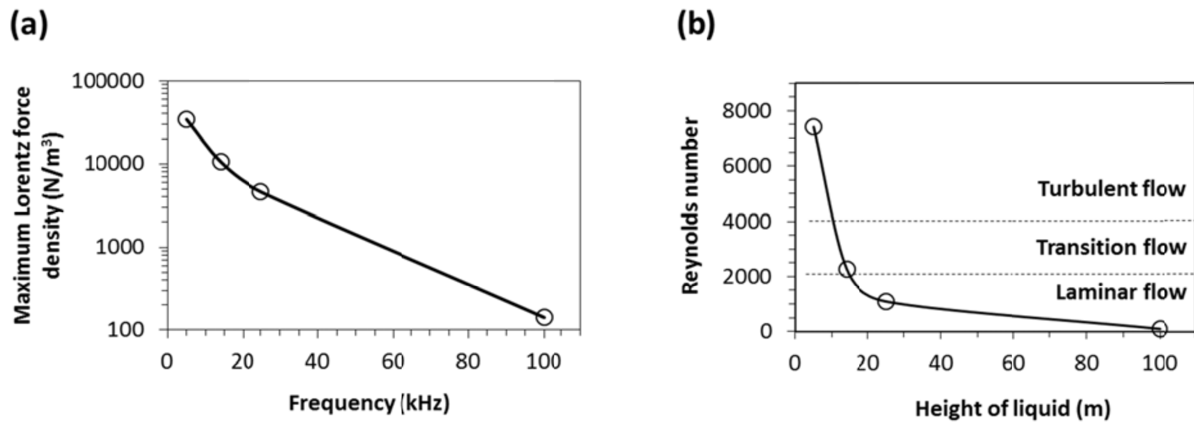

Fig. 6.13 (a) Maximum Lorentz force density in liquid as a function of coil frequency and (b) stability diagram for the electromagnetic convection

The temperature distribution and fluid velocity are shown in Fig. 6.14. For a very low frequency (5 kHz), the flow pattern is completely dominated by the EM convection and highly turbulent as predicted from the Reynolds number. The high velocity vortexes are observed at the top and bottom corner of liquid next to the crucible wall. The Lorentz force is further extended to the inner part of liquid due to the larger skin depth. The liquid at the middle part is pushed toward the symmetry axis, thus both upward and downward flows are predicted along the symmetry axis. When increasing the frequency to 25 kHz, the turbulent seems to vanish at the lower half of liquid. This is in agreement with the Laminar flow suggested by the calculated Reynolds number. The flow follows the counterclockwise direction in the lower part of liquid.

However, the fluid flow in clockwise direction is observed close to the liquid surface with a small vortex at the seed periphery. At 100 kHz, the Lorentz force density in liquid is very small (the same order of magnitude as the buoyancy force density) and extremely localized at the wall due to a very small skin depth and the Reynolds number is also very small. Thus in this investigated case, the flow is governed by the combined buoyancy and Marangoni convections. The flow pattern is quite similar to Fig. 6.5a where the electromagnetic convection is neglected. The temperature at the hottest point is also increased when increasing the frequency due to the reduction of the fluid velocity which reduces the convective heat transfer rate.

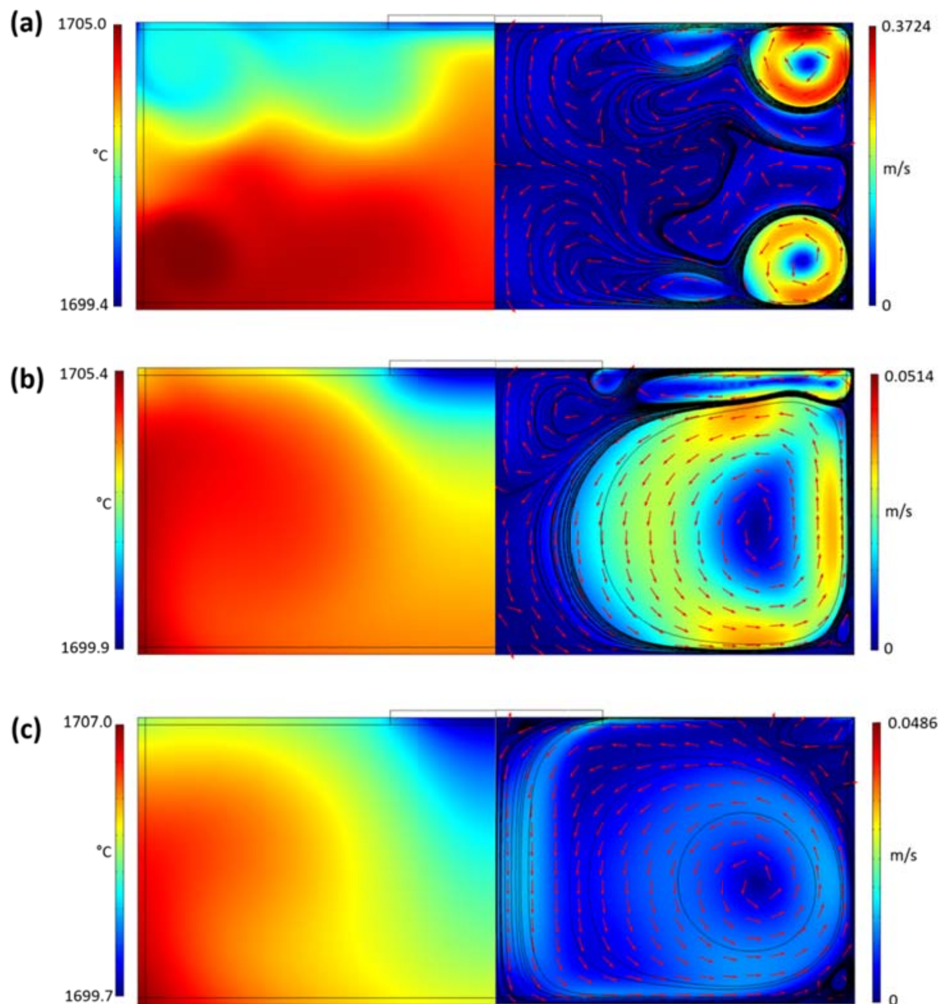

Fig. 6.14 (left-hand side) Temperature and (right-hand side) velocity profiles in liquid for difference coil frequency: (a) 5 kHz, (b) 25 kHz, and (c) 100 kHz

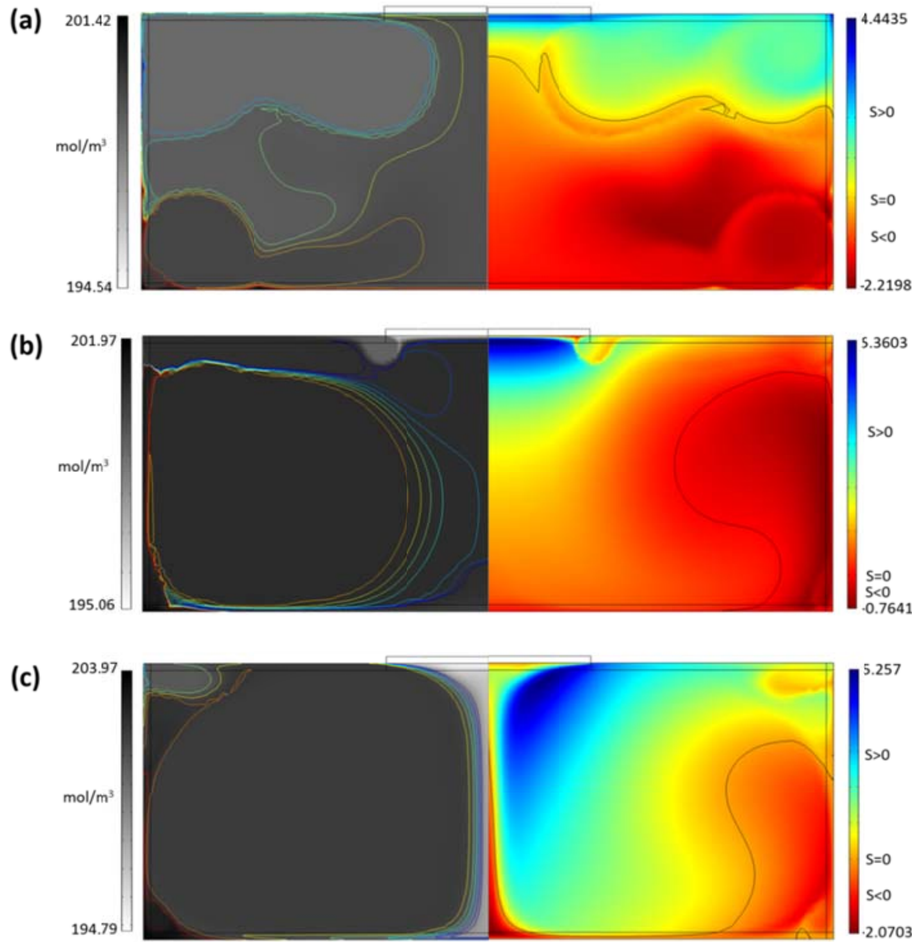

Fig. 6.15 (left-hand side) Carbon concentration and (right-hand side) supersaturation distributions in liquid for difference coil frequency: (a) 5 kHz, (b) 25 kHz, and (c) 100 kHz. The color lines in carbon concentration profiles are the iso-concentration lines added for a better visualization of the distribution of carbon. The red and blue lines correspond to the higher and lower carbon concentration, respectively. The ranges of these iso-concentration lines are (a) 198-200, (b) 200.75-200.85, and (c) 199-203 mol/m^3.

The carbon concentration and supersaturation profiles are shown in Fig. 6.15. The carbon concentration is directly correlated with the convection pattern. At 5 kHz, the carbon transport from the bottom part of crucible to the seed is still in the direction along the symmetry axis similar to the case of 14 kHz. At higher frequency (25 and 100 kHz), the carbon atoms are transported to the seed mainly along the side wall and the top part of liquid. The low carbon concentration is predicted for the flow along the symmetry axis. This is associated with the flow of liquid. Since the equilibrium carbon concentration is proportional to the temperature and the temperature in liquid is lower at the top part of liquid, then the low carbon concentration along

the symmetry axis is caused by the flow transporting the carbon dissolved either from the seed or the upper part of the crucible side wall. The supersaturated and undersaturated areas for the case of 5 kHz are quite similar to 14 kHz. The dissolution areas remain to be at the bottom half of the crucible. In case of 25 kHz, the dissolution area extends to the upper half of liquid. This may benefit the growth process concerning the decreasing of the parasitic depositions especially close to the seed since they can disturb the flow pattern and cause the instability to the growth. However, the non-uniform distribution of supersaturation is predicted along the seed surface due to the presence of a small localized vortex at the seed periphery. At 100 kHz, the supersaturation is very small at the seed center and getting larger at the seed periphery. The growth rates plotted along the seed radius are shown in Fig. 6.16. Following the supersaturation profile in front of the seed, there is almost no growth at the center of the seed for the case of 100 kHz. The non-unifrom distribution of supersaturation using 25 kHz results in the non-uniform growth rate. The growth rate using 5 kHz coil frequency is shown to be quite uniform and the growth rate can be increased by a factor of two compared to the case of 14 kHz. This increase in the growth rate is mainly attributed to the decrease in the boundary layer thickness when using the very low frequency since the fluid velocity is substantially increased.

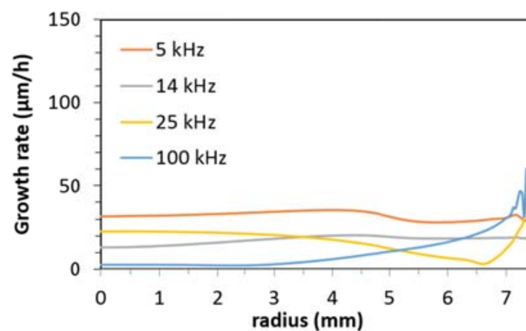

Fig. 6.16 Distribution of growth rate along the seed radius for different coil frequency

6.4 Combined numerical and analytical modeling

The analytical model for qualitative analysis is proposed concerning the interaction between fluid flow and step flow directions. Such consideration is important since the fluid flow direction was experimentally found to cause the step bunching in the growth of SiC from solution [17]. Thus we need to consider first the crystallographic orientation of the seed surface. The simplest surface morphology considered here is a regular array of step trains. Concerning

the fluid convection, there are two components of fluid velocity tangential to the seed surface: azimuthal and radial components. If the circular seed is mounted to the graphite rod at the symmetry axis, the schematic representations of tangential flow is shown in Fig. 6.17. By considering the seed at rest, we define the fluid velocity relative to the seed velocity (Δv) which will be called from now on as the fluid flow or the fluid velocity. In order to investigate the interaction between step flow and fluid flow, the parallel and antiparallel flows are defined. The former refers to the case where the fluid flow and step flow have the same direction while the latter refers to the case where the flows oppose to each other. Fig. 6.17a represents the fluid flow with only azimuthal component ($\Delta v_\phi>0$, $\Delta v_r=0$) while Fig. 6.17b is the one with only radial component ($\Delta v_\phi=0$, $\Delta v_r>0$). For ϕ component, the positive and negative fluid velocities are defined for clockwise and counterclockwise directions, respectively. For r component, the positive value refers to the flow out of the seed center, while it is negative for the opposite flow direction. The boundary line is drawn to separate the surface area having the parallel or antiparallel flow. In Fig. 6.17a the boundary line is the horizontal line crossing the seed center. Defining this horizontal line parallel to the off-cut direction as a reference line, the boundary line will be deviating ξ degree from the reference line if the fluid flow has both azimuthal and radial components (Fig. 6.17c). This angle of deviation is derived from the trigonometry consideration:

$$\xi(r) = \tan^{-1}\left(\frac{\Delta v_r}{\Delta v_\phi}\right) = \tan^{-1}\left(\frac{v_r(r, z_{fluid}) - v_r(r, z_{seed}=0)}{v_\phi(r, z_{fluid}) - v_\phi(r, z_{seed}=0)}\right), \tag{6.27}$$

where r is a distance from the seed center, and z is the position in liquid below the seed-liquid interface. This formula is verified for $\Delta v_r=0$ where ξ is 0º ($\Delta v_\phi>0$) or 180º ($\Delta v_\phi<0$), and for $\Delta v_\phi=0$ where ξ is 90º ($\Delta v_r>0$) or -90º ($\Delta v_r<0$). The positive and negative values of ξ represent the rotation of the boundary line in clockwise and counterclockwise directions, respectively. In fact, the question arises in which z position in liquid (z_{fluid}) should be considered when using Eq. (6.27). If the ratio between the solute (δ_D) and momentum (δ_v) boundary layer thicknesses is much less than unity, the near solid-liquid interface can be considered as a motionless fluid and the mass transport in this region is governed only by the diffusion process [18]. This criterion may allow us to define the velocities at the diffusion layer thickness as representative for fluid velocities near the seed. The ratio between solute and momentum layer thicknesses is related to the Schmidt number (Sc) as [19]

$$\frac{\delta_D}{\delta_v} \approx \left(\frac{D}{\upsilon}\right)^n = Sc^{-n}. \tag{6.28}$$

The exponent n is in general in the range $1 \geq n \geq 1/3$ for fluids having $0 \leq Sc \leq \infty$. In our case using silicon as a solvent we obtain $0.05 \leq \left(\delta_D/\delta_v\right) \leq 0.37$. The assumption of motionless fluid near the seed-liquid interface verifies if the momentum boundary layer is much thicker than the solute boundary layer, i.e. an order of magnitude $\left(\delta_D/\delta_v\right) \leq 0.1$. This is the case for n=1 but not for $n=1/3$. In this model, we are considering that the transport within the solute boundary layer thickness play an important role for the growth at the seed crystal as discussed in section 6.3.1. Thus, we will assign a mean value of the fluid velocity within the solute boundary layer such that $\mathrm{v}(r, z_{fluid}) = 1/\delta_D \int_0^{\delta_D} \mathrm{v}(r,z)dz$. This is applied for both radial and azimuthal velocity components.

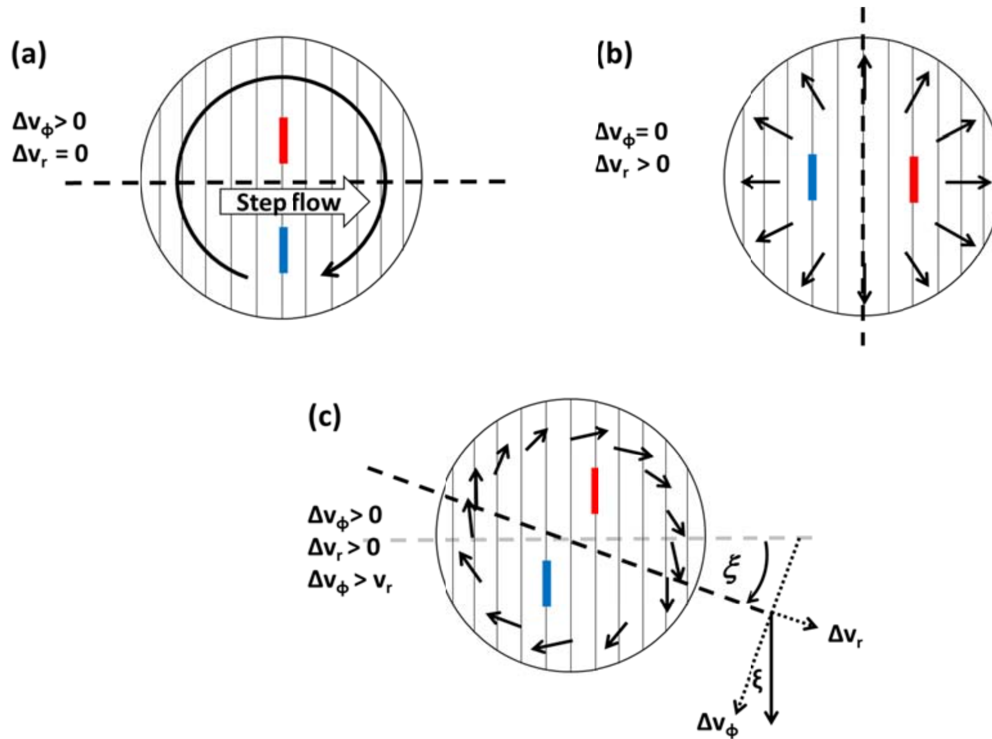

Fig. 6.17 Schematic representation of the fluid flow and step flow on a circular seed crystal. The arrows represent the fluid flow direction tangential to the seed surface. Parallel and antiparallel flows are separated by the boundary line (dashed line) where red and blue lines correspond to the parallel and antiparallel flows region, respectively.

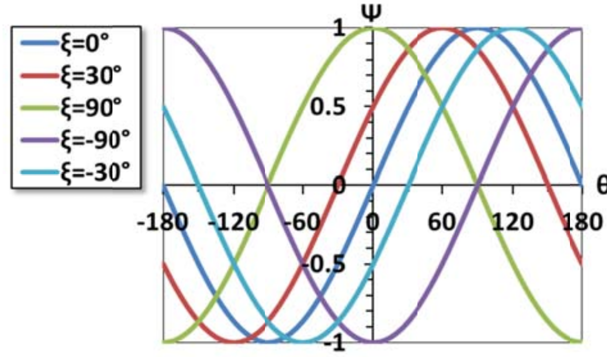

Fig. 6.18 Phase parameter diagram representing the interaction between fluid flow and step flow. δ=0° and δ=90º correspond to Fig. 6.16a and Fig. 6.16b, respectively

For further quantitative description of the flows behaviors, we define the phase parameter

$$\Psi = \sin(\theta + \alpha + \xi), \tag{6.29}$$

where θ is the angle defined in a unit circle and is used to define the position on the seed crystal. α is the angle between the step orientation and the crystal off-cut direction where the positive and negative values denote the angle rotates in clockwise and counterclockwise directions, respectively. The phase parameter varies from -1 for antiparallel flow to 1 for parallel flow. The value becomes zero if the step flow and fluid flow directions are perpendicular. For the regular step train oriented in [11-20] direction, α becomes zero. In this way, the positive and negative values of the phase parameter refer to the parallel and antiparallel flows, respectively. A simple phase parameter profile can be plotted in Fig. 6.18 for different ξ values. In order to directly compare to the cases shown in Fig. 6.17, the boundary line corresponds to the angles where the curves cross the horizontal axis.

The situation becomes more complex regarding the six-fold symmetry representing the hexagonal system of SiC (Fig. 6.19a). In the typical growth experiment, the seed with off-cut few degrees from (0001) toward [11-20] direction was used providing the homoepitaxy via the step flow growth. For the SiC single crystal growth under the low supersaturation, the average growth rate is larger on the {11-2n} than on the {1-10n} planes [20]. This is the case for the typical growth conditions for TSSG process where the crystal growth was carried out close to the equilibrium environment. Moreover the surface steps are bunched especially during the solution

growth process. Thus instead of having a single step and a regular straight step train, the possible morphology of surface could be the bunched steps and become zigzag with (10-1n) and (01-1n) faceted planes considering that the crystal shape is limited by the slow moving planes. In this work, only the two-dimensional model will be considered. Thus, the bunched surfaces (facetted) in [10-1n] and [01-1n] directions can be projected on the c-plane (0001). This allows us to consider the step orientation on the c-plane such that (10-10) and (01-10) planes represent (10-1n) and (01-1n) facets, respectively.

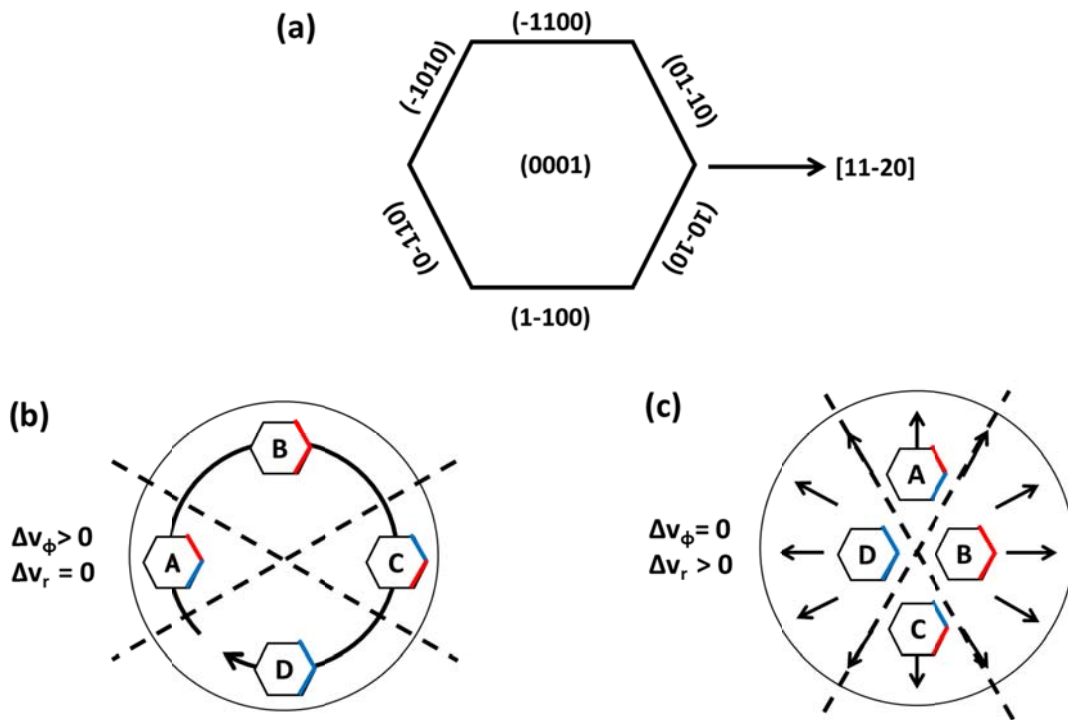

Fig. 6.19 (a) Schematic representation of the (0001) plane in the hexagonal system and (b-c) interaction between the fluid flow and step flow on the circular SiC seed crystal off-cut few degrees toward [11-20] direction. The arrows show the fluid flow direction. Red and blue lines on the hexagon represent the parallel and antiparallel flow conditions, respectively. The parallel flow condition is fulfilled only on (01-10) plane in area A. In area B, the parallel flow is realized for both (10-10) and (01-10) planes. Only (10-10) plane satisfies the parallel flow in area C. Both (10-10) and (01-10) planes obey the antiparallel in area D. Areas A-D are separated by the boundary lines (dashed lines)

The seed having different fluid flows are shown in Fig. 6.19b-c. In this case, two boundary lines can be drawn since the two adjacent {1-100} facets are considered. The surface area of the growing crystal is then divided into four regions denoted by A, B, C, and D. In area

A, the parallel flow condition is realized only for (01-10) facet. The parallel flow for both (10-10) and (01-10) facets are achieved in area B. Only the (10-10) facet fulfills the parallel flow in area C. Finally, only the antiparallel flow is possible in area D. The boundary lines in Fig. 6.19b for the case that $\Delta v_\phi>0$ and $\Delta v_r=0$ are used as the reference lines. If the fluid velocity composes of two components, the deviation of the boundary lines from the reference lines can be calculated in the same way as Eq. (6.27). In this case, α are -30º for (01-10) and 30º for (10-10) facets. The case for the positive radial fluid flow is shown is Fig. 6.19c. The phase parameter diagram for Fig. 6.19b (ξ=0º) is plotted in Fig. 6.20 where the corresponding areas A-D are separated by the boundary lines. The parallel flow conditions are fulfilled for both {1-100} facets when Ψ of both facets are positive (area B). The individual (10-10) or (01-10) complete the parallel flow in area C and A, respectively. Only antiparallel flow was realized in area D for both {1-100} facets.

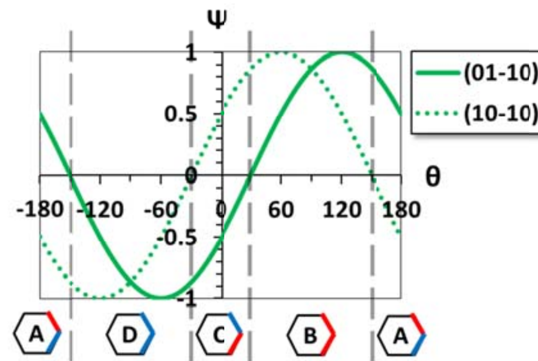

Fig. 6.20 Phase parameter diagram for the condition shown in Fig. 6.19b. Areas A, B, C, and D are separated by boundary lines (dashed lines) as shown in Fig. 6.19b

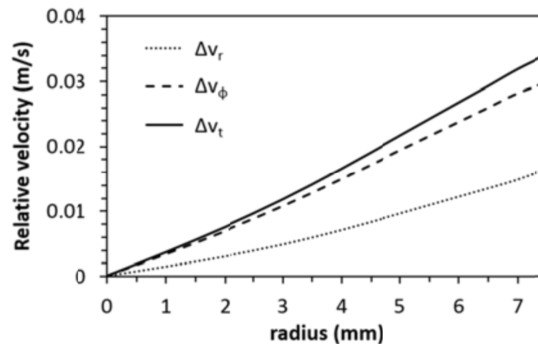

Fig. 6.21 Profile of fluid velocity relative to the seed along the seed radius for both radial (r) and azimuthal (ϕ) components. The tangential (t) fluid velocity is computed from a vector sum of r and ϕ velocity components.

Since the model has been verified concerning the growth rate, it should be possible to use other calculated parameters for the qualitative analysis. This is the case for the angle of deviation ξ defined in Eq. (6.27). For the case of high rotation speed of 100 rpm in counterclockwise direction, the values of fluid velocity for both radial and azimuthal components relative to the seed are plotted along the radius (Fig. 6.21). Both radial and azimuthal components of fluid velocity increase along the seed radius. In such case, the solute boundary layer thickness is almost constant δ_D=0.2 mm along the seed radius. The ξ value at r=6 mm is calculated to be around 28º. The phase parameter diagram for these growth conditions is plotted in Fig. 6.22 for both (10-10) and (01-10) facets where the A-D areas are separated by the boundary lines. The surface of the as grown crystal using 4H-SiC (0001) seed crystal 4º off-axis towards [11-20] is compared with the diagram. The seed rotation speed was set to 100 rpm in counterclockwise direction (clockwise as observe from above the liquid surface). Each image was taken in the area r>4 mm where its azimuthal location on the crystal surface is defined by the angle θ relative to the [11-20] direction. The formation of macrosteps (the dark lines formed by the accumulations of several microsteps) is correlated to the phase parameter diagram. The parallel flow for (01-10) facet (area A) give rises to the macrosteps formation predominantly close to (01-10) plane. The parallel flow criteria in both (01-10) and (10-10) facets (area B) result in possibility to form the zigzag-shape macrosteps while the main feature is still governed by the dominant phase parameter. The predominant macrosteps close to (10-10) plane are observed in the C area where the parallel flow condition is fulfilled only for (10-10) facet. In area D, only the antiparallel flow is predicted and the macrosteps should not be formed. The phase parameter diagram shows good agreement in correlating the flow conditions with the macrostep formations with some deviation for -85º and 175º. However, if we neglect the radial flow such as the diagram for the purely azimuthal flow shown in Fig. 6.20, the behavior of macrosteps formation become poorly described. For example, for θ = -40º, Fig. 6.20 shows the only antiparallel flow while macrosteps close to (10-10) plane were experimentally observed. Another example is the case for θ=140º, Fig. 6.20 predicts only the parallel flows for both (10-10) and (01-10) whereas only the macrosteps predominantly close to (01-10) plan were observed. Moreover, the deviations for the cases of -85º and 175º will become even larger. Thus the effects of the fluid flow in both components tangential to the seed have to be considered since they provide better description of the macrosteps orientations.

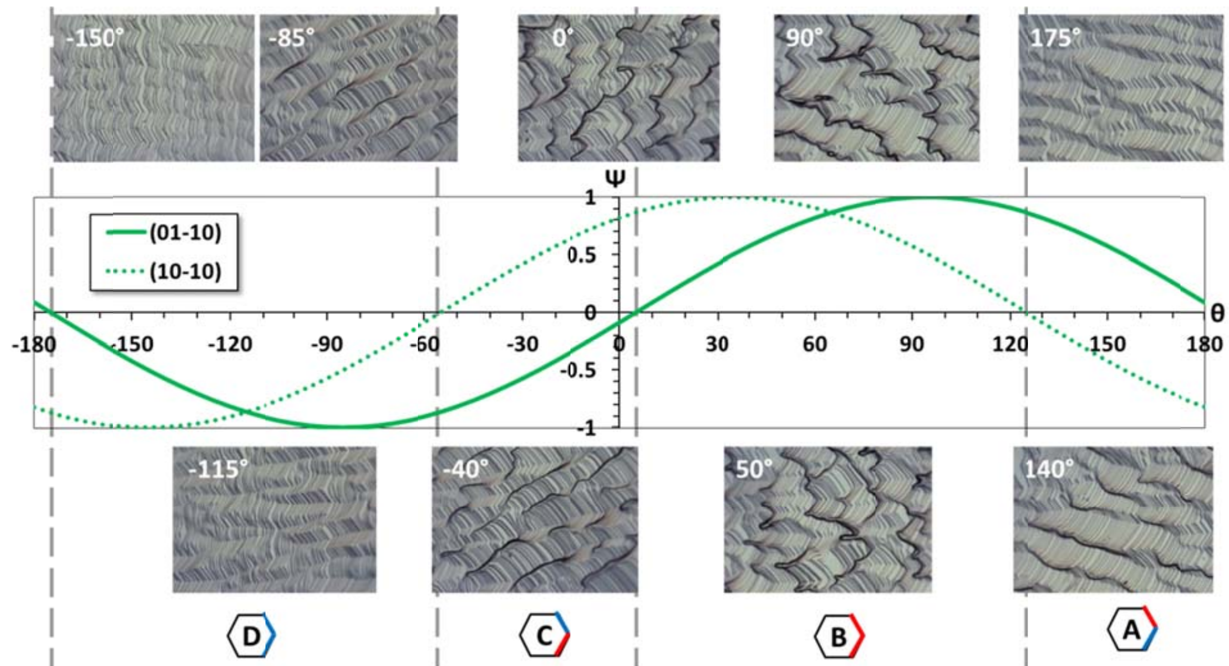

Fig. 6.22 Comparison between the macrosteps formation observed from the experiment and their behavior predicted from the phase parameters calculated using the combined numerical and analytical modeling. Angle θ shown in each image refer to the position where the image was taken on the crystal relative to the [11-20]

As point out in [21], there exists a critical negative shear rate for which the stable surface becomes unstable with respect to step bunching by increasing the shear rate magnitude. Differently said, the fluid flow has a strong effect on the growth front stability in the parallel flow condition if the fluid velocity is high enough to overcome the stability limit. If such limit involves in the surface energy, this type of instability should not affect the crystal surface to the same extend compared between Si- and C-face depending also on the deviation from such limit. Then the surface morphology should be more stable at lower rpm, and at the area closer to the seed center since the tangential velocity is very small close to the center of the seed (Fig. 6.21).

Concerning the reason why the macrosteps formations were not exactly following the equilibrium shape of the {1-100} facets, we consider that the growth process was not done exactly in equilibrium but with a small deviation from equilibrium conditions. Thus the crystal shape should be kinetically driven but still in relation with the surface energy. Which effect dominates the crystal and interface shapes should depend on how much deviation from equilibrium. In addition, the surface is more stable using the low rpm and no macrostep is

formed. In such cases the fluid velocity are quite low. This might support the present of the critical point of stability discussed earlier.

The occurrence of the macrosteps increases the surface roughness and results in poor crystal quality. The improvement of the surface morphology roughness can be achieved by decreasing the area of parallel flow, such as changing the center of rotation at the seed [22]. However the formation of macrosteps may give some benefit owing to the dislocation conversion mechanism [23]. Thus the results from the combined numerical and analytical modeling show the possibility to use the phase parameters to control and optimize the quality of the SiC crystal grown from the TSSG process regarding the macrosteps formation.

6.5 Conclusion

We have discussed the modeling of the TSSG process in this chapter where the special attention has been paid to the contribution of the four main convections on the fluid dynamics. The process parameters, namely operating frequency and crystal rotation speed, have been investigated. The electromagnetic convection is the main contribution governing the growth process at the experimental conditions using low frequency (14 kHz) while the combined buoyancy and Marangoni dominates at high frequency (100 kHz). The enhancement of the growth rate at the experimental conditions is possible by increasing the rotation speed of the seed. The growth rate dependent on the rotation speed obtained from the calculations is successfully validated with the experiments. The use of very low frequency (5 kHz) and very high rotation speed (200 rpm) may cause the time-dependent and/or turbulent flow and results in the instability of the growth process which is not preferable for the growth even if it provides higher growth rate. Moreover, the combined numerical and analytical modeling has been developed to give a comprehensive visualization of the interactions between the fluid flow and the step flow that have effects on the surface morphology of the growing crystal. The phase parameter has been introduced to correlate the macrostep formation with the fluid flow. Such model has been successfully validated with the experiments.

References

1. Mercier, F., et al., *Coupled heat transfer and fluid dynamics modeling of high-temperature SiC solution growth.* Journal of Crystal Growth, 2010. **312**(2): p. 155-163.

2. Scheel, H.J. and E.O. Schulz-Dubois, *Flux growth of large crystals by accelerated crucible-rotation technique.* Journal of Crystal Growth, 1971. **8**(3): p. 304-306.
3. Kusunoki, K., et al., *Solution Growth of SiC Crystal with High Growth Rate Using Accelerated Crucible Rotation Technique.* Materials Science Forum, 2006. **527-529**: p. 119-122.
4. Durand, F. and J.C. Duby, *Carbon solubility in solid and liquid silicon—A review with reference to eutectic equilibrium.* Journal of Phase Equilibria, 1999. **20**(1): p. 61-63.
5. Pellew, A. and R.V. Southwell, *On Maintained Convective Motion in a Fluid Heated from below*. Vol. 176. 1940. 312-343.
6. Touihri, R., H. Ben Hadid, and D. Henry, *On the onset of convective instabilities in cylindrical cavities heated from below. I. Pure thermal case.* Physics of Fluids (1994-present), 1999. **11**(8): p. 2078-2088.
7. Carruthers, J.R. and K. Nassau, *Nonmixing Cells due to Crucible Rotation during Czochralski Crystal Growth.* Journal of Applied Physics, 1968. **39**(11): p. 5205-5214.
8. Jones, A.D.W., *Scaling analysis of the flow of a low Prandtl number Czochralski melt.* Journal of Crystal Growth, 1988. **88**(4): p. 465-476.
9. Holman, J., *Heat Transfer. 2002.* McGrawHill, New York, USA.
10. Camel, D., P. Tison, and J.P. Garandet, *Experimental study of Marangoni flows in molten and solidifying Sn and Sn-Bi layers heated from the side.* Eur. Phys. J. AP, 2002. **18**(3): p. 201-219.
11. Moreau, R., *Magnetohydrodynamics, 1990*. Kluwer Academic Publishers, Dordrecht.
12. Lefebure, J., et al., *Modeling of the Growth Rate during Top Seeded Solution Growth of SiC Using Pure Silicon as a Solvent.* Crystal Growth & Design, 2011. **12**(2): p. 909-913.
13. Wilcox, W.R., *Transport phenomena in crystal growth from solution.* Progress in Crystal Growth and Characterization of Materials, 1993. **26**(0): p. 153-194.
14. Mercier, F. and S. Nishizawa, *Solution growth of SiC from silicon melts: Influence of the alternative magnetic field on fluid dynamics.* Journal of Crystal Growth, 2011. **318**(1): p. 385-388.
15. Mercier, F. and S.-i. Nishizawa, *Numerical Investigation of the Growth Rate Enhancement of SiC Crystal Growth from Silicon Melts.* Japanese Journal of Applied Physics, 2011. **50**(3R): p. 035603.
16. Mercier, F. and S.-i. Nishizawa, *Comparative numerical study of the effects of rotating and traveling magnetic fields on the carbon transport in the solution growth of SiC crystals.* Journal of Crystal Growth, 2013. **362**(0): p. 99-102.
17. Zhu, C., et al., *Influence of Solution Flow on Step Bunching in Solution Growth of SiC Crystals.* Crystal Growth & Design, 2013. **13**(8): p. 3691-3696.
18. Bredikhin, V.I. and O.A. Malshakova, *Step bunching in crystal growth from solutions: Model of nonstationary diffusion layer, numerical simulation.* Journal of Crystal Growth, 2007. **303**(1): p. 74-79.
19. Hurle, D., *Handbook of Crystal Growth 2: Bulk Crystal Growth, Part B: Growth Mechanisms and Dynamics*. 1994, North-Holland, Amsterdam.
20. Nordell, N., S. Karlsson, and A.O. Konstantinov, *Equilibrium crystal shapes for 6H AND 4H SiC grown on non-planar substrates.* Materials Science and Engineering: B, 1999. **61–62**(0): p. 130-134.
21. Chernov, A.A., S.R. Coriell, and B.T. Murray, *Morphological stability of a vicinal face induced by step flow.* Journal of Crystal Growth, 1993. **132**(3–4): p. 405-413.
22. Umezaki, T., Koike, D., Harada, S., Ujihara, T., *Improvement of surface morphology by solution flow control in solution growth of SiC on off-axis seeds.* to be published in Materials Science Forum, 2015.
23. Harada, S., et al., *Evolution of threading screw dislocation conversion during solution growth of 4H-SiC.* APL Materials, 2013. **1**(2): p. 022109.

Chapter 7

General conclusions and perspectives

In this thesis, we made use of the numerical modeling as a tool for “process characterization”. This tool was able to provide an assessment of the physico-chemical parameters and their distributions inside the growth chamber. Such information is not possible or at least extremely difficult to obtain during the experiment. This is the case especially for the growth of SiC using PVT and TSSG techniques since the experiments were carried out in a quasi-closed graphite crucible, often called as a “black box” process. Thus the modeling approach can be used as an alternative way to make a link between the controllable parameters and the observable results providing better monitoring and better understanding of the growth processes.

With the modeling of induction heating and heat transfer, the temperature distribution in the growth reactor can be obtained. This is one of the crucial information for the crystal growers since the temperature gradient creates a driving force for the crystal growth. The model was verified by the similar tendency of the I-V curves, and the correlation between the diffusion path of the SiC vapor species and temperature gradient streamlines in the powder source. Concerning more details of the model, the heat transfer by gas convection was shown to be negligible due to the dominant radiative heat transfer at the high growth temperature. The semi-transparency of SiC was shown to strongly affect the temperature profile in the vicinity of the crystal and the temperature gradient. However, such effect was not taken into account in the modeling of our reactor for three main reasons. First, the crystals may become opaque since the experimental observations reveal that the doping level is quite high in the crystals even in the case of unintentionally doping experiments. Second, the present band energy model for taking into account a semi-transparency behavior is somewhat simplified where the interactions between the transmitted wave and the crystal were neglected. Finally, the discrepancies in an absorption coefficient dependent on the wavelength, temperature, doping level, and polytype can lead to

completely different conclusions. These points should be examined in more details, possibly with a proper experiment and measurement design for the materials properties related issue.

The mass transport model combined the fluid dynamics and the species transport models. In the PVT growth, special attention was paid to the boundary conditions and the chemical model at the solid vapor interfaces. Two approaches were proposed to take into account the stoichiometry condition at the growing surface. The comparative approach was able to provide the results respecting such condition. However, the first approach was not very convenient for further development of the model since it dealt with the kinetic parameters, sticking coefficient, which is very complex and difficult to determine and verify. The coupled approach provides better comprehension of the growth process since the prior assumption for the three-phase heterogeneous equilibrium was not required. The stoichiometry condition was successfully respected with additional information on the crystal chemistry. Modeling results were validated with good agreement with the experiments. More importantly, this approach really opened the way to get access to the physico-chemical parameters in the crystal, the activities of Si and C atoms in SiC solid solution, during the growth process and their dependency on the process parameters. The correlations between the state of the growing crystals and the occurrence of cubic or hexagonal polytype and defects density were made. The correlation with the doping concentration was also suggested as a possible extension of the model. Those results were discussed base on the evidences found in the literature while the real mechanisms are still unclear. Thus, the extension of the present model and further studies on the mechanisms responsible for any valid correlations are required.

In the full modeling of the TSSG process, the induction heating, heat transfer, and fluid dynamics were coupled. The heat transfer by the fluid convection was shown to be more efficient than the diffusion since the temperature profile in liquid clearly followed the convection pattern. Such convection pattern was governed by the four main contributions: buoyancy convection, forced convection, Marangoni convection, and electromagnetic convection. The effects of the process parameters, namely, crystal rotation speed and operating frequency were studied. Four main parameters could be monitored during the growth: temperature, velocity field, concentration profile, and supersaturation. The electromagnetic convection was the main contribution governing the growth process using the low frequency while the combined

buoyancy and Marangoni became dominant at high frequency. At the growth conditions, the enhancement of the growth rate could be obtained by increasing in the rotation speed of the seed. This effect is mainly due to the reduction of the boundary layer thickness in front of the seed. The calculated growth rate as a function of rotation speed exhibit good agreement with the experiments while some deviation at very high rpm was found. With the dimensionless analysis, such flow should be already in the turbulent regime. This is the case also for the growth using very low frequency (5 kHz). Thus, it will be necessary in the future to reconsider the model in the transient and/or three-dimensional system for higher accuracy. In addition, the combined numerical and analytical modeling was developed granting a comprehensive visualization of the interaction between the fluid flow and the step flow that affects the surface morphology of the crystal. The phase parameter was introduced to correlate the macrostep formation with the fluid flow. Such model was successfully validated with the experimental results. Apart from those achievements, the TSSG process is still needed to be optimized to fully utilize its capability for growing high quality SiC crystal. This will include the control of the fluid convection and suppression of the growth instabilities. The basic mechanism for the interaction at the crucible-liquid interface also remains to be studied. This will possibly provide more appropriate boundary condition, rather than the equilibrium concentration, to be implemented in the mass transport modeling.

The present thesis really emphasizes on developing a better understanding of the SiC growth processes. The complete experiment, characterization, and process modeling approach will be a key to obtain a full description of the processes. This obviously requires further extension of the model as well as additional experiments and characterizations.

Appendix A
Physical properties

A.1 Electromagnetic properties

The physical properties related to the electromagnetic problem are magnetic permeability, electrical current density, electrical conductivity, and angular frequency. The permeability of all materials is set equal to that one of the air (1.2566×10^{-6} H/m). Thus the relative permeability of all material equals to unity. The electrical current density is dependent on the desired growth temperature. The electrical conductivity varies in each material and is dependent on the temperature.

A.2 Properties of the gas phase

A.2.1 Thermal properties

Several models have been presented for the determination and estimation of physical properties of materials used in the growth process. For the gas phase, the simulations were performed assuming an ideal gas. Thus the gas density is written by

$$\rho = \frac{PM}{RT} \text{ kg/m}^3. \tag{A.1}$$

In the mixture of N species (growth cavity), the mean molar mass can be calculated from

$$M = \sum_{i=1}^{N} x_i M_i = \frac{1}{\sum_{i=1}^{N} (\omega_i / M_i)} \text{ kg.} \tag{A.2}$$

Similarly, the specific heat of gas for a mixture of N species is calculated according to the molar fraction of each species reads

$$C_p = \sum_{i=1}^{N} x_i C_{p_i} \text{ J/(kg·K)}. \tag{A.3}$$

For specific heats of all gas species, the data are obtained from NIST-JANAF Thermochemical Tables. The tabulated functions have been extracted from these discrete temperature dependent data sets in order to use in the simulation. The thermal conductivity of solid materials is written in forms of analytic function depending on the temperature. In the gas phase, the Mason-Saxena-Wassiljewa expressions have been used. This MSW method gives the accuracy of ±6-8%. The thermal conductivity of the gas mixture using MSW mixing rules is in the forms of

$$k = \sum_{i=1}^{N} \frac{x_i k_i}{\sum_{j=1}^{N} x_i \Phi_{ij}} , \tag{A.4}$$

where Wassiljewa function (Φ_{ij}) can be calculated by Mason and Saxena expression written as

$$\Phi_{ij} = \frac{1}{\sqrt{8}} \left(1 + \frac{M_i}{M_j}\right)^{-\frac{1}{2}} \left(1 + \left(\frac{k_i}{k_j}\right)^{\frac{1}{2}} \left(\frac{M_j}{M_i}\right)^{\frac{1}{4}}\right)^2 . \tag{A.5}$$

For each gas species, the thermal conductivity can be calculated from the Chapman-Enskog's formulae based on the kinetic theory of gases assuming Lennard-Jones potentials:

$$k_i = 2.6318 \times 10^{-3} \frac{\sqrt{T/M_i}}{\sigma_i^2 \Omega_k} \text{ W/(m·K)}. \tag{A.6}$$

The collision integral (Ω_k) represented the deviation from rigid sphere behavior is defined by

$$\Omega_k\left(T_i^*\right) = \frac{1.16145}{\left(T_i^*\right)^{0.14874}} + \frac{0.52487}{\exp\left(0.7732\, T_i^*\right)} + \frac{2.16178}{\exp\left(2.43787\, T_i^*\right)} , \tag{A.7}$$

where $T_i^* = kT/\varepsilon_i$. σ_i and ε_i are the Lennard-Jones coefficients of the ith species. Moreover, in this work, we have also taken into account the influence of source powder porosity on its thermal conductivity. The heat transfer by radiation in the powder bulk is integrated with the heat transfer by conduction. Thus the effective thermal conductivity is estimated by

$$k_{eff} = \phi\left(k_{gas} + \frac{32}{3}\varepsilon_e \sigma T^3 d\right) + (1-\phi)k_{solid} \ , \tag{A.8}$$

where d is the equivalent average diameter of the powder granules.

A.2.2 Fluid flow properties

The fluid flow problem needs the density and the dynamic viscosity of the gas mixture. The former case is the same property used in the heat transfer model. The latter one, the dynamic viscosity has been calculated utilizing again MSW mixing rules:

$$\mu = \sum_{i=1}^{N} \frac{x_i \mu_i}{\sum_{j=1}^{N} x_i \Phi_{ij}} \ . \tag{A.9}$$

In this case, Wassiljewa function for dynamic viscosity is in the forms of

$$\Phi_{ij} = \frac{1}{\sqrt{8}}\left(1 + \frac{M_i}{M_j}\right)^{-\frac{1}{2}}\left(1 + \left(\frac{\mu_i}{\mu_j}\right)^{\frac{1}{2}}\left(\frac{M_j}{M_i}\right)^{\frac{1}{4}}\right)^2 \ . \tag{A.10}$$

Chapman-Enskog's formulae based on the kinetic theory of gases assuming Lennard-Jones potentials are implemented for calculating the dynamic viscosity of the ith species:

$$\mu_i = 8.441 \times 10^{-5} \frac{\sqrt{M_i T}}{\sigma_i^2 \Omega_\mu} \text{kg/(m·s)}, \tag{A.11}$$

where $\Omega_\mu = \Omega_k$ as defined in Eq. (A.7).

A.2.3 Mass transport properties

In this mass transport model, the diffusion coefficients are required. There are two types of diffusion coefficients according to two different mass transport mechanisms considered here: thermal diffusion and isothermal diffusion. The thermal diffusion coefficients of all gas species are very small in PVT growth. Their values can be found in an order of 10^{-10} (kg m^{-1} s^{-1}) in our growth process. Thus, the isothermal diffusion mechanism dominates. The multicomponent

Maxwell-Stefan diffusion coefficients are used in the mass transfer equations. In our case, we assume the low-density gas mixtures condition in which Maxwell-Stefan diffusivities can be replaced with the binary diffusivities for the species pairs presented in the mixture. Thus the binary diffusivities will be used as the input data to compute multicomponent Fick diffusivities using matrix transformation. The diagonal terms of Maxwell-Stefan diffusivity matrix defined by D_{ii} representing the diffusion of species through itself are equal to unity. The off-diagonal terms D_{ij} representing the mutual-diffusion of species *i* at infinite dilution through species *j* equal to the diffusion of species *j* at infinite dilution of species *i*. Thus, the binary diffusivity matrix is symmetric $\left(D_{ij} = D_{ji}\right)$. The binary diffusion coefficients D_{ij} for the gas mixture are given by

$$D_{ij} = 5.876 \times 10^{-4} \frac{\sqrt{T^3\left(\frac{1}{M_i} + \frac{1}{M_j}\right)}}{P\sigma_{ij}^2 \Omega_D\left(T_{ij}^*\right)} \text{ m}^2\text{/s}, \tag{A12}$$

where $\sigma_{ij} = \left(\sigma_i + \sigma_j\right)/2$. The function $\Omega_D\left(T_{ij}^*\right)$ is defined by

$$\Omega_D\left(T_{ij}^*\right) = \frac{1.06036}{\left(T_{ij}^*\right)^{0.15610}} + \frac{0.19300}{\exp\left(0.47635\,T_{ij}^*\right)} + \frac{1.03587}{\exp\left(1.52996\,T_{ij}^*\right)} + \frac{1.76474}{\exp\left(3.89411\,T_{ij}^*\right)}, \tag{A13}$$

where $T_{ij}^* = kT/\varepsilon_{ij}$ and $\varepsilon_{ij} = \sqrt{\varepsilon_i \varepsilon_j}$.

In the TSSG process, the diffusion coefficient of C in liquid Si is set to $1.7 \times 10^{-8} \frac{m^2}{s}$.

A.3 Properties of various materials used in the modeling

In some cases, the materials venders provide the property data of their products. However, those data do not cover the entire range of our experimental conditions, i.e., the lack of data at high temperature. Thus it is necessary to extrapolate those properties and/or compare the given properties with the models presented in the literatures in order to utilize the appropriate ones as well as to improve the accuracy of the model and minimize the error that may occur. Physical properties of materials used in the simulation are listed as follow.

Insulator

Electrical conductivity: $\sigma^{Insulator} = \dfrac{400}{3.5\times10^{-4}T + 0.375 + \dfrac{144.7}{T}} \; \dfrac{1}{\Omega\cdot m}$

Thermal conductivity: $k^{Insulator} = 9\times10^{-8}T^2 + 0.0001T + 0.0426 \; \dfrac{W}{m\cdot K}$

Heat capacity: $C_p^{Insulator} = 2000 \; \dfrac{J}{kg\cdot K}$

Density: $\rho^{Insulator} = 130 \; \dfrac{kg}{m^3}$

Surface emissivity: $\varepsilon_e^{Insulator} = 0.53$

Graphite crucible

Electrical conductivity:

$$\sigma^{Crucible} = \begin{cases} -6.519\times10^{-9}T^4 + 6.091\times10^{-5}T^3 - 1.915\times10^{-1}T^2 + \\ 2.242\times10^{2}T + 3.247\times10^{4} & T \le 2300K \\ 93758.62 & T > 2300K \end{cases} \quad \frac{1}{\Omega\cdot m}$$

Thermal conductivity: $k^{Crucible} = 76.2\left(\dfrac{1}{2.2\times10^{-3}T} + 0.3\right) \dfrac{W}{m\cdot K}$

Heat capacity: $C_p^{Crucible} = \dfrac{1}{441.12T^{-2.30676} + 7.97093\times10^{-4}T^{-6.65256\times10^{-2}}} \; \dfrac{J}{kg\cdot K}$

Density: $\rho^{Crucible} = 1780 \; \dfrac{kg}{m^3}$

Surface emissivity: $\varepsilon_e^{Crucible} = 0.72$

SiC powder source

Electrical conductivity: $\sigma^{Powder} = 1\times10^{3}\ \frac{1}{\Omega\cdot m}$

Thermal conductivity: $k_{solid}^{Powder} = 20$, $k_{gas}^{Powder} = 0.05\ \frac{W}{m\cdot K}$

Heat capacity: $C_p^{Powder} = 1000\ \frac{J}{kg\cdot K}$

Density: $\rho^{Powder} = 1324\ \frac{kg}{m^3}$

Surface emissivity: $\varepsilon_e^{Powder} = 0.85$

Porosity: $\phi^{Powder} = 0.6$

SiC seed

Electrical conductivity: $\sigma^{SiC} = 770\ \frac{1}{\Omega\cdot m}$

Thermal conductivity: $k^{SiC} = \begin{cases} \frac{451700}{T^{1.29}} & T \le 2300K \\ 20.8 & T > 2300K \end{cases} \quad \frac{W}{m\cdot K}$

Heat capacity: $C_p^{SiC} = 925.65 + 0.3772T - 7.9259\times10^{-5}T^2 - \frac{3.1946\times10^{7}}{T^2}\ \frac{J}{kg\cdot K}$

Density: $\rho^{SiC} = 2986.43 - 0.02094117T - 1.614493\times10^{-5}T^2 + 3.655528\times10^{-9}T^3\ \frac{kg}{m^3}$

Surface emissivity: $\varepsilon_e^{SiC} = 0.85$

Si liquid

Electrical conductivity: $\sigma^{Si} = 1.2 \times 10^{6} \dfrac{1}{\Omega \cdot m}$

Thermal conductivity: $k^{Si} = 56 \dfrac{W}{m \cdot K}$

Heat capacity: $C_p^{Si} = 1032 \dfrac{J}{kg \cdot K}$

Density: $\rho^{Si} = 2550 \dfrac{kg}{m^3}$

Surface emissivity: $\varepsilon_e^{Si} = 0.3$

Thermal expansion coefficient: $\alpha^{Si} = 1.4 \times 10^{-4} \dfrac{1}{K}$

Dynamic viscosity: $\mu^{Si} = 8 \times 10^{-4} \dfrac{kg}{m \cdot s}$

Marangoni coefficient: $\chi^{Si} = -2.5 \times 10^{-4} \dfrac{N}{m \cdot K}$

Vapor species

Species	Molar mass (g/mol)	σ_i (Å)	ε_i/k_B (K)	D_i^T (kg/(m·s))
Si	28	2.91	3036	5×10^{-10}
Si_2C	68	3.84	304.8	4×10^{-10}
SiC_2	52	4.077	304.8	8×10^{-10}
Ar	40	3.432	122.4	-

Appendix B
List of symbols

The symbols used in this thesis will be listed in the table below. The vector quantities are shown in bold. Some symbols that are not listed here can be found in the text.

Symbols	**Description**	**Units**
$\mathbf{A}$	Magnetic vector potential	V*s/m
$\mathbf{B}$	Magnetic flux density	T
C	Carbon concentration	mol/m^3
C_p	Specific heat	J/(kg*K)
$\mathbf{D}$	Electric displacement	C/m^2
D_{ij}	Diffusion coefficient	m^2/s
$\mathbf{E}$	Electric field	V/m
F_{amb}	Ambient view factor	
G	Irradiation	W/m^2
G_m	Mutual irradiation	W/m^2
G_{amb}	Ambient irradiation	W/m^2
$\mathbf{H}$	Magnetic field	A/m
$\mathbf{I}$	Identity matrix	
$\mathbf{J}$	Current density	A/m^2
J	Radiosity	W/m^2
K_p	Equilibrium constant	
L	Characteristic length	m
M	Mean molar mass	kg/mol
M_i	Molar mass	kg/mol

N_i	Molar flux	mol/(m^2*s)
P	Total pressure	Pa
P_i	Partial pressure	Pa
P_i^*	Equilibrium partial pressure	Pa
Q	Power density	W/m^3
Q_r	Total radiative heat flux	W/m^2
R	Universal gas constant	J/(mol*K)
Rg	Growth rate	m/s
S	Supersaturation	mol/m^3
T	Temperature	K
T_{amb}	Ambient temperature	K
V	Electric scalar potential	V
a	Activity	
g	Gravity	m/s^2
h	Exchange coefficient	W/(m^2*K)
i	Imaginary unit ($\sqrt{-1}$)	
j_i	Total diffusive flux	kg/(m^2*s)
k	Thermal conductivity	W/(m*K)
n	Normal of the surface	
p	Relative pressure	Pa
r	Radial coordinate	m
s	Tangential of the surface	
t	Time	s
v	Velocity	m/s
x_i	Mole fraction	
z	Axial coordinate	m
α_i	Evaporation coefficient	

β	Thermal expansion coefficient	1/K
χ	Marangoni coefficient	N/(m*K)
δ_D	Diffusion boundary layer thickness	m
δ_v	Momentum boundary layer thickness	m
ε_0	Electric permittivity of free space	$C^2/(N*m^2)$
ε_e	Emissivity	
ε_r	Relative electric permittivity (dielectric constant)	
ϕ	Azimuthal coordinate	rad
γ_i	Sticking coefficient	
Γ	Boundary integration	
κ	Thermal diffusivity	m^2/s
λ	Wavelength	m
μ	Dynamic viscosity	Pa*s
μ_0	Magnetic permeability of free space	N/A^2
μ_r	Relative magnetic permeability	
Ψ	Phase parameter	
υ	Kinematic viscosity	m^2/s
ω	Angular frequency	rad/s
ω_i	Mass fraction	
Ω	Domain integration	
Ω_{seed}	Seed rotation speed	rad/s
ξ	Angle of deviation	rad
ρ	Density	kg/m^3
ρ_f	Free charge density	C/m^3
σ	Electrical conductivity	1/ (Ω*m)
θ	Angle defined in a unit circle	rad
$\bar{\tau}$	Viscous stress tensor	Pa

Résumé

Introduction

Le carbure de silicium (SiC) est un matériau semi-conducteur à large bande interdite. C'est un composé solide composé de 50 % de carbone et 50 % de silicium. En ce qui concerne la structure des atomes de carbone et de silicium dans le SiC, tous les atomes de silicium (carbone) sont entourées de quatre atomes de carbone (silicium) formant un tétraèdre (Fig. 1). Le SiC a des performances supérieures par rapport aux autres matériaux semi-conducteurs, par exemple un champ de claquage diélectrique plus élevé, une conductivité thermique plus élevée, une plus grande mobilité électronique, une plus grande vitesse de saturation des électrons (Fig. 2). Cela rend le SiC avantageux pour les dispositifs électroniques et notamment pour les applications haute fréquence, haute température et haute puissance.

Dans le processus de cristallisation, le SiC établit un cas particulier du polymorphisme appelé polytypisme qui est le phénomène de polymorphisme unidimensionnel qui prend des structures cristallines différentes avec la même composition chimique. La différence entre les séquences d'empilement conduit à des propriétés différentes de chaque polytype, par exemple, la largeur de bande interdite, la tension de claquage diélectrique. Cela élargit le champ d'application du SiC. Les polytypes les plus importants technologiquement sont le 3C, le 4H, le 6H et le 15R-SiC.

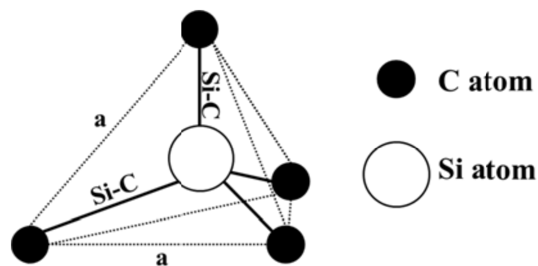

Fig. 1 La structure tétraédrique des atomes de Si et de C dans le SiC

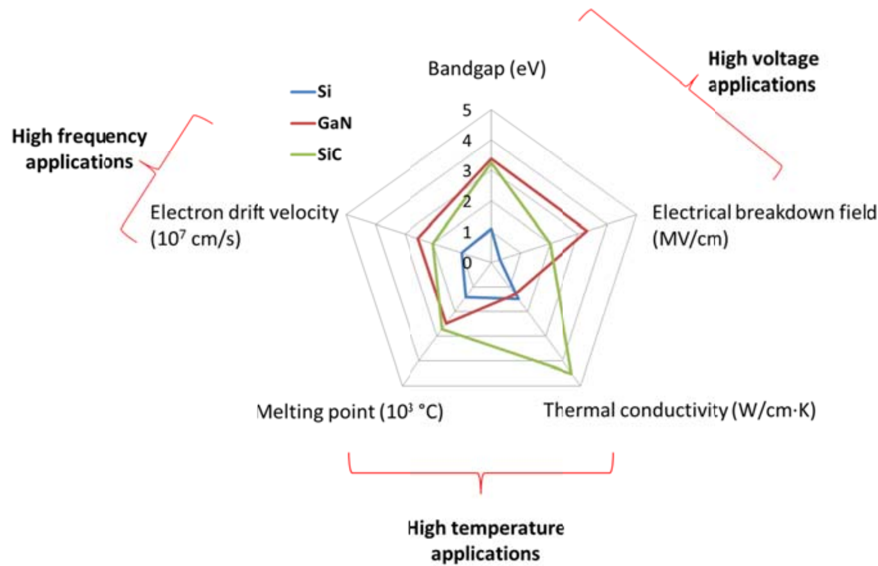

Fig. 2 Comparaison des propriétés du Si, GaN et SiC pour les applications en électronique de puissance

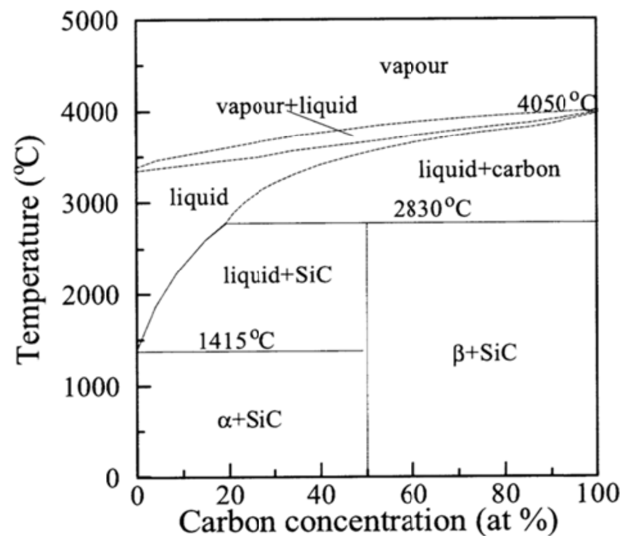

Fig. 3 Diagramme de phase du système Si-C où α et β sont respectivement les solutions solides du C dans le Si et du Si dans le C

A partir du diagramme de phase (Fig. 3), on peut remarquer que le SiC n'existe pas en phase liquide puisque le mélange est non-congruent. Deuxièmement, la solubilité du C dans le Si liquide est très basse, moins de10% pour des températures inférieures à 2000°C. De plus, le diagramme de phase du Si-C à basse pression suggère que le SiC commence à sublimer à une

température de l'ordre de 1800°C. Ce qui veux dire que le procédé de croissance du SiC nécessite de très hautes températures et que les méthodes conventionnelles utilisées pour la croissance du Si et des autres semi-conducteurs, basées sur la solidification à partir de la phase liquide ne sont pas utilisables. Il est plus souvent difficile de stabiliser une structure cristallographique (polytypisme) parmi plusieurs structures cristallines possibles. Des techniques alternatives de croissance sont alors nécessaires pour réaliser la croissance du SiC. Concernant le procédé de croissance massive, plusieurs techniques sont étudiées, comme la méthode de Lély, la méthode Lély modifiée, le dépôt chimique à haute température (HTCVD), le transport physique en phase vapeur (PVT) à alimentation continue (CF-PVT) et le procédé de croissance en solution (TSSG).

Pour la croissance de monocristaux de SiC, le procédé de croissance en phase vapeur (PVT) a montré ses capacités dans le domaine de la croissance de cristaux de grande taille et de haute qualité. Démonstration a été faite qu'il était possible de réaliser des wafers de 6 pouces de diamètre. Des wafers sans défauts sont censés être réalisé. Toutefois, seuls les polytypes 4H et 6H-SiC sont disponibles dans le commerce. Il n'y a aucun wafers 3C ou 15R-SiC avec une qualité suffisante pour les dispositifs électroniques en raison des difficultés à obtenir des conditions de croissance stable pour ces deux polytypes.

En outre, la possibilité de la phase liquide, surtout le procédé de croissance en solution (TSSG) a focalisé une attention particulière en matière de recherche et développement sur les dix dernières années. Les températures de croissance "inférieures" utilisés dans ce procédé et les conditions proches de l'équilibre thermodynamique sont censés fournir un meilleur contrôle de la génération de défauts. Bien qu'inférieur à la PVT, les températures de croissance sont encore élevés, ce qui rend le processus très difficile à contrôler.

En raison des températures élevées (typiquement de l'ordre de 2000°C), il n'y a aucun moyen de mesurer les paramètres du procédé. C'est la raison pour laquelle l'expérience seule ne sera pas en mesure de fournir une pleine compréhension des phénomènes et contrôler le procédé. Mes propos sont illustrés par la figure 4. Sans compter que compte tenu de la géométrie du réacteur, les paramètres du réacteur qui peuvent être contrôlés sont la fréquence des courants circulant dans l'inducteur, la température sur les zones supérieures et inférieures du creuset, la pression et la vitesse de rotation du substrat. Afin d'établir un lien entre les paramètres

contrôlables et les paramètres observables après l'expérience, une approche empirique est souvent utilisée.

Cependant une telle approche, ne peut pas être en mesure de fournir des preuves concrètes étayant les résultats. Une autre approche concerne l'utilisation de la modélisation numérique comme un outil de caractérisation du procédé permettant d'accéder aux paramètres physico-chimiques et à leurs distributions dans le réacteur comme par exemple la température, la concentration des espèces chimiques en jeu, la vitesse du fluide. Cette approche macroscopique permet de créer un lien entre l'expérience et la caractérisation et agit comme une clé pour ouvrir peu à peu la boîte noire du procédé, ayant premièrement pour résultat la compréhension des phénomènes physiques et chimiques et deuxièmement un meilleur contrôle du procédé de croissance.

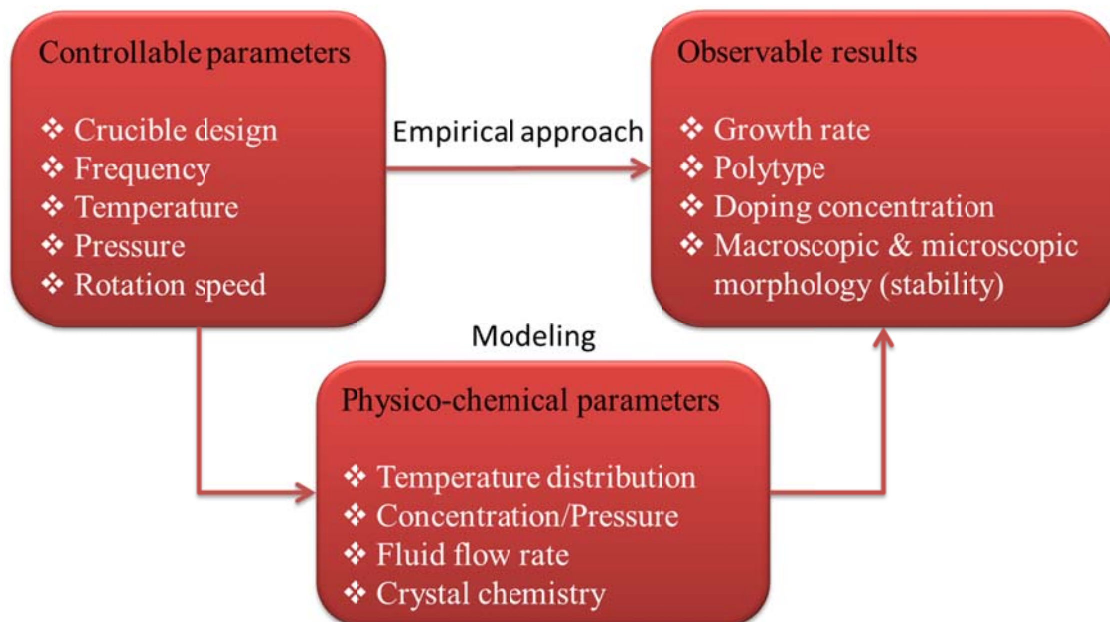

Fig. 4 Diagramme montrant que la modélisation peut-être une approche alternative permettant d'établir des liens entre les paramètres contrôlables et les résultats observables

En effet, de nombreuses recherches sur la modélisation des procédés de croissance SiC ont été réalisées depuis plus de 20 ans. Sans compter les nombreux succès dans l'utilisation de la modélisation numérique pour décrire les procédés de croissance de SiC, il y a encore quelques enjeux majeurs qui ne sont pas traités de manière satisfaisante, même dans le cas d'un procédé

plus mature, comme la PVT. Il y a (au moins) trois questions principales en suspens pour une meilleure compréhension du procédé PVT.

i.) Comment décrire correctement les réactions hétérogènes aux interfaces solide-vapeur ?
ii.) Il y a t'il un lien entre la chimie et le polytype du cristal ?
iii.) Comment peut-on décrire l'incorporation d'un dopant ?

En ce qui concerne le procédé TSSG, le contrôle de la convection du fluide et la stabilité du front de croissance sont les principales interrogations auxquelles il faudra répondre afin d'être en mesure d'élaborer un cristal de SiC de haute qualité, dans le but de fabriquer des dispositifs électroniques.

De ce fait, dans ce travail de thèse, nous visons à utiliser la modélisation numérique comme un outil permettant de répondre aux questions fondamentales et technologiques difficiles, tant pour le procédé de PVT industriellement utilisé que pour le processus TSSG émergent. Les résultats de la modélisation numérique seront comparés et discutés avec nos résultats expérimentaux disponibles ou avec les données proposés dans la littérature.

Table 1 Comparaison des différentes méthodes numériques

Method	**FDM**	**FVM**	**FEM**
Principle	Taylor development	Strong form (Stokes formula)	Weak form (Galerkin method)
Geometry	simple	complex	complex
Discretization	regular grid	structured/unstructured	structured/unstructured
Programming	easy	easy for structured difficult for unstructured	difficult
Matrix	sparse	sparse	sparse
Boundary conditions	to be constructed	to be constructed	naturally constructed
Implementation	rarely implemented in commercial software	available in commercial software especially for: - Fluid mechanics - Heat transfer - Coupled multiphysics	available in commercial software especially for: - Solid mechanics - Electromagnetism - Heat transfer - Coupled multiphysics

Les procédés de croissance SiC mettent en jeu de nombreux phénomènes physiques et chimiques. Le système d'équations contient des fonctions de plusieurs variables, des inconnues, ainsi que leurs dérivées partielles ; l'ensemble du procédé peut être décrit par un système d'équations aux dérivées partielles (EDP). En fait, les équations aux dérivées partielles sont issues naturellement des lois de conservation de la masse et de la concentration des espèces, du moment, de l'énergie, du flux magnétique etc... . Tous ces phénomènes conservatifs habituellement exprimées en terme de bilan sous la forme d'équations intégrales sur un domaine, sont traduites mathématiquement sous la forme d'équations aux dérivées partielles exprimées dans le cadre de la physique des milieux continus. Ainsi, le système peut-être résolu de façon exacte dans des cas simplistes et de façon approximative (méthodes numériques) dans des cas réalistes.

Dans le but d'obtenir des solutions réalistes sans simplifications excessives, plusieurs méthodes numériques de discrétisation des équations aux dérivées partielles ont été proposés, par exemple, la méthode des différences finies (MDF), la méthode des volumes finis (MVF) et la méthode des éléments finis (MEF). Même si les approches de résolution des équations aux dérivées partielles sont différentes, elles partagent des caractéristiques communes importantes. Tout d'abord le domaine continu est discrétisé en un ensemble de sous-domaines discrets appelés éléments dans lesquels leurs lois de comportement sont définis par un nombre fini de paramètres.

De plus, les fonctions approchées sur chaque éléments doivent respecter les conditions de continuité entre les différents éléments du domaine. Les avantages et les inconvénients de l'utilisation de ces méthodes numériques sont synthétisés dans le tableau 1. La méthode des différences finies est relativement facile à programmer, mais sa capacité est limitée à des géométries simples et une grille régulière. La méthodes des éléments finis permet de traiter de façon naturelle les conditions aux interfaces entre deux milieux différents, même si cette méthode est moins triviale pour la mécanique des fluides que la méthode des volumes finis. Étant donné que la croissance des cristaux est principalement associée à des phénomènes aux interfaces et donc mathématiquement à des problèmes de conditions aux limites, la méthode des éléments finis est plus adaptée pour le sujet de la thèse de doctorat. Tout au long de cette thèse, un logiciel commercial basé sur la méthode des éléments finis servira comme un outil de

résolution du système d'équations aux dérivées partielles, associé à un ensemble de conditions aux limites régissant le procédé de croissance de SiC.

Chauffage par induction et transfert de chaleur

La distribution de température dans la cavité de croissance a été étudiée en résolvant les équations décrivant le chauffage par induction couplées aux transferts dans l'ensemble des régions du four. Tous les calculs ont été menées par méthode des éléments finis (FEM) dans l'hypothèse d'une géométrie axisymétrique en deux dimensions, puisque le réacteur de croissance peut-être considéré de symétrie axiale. Le chauffage par induction électromagnétique est une méthode pratique pour le chauffage haute température du creuset. Dans ce régime de chauffage par induction RF, le phénomène électromagnétique est décrit par les équations de Maxwell qui permettent de calculer la distribution de champ électromagnétique. L'équation pour résoudre le problème électromagnétique peut être réduite à l'équation de la magnétodynamique en potentiel vecteur :

$$\frac{1}{\mu_0 \mu_r} \nabla \times \nabla \times \mathbf{A} + \left(i\omega\sigma - \omega^2 \varepsilon_0 \varepsilon_r \right) \mathbf{A} - \sigma \mathbf{v} \times \left(\nabla \times \mathbf{A} \right) = \mathbf{J}_e . \quad (1)$$

Les courants de Foucault induits sont générés selon la loi de Lenz. Les courants induits circulant dans les parties résistives (conductrices) provoque une dissipation d'énergie nommée effet Joule. Le creuset est chauffé en conséquence par effet de Joule, la densité de puissance fournie peut être formulée par :

$$Q = \sigma \langle -\mathbf{E} \cdot \mathbf{J} \rangle = \frac{1}{2} \sigma \omega^2 \left(\mathbf{A} \cdot \mathbf{A}^* \right). \quad (2)$$

La densité de pertes Joule servira comme source dans l'équation de transfert de chaleur. Trois mécanismes sont considérés : la conduction, la convection et le rayonnement. L'équation de l'énergie utilisée pour calculer la distribution de température dans le réacteur de croissance est de la forme :

$$C_p \nabla \cdot \left(\rho \mathbf{v} T \right) - \nabla \cdot \left(k \nabla T \right) = Q . \quad (3)$$

Un ensemble de conditions aux limites sont formulées pour résoudre le problème de transfert de chaleur. Tout d'abord, sur l'axe de symétrie on impose un flux de chaleur nul. En second lieu, les conditions aux limites des flux thermiques associées au rayonnement sont fixées aux limites des cavités. L'expression pour le rayonnement de surface-surface en supposant que les corps gris sont idéaux, est définie par :

$$-\mathbf{n} \cdot (-k\nabla T) = \varepsilon_e \left(G - \sigma T^4\right), \tag{4}$$

puis la condition aux limites pour le rayonnement de surface vers l'ambiant s'écrit :

$$-\mathbf{n} \cdot (-k\nabla T) = \varepsilon_e \sigma \left(T_{amb}^4 - T^4\right). \tag{5}$$

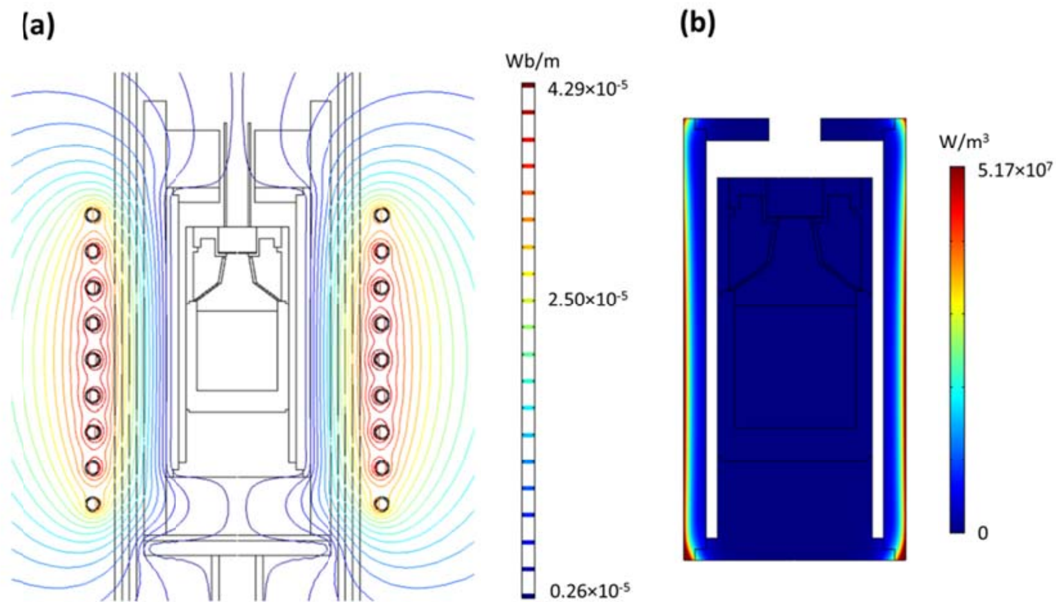

Fig. 5 (a) Isovaleurs du potentiel vecteur magnétique dans le réacteur et (b) densité de pertes résistives dissipée dans le réacteur

La distribution du potentiel vecteur magnétique à la température de croissance est montrée sur la Fig. 5 a. Les pertes Joule sont déduites de cette distribution. La puissance de chauffe est axée principalement sur la surface extérieure du four comme indiqué en Fig. 5 b en raison de la profondeur de pénétration du champ électromagnétique en haute fréquence (100 kHz). Ainsi le problème de transfert de chaleur dans le réacteur à l'aide de la distribution de pertes Joule calculée peut-être résolu. La distribution de température dans le réacteur est obtenu et illustré sur

la Fig. 6. La position de la bobine est ajustée afin de créer le point chaud dans la poudre et le point "froid" sur le substrat. Ainsi, le gradient de température créé la force motrice pour la sublimation de la poudre source et la condensation sur le substrat.

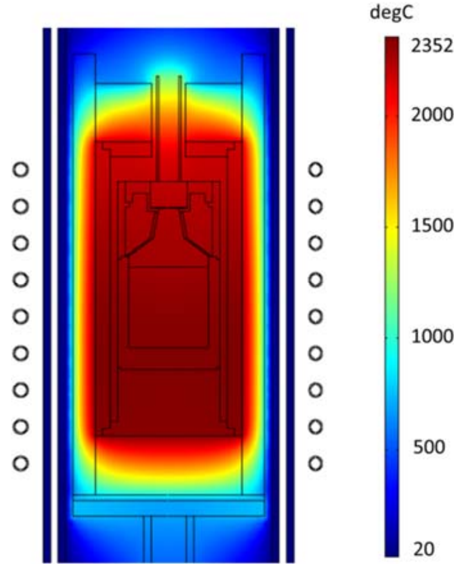

Fig. 6 Distribution de température (a) dans le réacteur de croissance et (b) dans la cavité de croissance

Transfert de masse

Le transport de masse des espèces dans le mélange gazeux est résolu en couplant le transport d'espèces et la distribution de vitesse du mélange gazeux tout en utilisant le profil de température calculé par la résolution des équations décrivant le chauffage par induction tel qu'il est décrit dans le paragraphe précédent. La forme générale de l'équation (équation de Navier-Stokes) pour le mouvement du gaz est exprimée par :

$$\rho(\mathbf{v}\cdot\nabla)\mathbf{v} = \nabla\cdot\left(-p\mathbf{I} + \mu\left(\nabla\mathbf{v} + (\nabla\mathbf{v})^T\right) - \frac{2}{3}\mu(\nabla\cdot\mathbf{v})\mathbf{I}\right) + \mathbf{F}\,. \tag{6}$$

Afin de tenir compte de la conservation de la masse, l'équation de continuité de la masse est prise en compte :

$$\nabla\cdot(\rho\mathbf{v}) = 0\,. \tag{7}$$

En outre, la conservation de la i^{ème} espèce dans un mélange gazeux est donnée par l'équation de bilan des espèces :

$$\nabla \cdot \mathbf{j}_i + \rho(\mathbf{v} \cdot \nabla)\omega_i = 0 . \quad (8)$$

Le flux molaire N_i aux frontières réactives est décrit par la somme de deux contributions :

$$\mathbf{N_i} = \frac{\mathbf{j_i}}{M_i} + \frac{\rho x_i}{M}\mathbf{v} . \quad (9)$$

Le premier et second terme sont respectivement les flux molaires diffusif et convectif. À l'interface solide-vapeur, le changement de volume important causé par les réactions de sublimation ou de la condensation produit un flux d'advection, nommé aussi vitesse de Stefan et s'écrit de la façon suivante :

$$\mathbf{v} = -\left(\frac{RT}{PM} \sum_{i=1}^{N-1} M_i N_i \right)\mathbf{n} . \quad (10)$$

Ici, la somme comprend uniquement les espèces réactives, car le gaz inerte ne participe pas aux réactions hétérogènes. Les équations (9) et (10) montrent qu'il existe un couplage entre l'écoulement du fluide et le transfert de masse puisque la vitesse du gaz à la frontière de la réaction doit être calculé à partir du flux net des espèces.

Le gradient de température est calculé à partir de la température à la surface libre de la poudre de SiC et la température du substrat. La température à la surface de la poudre est supérieure à celle du substrat et créé ainsi une force motrice pour la croissance du SiC. À haute température, la poudre sublime produisant les trois espèces gazeuses principales : Si, Si_2C, SiC_2. Ces espèces gazeuses seront transportés à la fois par diffusion et convection. Ensuite l'espèce gazeuse sera à la fois condensé (ou adsorbé) et sublimé sur le substrat. Ainsi, le taux de dépôt net à l'interface de cristal-vapeur du substrat est la différence entre les flux adsorbés et désorbés. A l'interface le flux molaire de l'espèce réactive est calculé à partir du modèle de Hertz-Knudsen et peut être écrit de la façon suivante :

$$N_i = N_i^{ads} - N_i^{des} = \left(\gamma_i P_i - \alpha_i P_i^*\right)\sqrt{\frac{1}{2\pi M_i RT}} \quad (11)$$

où N_i est le flux molaire net de la i[ème] espèce gazeuse participant à des réactions hétérogènes, P_i est la pression partielle P_i^* est la pression partielle d'équilibre, M_i est la masse molaire, R est la constante des gaz parfait, T est la température, γ_i et α_i sont respectivement les coefficients de collage et d'évaporation.

La pression partielle de l'espèce réactive peut être calculée par la modélisation globale du transfert de chaleur et du transport de masse. Les trois phases en équilibre hétérogène (SiC-C-gaz avec variance=0) ne sont pas pris en compte dans ce travail, donc la pression partielle d'équilibre ne peut pas être calculée directement à partir de la température de la phase solide (SiC-gaz avec variance = 1) parce que la SiC a été considérée comme une solution solide (s, s). Les atomes de Si et de C peuvent être considérés dans le composé non-stoechiométrique Si_xC_y comme à l'équilibre :

$$Si_xC_y = x\text{Si (in } SiC_{(s,\,s)}) + y\text{C (in } SiC_{(s,\,s)}) \quad \text{with} \quad K_p^1(T) = \frac{a_{Si} \cdot a_C}{a_{SiC}}. \quad (12)$$

La constante d'équilibre K^1_p est écrite pour x et y proche de l'unité, puisque le cristal de SiC est proche de la stœchiométrie. L'activité des composés stœchiométriques est égale à l'unité par définition de l'état standard, donc $a_{SiC} = 1$. La constante d'équilibre K^1_p est calculée à partir des enthalpies libres provenant de la base de données thermochimique JANAF. La formation de trois espèces gazeuses principales à l'interface cristal-vapeur peut être attribuée aux réactions hétérogènes suivantes :

$$\text{Si (in } SiC_{(s,\,s)}) = \text{Si(g)} \quad \text{with} \quad K_p^2(T) = \frac{P_{Si}^*}{a_{Si}}, \quad (13)$$

$$2\text{Si (in } SiC_{(s,\,s)}) + \text{C (in } SiC_{(s,\,s)}) = Si_2C\text{(g)} \quad \text{with} \quad K_p^3(T) = \frac{P_{Si_2C}^*}{a_{Si}^2 a_C}, \quad (14)$$

$$\text{Si (in } SiC_{(s,\,s)}) + 2\text{C (in } SiC_{(s,\,s)}) = SiC_2\text{(g)} \quad \text{with} \quad K_p^4(T) = \frac{P_{SiC_2}^*}{a_{Si} a_C^2}. \quad (15)$$

L'équation de bilan massique exprimant l'incorporation stœchiométrique d'atomes de Si et C dans le cristal en croissance, ferme l'ensemble des équations :

$$N_{Si} + 2 \cdot N_{Si_2C} + N_{SiC_2} = N_{Si_2C} + 2 \cdot N_{SiC_2} \ . \quad (16)$$

En substituant (11) et (15) dans (16), on obtient l'équation représentant le couplage entre la modélisation numérique et la thermodynamique, ainsi la chimie des cristaux de SiC en terme d'activité des composants solides peut être déterminée.

À l'aide de l'ensemble des équations gouvernant la mécanique des fluides et le transport d'espèces d'une part et l'ensemble des conditions aux limites d'autre part, on obtient les résultats de simulation globale. La distribution de sursaturation calculée à partir de la différence entre la pression de l'espèce limitante (carbone) et sa pression partielle d'équilibre (SiC-gaz) dans la cavité de croissance est indiquée sur la Fig. 7 a. La zone où s'effectue la croissance de carbure de silicium est caractérisée par une sursaturation positive. En dehors de la zone du substrat, le dépôt dans la partie inférieure du guide graphite est prédit. Ces dépôts indésirables limitent la croissance du cristal de SiC en consommant la poudre de carbure de silicium.

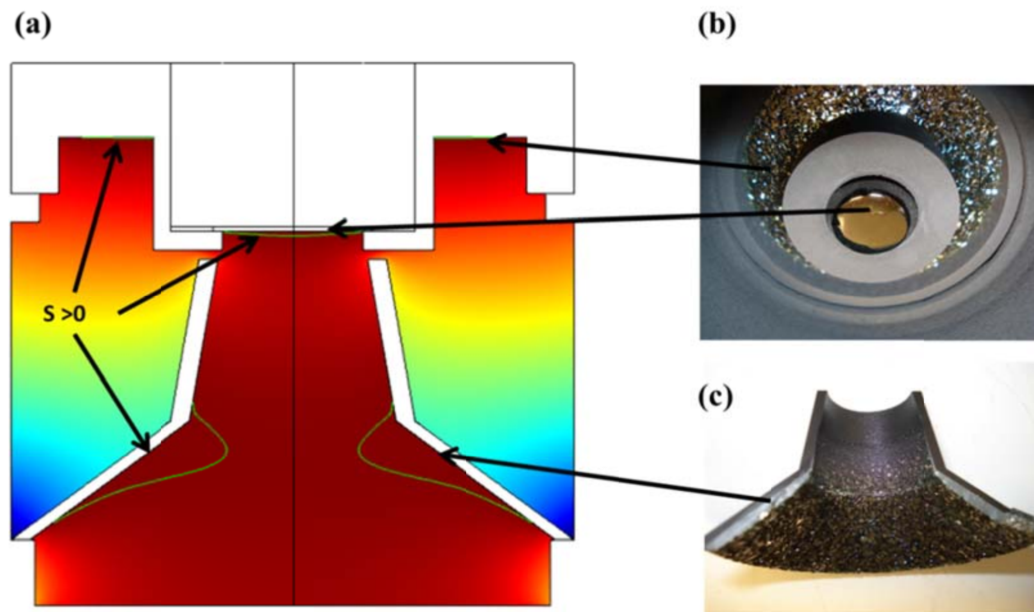

Fig. 7 (a) distribution de la sursaturation (S) dans la cavité de croissance et les observations expérimentales (b) sur le support du germe (c) sur le guide en graphite

Les dépôts à la périphérie du porte substrat en graphite est également prédit par le modèle. La chambre supplémentaire créée par la modification du porte-substrat permet de générer un autre dissipateur de chaleur dans la cavité de croissance. Ce dissipateur de chaleur supplémentaire ayant une température plus basse par rapport à la partie en graphite à proximité

du substrat contribue à supprimer la croissance des polycristaux de SiC près du monocristal de SiC. Il y a néanmoins un dépôt sur le porte-substrat à proximité du germe, mais pas sur la partie supérieure du guide en graphite. Ailleurs, sur le creuset en graphite entourant la cavité de croissance, sont également exempts de dépôt de SiC poly cristallin. Ces résultats sont en bon accord avec les observations expérimentales (figure 7 b-c).

La dépendance de la vitesse de croissance avec la pression est illustrée à la Fig. 8 a. La vitesse de croissance calculée à partir de la modélisation est en bon accord avec les expériences. La vitesse de croissance diminue avec l'augmentation de la pression totale. Comme mentionné précédemment, le flux total d'espèces se compose des deux principales composantes : flux diffusif et convectif. La vitesse de croissance totale peut être également décomposée en deux contributions qui sont illustrées à la Fig. 8 b. La contribution de la diffusion est toujours supérieure à celle de la convection. À haute pression de croissance, la vitesse de croissance totale est presque similaire à la vitesse de croissance calculée uniquement à partir de la diffusion. À mesure que la pression diminue, la contribution de la convection se renforce.

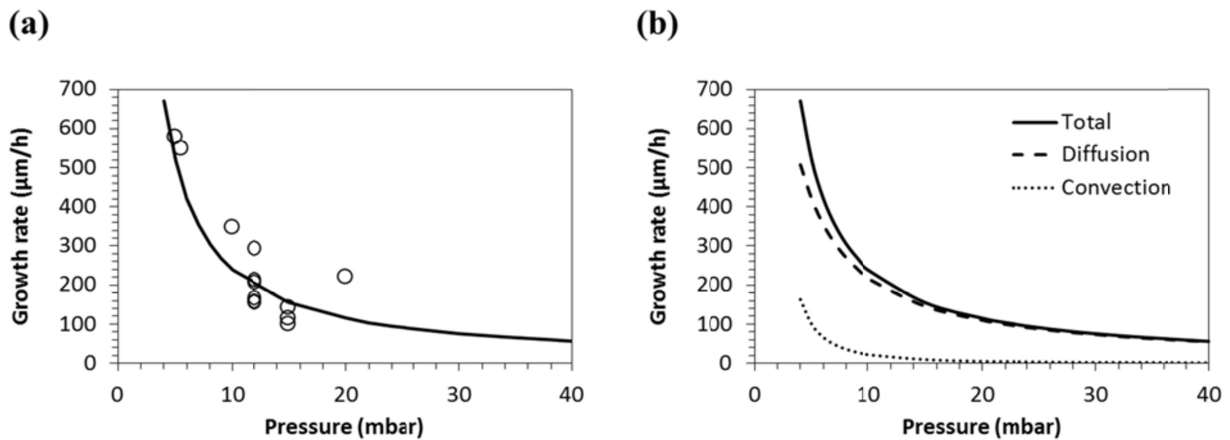

Fig. 8 (a) vitesse de croissance en fonction de la pression, comparée avec les résultats expérimentaux et les contributions (b) de la diffusion et de la convection dans le calcul de la vitesse de croissance

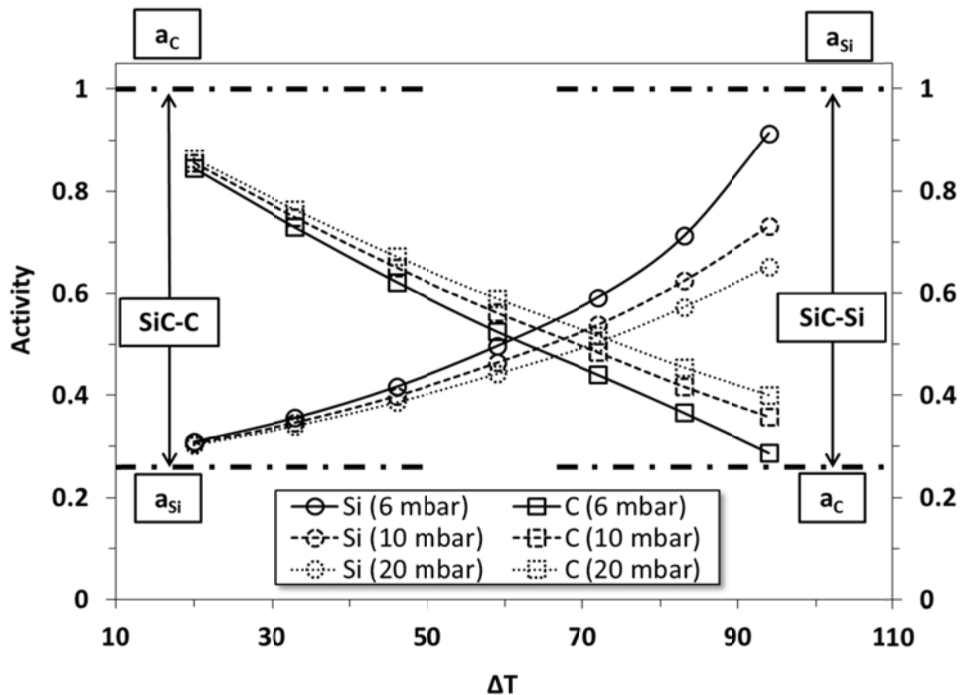

Fig. 9 Activités de Si et C dans le cristal de SiC solide en fonction de la différence de température entre le germe et la source et en fonction de la pression. La température du germe est fixée à 2 225 ° C (±2 ° C). Les lignes en traits pointillés montrent la limite des activités à la frontières des phases SiC-Si et SiC-C

En sachant que le modèle est correctement validé avec les expériences, il est possible d'aller plus loin dans la description de la chimie du cristal en se concentrant sur la variation des activités des atomes de C et de Si avec les paramètres du procédé. Pour une température constante de substrat, l'effet de la pression et de la différence température ($\Delta T = T_{source}$-$T_{substrat}$) entre la source et le substrat sur les activités des atomes de Si et de C dans le solide SiC est montré puis comparé aux activités des atomes de Si et de C aux limites des phases SiC-C et SiC-Si (Fig. 9). Sur cette figure, les activités et les différences de température ΔT sont prises sur l'axe de symétrie. Les différences de température ΔT sont obtenus en ajustant la position de la bobine. À faible ΔT, les activités des atomes de Si et C sont à proches de la frontière de la phase SiC-C tout en se rapprochant progressivement vers la frontière de la phase SiC-Si en augmentant ΔT. Si ΔT est trop grand, soit en augmentant la température de la source ou en diminuant la température du cristal, le cristal ne sera plus en mesure de produire suffisamment de flux arrière de Si et à ce moment-là, la condensation va produire un mélange de SiC-Si. Ceci peut être vu en extrapolant

les courbes de la figure 9. Si ΔT est négatif, ce qui signifie un gradient inverse de température, la composition du cristal doit être un mélange de SiC-C si on s'appuie sur l'extrapolation. C'est le cas lorsque le substrat sublime au lieu de croitre, il se graphitise à cause de la sublimation non congruente.

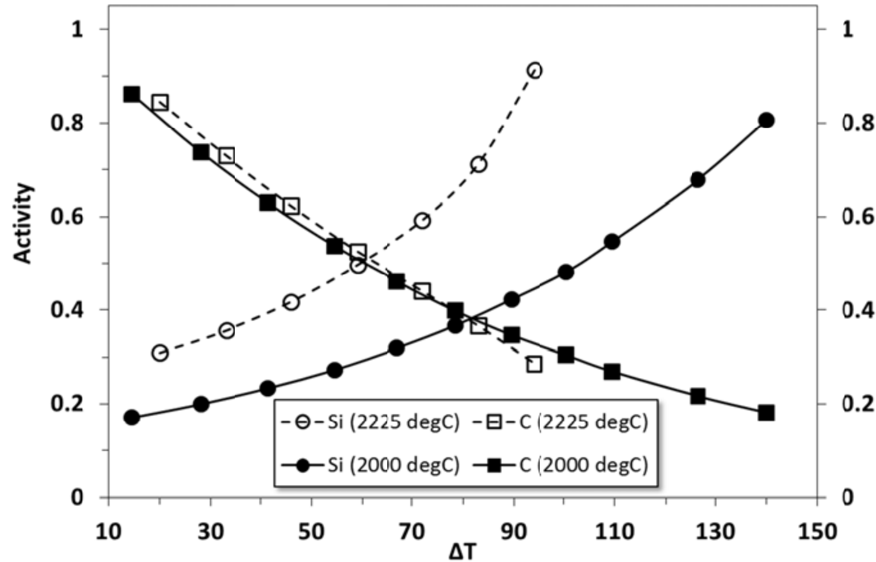

Fig. 10 Comportement des activités des atomes de Si et de C dans le cristal de SiC en fonction de ΔT mais pression identique de 6 mbar

Depuis la phase SiC-C vers les limites de la phase SiC-Si, la variation des activités est augmenté quand on diminue la pression totale. Ce comportement est attribué aux interactions entre les espèces gazeuses réactives et le gaz porteur l'argon. Puisque l'argon ne s'incorpore pas dans le composé SiC, il y a un flux de diffusion arrière fort de ce gaz du substrat vers la source qui retarde les taux de sublimation et de dépôt. En diminuant la pression d'argon on améliore le taux de sublimation et l'excès de Si dans la composition du gaz. En conséquence il y aura plus de flux arrière de Si. En conséquence, les activités de Si et C sont décalées vers la limite de la phase SiC-Si.

Le comportement des activités de Si et de C en solution solide SiC en fonction de ΔT en fonction de la température du substrat est illustrée à la Fig. 10. Les résultats sont comparés avec le cas précédent. On voit que la zone de croissance d'une phase pure SiC est plus large, lorsque que l'on utilise une température du substrat inférieure, alors un plus grand écart de température

ΔT est utilisable. De plus, le croisement entre les deux activités se déplace vers un ΔT supérieur. La différence dans les flux de Si et de C condensés sur la surface du cristal est plus petite à plus basse température tout en gardant un ΔT constant. Le système requiert donc un ΔT plus grand afin de passer de carbone riche à silicium riche dans le cristal de SiC.

Les résultats obtenus par la prise en compte de la chimie du cristal peuvent être utilisés en corrélation avec les observations expérimentales. Concernant tout d'abord l'apparition du polytype cubique de SiC, les nombreux résultats expérimentaux disponibles dans la littérature suggèrent que le polytype cubique de carbure de silicium est préférable pour la croissance sous condition riche en silicium. Ainsi, nous pouvons proposer une ligne directrice pour la stabilisation du polytype de SiC selon la chimie à la surface de croissance prévue à partir de notre modèle. Tout d'abord, le milieu de croissance offrant une chimie du cristal la plus proche de la limite de la phase SiC-Si, c'est à dire, un ΔT important ou une pression basse, devrait se traduire par une probabilité plus élevée de nucléation de polytype cubique.

Les imperfections du cristal comme les contraintes et les défauts devraient être également minimisées afin d'éviter la transformation du polytype. En outre, la croissance sous ΔT faible ou haute pression, ce qui conduit à une chimie du cristal plus près de la limite de la phase SiC-C devrait être préférable pour stabiliser le polytype hexagonal. Par ailleurs, afin de quantifier l'incorporation de dopant, les informations prévues à partir de notre modèle pourraient être corrélées avec la couverture de la surface SiC. Par exemple, les conditions de croissance, ce qui porte la chimie de surface loin de la limite de la phase SiC-C devrait multiplier la compétitivité de l'azote offrant le plus haut taux d'incorporation d'azote selon le modèle de compétition de site. Néanmoins, cela nécessite l'extension du modèle afin d'inclure l'azote dans le système.

Top Seeded Solution Growth (TSSG) process

La configuration typique du réacteur TSSG est illustrée à la Fig. 11. Du silicium liquide pur est utilisé comme solvant et est placé dans un creuset graphite haute densité. Similaire au processus PVT décrit précédemment, le chauffage par induction est utilisé comme méthode pour chauffer le creuset en graphite. Pratiquement toutes les équations décrivant les phénomènes physiques et la procédure numérique sont les mêmes. Dans ce procédé, le creuset en graphite n'agit pas seulement comme un conteneur, mais aussi comme source de carbone. Ainsi, la

compréhension du transport du carbone depuis la source, c'est-à-dire depuis le creuset en graphite jusqu'au cristal est un enjeu majeur pour le développement d'une grande partie du procédé de croissance en solution de SiC. Ce transport de carbone repose sur un modèle d'écoulement de fluide qui est en fait loin d'être maitrisé. Ce problème deviendra d'autant plus critique que nous nous intéresserons sur la croissance de cristaux de grande taille, de grande qualité et à haute température. En pratique, la distribution de carbone et le transport dans le liquide affectera directement :

i.) le contrôle de la nucléation et la stabilité du front de croissance,
ii.) le contrôle des dépôts parasites,
iii.) le contrôle de la croissance dendritique après nucléation,
iv.) l'augmentation de la vitesse de croissance.

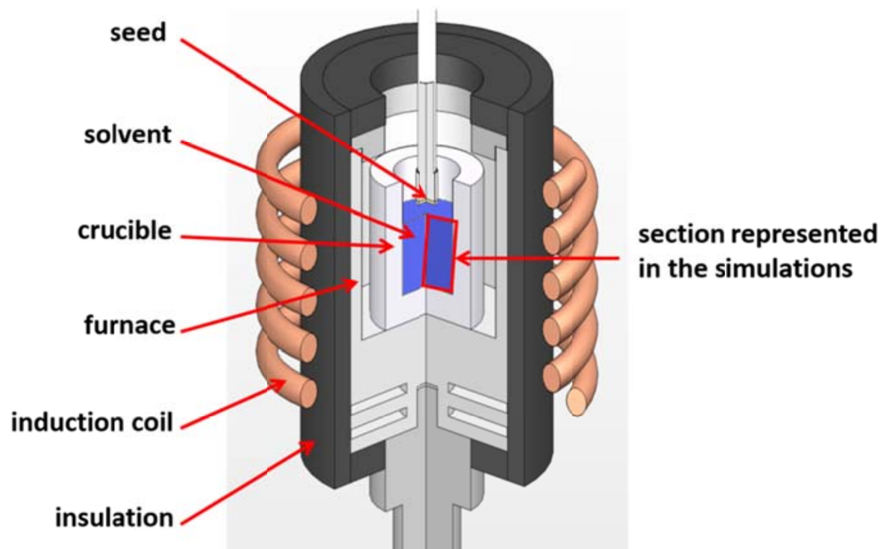

Fig. 11 Représentation schématique du réacteur TSSG. Le parallélépipède rouge est la section liquide que l'on utilisera pour la représentation des résultats de modélisation présentés plus loin dans ce chapitre

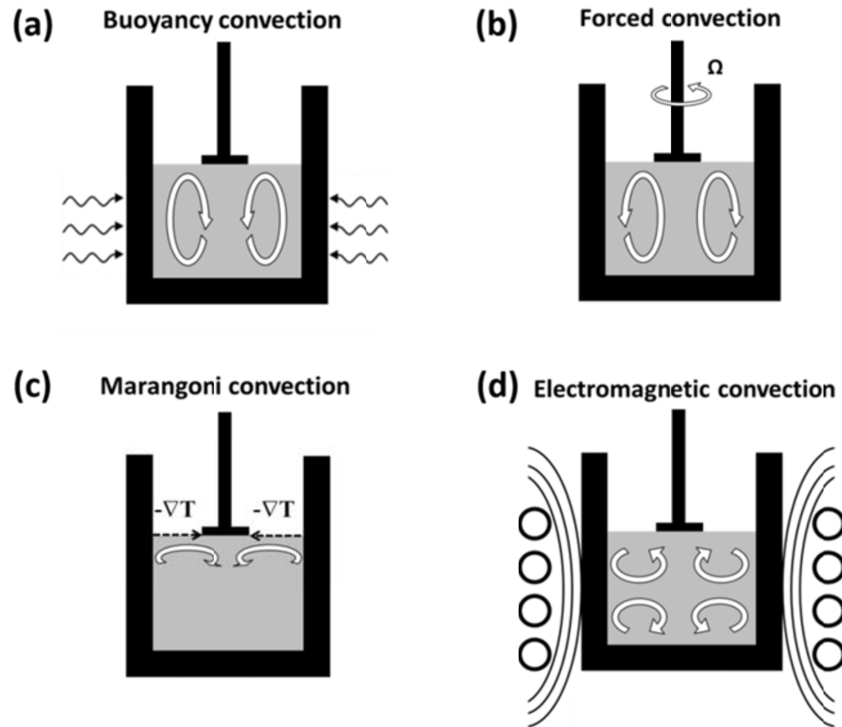

Fig. 12 Les principales contributions régissant les mouvements du fluide : (a) convection naturelle, (b) convection forcée, (c) convection Marangoni et (d) la convection électromagnétique

Dans le cas du silicium pur, la solubilité du carbone est toujours très faible pour des températures inférieures à 2000°C. Ainsi la contribution à la convection solutale peut être négligée et les mouvements du fluide sont régis principalement par quatre modes de convection (Fig. 12): la convection naturelle due à la variation de la densité du liquide en fonction de la température, la convection forcée conséquence de la rotation du cristal ou la rotation du creuset, la convection Marangoni liée à la tension de surface dépendant de la température du liquide et la convection électromagnétique provoquée par les phénomènes électromagnétiques. Toutes les contributions sont implémentées dans le modèle du procédé de croissance TSSG, en y associant des conditions aux limites pour le transport de carbone. Ce type de conditions aux limites sont mises en œuvre en spécifiant la concentration de carbone à l'équilibre aux interfaces liquide-solide.

Les paramètres accessibles dans le liquide à l'aide de la modélisation numérique sans rotation du germe sont indiqués sur la Fig. 13. La distribution de la température dans le liquide

montre l'emplacement du point chaud dans le coin inférieur du creuset, alors que le point froid se situe au niveau du cristal (Fig. 13 a). La différence de température axiale est d'environ 4°C correspondant à un gradient de température axial de 2˚C/cm. Le résultat combiné des différents modes d'écoulements convectifs est complexe (Fig. 13 b). L'écoulement est principalement causé par la convection électromagnétique en raison de la forte densité de force de Lorentz concentrés près de la paroi du creuset. On observe un écoulement direct du fond du creuset vers le germe le long de l'axe de symétrie et un écoulement comprenant des vortex à proximité du mur du creuset. La distribution de la concentration de carbone est directement lié au modèle d'écoulement. Une forte teneur en carbone est observée à proximité de l'axe de symétrie (c Fig. 13). La sursaturation en silicium liquide est illustrée à la Fig. 13d. Le carbone est dissout du creuset en graphite dans la zone sous-saturée (S<0), transport par diffusion et convection et cristallise dans la zone sursaturée (S>0), c'est-à-dire sous le germe.

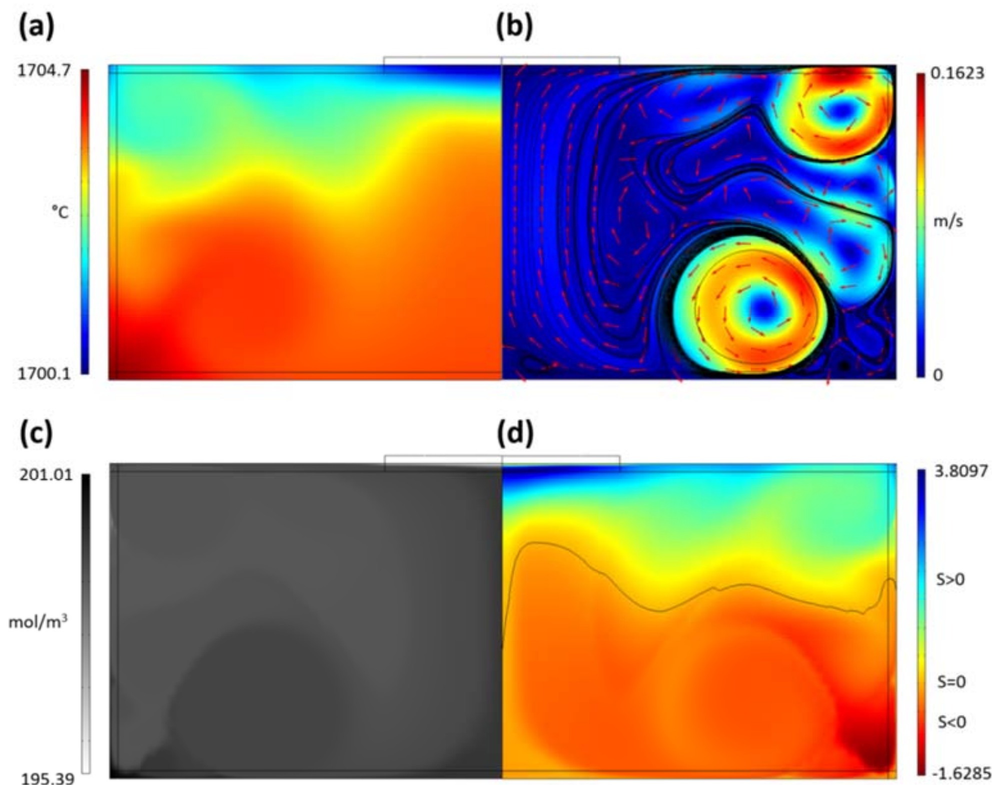

Fig. 13 Résultats de la simulation pour (a) la température, (b) la vitesse du fluide, (c) la concentration en carbone et (d) la sursaturation dans le liquide. Sur (b), les flèches rouges indiquent que les vecteurs vitesse normalisée du fluide et les lignes noires solides représentent des lignes de vitesse. La ligne noire (S = 0) en (d) est dessinée pour séparer les zones sursaturées et sous-saturées. La fréquence de fonctionnement de la bobine d'induction est de 14 kHz

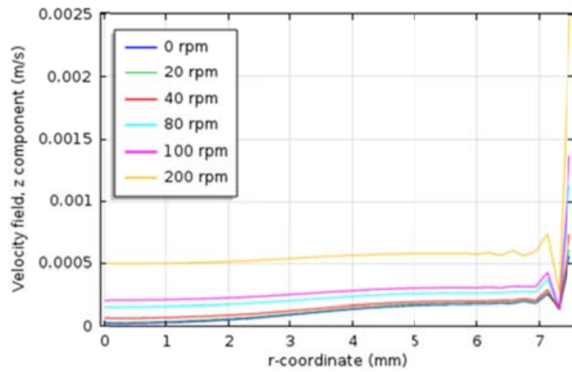

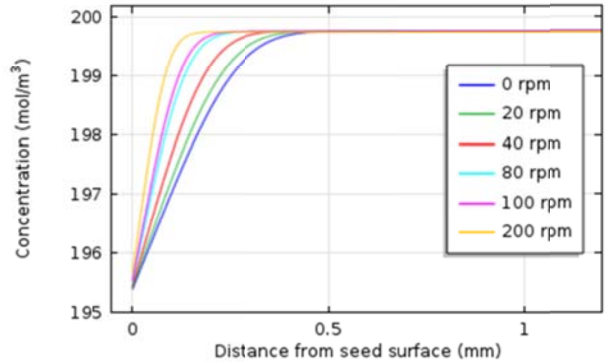

Fig. 14 (a) Distribution de la composante axiale du champ de vitesse dans le liquide à 0,1 mm en dessous du germe le long d'un rayon du germe (b) la concentration en carbone le long de l'axe de symétrie dans la zone proche du germe pour différentes vitesses de rotation

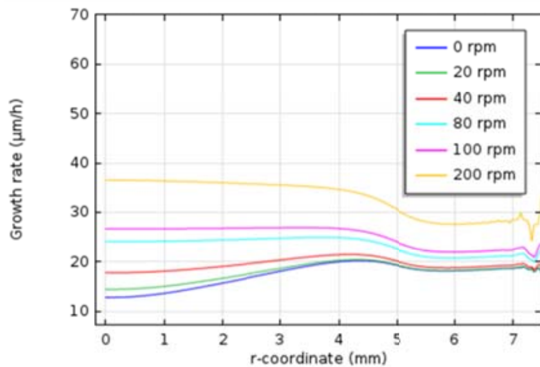

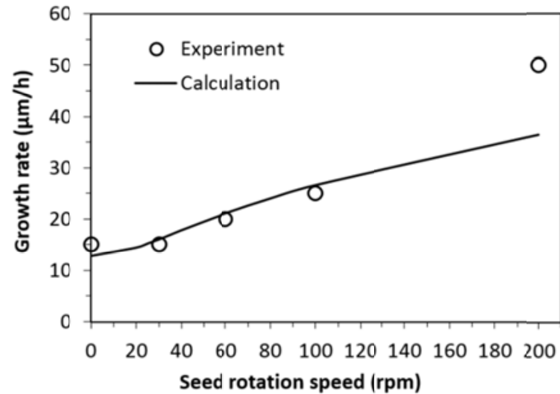

Fig. 15 (a) profil de vitesse de croissance le long du rayon du germe pour différentes vitesses de rotation (b) vitesse de croissance au centre du germe tracée en fonction de la vitesse de rotation superposée aux résultats expérimentaux

Lorsque la rotation du germe est introduite dans le modèle, les résultats obtenus semblent très similaires aux résultats sans rotation (Fig. 13 b). Cependant, la vitesse du fluide juste en dessous du cristal augmente lorsque la vitesse de rotation du germe augmente. Un exemple de la composante axiale de la vitesse du fluide est illustré à la figure 14a. La composante axiale de la vitesse (v_z) est l'un des paramètres principaux qui régit le transport de masse dans le sens axial. L'augmentation de la composante axiale de la vitesse du fluide lors de l'augmentation de la

vitesse de rotation permet d'améliorer la vitesse de transport du carbone dans le liquide vers la surface du cristal (réduction de l'épaisseur de la couche limite) comme en témoigne l'augmentation du gradient de concentration du carbone vers le germe (figure 14b).

La vitesse de croissance augmente avec la vitesse de rotation du substrat. En fait, le gradient de concentration axial varie le long du germe. La vitesse de croissance tracée le long du rayon du germe en fonction de la vitesse de rotation est représentée sur la Fig. 15a. La vitesse de croissance au centre du germe est tracée en fonction de la vitesse de rotation et est comparée avec les résultats expérimentaux en utilisant les mêmes conditions de croissance (Fig. 15b). Les résultats numériques obtenus sont en accord avec les expériences.

L'utilisation d'une vitesse de rotation élevée du substrat améliore la vitesse de croissance du cristal. Cependant, les expériences de croissance utilisant des germes ayant un angle de désorientation avec une vitesse de rotation élevée du substrat met en évidence des instabilités (macros-marches) à la surface du cristal. Ces observations ont été plutôt inattendues, tout comme sous les mêmes conditions une morphologie de surface lisse a été obtenue. Pour cette raison, il est intéressant d'étudier ce type d'instabilité pour ce type de germe et à haute vitesee de rotation du cristal. Étant donné que le modèle pour le processus de croissance TSSG est correctement validé avec l'expérience, il est possible d'aller plus loin afin de décrire l'interaction entre l'écoulement du fluide et la direction de croissance des marches sur la formation des macros marches.

En ce qui concerne la description quantitative de la croissance des marches, nous introduisons le "paramètre de phase" :

$$\Psi = \sin(\theta + \alpha + \xi), \tag{17}$$

où θ est l'angle défini dans un cercle unité et sert à définir la position sur le cristal. α est l'angle entre l'orientation des marches et la direction de désorientation où les valeurs positives et négatives indiquent que l'angle tourne respectivement dans les sens horaire et antihoraire. Un calcul trigonométrique nous donne l'angle de déviation ξ :

$$\xi(r) = \tan^{-1}\left(\frac{\Delta \mathrm{v}_r}{\Delta \mathrm{v}_\phi}\right) = \tan^{-1}\left(\frac{\mathrm{v}_r(r, z_{fluid}) - \mathrm{v}_r(r, z_{seed} = 0)}{\mathrm{v}_\phi(r, z_{fluid}) - \mathrm{v}_\phi(r, z_{seed} = 0)}\right), \tag{18}$$

où r est la distance depuis le centre du germe et z est la position dans le liquide sous l'interface liquide-germe. Le paramètre de phase varie entre -1 et 1, où les valeurs positives et négatives correspondent respectivement aux écoulements parallèles et antiparallèles. La valeur devient nulle si le la direction d'avancée de marches et la direction de l'écoulement du fluide sont perpendiculaires. Pour un train de marches orienté dans la direction [11-20], α devient nul. En ce qui concerne la symétrie d'ordre 6, représentant le système hexagonal de SiC (Fig. 16 a), α est égal à pour les facettes (01-10) - 30º et les facettes (10-10) 30º.

Dans les expériences de croissance, un germe avec un angle de quelques degrés de désorientation (0001) vers la direction [11-20] a été utilisé fournissant l'homoepitaxy par l'intermédiaire de la croissance par avancée de marches. Pour la croissance de monocristaux de SiC sous condition de sursaturation faible, la vitesse de croissance moyenne est plus grande sur les plans {11-2n} que sur les plans {1-10n}. C'est le cas pour les conditions typiques de croissance pour le procédé TSSG effectué dans des conditions proches de l'équilibre thermodynamique. En outre les marches à la surface sont concentrées surtout pour le procédé de croissance en solution. Donc au lieu d'avoir une seule marche et un train de marches droit et régulier, une morphologie possible de la surface peut être constitué de recouvrement de marches et devenir des marches en zig-zag avec des fronts de marche dans les directions (10-1n) et (01-1n) considérant que la forme cristalline est limitée par les fronts de marche lents. Dans ce travail, seul le modèle bidimensionnel est considéré.

Ainsi, les surfaces de recouvrement (facettes) dans les directions [10-1n] et [01-1n] peuvent être projetées sur le plan c (0001). Cela nous permet d'envisager l'orientation des marches sur le plan c tel que les plans (10-10) et (01-10) représentent respectivement les facettes (10-1n) et (01-1n). Les résultats pour des écoulements azimutaux et radiaux positifs sont indiquées respectivement sur la Fig. 16 b et Fig. 16 c. Quatre domaines A-D sont séparées par des lignes de transition. Les conditions d'écoulements parallèles sont remplies pour les deux facettes {1-100} quand la valeur de Ψ de ces deux facettes sont positifs (zone B). Les facettes (10-10) ou (01-10) permettent de compléter respectivement, les résultats pour un écoulement parallèle dans les zones C et A. Seul un écoulement antiparallèle a été obtenu dans la zone D pour les deux facettes {1-100}.

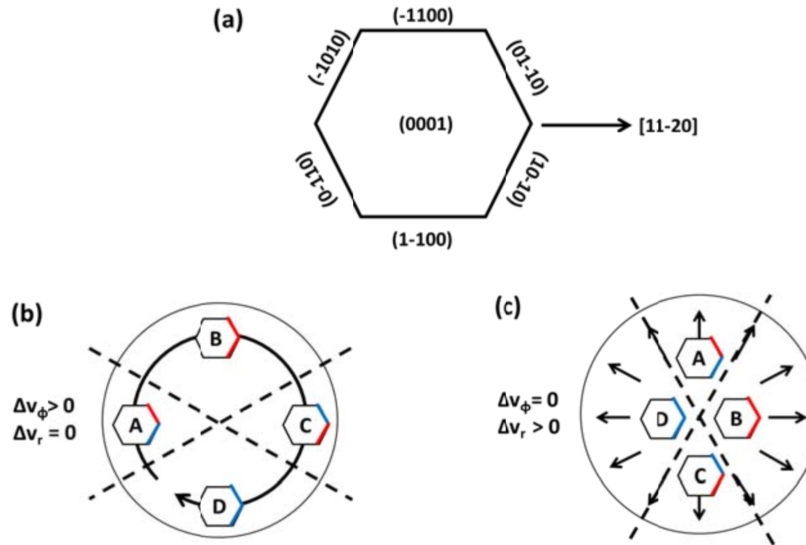

Fig. 16 (a) Représentation schématique du plan (0001) dans le système hexagonal et (b-c) interaction entre l'écoulement du fluide et la croissance par avancée de marches sur un germe circulaire de SiC désorienté de quelques degrés dans la direction [11-20]. Les flèches indiquent la direction de l'écoulement. Les lignes rouges et bleues sur l'hexagone représentent respectivement les conditions d'écoulement parallèle et antiparallèle

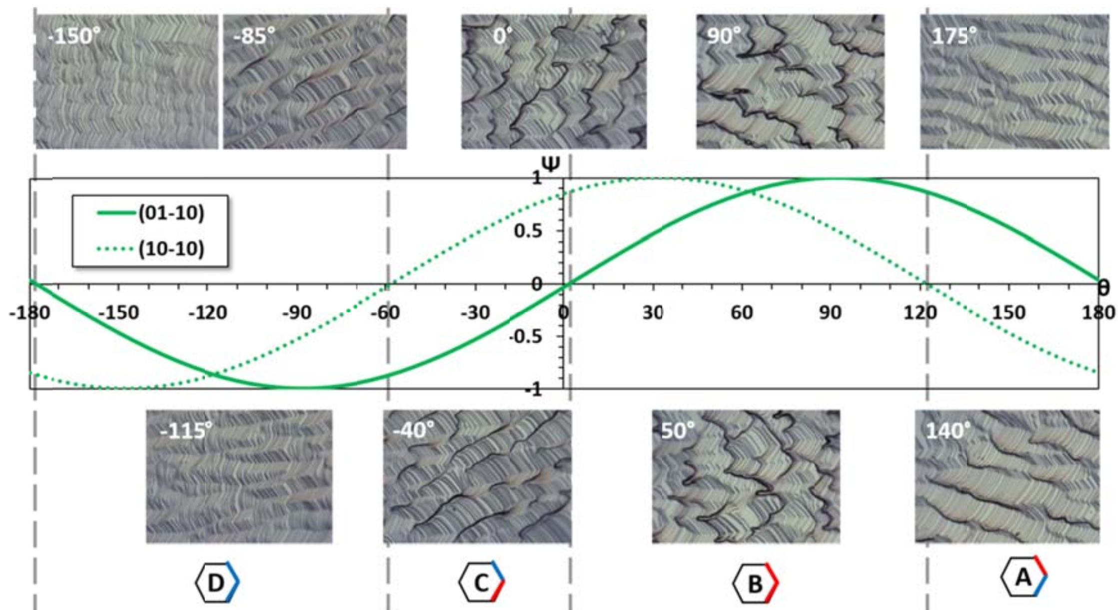

Fig. 17 Comparaison entre la formation des macro-marches, observée à partir de l'expérience et du comportement prévues à partir des paramètres de phase en utilisant de manière combinée la modélisation analytique et numérique. L'angle θ indiqué dans chacune des photos, se réfère à la position où la photo a été prise sur le cristal, par rapport à la direction [11-20]

Dans le cas d'une vitesse de rotation élevée de 100 tr/min dans le sens antihoraire, les valeurs de vitesse du fluide pour les composantes radiales et azimutales par rapport au germe peuvent être calculées. Près de la périphérie du germe, ξ est évaluée à près de 28º. Le diagramme des paramètres de phase, pour ces conditions de croissance est tracé sur la Fig. 17 pour les deux facettes (10-10) et (01-10), où les zones de A à D sont séparés par des lignes de transition. La surface du cristal obtenu à partir d'un germe 4H-SiC (0001) avec 4º de désorientation vers [11-20] est comparée avec le diagramme. La formation de macro-marches (les lignes sombres formées par accumulation de plusieurs micro-marches) est en corrélation avec le diagramme des paramètres de phase. Le critère d'écoulement parallèle pour la facette (zone A) (01-10) permet la formation de macro-marches principalement à proximité du plan (01-10). Le critère d'écoulement parallèle pour les deux facettes (01-10) et (10-10) (zone B) et provoque la possibilité de former des macro-marches en zig-zag tandis que la caractéristique principale est toujours régie par le paramètre de phase dominant. Les macro-marches plus nombreuses à proximité du plan (10-10) sont observées dans la zone C où la condition d'écoulement parallèle est remplie uniquement pour les facettes (10-10). Dans la zone D, seulement un écoulement antiparallèle est prévu et la morphologie de surface est beaucoup plus lisse que dans les autres zones. Le diagramme de paramètre de phase montre une bonne corrélation entre les conditions d'écoulement et la formation des macro-marches.

Conclusion

Dans le cadre de cette thèse, nous avons utilisé la modélisation numérique comme un outil pour la caractérisation de procédés. Cet outil a été en mesure de fournir une évaluation des paramètres physico-chimiques et leurs distributions dans la cavité de croissance permettant d'améliorer le contrôle du procédé de croissance et de mieux les comprendre.

Avec la modélisation du transfert de chaleur et des phénomènes électromagnétiques, la distribution de température dans le réacteur de croissance peut être obtenue. C'est l'une des informations fondamentales pour les fabricants de cristaux car le gradient de température créé une force motrice permettant la croissance des cristaux. Le modèle de transport de masse est combinée avec la mécanique des fluides et le transport des espèces gazeuses. Dans le cadre de la croissance en phase vapeur (PVT), une attention particulière a été portée sur les conditions aux limites et le modèle chimique aux interfaces solide vapeur. En utilisant la modélisation

numérique avec une approche couplée et la thermodynamique, la condition de stœchiométrie a été respecté avec succès, donnant des informations supplémentaires sur la chimie des cristaux. Les résultats de la modélisation ont été validés et un bon accord avec les expériences a été obtenu.

Plus important encore, cette approche a vraiment ouvert la voie pour accéder aux paramètres physico-chimiques dans le cristal et plus précisément les activités des atomes de Si et de C en solution solide de SiC, durant la phase de croissance et de leur dépendance sur les paramètres du procédé. Des corrélations entre la qualité des cristaux et l'apparition de polytype cubique ou hexagonal et la densité de défauts ont été proposés. La corrélation avec la concentration de dopage a également été suggérée comme une possible extension du modèle. Ces résultats ont été discutés sur la base des articles trouvés dans la bibliographie, tandis que les mécanismes réels ne sont pas encore clairs. Ainsi, l'extension du modèle actuel et d'autres études sur les mécanismes responsables des corrélations sont requis.

Pour la modélisation complète du procédé de croissance en phase liquide (TSSG), il est nécessaire de coupler les phénomènes électromagnétiques, les transferts thermiques et la mécanique des fluides. On a étudié les effets des paramètres du procédé tel que la vitesse de rotation de cristal. Quatre paramètres principaux peuvent être étudiés en cours de la croissance : la température, le champ de vitesse, le profil de concentration et la sursaturation. La convection électromagnétique à basse fréquence est la principale contribution régissant le procédé de croissance. Pour des conditions de croissance donnée, on peut améliorer la vitesse de croissance en augmentant la vitesse de rotation du substrat. Le calcul de la vitesse de croissance en fonction de la vitesse de rotation est en bon accord avec les expériences.

De plus, l'association de la modélisation analytique et numérique a été développée permettant une meilleure compréhension de l'interaction entre l'écoulement du fluide et la croissance par avancée de marches qui affecte la morphologie du cristal. Le paramètre de phase vise à établir une corrélation entre la formation des macro-marches avec l'écoulement du fluide. Ce modèle a été validé avec succès avec les résultats expérimentaux. En delà de ces avancés, le procédé de croissance TSSG doit être amélioré afin d'obtenir une croissance de monocristaux de SiC de haute qualité.

Il devra permettre le contrôle de la convection du fluide et la suppression des instabilités de croissance. Le mécanisme de base décrivant l'interaction à l'interface liquide-creuset reste à étudier, afin de donner des conditions aux limites plus appropriées (plutôt que d'imposer concentration d'équilibre) dans le cadre de la modélisation du transport de masse.

La présente thèse contribue au développement d'une meilleure compréhension des procédés de croissance de SiC. L'utilisation simultanée de l'expérience, la caractérisation et la modélisation numérique est un facteur clé pour obtenir une description complète des procédés. Il est nécessaire de poursuivre les extensions au modèle existant en associant des expériences et des caractérisations additionnelles.

Summary of the thesis

Silicon Carbide (SiC) is one of the most desirable materials for power electronic devices. The development of the growth process, to achieve larger size and higher quality is on the way. Even if modeling has proved its ability to assist the optimization of the growth processes, there are still some strong issues which are not considered in a satisfactory way. This thesis aims to use the modeling tools to tackle those challenging fundamental and technological issues on both industrially used PVT and emerging TSSG processes.

In the PVT process, special attention is paid to the physical chemistry at the solid-vapor interfaces. Especially, we investigated the way to model the stoichiometric crystallization of SiC from a non-congruent vapor as the Hertz-Knudsen model was shown to be not adapted. We thus considered SiC as a solid solution using coupled mass transport modeling and thermodynamics. This approach gives an assessment to the chemistry of the SiC crystal which can be linked to the controllable parameters. Such correlations may serve as a basis to control the points defect density, stable polytypes, and doping concentration. Concerning the TSSG process, the effects of crystal rotation speed and operating frequency are studied. The electromagnetic convection is the main contribution governing the growth process using low frequency while the combined buoyancy and Marangoni convections become dominant at high frequency. In the experimental conditions using low frequency, the crystal growth rate could still be enhanced by increasing the rotation speed. The phase parameter is also introduced using the combined fluid dynamics and analytical modeling. This provides a comprehensive visualization of the interactions between fluid flow and step flow and a guideline to improve the surface morphology of the crystal.

Résumé de la thèse en français

Le carbure de silicium (SiC) est l'un des matériaux les plus prometteurs pour les dispositifs électroniques de puissance. Même si la modélisation a prouvé sa capacité à assister le développement du procédé de croissance des cristaux de SiC, de nombreux aspects ne sont toujours pas décrits de façon satisfaisante. Cette thèse a pour but d'utiliser les outils de modélisation pour étudier les phénomènes fondamentaux ayant lieu dans la croissance massive du SiC, que ce soit en phase vapeur (PVT) ou en phase liquide (TSSG).

Pour la méthode PVT, une attention particulière est portée sur la physico-chimie de l'interface solide-vapeur. Pour simuler la cristallisation stœchiométrique du SiC à partir d'une phase gazeuse non-congruente, phénomène mal décrit par le modèle d'Hertz-Knudsen, nous avons considéré le SiC comme une solution solide en utilisant la modélisation couplée du transfert de masse et de la thermodynamique. Cette approche donne une évaluation de la composition du cristal de SiC qui peut être liée à des paramètres contrôlables. De telles corrélations peuvent servir de base pour contrôler la densité de défauts ponctuels, la stabilité des polytypes et la concentration de dopage. Dans le cas du procédé TSSG, les effets de la vitesse de rotation du cristal et de la fréquence du champ magnétique sont étudiés. La convection électromagnétique est la principale contribution régissant les mouvements de fluide à basse fréquence alors que la convection naturelle et l'effet Marangoni deviennent dominants à haute fréquence. Dans les conditions expérimentales utilisant les basses fréquences, la vitesse de croissance du cristal pourrait encore être accrue en augmentant la vitesse de rotation. Une modélisation analytique, couplée aux calculs de dynamique des fluides a permis de décrire les interactions entre le flux de liquide et la direction de propagation des marches de croissance à la surface du cristal. Un paramètre de phase a été introduit comme critère d'apparition de macromarches, à l'origine d'instabilités morphologiques.